

**Mechanism of Hot-Cracking during Electron Beam Powder  
Bed Fusion of Co-29Cr-10Ni-7W Alloy**

Minh Anh Luan Phan

A thesis submitted to Auckland University of Technology in fulfilment of the requirements for  
the degree of Doctor of Philosophy (PhD)

**2019**

School of Engineering, Computer and Mathematical Sciences

## Abstract

Powder-bed fusion (PBF) additive manufacturing has emerged as an innovative and new way of fabricating highly complex geometrical parts. However, applying electron beam powder bed fusion (EB-PBF), one of the two major PBF processes, to the difficult-to-weld Co-29Cr-10Ni-7W alloy result in extensive hot cracking along the columnar grains boundaries. Current literature is not clear as to whether solidification or liquation cracking is the initiation mechanism and how these two contribute to crack growth during EB-PBF of difficulty-to-weld alloys. The major aim of this work is to understand the solidification, how cracks develop and the contributions of liquation and hot tear to crack growth during EB-PBF.

To understand solidification sequence and phase transition temperatures of the alloy, differential scanning calorimetry (DSC) experiments were conducted. This is followed by a series of EB-PBF experiments using an Arcam® A1 machine. EB-PBF parameters were selected from the preliminary work to ensure samples to be fully dense. For the main study, EB-PBF specimens were made with one focused and one defocused beam while other parameters kept unchanged. This is to provide conditions of two different track shapes for studying grain growth. To study the solidified microstructure (including cracks), optical and scanning electron microscopy (SEM) were used. To reveal the crack network, EB-PBF samples were progressively ground off layer-by-layer starting from the top surface. Numerical simulation of a single scan using ANSYS-APDL software was carried out to illustrate how the scan direction may relate to directions of thermal stresses during track solidification. Finally, single track experiments by having a single track in the last layer were conducted to provide samples so that how crack initiated may be understood.

DSC plots have shown and confirmed the wide freezing range of about 180°C, thus indicating the alloy being susceptible to hot cracking. The two different focus offset values have resulted in the shape of melt pool/track being varied significantly and thus the grain growth direction changed considerably for a significant portion of the track. It has been found that as the beam became more focused, the cross-section of the melt track became more U-shaped. The lateral heat transfer dominance in the top region then resulted in the growth of dendrites, epitaxial and in columnar form, horizontally. The layer thickness of these horizontal dendrites is up to 80 µm and is significant considering the additive layer thickness being 70 µm. Horizontal grain growth has been found to effectively stop crack propagation. Thus, further modification on the EB-PBF parameters has successfully resulted in a novel grain structure that no cracks are observed.

Examination of surface morphologies shows that cracks appear on the samples' top surface have hot tearing characteristics while inter-granular cracks indicate liquation cracking features. On examining the crack network, firstly, it has been observed that surface cracks tend to orientate normal to the scan direction which changes after each layer. Computer simulation has

demonstrated the dominant tension parallel to scan direction. Secondly, the relationship between the orientated cracks on the surface and crack networks beneath the top layer has been shown to be the result of scan direction change after each layer. From this, how crack networks have grown and how liquation has assisted this growth have been demonstrated.

Single track experiments have been found to be useful to reveal crack initiation. Examination of the single-track samples has shown that cracks in single tracks originated from outside of the track. It can be suggested that at one point of time during the building process of multi-layers, hot cracking initiated from liquation cracking. On the other hand, as identified in this research, the cracking propagation is a combined event of liquation cracking, liquid-backfill healing, and hot tearing, which is the overall mechanism of crack initiation and growth specific to EB-PBF. The dominance of high angle misorientation grain boundaries to assist the crack growth will also be demonstrated. The approximate length of liquation that has been observed has suggested a maximum temperature of reached  $2 \times 10^6$  K/m during the current EB-PBF. This value is close to those predicted by simulations stated in the literature.

## List of Publications

1. M. Phan, D. Fraser, S. Gulizia, and Z. Chen, "Horizontal growth direction of dendritic solidification during selective electron beam melting of a Co-based alloy," *Materials Letters*, vol. 228, pp. 242-245, 2018
2. M. Phan, D. Fraser, Z. W. Chen, and S. Gulizia, "Solidification and Microstructural Control in Selective Electron Beam Melting of Co-29Cr-10Ni-7W Alloy," in *Materials Science Forum*, 2018, pp. 902-907.

To be submitted:

(The manuscript has been written and will be submitted after the thesis embargo period)

3. M. Phan, D. Fraser, S. Gulizia, and Z. Chen, "On the mechanism of hot cracking during selective electron beam melting of a difficult-to-weld Co-based superalloy"

## **Acknowledgement**

I would like to express my deep gratitude and appreciation to my primary supervisor, Professor Zhan Chen for his dedication, support, and patience to my PhD study. Professor Zhan Chen has shaped my research career not only in the role of a supervisor but also as an examiner. His wisely and comprehensive critiques have helped me to gain valuable research experience.

I would also appreciate my second supervisor, Dr. Darren Fraser for his enthusiasm and patience in providing specific answers to all my questions. With his expertise, Dr. Darren Fraser has assisted me to understand the state-of-the-art of the electron beam powder bed fusion process so that I have fundamental knowledge to complete the study.

I would also like to thank CSIRO Manufacturing and the ASC Pty Ltd for financial and technical support to the project.

I would like to extend my sincere thanks to Mr. Stefan Gulizia from CSIRO Manufacturing for all his encouragement, to Dr. Mikael Johansson from the ASC Pty Ltd for his technical advice, to Dr. Mona Aziziderouei, Dr. Yuan Tao for their contributing suggestion and discussion to my study.

I wish to thanks to various people who have supported me throughout my study: Professor Tim Pasang and Dr. Maziar Ramezani, the AUT lab technicians and Ms. Josephine Prasad.

Last but not least, I would like to express my deepest appreciation to my beloved wife, Ms. Ngoc Thanh My Nguyen, who has loved me wholeheartedly. She is always by my side, encourages me whenever I feel tired. She has been with me in all the difficult times for the last 12 years and been the energy source that motivates me to the completeness of my PhD study.

# Table of Contents

Abstract.....	ii
List of Publications .....	iv
Acknowledgement .....	v
Table of Contents.....	vi
List of Figures.....	ix
List of Tables .....	xviii
Nomenclature.....	xix
Attestation of Authorship.....	xxi
CHAPTER 1: INTRODUCTION .....	1
1.1. Introduction to powder bed fusion additive manufacturing.....	1
1.2. Electron beam powder bed fusion process.....	1
1.3. Introduction to Co-29Cr-10Ni-7W alloy .....	4
1.4. Extensive cracking in EB-PBF of Co-29Cr-10Ni-7W alloy.....	5
CHAPTER 2: LITERATURE REVIEW .....	8
2.1. Solidification of Co-29Cr-10Ni-7W alloy .....	8
2.2. Solidification during EB-PBF process.....	14
2.2.1. Solidification modes .....	14
2.2.2. Melt pool and track formation .....	22
2.2.3. Grain growth directions during solidification .....	27
2.3. Observation and characterization of cracking in PBF-AM processes.....	33
2.3.1. Hot tearing/Solidification cracking.....	33
2.3.2. Liquation cracking .....	38
2.3.3. Ductility-dip cracking .....	40
2.3.4. Reheat cracking and strain-age cracking.....	43
2.3.5. Identification of hot cracking and solid-state cracking .....	44
2.4. Current understanding of cracking in PBF-AM processes .....	47
2.4.1. Cracking during EB-PBF .....	47
2.4.2. Cracking reported in other PBF-AM processes .....	56
2.5. Summary of the literature review.....	61

CHAPTER 3: EXPERIMENTAL PROCEDURE .....	64
3.1. EB-PBF process .....	64
3.2. Powder materials.....	71
3.3. Preliminary design of EB-PBF experiments.....	72
3.4. Design of EB-PBF experiments.....	77
3.5. Differential Scanning Calorimetry (DSC): .....	81
3.6. Specimen preparation for metallurgical analysis .....	84
3.7. Specimen preparation for characterizing the crack network.....	85
3.8. Macro and microstructure analytical techniques.....	87
3.9. X-ray diffraction analysis.....	90
3.10. Tensile testing for fracture surface obtaining.....	90
3.11. Numerical simulation by ANSYS ADPL 16.2 .....	91
CHAPTER 4: SOLIDIFICATION DURING ELECTRON BEAM POWDER BED FUSION	94
4.1. Phase transition temperatures during heating and cooling of Co-29Cr-10Ni-7W and Co-29Cr-6Mo alloys .....	94
4.2. Microstructure characterization of EB-PBF of Co-29Cr-10Ni-7W alloy .....	104
4.2.1. Observation of as-built samples.....	104
4.2.2. Grain structures .....	106
4.2.3. Correlation between grain structures and the used EB-PBF conditions .....	109
4.3. Solidification microstructure and cells/dendrites-growth directions in EB-PBF of Co-29Cr-10Ni-7W alloy .....	114
4.3.1. Solidification microstructure.....	114
4.3.2. Effect of focus offset values on formation and geometry of the scanned track .....	120
4.3.3. Melt/track geometries dependent cells/dendrites-growth direction .....	122
4.3.4. Controlling/maintaining horizontal dendrites growth structure .....	123
CHAPTER 5: CHARACTERIZATION OF HOT-CRACKING NETWORKS.....	129
5.1. Observation of cracks .....	129
5.2. Examination of cracks' surface morphologies.....	132
5.3. Crack network along build direction.....	137
5.3.1. Crack network mapping for the FO25 sample .....	138
5.3.2. Crack network mapping for the FO50 sample .....	144

CHAPTER 6: THE HOT-CRACKING MECHANISM.....	149
6.1. Formulating hot cracking mechanism.....	149
6.1.1. Cracks initiation.....	149
6.1.2. Cracks propagation.....	153
6.2. Other influential factors to hot cracking.....	161
6.2.1. Grain boundary misorientation.....	162
6.2.2. Thermal stresses prediction.....	164
CHAPTER 7: CONCLUSION.....	174
References.....	177

## List of Figures

Figure 1. Schematic illustration of the hardware of an EB-PBF machine [4] .....	2
Figure 2. The EB-PBF process cycle [3] .....	3
Figure 3. Schematic illustration on major parameters used in EB-PBF process.....	3
Figure 4. Applications of Co-29Cr-10Ni-7W alloy: First stage vanes/nozzles [10].....	5
Figure 5. Extensive hot cracking networks observed in EB-PBF-fabricated sample .....	6
Figure 6. Effect of adding elements on type of carbides formed in Co-based alloys (assumed %wt of C from 0.1-0.6%) [11].....	9
Figure 7. Microstructure of as-cast FSX-414 alloy: a) Hot tears with $M_{23}C_6$ eutectic carbides; b) $M_{23}C_6$ eutectic carbides and secondary $M_{23}C_6$ carbides; c) $M_7C_3$ , $M_{23}C_6$ primary carbides and secondary $M_{23}C_6$ carbides [13] .....	12
Figure 8. DTA results of seven as-cast FSX-414 specimens: a) on-heating curves and b) on- cooling curves [13] .....	12
Figure 9. Microstructure of sample experienced the standard heat treatments.....	13
Figure 10. Solidification path of Co-29Cr-10Ni-7W alloy summarized based on the literature review of FSX-414 alloy.....	14
Figure 11. Phase diagram, temperature distribution, and solute built-up zone during solidification [16].....	15
Figure 12. The transition of growth morphology from planar, to cellular, to dendritic as compositionally induced undercooling increases. $T$ and $T_{mp}$ [16] .....	16
Figure 13. Schematic summary of solidification morphologies in regards to thermal gradient $G$ and solidification growth rate $R$ (denoted as $V$ in the figure) [17].....	18
Figure 14. a) A moving molten pool with the solid-liquid interface illustration. b) Relationship between solidification modes and $G$ , $R$ [18].....	18
Figure 15. The transition from dendritic to cellular growth morphology observed in [21].....	19
Figure 16. Columnar grains with fine secondary dendrite arms implies dendritic solidification mode in the work of Karimi et al. [23] .....	20
Figure 17. Solidification mode as cellular growth observed in the work of Wang et al. [24] ....	20
Figure 18. Columnar grains structure with sub-cells observed in EB-PBF Co-29Cr-6Mo alloy [35, 36].....	22
Figure 19. Effect of (a). Scanning speed (via SF values) and (b). Beam diameters on the melt pool length and width in EB-PBF of Ti-6V-4Al alloy [61] .....	23
Figure 20. (a). The increasing the cooling rate in EB-PBF Ti-6Al-4V as increasing SF values; (b). Features of tear-drop ripples observed on samples fabricated with different SF values [61] .....	24

Figure 21. (a). Influence of beam offset on melt pool shape and the overlapping area between two adjacent melt pools and (b). Solidified top surface of EB-PBF samples fabricated by different focus offset values at SF98 [62].	25
Figure 22. Single track and multiple tracks experiments in [23] showing the effect of heat accumulation on the formation of melt/track geometries	26
Figure 23. Easy-growth-directions epitaxially follow <100> crystallographic directions in welding solidification [67]	28
Figure 24. Cells-growth directions at the melt pool boundary and the corresponding crystallographic orientation (of grains) in LB-PBF-fabricated Co-29Cr-6Mo alloy [53]	29
Figure 25. (a). EB-PBF-built of Co-29Cr-6Mo alloy [36] and (b). EB-PBF of high-purity copper showing 90° alternating cells/dendrites-growth directions [68]	30
Figure 26. Optical micrographs illustrate the influence of (a). A defocused beam of 500 μm and (b). A focused beam of 400 μm on the melt pool shape in EB-PBF of IN718 Ni-based alloy [21]	31
Figure 27. Observation of a 90° change in cells growth direction in Karimi et al.'s study [23].	31
Figure 28. Tensile properties for Ti-6Al-4V and Co-29Cr-6Mo alloy. YS stands for yield stress at 0.2% engineering offset and UTS stands for ultimate tensile strength [38]	32
Figure 29. (a). Hot tearing in the casting of M206 aluminum alloy [74] and (b). Solidification cracking in laser welding stainless steel 316FR [75]	35
Figure 30. Schematic illustration of hot tearing/solidification cracking mechanism. Larger $\Delta T^*$ results in longer the inter-dendritic liquid film. (image adapted and modified from [76])	36
Figure 31. Model of two grains separated by a uniform liquid metal film in the assumption of complete wetting between grains and melts [70] (original from the work of Dickhaus et al. [85])	37
Figure 32. Two types of the temperature dependence of elongation to failure ( $\epsilon_p$ ) and linear shrinkage $\epsilon_{sh}$ in the semi-solid brittle temperature range [70]	38
Figure 33. Schematic illustration showing a correlation between various zones in a fusion weld in an alloy and the corresponding equilibrium diagram [89]	39
Figure 34. Liquation cracking in the PMZ. The darker area is the fusion zone [90]	39
Figure 35. Illustration of liquation cracking mechanism in welding [73, 91]	40
Figure 36. Sensitive temperature range to ductility-dip cracking [63]	41
Figure 37. (a). Solidification grain boundaries (SGB) and Migrated grain boundaries (MGB). DDC occurs at MGB [92]	42
Figure 38. Pure Ni-200 alloy fracture morphology shows a smooth inter-granular DDC. Pure Ni-200 alloy has no precipitates which increase DDC susceptibility [101]	43
Figure 39. Schematic illustration of thermal cycle associated with reheat cracking in low-alloy steels: (a). Grains in PMZ before welding; (b). Coarser grains due to heat affected by welding; (c). Development of residual stresses incorporating with martensite/bainite transformation; (d).	

Relaxation of stresses, re-precipitation of strengthening precipitates, cracking along grain boundaries [63] .....	44
Figure 40. Solidification crack's the fractured surface of (a). Ni-based alloy and (b). Duplex stainless steel [63] .....	45
Figure 41. Liquation crack's fracture surface of (a). Low-alloy steel HY-100 [109] and (b). Ni-based alloy (Waspaloy) [110] (obtained by Lippold [63]).....	45
Figure 42. DDC fracture surface in Type 310 stainless steel at (a). 750 °C; (b). 950 °C and (c). 1100 °C; (d). Higher magnification of selected location in (c) [63] .....	46
Figure 43. The fracture surface of strain-age cracking in Ni-based alloy 718. (a). Ductile intergranular and (b). Mixed flat and ductile intergranular [63] .....	47
Figure 44. EB-PBF as-built microstructure (along build direction): a) specimens with $E_{line}$ from 0.19~0.205 J/mm. b) Crack-free specimens built with $E_{line}$ from 0.6~0.72 J/mm [117] .....	48
Figure 45. (a) Cracks observed and (b). Relationship between crack density and EB-PBF parameters [118] .....	49
Figure 46. Microstructure of an as-built specimen observed in the central part on an XZ cross-section showing cracks of several millimeters [113] .....	50
Figure 47. Schematic illustration of the last stage of columnar dendritic solidification. (a). "Repulsive" HAGB and (b). "Attractive" LAGB. The liquid is colored white, solid is grey [113] .....	51
Figure 48. Hot cracking observed of various linear energies in EB-PBF non-weldable Ni-based alloy. A single crystal structure was produced and the crack-free sample was achieved [120]	52
Figure 49. Hot cracking in EB-PBF of DZ125 Ni-based alloy. CCG and FCG stand for coarse columnar grain and fine columnar grain structures [121] .....	53
Figure 50. Cracks appear at the top surface in the work of Ramirez et al. [122] showing more severity for the orientation that is normal to the scan direction .....	54
Figure 51. Optical images of EB-PBF build Co-29Cr-6Mo F75 alloys with (a). 0.05 %wt C; (b). 0.1 %wt C and (c). 0.15 %wt C. Crack is shown by red arrows in (c). .....	56
Figure 52. The cracking problem in LB-PBF CM247LC Ni-based samples: (a). Suggested solidification cracking and (b). Suggested solid-state cracking [116] .....	57
Figure 53. Cracking observed in LB-PBF Al7075 alloy samples with various addition of Si content: (a). 0wt%, (b). 1wt%, (c). 2wt%, (d). 3wt% and (e). 4wt%. Cracks are shown by the arrows [124] .....	58
Figure 54. Suggested scenarios for the hot cracking mechanisms in LB-PBF IN738LC [112] .	59
Figure 55. (a). Micro-cracks in as-built LB-PBF of Hastelloy-X. (b). EDS line scans of a crack at medium and high magnification [115] .....	60
Figure 56. Liquation cracking in LAM process showing the initiation of liquation crack started at the 2 <sup>nd</sup> layer after the 3 <sup>rd</sup> deposited [126] .....	61
Figure 57. Traces of liquated Laves phase at the crack surface [126] .....	61

Figure 58. The EB-PBF Arcam A1 machine .....	65
Figure 59. “Smoking” caused by electrostatic repulsion: (a). powder before applying beam, (b). beam-powder interaction and (c). blown-up of powder particles [127] (images originally from the work of Kahnert et al. [128])......	65
Figure 60. Main steps of a EB-PBF building process [129] .....	66
Figure 61. Numerical heat transfer model in EB-PBF of IN718 alloy [130].....	66
Figure 62. The temperature history of EB-PBF build of TiAl alloy [131] .....	67
Figure 63. Melt pool geometries with different focus offset values .....	68
Figure 64. The relationship between (a). Beam current and (b). Scan speed of respective SF values and the building height .....	69
Figure 65. (a). Cross-snacking with the 90° rotation of scan direction every layer and other possible scanning strategies in the EB-PBF Arcam A1 machine (b). 1-D scanning without 90° rotation, (c). Cross-snacking without 90° rotation and (d). Multi-spots scanning .....	70
Figure 66. Powder recycling system. ....	71
Figure 67. Optical systems of the Malvern Mastersizer S .....	72
Figure 68. SEM images of the Co-29Cr-10Ni-7W powder particles.....	72
Figure 69. (a) – (d) The top surface and cross-sectional images of samples with constant LO at 0.13 mm. Note that sample 1 and sample 4 are different in size compared to the others. The SF increases from 24 to 100 from left to right. ....	74
Figure 70. (a) – (d) The top surface and cross-sectional images of samples with constant LO at 0.05 mm. The SF increases from 24 to 100 from left to right.....	75
Figure 71. (a) – (d) The top surface of samples and cross-sectional images of samples with constant LO at 0.0375 mm. The SF increases from 24 to 100 from left to right. ....	76
Figure 72. EB-PBF builds and arrangement of samples per build. Scanning order is also illustrated .....	78
Figure 73. As-fabricated samples from the new EB-PBF experiments. ....	80
Figure 74. Cracking severity in two selected samples. FO values are different while other parameters remained unchanged.....	81
Figure 75. DTA melting of 211.6 mg pure Ag at 10 K/min. (a). $T_{sample}$ and $T_{ref}$ versus time and (b). Differential signal $\Delta T = T_{sample}$ (solid black) – $T_{ref}$ (dashed black) vs time [136].....	82
Figure 76. Interpreter of DTA results [13].....	82
Figure 77. Schematic illustration of a heat-flux DSC furnace.....	83
Figure 78. DSC Netzsch STA 449 F1 system.....	84
Figure 79. Schematic illustration of sectioning of cubic sample for observation of XZ, YZ, and XY cross-sections. ....	85
Figure 80. Illustration of the mounted specimen with two different layers of mounting resins .	85

Figure 81. (a). Illustration on how micro-Vicker indentation was used to control the ground/polished of the amount of material and (b). Geometrical calculation of the impression depth [139].....	87
Figure 82. Illustration of an SEM [140].....	88
Figure 83. (a). Back-scatter Kikuchi pattern from cadmium at 20 keV acquired by an analog video camera; (b). Schematic illustration of diffracting cones with respect to the reflecting plane, the specimen and the phosphor screen [141].....	89
Figure 84. Principal components in an EBSD system [142].....	89
Figure 85. As-fabricated hexagonal bar and as-machined dog-bone tensile sample .....	91
Figure 86. Simulation block model of 10x10x5 mm. ....	93
Figure 87. The DSC on-heating curves of (a). Co-29Cr-10Ni-7W alloy and (b). Co-29Cr-6Mo alloy .....	95
Figure 88. XRD analysis of (a). Co-29Cr-10Ni-7W alloy powder and (b). Co-29Cr-6Mo alloy powder .....	97
Figure 89. Effect of alloying additions on the HCP-FCC transformation in cobalt as a function of solubility in FCC Co [11]. ....	98
Figure 90. The DSC on-heating curve of powder and as-cast Co-29Cr-10Ni-7W samples .....	99
Figure 91. SEM images showing the microstructure of (a) as-cast sample and (b) powder of Co-29Cr-10Ni-7W alloy .....	100
Figure 92. The DSC on-cooling curves of a) Co-29Cr-10Ni-7W alloy and b) Co-29Cr-6Mo alloy .....	101
Figure 93. The specimens after DSC test: a) Co-29Cr-10Ni-7W alloy and b) Co-29Cr-6Mo alloy .....	102
Figure 94. SEM images showing: (a). The surface of FO25 sample; (b) and (c). Higher magnifications of the selected area in (a). Dendrites are seen growing normal to the track boundary .....	105
Figure 95. SEM images showing: (a). The surface of FO50 sample, (b). Higher magnification of the selected area in (a).....	106
Figure 96. Cross-sectional SEM images showing the FO25 sample at (a). The upper part close to the top surface and (b). 7 mm away top surface downward. Cracks are seen at the upper part .....	107
Figure 97. Cross-sectional SEM images showing the FO50 sample at (a). The upper part close to the top surface and (b). 7 mm away top surface downward. Cracks are seen at the upper part .....	108
Figure 98. Recorded data of $v$ , $I$ and the calculated $E_{line}$ along the build direction.....	110
Figure 99. The temperature history of the start plate versus the building height.....	111
Figure 100. Extrapolated melt/track geometries of (a). the FO25 sample and (b). the FO50 sample. Layer boundary can also be identified.....	111

Figure 101. Schematic illustration of the change in grains structure following the change in the thermal gradient along the build direction. Melt/track geometries can be seen to have a significant effect on heat flux directions.....	112
Figure 102. SEM images showing solidification microstructure in the last layer of (a). FO25 sample and (b). FO50 sample. Locations are selected for further examination.....	114
Figure 103. SEM images showing higher magnifications of selected areas in Figure 102a: (a). Top, (b). Mid and (c). Layer boundary .....	115
Figure 104. SEM images showing higher magnifications of selected areas Figure 102b: (a). Top and (b). Layer boundary.....	115
Figure 105. EBSD map and corresponding SEM image showing crystallographic orientation near the top surface of the FO50 sample. The images were obtained in the XZ cross-sections	116
Figure 106. Illustration of how the average value of $\lambda_l$ is obtained by using SEM image in XY cross-section.....	118
Figure 107. Solidification map for LB-PBF Co-29Cr-6Mo alloy and several metallic alloys (adapted from [149]).....	120
Figure 108. a) Optical micrograph of cross-sectional view and (b) SEM image and EBSD orientation map showing the horizontal dendrite layer up to $\sim 80 \mu\text{m}$ . .....	121
Figure 109. Optical micrograph of cross-sectional view displaying columnar dendrites grown completely along the build direction. Track boundaries are indicated. ....	122
Figure 110. Schematic illustration of a melt track, colored red, during EB-PBF with heat flow direction normal to track boundary indicated. ....	123
Figure 111. Illustration of layer thickness selection for maintaining H-dendrites.....	124
Figure 112. Optical micrograph showing the microstructure of EB-PBF fabricated sample using FO25 conditions with layer thickness $300 \mu\text{m}$ and line offset $0.1 \text{ mm}$ .....	125
Figure 113. Optical micrograph showing the microstructure of EB-PBF fabricated sample using FO25 conditions with layer thickness $300 \mu\text{m}$ and line offset $0.05 \text{ mm}$ .....	126
Figure 114. 3D illustration of the novel grain structure obtained showed in Figure 113. Track boundary, layer and dendrites growth direction is indicated. The blue grain can be seen to have an irregular shape.....	128
Figure 115. Stereo-optical microscopy images showing the top surface of (a). FO25 and (b). the FO50 samples.....	129
Figure 116. (a) & (c). OM and SEM images showing groove and cracks in the FO25 sample and (b) & (d). OM and SEM images showing rugged cracks in the FO50 sample. It is noted that a groove as pointed by the arrow is not easy, but still able to be observed on the FO25 sample's surface.....	130
Figure 117. XZ and YZ cross-sectional SEM images showing the topmost layers of (a). FO25 sample and (b). FO50 sample .....	131

Figure 118. SEM images at low and high magnification showing hot tears identified as the cracking mechanism for the surface cracks in (a). FO25 sample and (b). FO50 sample.....	133
Figure 119. (a). Stereo OM image and (b). SEM image showing the fracture surface of the tensile tested sample. ....	134
Figure 120. SEM image showing high magnification of location I in Figure 119a. The relatively smooth surface in the upper area indicates that no deformation may have occurred.....	135
Figure 121. SEM images showing cracks observed from the fracture surface at (a). Location II and (b). Location III, as depicted in Figure 119b.....	136
Figure 122. Cross-sectional SEM images showing intergranular cracks and grain boundaries decorated with carbides/precipitates in the FO25 sample.....	137
Figure 123. SEM image showing the top surface of the FO25 sample contains Crack-1 and Crack-2.....	138
Figure 124. Cross-sectional SEM images showing (a). after a first 16 $\mu$ m ground off and (b). after an additional 32 $\mu$ m ground off from the second time grinding.....	139
Figure 125. SEM image showing a superimpose of cracks in Figure 123 onto Figure 125a. Red arrows are cracks in Figure 125a and blue arrows are cracks in Figure 123 .....	140
Figure 126. Cross-sectional image after 95 $\mu$ m ground off from the top surface. H-dendrites layer is no longer be seen. Crack network starts to show up .....	141
Figure 127. Superimpose of Crack-1a (blue arrows) onto the underneath cracks (red arrows) of the respective location.....	142
Figure 128. Cross-sectional SEM images (left) and OM images (right) of (a). Last portion of Layer 1 <sup>st</sup> , (b). Layer 2 <sup>nd</sup> and (c). Layer 3 <sup>rd</sup> .....	143
Figure 129. High magnification SEM images showing the outlined area 2 in Figure 128, demonstrated cracks start to be seen as consecutive grinding downward from Layers 1 <sup>st</sup> -3 <sup>rd</sup> ..	144
Figure 130. SEM image showing the top surface of the FO50 sample with highlighted cracks (white arrows) and the scan direction (red arrows).....	145
Figure 131. Cross-sectional SEM images (left) and OM images (right) of (a). Layer 1 <sup>st</sup> , (b). Layer 2 <sup>nd</sup> and (c). Layer 3 <sup>rd</sup> , (d). Layer 4 <sup>th</sup> and (e). Layer 5 <sup>th</sup> .....	147
Figure 132. High magnification SEM images showing the outlined area 1 of five layers obtained in Figure 131, demonstrated cracks start to be seen as consecutive grinding downward .....	147
Figure 133. (a). SEM image showing the top surface of the single track sample and selected locations for examination and (b). OM image showing 3D views of the sample's microstructure .....	151
Figure 134. SEM images showing examined locations TB1 to TB4 outlined in Figure 133a, (a) to (d) respectively. Red arrows represent heat flux directions. Evidence of grain boundary liquation, re-solidified microstructure, and liquation cracking can be observed and pointed out by black arrows.....	152

Figure 135. Schematic illustration suggesting the liquation cracking initiation. (a). Grain boundary liquation always occurs but no liquation cracking at $H < H'$ ; (b). As $H > H'$ , thermal stresses are sufficient to trigger liquation cracking to occur. The value of $h'$ depends on the sample's geometry and the used EB-PBF parameters .....	153
Figure 136. Schematic illustration the sequence of crack growth from Layer 5 <sup>th</sup> to a hypothetical Layer 0 of area 1 outlined in Figure 131 for the FO50 sample. The suggestion of a liquid film backfills the crack and how the crack is healed and re-cracked with respect to the scan direction .....	154
Figure 137. SEM images showing (a). Observation of the re-solidified microstructure indicating backfilled healing that prevents crack to propagate to the top surface. (b). Higher magnification of the selected area in (a); (c). Higher magnifications of the selected area in (b) and (d). Higher magnifications of the selected area in (c). The re-solidified microstructure is shown by the black arrow .....	155
Figure 138. Illustration of (a). Hot cracking through cycles of liquation cracking and solidification cracking, healing of crack and then liquation cracking and solidification cracking again during building and (b). Temperature distribution near layer boundary. ....	156
Figure 139. OM images showing the as-polished the FO50 sample: (a) ZY cross-section and (b) ZX cross-section. ....	157
Figure 140. SEM images showing EB-PBF Co-29Cr-6Mo sample: (a). ZX cross-section of the last layer; (b). YX cross-section of the last layer; (c). High magnification of selected location in Figure 140a and (d). High magnification of selected location in Figure 140c. Grain boundary with no re-solidified microstructure shown in (b), (c-d) indicates very low grain boundary liquation .....	159
Figure 141. SEM image showing a considerable amount of the second phase observed at grain boundaries in EB-PBF Co-29Cr-10Ni-7W alloy .....	160
Figure 142. $\Lambda$ -shape curve showing concentration dependence of the HCS criterion as compared from various studies by Rappaz et al. [83].....	161
Figure 143. Hot cracking sensitivity versus carbon content suggested for Co-29Cr-6Mo alloy. ....	161
Figure 144. Evidence showing crack growth may be more relating to growth of high misorientation of secondary dendrites. ....	163
Figure 145. Mechanical boundary conditions used in the model.....	166
Figure 146. Temperature-dependent material properties of Co-29Cr-10Ni-7W alloy: (a). Specific heat; (b). Thermal conductivity; c) Thermal expansion co-efficiency and (d). Young modulus.....	166
Figure 147. Simulation illustrating the melt pool and corresponding XY-stress component along the track at (a). $t = 0.01$ s and (b). $t = 0.03$ s .....	168

Figure 148. Simulation showing temperature distribution and corresponding XY-stress component along the track at (a).  $t = 0.06$  s and (b).  $t = 0.1$  s, after the scan ends at  $t = 0.05$  s 170

Figure 149. Simulation result showing the principal stresses' vectors distributed throughout the track at (a).  $t = 0.05$  s and (b).  $t = 0.1$  s (at higher magnification). White, yellow and blue arrows represent for the  $\sigma_1$ ,  $\sigma_2$  and  $\sigma_3$  principle stresses, respectively. The size of the arrows illustrates the stress intensity. Outward arrow demonstrates tensile stress and vice versa..... 172

## List of Tables

Table 1. Composition (wt%) of FSX-414 Co-based alloy.....	72
Table 2. EB-PBF parameters used in preliminary work .....	73
Table 3. EB-PBF parameters used in the new experiment.....	77
Table 4. Influence of alloying elements on the melting temperature of Co-Cr alloys.....	103
Table 5. Grain boundary (GB) number and the corresponding misorientation angle of the two neighboring grains. ....	164
Table 6. Parameters used in simulation .....	165

## Nomenclature

AM	Additive Manufacturing
PBF	Powder bed fusion
CAD	Computer-aided design
EB-PBF	Electron beam powder bed fusion
LB-PBF	Laser beam powder bed fusion
HCS	Hot cracking sensitivity
FS	Fusion zone
PMZ	Partially melted zone
HAZ	Heat affected zone
DDC	Ductility-dip cracking
DTA	Differential Thermal Analysis
DSC	Differential Scanning Calorimetry
OM	Optical Microscopy
SEM	Scanning Electron Microscopy
EBSD	Electron Backscatter Diffraction
XRD	X-ray diffraction
U (kV)	Accelerated voltage of the EB-PBF machine
I (mA)	The beam current of the EB-PBF machine
P (W)	Beam power
SF	Speed function
FO (mA)	Focus offset
v (mm/s)	Scanning speed
h (mm)	Line offset
t ( $\mu\text{m}$ )	Layer thickness
$\varnothing_{\text{beam}}$	Beam diameter
$E_{\text{line}}$	Line energy density
$E_{\text{Vol}}$	Volumetric energy density
BD	Building direction
SD	Scanning direction
TB	Track boundary
$f_s$	Fraction of solid
$T_L$	Liquidus temperature
$T_S$	Solidus temperature
$T_E$	Eutectic temperature
G (K/m)	Thermal gradient
R (m/s)	Solid-liquid interface velocity (or solidification growth rate)

$C_0$	Alloy's composition
$k$	Equilibrium partition coefficient
$T_{mp}$	Melting point temperature
$D_L$	Solute diffusion coefficient
$C_L$	Liquid composition
$C_S$	Solid composition
$m_L$	Liquidus slope
$\dot{T}$ (K/s) or (°C/s)	Cooling rate
$\lambda_1$	Primary dendrite arm spacing
$\lambda_2$	Secondary dendrite arm spacing
$\Gamma$	Gibbs-Thompson coefficient
$\Delta T_0$	Equilibrium solidification freezing range
$\Delta T^*$	Non-equilibrium solidification freezing range
$q$	Heat input
$AR$	Metal pool aspect ratio
$\varphi$	Angle made by solid-liquid interface velocity $\vec{R}$ and beam scanning speed $\vec{v}$
$\omega$	Angle made by heat flux direction and build direction
$\theta$	Angle made by build direction and tangent line to the track boundary
$l_{film}$	Liquid film length
$P_{tk}$	Track penetration depth

## **Attestation of Authorship**

I hereby declare that this submission is my own work and that, to the best of my knowledge and belief, it contains no material previously published or written by another person (except where explicitly defined in the acknowledgements), nor material which to a substantial extent has been submitted for the award of any other degree or diploma of a university or other institution of higher learning.

Auckland

Signature \_\_\_\_\_

## CHAPTER 1: INTRODUCTION

### 1.1. Introduction to powder bed fusion additive manufacturing

Additive manufacturing (AM) is a process of making parts from 3D model data (e.g. CAD files) by consolidating layers of material on top of one another. AM technology offers the ability to reduce waste material, as it is minimal or zero material removal processes after the initial production. The remaining material in powder bed fusion can be recycled. This increases the efficiency in material usage. In addition, AM can fabricate products without major concern about their complex design or geometry. Ordinarily, complex parts have to be divided into many stages that employ specific machining methods as well as fixtures. AM technology builds up parts vertically by a parts' cross-section; therefore, it can simplify the whole process [1]. Furthermore, AM will increase supply chain efficiencies by reducing time to market together with mass customization and environmental sustainability [2]. With those benefits, AM technology can be very promising and the future of “What you see is What you build” is not so far away [1].

Powder bed fusion (PBF) processes are widely used among the AM technologies. They range from solid-state sintering, chemically-induced sintering, liquid-phase sintering to partial melting, and completely full melting [1]. Currently, the full melting processes that include laser beam PBF (LB-PBF) and electron beam PBF (EB-PBF) are the most common techniques used. In these processes, high energy laser or electron beam not only melts the powder material but also re-melts the previous layer. Consequently, high-density as-fabricated parts can be easily and effectively achieved. In the scope of this thesis, the EB-PBF will be taken into consideration due to its popularity to the manufacturing industry as well as obtaining high performance in the fabrication of high density, well-bonded parts.

### 1.2. Electron beam powder bed fusion process

Electron beam powder bed fusion (EB-PBF) process uses a high-energy electron beam to melt the powder material. The EB-PBF process uses an input voltage of 60 kV and equips a vacuum build chamber connected to a so-called electron beam column. Figure 1 illustrates a simple structure of an EB-PBF machine. When heating up, the filament releases a tremendous high-speed and concentrated beam of electrons. The beam will then pass through the column where it is accelerated, focused and deflected by means of electro-magnetic coils. Theoretically, the electron beam can move from one spot to another almost instantly due to the fast response of those deflection electro-magnetic coils. When the beam penetrates to the powder, kinetic energy converts to thermal energy and melts the powder when the temperature reaches the melting point. The build chamber constructs with two powder hoppers, raking system, and the build platform. EB-PBF process uses a vacuum environment of  $10^{-4} - 10^{-5}$  mbar, which is very

important to metals and alloys having a high reaction to oxygen and nitrogen [3]. Moreover, the EB-PBF process offers users a very high-efficiency manufacturing method. Low energy consumption as well as the possibility to obtain very fast melting speed result in approximately 95% energy efficiency from an Arcam machine, which is 5-10 times higher compared to LB-PBF processes [4].

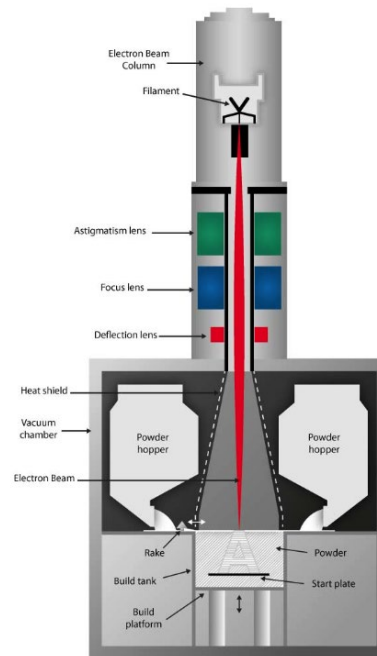


Figure 1. Schematic illustration of the hardware of an EB-PBF machine [4]

In EB-PBF process, prior to the building stage, the start plate and its underneath powders are preheated to a specific temperature depending on the used material. For example, preheat temperature for pure Cu is 300 °C, for Ti-alloys is around 600 °C or TiAl is 1100 °C [3]. As illustrated in Figure 2, the building stage of EB-PBF process comprises of four main steps: raking of a new powder layer, preheating that new powder layer, selectively melting the powder and lowering the platform for repeating a new cycle. Both the preheating stage and step use a defocused electron beam and very high scanning speed (8~14 m/s) to raster the whole of the start plate and powder material to the sintering state. This aims to heat up the start plate and the raked powders to a preset temperature. This is crucial since sintered powders increase electric conductivity in order to prevent the repulsion of charged powder particles [3]. In the melting step, a combination of parameters such as scanning speed, beam power, focus offset, line offset is employed to fully melt the powder.

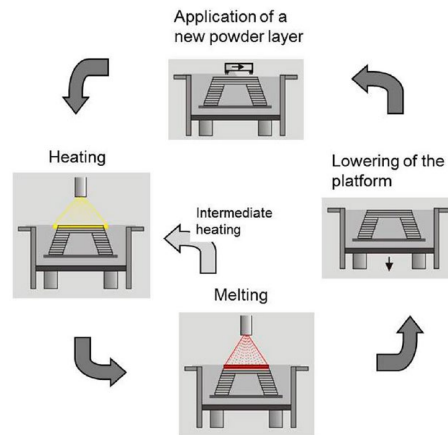


Figure 2. The EB-PBF process cycle [3]

Figure 3 illustrates parameters that are important in EB-PBF process. The accelerated voltage  $U$  is fixed at 60 kV. In a practical situation, an EB-PBF machine uses a unique parameter named as Speed Function (SF) Index to simultaneously and automatically control the beam current  $I$  (mA) and scanning speed  $v$  (mm/s). The SF index has no unit of measurement and its algorithm has been a black box to researchers due to Arcam GE's patent and copyright. The actual scanning speed and beam current will vary during EB-PBF process.

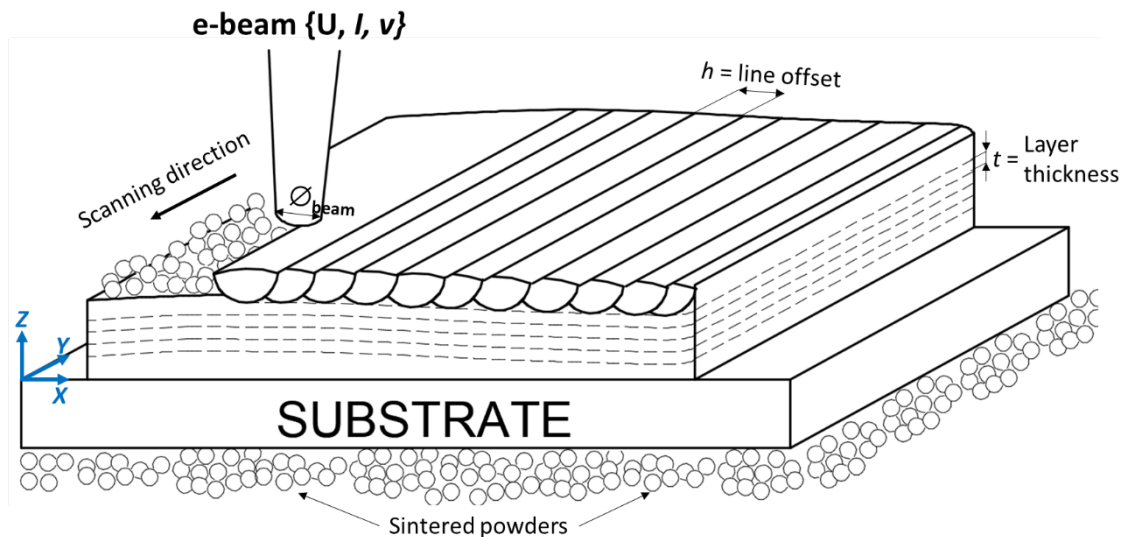


Figure 3. Schematic illustration on major parameters used in EB-PBF process

The values of  $I$  and  $v$  are stored in the machine's log files which can be exported later. In addition, SF index can be turned off to manually pre-set the scanning speed and beam current,

which will then be fixed for the whole process. Hereby, the line energy density is commonly used in literature when evaluating the effect of  $I$  and  $v$ , is defined as:

*Line energy density*: the calculated energy over a scanning track's length:

$$E_{line} = \frac{U.I}{v} \quad \text{Eq. 1}$$

The focus offset parameter (unit of measurement is mA) controls the beam spot size  $\phi_{beam}$ , as illustrated in Figure 3. However, as similar to SFI, there is no correlation between the focus offset value (mA) and the resultant beam spot size  $\phi_{beam}$  instructed from the machine manufacturer. The focus offset's unit of measure  $mA$  may suggest the value of the electric current running through those electro-magnetic coils that are used to accelerated, focused and deflected the e-beam [5]. Based on the system operational manual, increasing the focus offset will increase  $\phi_{beam}$  and vice versa. Line offset  $h$  (mm) and layer thickness  $t$  ( $\mu\text{m}$ ) are the distance between two consecutive track's edges (or centerline) and two consecutive layers, respectively. Hereby, the volume energy density which takes into account the effect of  $h$  and  $t$  is defined as:

*Volumetric energy density*: the calculated energy over a scanning track's volume:

$$E_{vol} = \frac{U.I}{v.t.h} \quad \text{Eq. 2}$$

### 1.3. Introduction to Co-29Cr-10Ni-7W alloy

Co-29Cr-10Ni-7W alloy is one member of the Co-Cr alloys family. The main element cobalt (Co) has two crystallographic structures: hexagonal close-packed ( $\epsilon$ -Co) and face-centered cubic ( $\gamma$ -Co). For elemental Co,  $\epsilon$ -Co exists below 417 °C while  $\gamma$ -Co exists above 417 °C to its melting point of 1493 °C. Cobalt is used in a wide range of applications from making heat resistant superalloys, corrosion resistant and wear resistant alloys. Therefore, cobalt has been classified as an important and strategic element in modern industrial applications [6].

Co-29Cr-10Ni-7W alloy is classified as cast heat resistant alloy [6]. The cast heat resistant alloy is known under the commercial name as FSX-414, FSX-418, X-40, and X-45 alloys and was developed by General Electric. They have been used for many years in the gas turbine industry and provide excellent properties in terms of thermal fatigue resistance, oxidation and sulfidation resistance, and hot corrosion resistance. The elemental additions have their own distinctive roles. Chromium (Cr) addition aims to increase oxidation and sulfidation resistance. Moreover, by combining with carbon, chromium acts as carbide former which provides the major strengthening mechanism of Co-29Cr-10Ni-7W alloys. Tungsten (W) is added to the alloy to be

a solid-solution strengthener as well as carbide former. The addition of nickel (Ni) helps to stabilize the fcc-matrix and form intermetallic compounds.

Co-29Cr-10Ni-7W alloy is often fabricated by using investment casting. The typical products are the first or second stage vanes/nozzles used in gas turbine engines, as shown in Figure 4. These stationary vanes/nozzles have very complex geometry and their design comprises of angled airfoils for directing high temperature and pressure air. Therefore, application of EB-PBF process as an innovative manufacturing method for these products show potential. However, the hot cracking problem has been reported for casting and welding of the alloys [7-9]. Since EB-PBF is fundamentally a solidification process of powder materials melted by the moving heat source from the e-beam (thus a moving molten pool), hence it is similar to the welding process. The high-temperature fabrication environment of EB-PBF may also result in the cracking problem when applying to the alloys. Therefore, there is a need for an extensive research effort on the investigation of the possibilities of applying EB-PBF process to the Co-29Cr-10Ni-7W alloys as well as studies about the accompanied hot cracking problem.

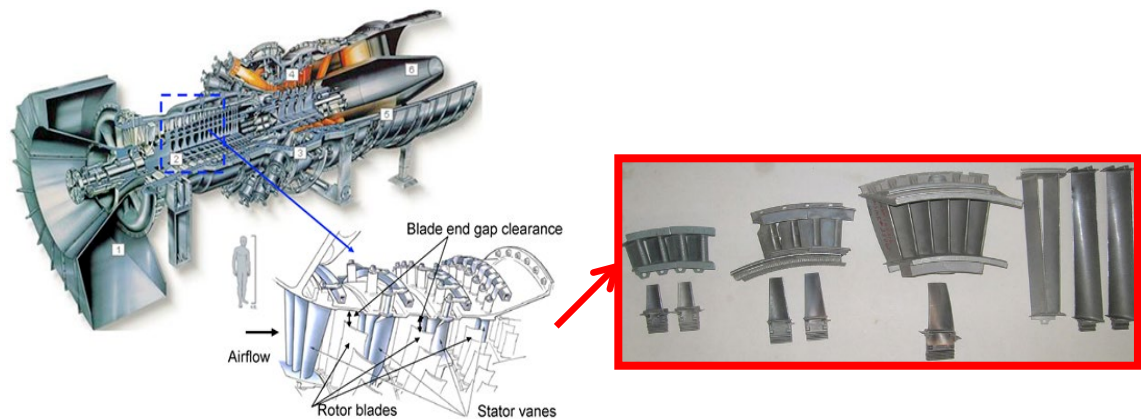


Figure 4. Applications of Co-29Cr-10Ni-7W alloy: First stage vanes/nozzles [10]

#### 1.4. Extensive cracking in EB-PBF of Co-29Cr-10Ni-7W alloy

From manufacturing perspectives, cracking will result in detrimental impacts to parts' mechanical properties, which makes it impossible for use in industrial applications. EB-PBF fundamentally is a process of melting and solidification of metallic powder materials. Similar to welding, therefore, it is possible to have cracking problem in the as-built samples. Intensive investigation and well-established understanding of possible forms of cracking have been done for casting and welding processes. However, the case for PBF-AM in general and EB-PBF, in particular, has still been limited. Understanding the underlying mechanism governing the cracking in EB-PBF, therefore, will be crucial for future process development and advance the technology to a wider range of industrial alloys, especially to difficult-to-weld alloys.

Figure 5 shows visible cracks during the EB-PBF of Co-29Cr-10Ni-7W alloy. The cracking was found to be a problem in part integrity when the alloys were processed in an Arcam A1 machine at CSIRO Manufacturing in 2014. This work was initiated and this thesis aims to investigate and conduct analysis on the identified cracking. Studies were made at CSIRO on the Arcam A1 machine and then analysis both at CSIRO and at the Auckland University of Technologies (AUT) was conducted. The mechanism of solidification and characterization of the crack network in EB-PBF was studied to gain an understanding of the cracking mechanism. It is hoped that the findings from this work would contribute as a foundation for further investigation and application of EB-PBF of Co-29Cr-10Ni-7W alloy in the future.

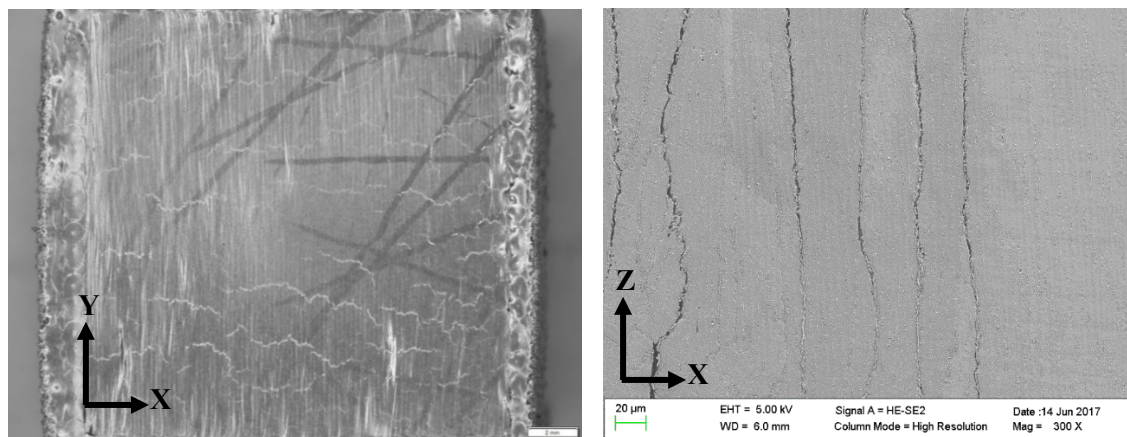


Figure 5. Extensive hot cracking networks observed in EB-PBF-fabricated sample

In this thesis, solidification during EB-PBF of Co-29Cr-10Ni-7W alloy and the as-built cracking defect are the core targets. Chapter 2 is an intensive literature review about solidification during EB-PBF of various alloys regarding the relationship between EB-PBF thermal conditions and solidification modes, the formation of the melt/track and the grain growth direction. In addition, up-to-date reports on cracking in EB-PBF process will be reviewed in terms of identification of forms of cracks, how they initiated and propagated/networked with respect to the nature layer-by-layer building of the technique. Chapter 3 will list out the experimental procedure of involving techniques and equipment used in order to achieve the objectives that are pointed out at the end of Chapter 2. Chapter 4 will present the result and discussion regarding solidification during EB-PBF of Co-29Cr-10Ni-7W alloy. Chapter 5 will present how the form of cracks is identified and how the crack network is characterized. Chapter 6 discussed more in-depth on how the identified cracking initiated and propagated during EB-PBF process. In addition, influential factors relevant to the cracking are determined.



## CHAPTER 2: LITERATURE REVIEW

In this chapter, the literature on solidification of Co-29Cr-10Ni-7W (FSX-414) alloy is discussed first. Then, how they might behave in EB-PBF compared to the range of materials already studied in the literature will be discussed. The context will be considered in the correlative relationship between EB-PBF thermal conditions, solidification morphologies, melt/track formation, and grain growth directions. Then, hot cracking and solid-state cracking phenomenon will be introduced and the current understanding of cracking in the field of PBF-AM is reviewed. The focus will be given to how different cracking mechanisms are distinguished and how the cracking network has been characterized regarding its initiation, sides, and propagation pathways, during PBF-AM. At the end of the chapter, a summary of gaps identified will be given together with the formation of specific research questions/objectives.

### 2.1. Solidification of Co-29Cr-10Ni-7W alloy

The Co-29Cr-10Ni-7W alloys are classified as Co-based superalloys. According to Sims [11], Co-based superalloys appear to be used basically for three reasons:

1. The problem of hot corrosion resistance in many turbine applications in which Co-based superalloys have demonstrated their advantages.
2. The requirement of longer lives in aircraft turbines. Co-based superalloys perform a flatter stress-rupture/time-temperature parameters properties, especially for static components.
3. The limitation in raising the use temperature of Ni-based alloys. Co-based superalloys act as a promising replacement.

Co-based alloys consist of various phases: major austenitic matrix having face-centered cubic (FCC) crystal structure at high temperature (named as  $\gamma$  phase) or hexagonal close-pack (HCP) crystal structure at low temperature (named as  $\epsilon$  phase), carbides (e.g.  $M_7C_3$ ,  $M_{23}C_6$ ...) and intermetallic compounds (geometrically close-pack and topologically close-pack). The resultant phases after casting depend on the individual alloys' compositions. For the studied Co-29Cr-10Ni-7W alloy, the matrix phase is FCC-matrix with the decoration of carbides in the interdendritic regions. The formation of carbide types is decided by the amount of adding reactive metal as well as carbon. Figure 6 shows a relationship between carbide types versus the addition of metal elements. The assumed carbon content falls among 0.1-0.6 %wt.

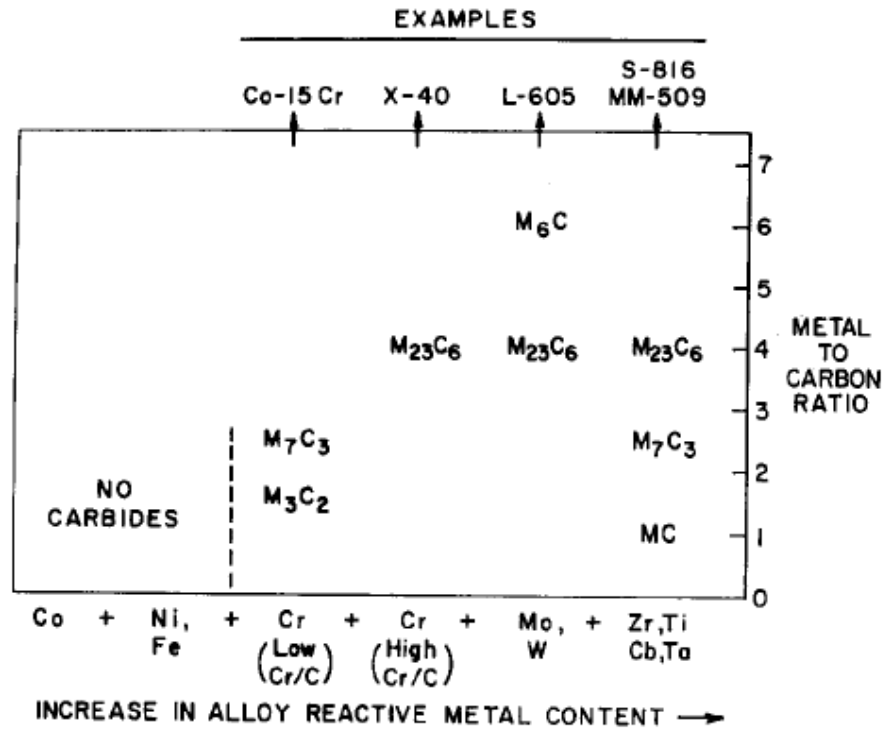
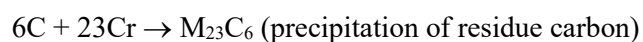


Figure 6. Effect of adding elements on type of carbides formed in Co-based alloys (assumed %wt of C from 0.1-0.6%) [11].

Since the compositions of the studied alloy are identical to those of the X-40, X-45, and FSX-414 commercial alloys, the carbide type reported is only  $M_{23}C_6$  [12]. The  $M_{23}C_6$  carbides can form directly from the alloy matrix as results of solidification, aging or service. However, they can be a product of the degeneration of MC carbides or decomposition of  $M_7C_3$  carbides as below:

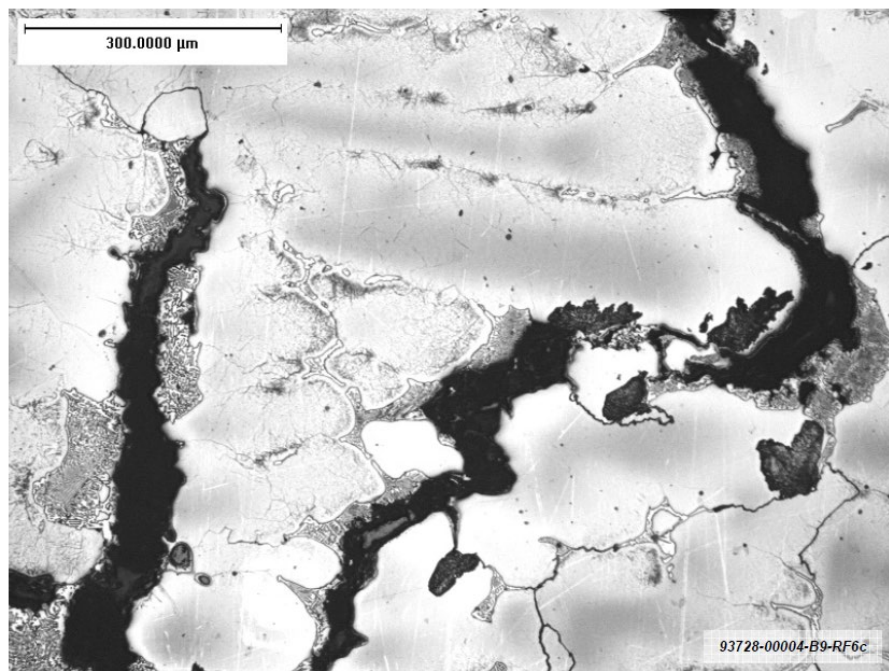


where M stands for the metallic elements (e.g. Cr, W, Ta...)

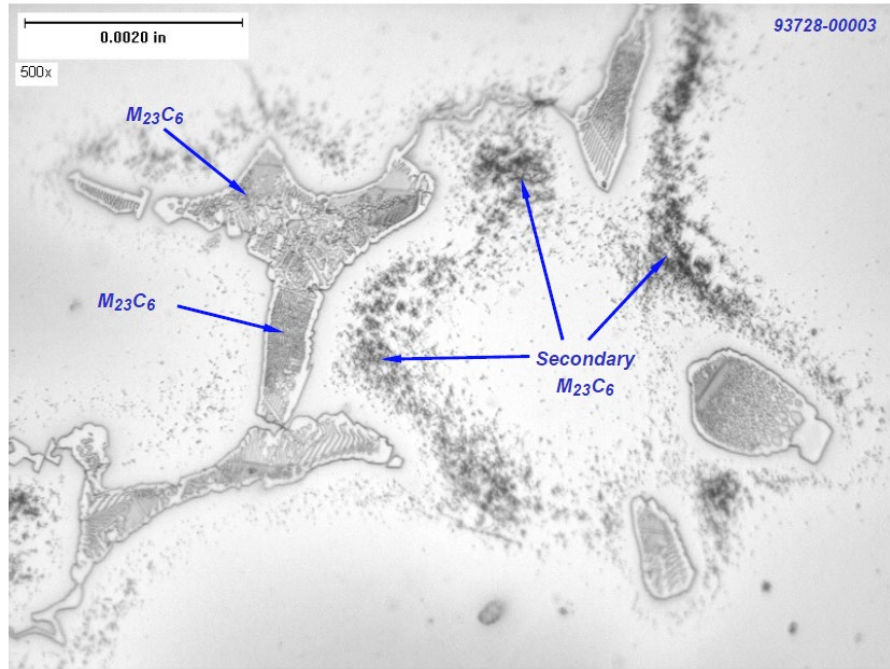
In casting, during cooling, the primary carbide firstly precipitates intra-granular and appears in coarse and blocky forms with semi-rounded morphologies. The last liquid to solidify is the combination of the  $\gamma$ -matrix and the  $M_{23}C_6$  pseudoeutectic carbide in a lathlike structure. These distribute along the grain boundaries as well as between the secondary dendrite arms. The lathlike  $M_{23}C_6$  carbide can be dominant by  $\gamma$ -matrix or  $M_{23}C_6$  phase depending on the chromium-carbon ratio and the cooling rate. Additionally, secondary  $M_{23}C_6$  carbide can precipitate in the thicker casting section, which means a longer local cooling time. In order to be used in industrial applications, the as-cast parts of Co-29Cr-10Ni-7W alloy have to pass through

the standard heat treatment including two stages. The first stage is solution treatment at around 1149-1204 °C (2100-2200 °F) that will dissolve some coarse grain boundaries carbides and homogenize the structure. Then, an aging treatment at 760-982 °C (1400-1800 °F) will re-precipitate the finer  $M_{23}C_6$  carbide particles. The secondary carbides disperse uniformly throughout the structure and act as one of the important strengthening mechanisms of the alloys. In addition, the eutectic islands of  $M_{23}C_6$  carbides remain stable after the heat treatments and start to melt at the incipient melting temperature of ~1330 °C (2425 °F) [12].

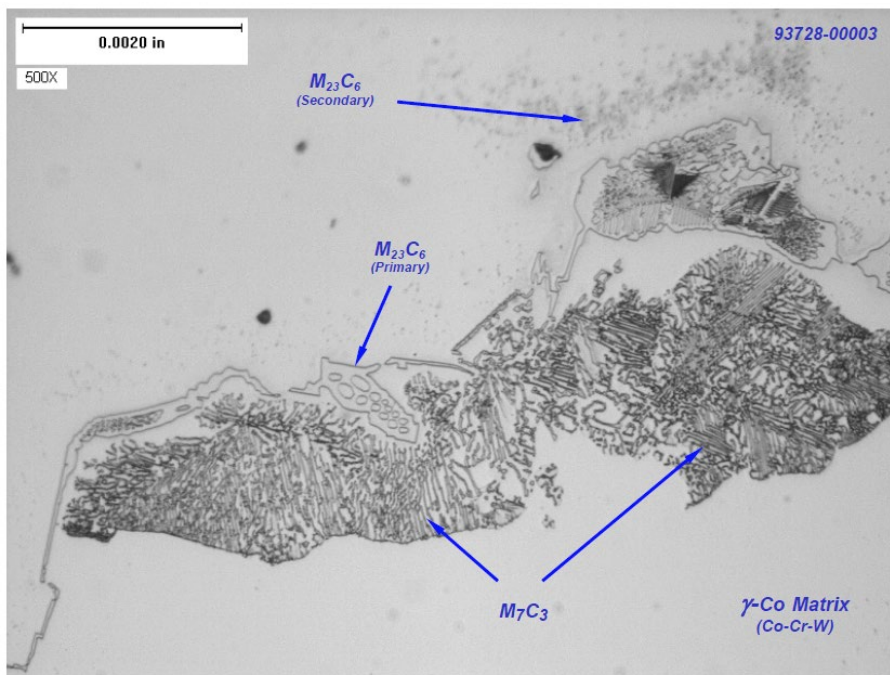
Regarding the microstructure characterization of the as-cast Co-29Cr-10Ni-7W alloy, it is quite limited in the literature. Ronan [13] in his master thesis investigated the effect of small changes in alloying compositions on the hot tearing of the as-cast FSX-414 alloy. Figure 7 illustrates the microstructure of the as-cast FSX-414 alloy including the captured hot tears and relevant carbides. In the experiment setup, 21 specimens were randomly obtained from different metal lots during a period of one year at the Precision Castparts Corp. The variation in the specimens' chemistries is ensured within the typical range of the foundry-controlled chemistry. The solidification behavior of the alloy was investigated by means of thermal analysis techniques incorporating microstructure characterization and analysis. The typical as-cast dendritic structure is observed with the decoration of the  $M_{23}C_6$  carbides along grain boundaries as well as within the interstices of secondary dendrite arms. Also, the  $M_{23}C_6$  eutectic islands can be seen, especially near the hot tearing locations. In addition, the author identified the  $M_7C_3$  carbide precipitates at the downsprue location. Since the downsprue is the last area to freeze in the casting process, there will be significant differences in the solute compositions. Consequently, this will affect the chromium-carbon ratio and result in the formation of the  $M_7C_3$  carbide.



a)



b)



c)

Figure 7. Microstructure of as-cast FSX-414 alloy: a) Hot tears with  $M_{23}C_6$  eutectic carbides; b)  $M_{23}C_6$  eutectic carbides and secondary  $M_{23}C_6$  carbides; c)  $M_7C_3$ ,  $M_{23}C_6$  primary carbides and secondary  $M_{23}C_6$  carbides [13]

Ronan [13] employed the Differential Thermal Analysis (DTA) technique to investigate the corresponding temperature ranges of formation of phases. Figure 8 illustrates the on-heating and on-cooling curves of seven specimens selected from the experiment. As can be seen in the on-heating curves, there are clear peaks at around 1300 °C that are identified as first and second carbides decompositions. This is, however, not identical to the description made in the work of Beltran [12] since this temperature range is possibly the eutectic melting point (for the heating stage). Moreover, the melting temperatures of the heating stage are within 1400-1425 °C temperature range.

On the contrary, the cooling curves show the melting points are around 1380-1410 °C. The deviations in the melting points between heating and cooling can be used to identify the total undercooling temperatures. In addition, there were some eutectic melting points detected at around 1225 °C. Thermodynamic modeling was also employed and the eutectic temperature is predicted to be from 1190-1215 °C [13]. The modeling result shows two distinct events during solidification, which occur at  $0.75 f_s$  and  $0.92 f_s$ . These events are identified as  $M_7C_3$  or  $M_{23}C_6$  primary carbides and the  $M_{23}C_6$  pseudoeutectic carbide, respectively.

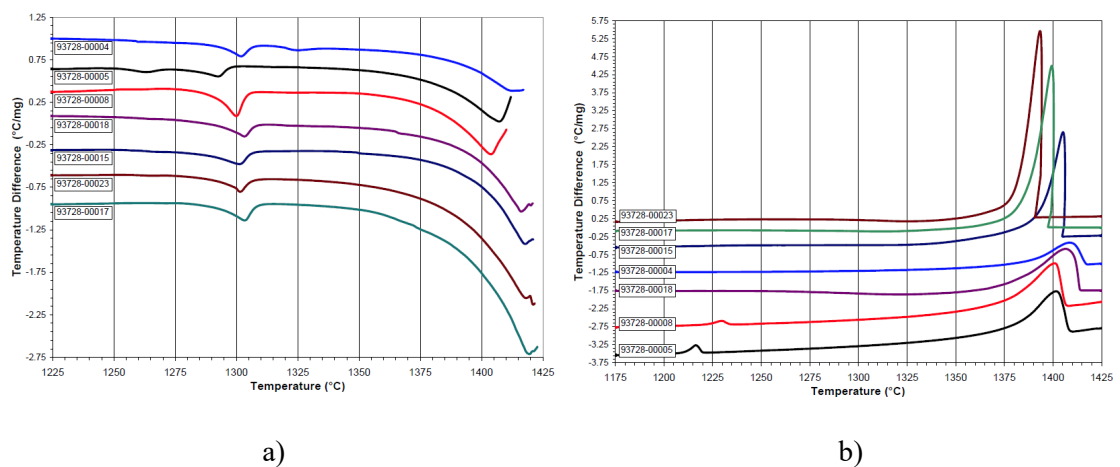


Figure 8. DTA results of seven as-cast FSX-414 specimens: a) on-heating curves and b) on-cooling curves [13]

Kasala et al. [14] reported similar DTA results for the on-heating and on-cooling curves of FSX-414 alloy. However, no further microstructure analyses are provided, hence the correlation between the thermal events and their respective phases has been unclear. Oates [15] observed the microstructure of the heat-treated FSX-414, which is shown in Figure 9. The interdendritic regions are heavily decorated with fine  $M_{23}C_6$  carbide particles. In contrast, the primary  $M_{23}C_6$

eutectic islands at grain boundaries, which may be the result of as-cast solidification, remain unchanged.

The information obtained from the works of Ronan, Kasala et al. and Oates [13-15] is significant since the compositions of the thesis' investigated Co-29Cr-10Ni-7W alloy are closely matched with the FSX-414 alloy. The solidification behavior of the FSX-414 can be briefly summarized in Figure 10. The liquid metal will solidify into the  $\gamma$ -matrix at its melting point. Along with the cooling down process, depending on the cooling rate, either primary  $M_7C_3$  or  $M_{23}C_6$  carbides will precipitate. The FSX-414 has its eutectic temperature at around 1200-1225 °C where the  $M_{23}C_6$  pseudoeutectic carbide together with the  $\gamma$ -matrix forms the lathlike eutectic islands at the grain boundaries. Thus, the alloy's wide solidification freezing range of about 180 °C can be the reason for its high susceptibility in hot tearing.

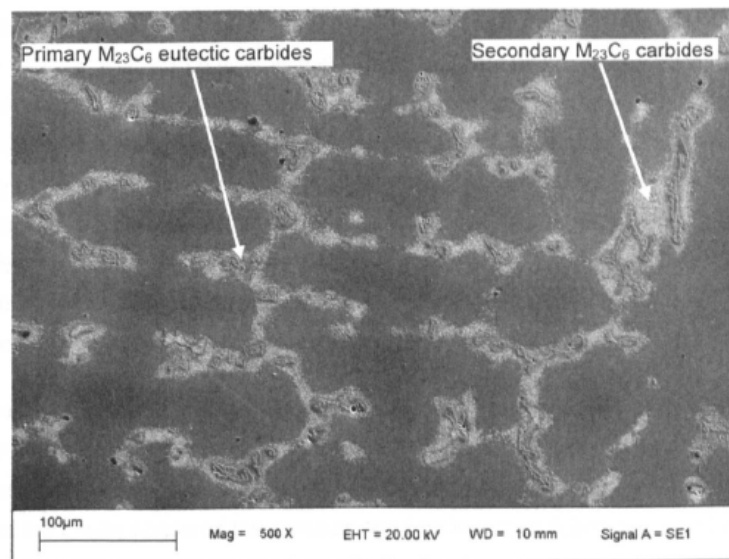


Figure 9. Microstructure of sample experienced the standard heat treatments for Co-29Cr-10Ni-7W alloys [15]

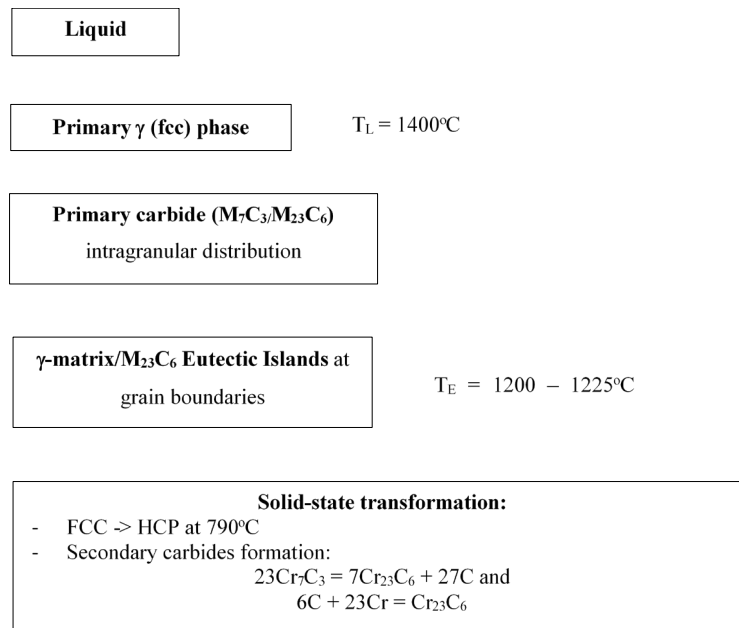


Figure 10. Solidification path of Co-29Cr-10Ni-7W alloy summarized based on the literature review of FSX-414 alloy

## 2.2. Solidification during EB-PBF process

Fundamentally, solidification is the extract of heat from the molten metal that causes the material to change its form from liquid to solid phase. In EB-PBF, solidification occurs after the fusion of powder material that is heated by the electron beam. As the beam moves, the fusion of powder particles will result in a moving molten pool and eventually a scanning track. The melt/track geometry is one of the influential factors to the solidification conditions in which thermal gradient ( $G$ ) and solidification rate ( $R$ ) are two important variables. Depending on  $G$  and  $R$ , solidification modes will vary from planar, cellular to dendritic morphologies. Moreover, the melt/track geometry determines the heat flux directions, which can affect the grain growth directions. Therefore, the following sub-sections are dedicated for the literature review in terms of studies having been done so far on the melt/track formation, the relationship between  $G$ ,  $R$  and the solidification modes as well as grain growth in EB-PBF process.

### 2.2.1. Solidification modes

Solidification is a process in which the liquid phase transforms into a solid phase. The solid-liquid interface advances until the fraction of solid becomes one. In alloys, solidification depends on the constituted compositions of solute elements. During solidification, due to the difference between the solubility of the solid and liquid metal, there will be excess solute in the solidified solid. Consequently, the excess solute will be rejected back into liquid and piles up ahead of the solid-liquid interface. As the solute continues to pile up when the solid-liquid

advances, there will be a change in concentration ahead of the interface. This change will affect the melting/freezing point of the liquid ahead of the interface. The so-called constitutional undercooling will occur if the actual temperature  $T$  is lower than the melting point of the liquid. In other words, the liquid ahead of the solid-liquid interface is locally supercooled. Figure 11 illustrates the link between the phase diagram, the temperature distribution ahead of the interface, and the solute built-up zone [16].

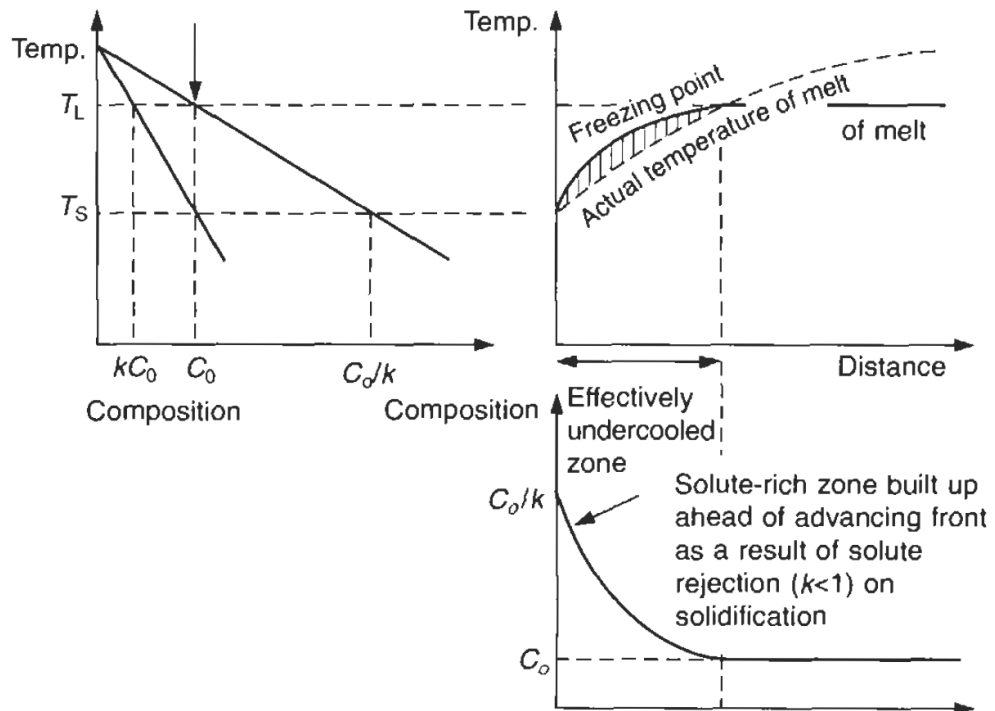


Figure 11. Phase diagram, temperature distribution, and solute built-up zone during solidification [16]

Campbell in his book [16] states that in most cases of alloys, the constitutional undercooling will define the solidification modes or growth morphologies. Figure 12 illustrates the three solidification modes. In Figure 12a, if there is an instability that causes a protuberance ahead of the solid-liquid interface, it will find itself in a superheated environment and eventually will melt back. Thus, planar growth is stable. On the other hand, in Figure 12b, the actual temperature  $T$  is equal or less than the temperature of the liquid  $T_{mp}$ , the protuberance exists at the interface will be in a supercooled liquid and will not disappear. Therefore, cellular growth is stable. In Figure 12c, when the constitutional undercooling increases, dendritic growth (growth of side branches) will take place.

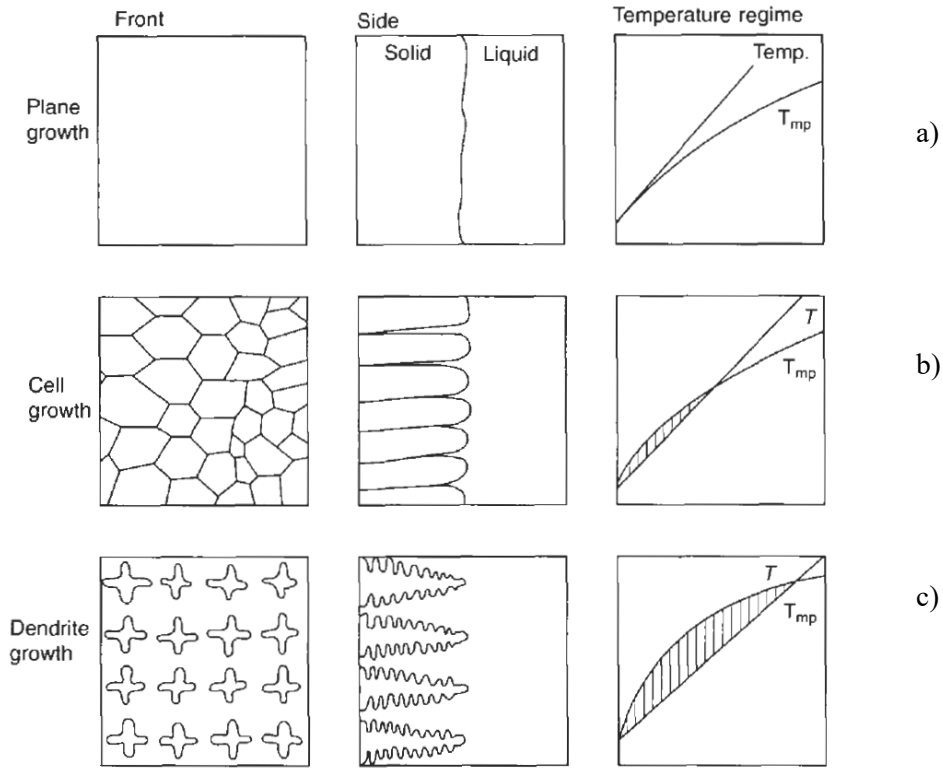


Figure 12. The transition of growth morphology from planar, to cellular, to dendritic as compositionally induced undercooling increases.  $T$  and  $T_{mp}$  [16]

In consideration of requirements for solute conversion at the interface which gives the gradient of the composition in the liquid at the interface:

$$-D_L \cdot \left( \frac{dC_L}{dx} \right)_{x=0} = R \cdot C_L^* (1 - k) \quad \text{Eq. 3}$$

or

$$\left( \frac{dC_L}{dx} \right)_{x=0} = \frac{R}{D_L} \cdot C_L^* (1 - k) \quad \text{Eq. 4}$$

The slope of the liquid line  $m_L$  in the phase diagram is:

$$m_L = \frac{dT_L}{dC_L}$$

or

$$\left( \frac{dT_L}{dx} \right)_{x=0} = m_L \left( \frac{dC_L}{dx} \right)_{x=0} \quad \text{Eq. 5}$$

The constitutional undercooling is absent when (for planar growth in Figure 12a):

$$G = \left(\frac{dT}{dx}\right)_{x=0} \geq \left(\frac{dT_L}{dx}\right)_{x=0} \quad \text{Eq. 6}$$

Combining the Eq. (4), (5) and (6), gives the general constitutional undercooling criterion; this is, a plane front is stable when:

$$\frac{G}{R} \geq \frac{m_L C_S^* (1-k)}{k D_L} \quad \text{Eq. 7}$$

At a steady-state and without convection in liquid,  $C_s^* = C_0$  and Eq. (7) becomes:

$$\frac{G}{R} \geq \frac{m_L C_0 (1-k)}{k D_L} \quad \text{Eq. 8}$$

where  $D_L$  is solute diffusion coefficients in liquid,  $C_L$  and  $C_S$  is the liquid and solid composition,  $C_0$  is alloy composition,  $k$  is equilibrium partition coefficient,  $G$  is the thermal gradient in liquid,  $R$  is the solid-liquid interface growth rate and  $T_L$  is the liquidus temperature.

A general statement can be made that the  $G/R$  determines the solidification modes which are planar, cellular, dendritic or equiaxed dendritic.

In addition, the cooling rate  $\dot{T} = G \times R$  determines the size of the solidified microstructure. Kurz and Fisher [17] proposed a theoretical model (Eq. 9) to estimate the primary dendrite arm spacing ( $\lambda_1$ ) in columnar dendritic growth during directional solidification. As can be seen in Eq. 9, increasing of  $\dot{T} = G \times R$  will cause a decrease in  $\lambda_1$ . The solidification morphologies in regards to  $G$  and  $R$  are fully illustrated in Figure 13.

$$\lambda_1 = 4.3 \frac{(\Delta T_0 \cdot D_L \Gamma)^{0.25}}{k^{0.25} R^{0.25} G^{0.5}} \quad \text{Eq. 9}$$

where  $\Delta T_0$  is equilibrium solidification freezing range and  $\Gamma$  is Gibbs-Thompson coefficient.

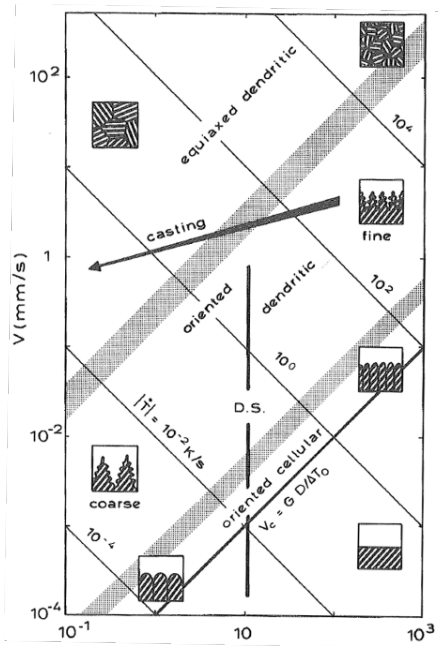


Figure 13. Schematic summary of solidification morphologies in regards to thermal gradient  $G$  and solidification growth rate  $R$  (denoted as  $V$  in the figure) [17].

The establishment of the ratio  $G/R$  and  $\dot{T}$  on the solidification modes were derived based on the casting process. Nevertheless, it is still applicable to all processes that include solidification. In PBF-AM, Collins et al. [18] comprehensively reviewed the relevant aspects of microstructural control. Among those are the solidification modes. The relationship between local solidification of the melt pool, the constitutional undercooling,  $G/R$  and the solidification modes is demonstrated in Figure 14. In Figure 14a, it can be seen that  $R$  mathematically relates to the beam scanning speed ( $v$ ),  $G$  relates to the heat input ( $q$ ) and the mushy zone thickness (solid+liquid) depends on the alloy's liquidus and solidus temperatures. Thus, by modifying the solidification freezing range (i.e. changing alloy compositions...) or the thermal fields (i.e. increase  $q$  or  $v$ ), the ratio  $G/R$  will be altered and the solidification modes may be controlled.

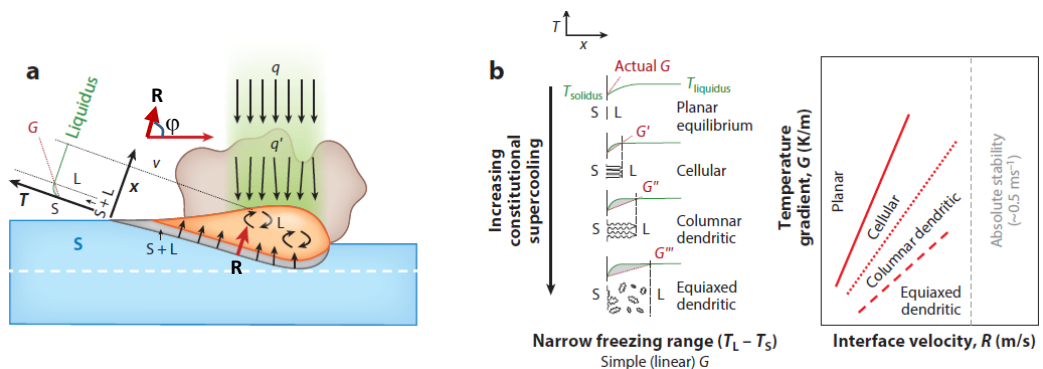


Figure 14. a) A moving molten pool with the solid-liquid interface illustration. b) Relationship between solidification modes and  $G, R$  [18]

In EB-PBF process, columnar dendritic solidification mode is commonly observed, especially for Ni-based alloys [19, 20]. Helmer et al. [21] noted a transition from dendritic to cellular solidification mode at the melt boundaries in the last layer from their work on EB-PBF of IN718 alloy, as shown in Figure 15. The transition is explained due to the increase of  $R$  and decrease of  $G$  starting at the melt boundary during solidification. The explanation is based on the work of Kurz and Trivedi [22] on solidification conditions within a laser/e-beam melt pool. The ratio  $G/R$  significantly reduces from melt boundary (bottom) to the melt surface. However, how much  $G$  and  $R$  changed has not been estimated by Helmer et al. [21].

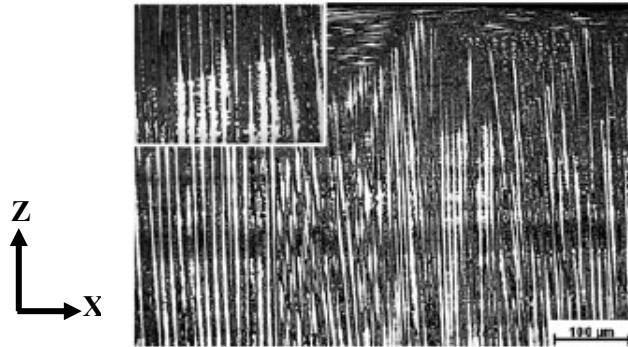


Figure 15. The transition from dendritic to cellular growth morphology observed in [21]

In the recent study, Karimi et al. [23] conducted an EB-PBF experiment of consecutive single tracks scanning to investigate the effect of thermal cycles on the solidified microstructure, as illustrated in Figure 16d. Columnar dendrites with fine secondary arms are observed as the dominant solidification mode (Figure 16a, b, c). The  $\lambda_1$  measured varies from  $\sim 1.15 \pm 0.27 \mu\text{m}$  to  $\sim 1.77 \pm 0.46 \mu\text{m}$  for the one-time melted and overlap zone, respectively. It is explained that the heat dissipation is slower for the overlap zone as the effect of heat accumulation. Thus,  $G$  may be lower and lead to a decrease in the cooling rate  $\dot{T}$ , which is experimentally estimated ranging from  $(0.5 \sim 2.5) \times 10^5 \text{ K/s}$ . Although  $G$  and  $R$  has not been figured out to correlate with the observed dendritic mode, the estimation on  $\dot{T}$  with respect to the  $\lambda_1$  from Karimi et al. [23] is very useful in understanding the effect of thermal cycles in EB-PBF. As secondary dendrite arms are observed, thus the secondary dendrite arms spacing ( $\lambda_2$ ) may be used to estimate  $\dot{T}$ . In addition, the theoretical model correlating between  $\lambda_1$ ,  $G$ ,  $R$  and  $\dot{T}$  as expressed by Eq. 9 may be used to estimate the solidification conditions of EB-PBF.

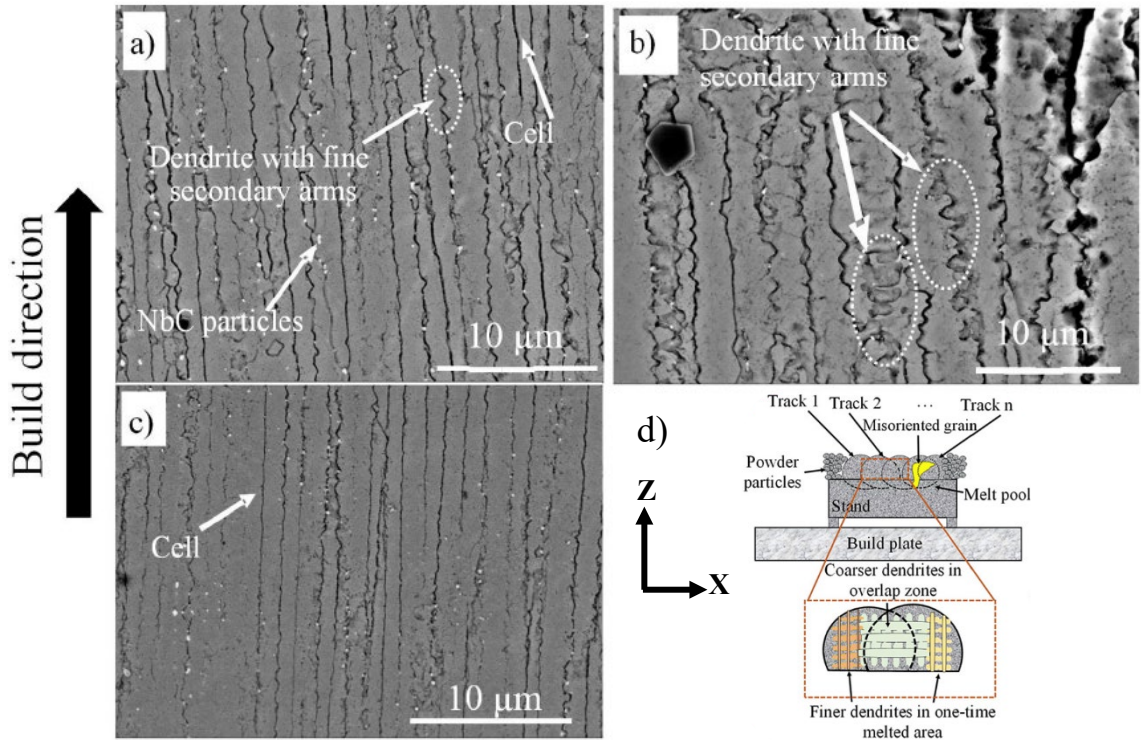


Figure 16. Columnar grains with fine secondary dendrite arms implies dendritic solidification mode in the work of Karimi et al. [23]

Wang et al. [24] and Zhong et al. [25] demonstrated the microstructure observed in their EB-PBF stainless steel 316L (SS-316L) samples. In both works, cellular solidification mode was observed. In the work of Wang et al. [24], intra-granular dendrites at an average size of  $\sim 1 \mu\text{m}$  were observed, as shown in Figure 17. No further discussion on the relationship between solidification conditions  $G$  and  $R$  on the solidified microstructure has been provided by Wang et al. [24] and Zhong et al. [25].

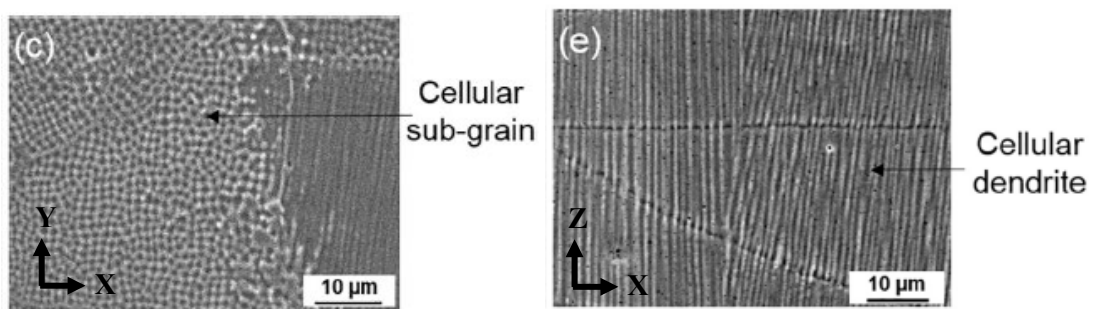


Figure 17. Solidification mode as cellular growth observed in the work of Wang et al. [24]

The difference in observation between dendritic and cellular solidification modes in EB-PBF of Ni-based alloys and SS-316L can be discussed by using Eq. 8, which can be expressed again using the alloy's solidification freezing range  $\Delta T_0$ . Thus, conditions for constitutional undercooling to take place will be:

$$\frac{G}{R} < \frac{\Delta T_0}{D_L} \quad \text{Eq. 10}$$

with  $\Delta T_0 = T_L - T_S = m_L C_0 (1-k)/k$  that is figured out based on the phase diagram in Figure 11. The satisfaction of Eq. 10 will result in the growth of cellular or dendritic morphologies that are observed in EB-PBF [19-21, 24, 25]. Determination of cellular or dendritic growth may depend on the right-hand side of Eq. 10, which is the ratio  $\Delta T_0/D_L$ . The larger of  $\Delta T_0/D_L$  indicates the more severe constitutional undercooling which likely promotes for dendritic growth. According to thermophysical properties cited from Valencia et al.'s study [26],  $\Delta T_0$  of Ni-based alloys (i.e. CMSX-4, IN-718) and SS-316L is ~120 K and 65 K, respectively.  $D_L$  of Ni-based alloys and SS-316L is  $\sim 10^{-15}$  m<sup>2</sup>/s and  $2 \times 10^{-8}$  m<sup>2</sup>/s, respectively [17, 27]. Therefore, the degree of constitutional undercooling of Ni-based alloys and SS-316 will be:

$$\left(\frac{\Delta T_0}{D_L}\right)_{Ni-based} = \frac{120K}{\sim 10^{-15}m^2/s} = 12 \times 10^{16} \frac{K}{m^2/s}$$

$$\left(\frac{\Delta T_0}{D_L}\right)_{SS-316} = \frac{65K}{2 \times 10^{-8}m^2/s} = 3.25 \times 10^9 \frac{K}{m^2/s}$$

$$\Rightarrow \left(\frac{\Delta T_0}{D_L}\right)_{Ni-based} \gg \left(\frac{\Delta T_0}{D_L}\right)_{SS-316}$$

In addition, the numerical prediction of  $G$  and  $R$  in EB-PBF of Ni-based alloys can be seen ranging around  $10^5 \sim 10^7$  K/m and  $10^{-2} \sim 1$  m/s [28-30]. In addition, the EB-PBF Arcam systems used in the works [19-21, 24, 25] were A2, A2X, and A2XX, therefore, it is expected that  $G$  and  $R$  may not be much different. According to Eq. 10,  $G/R \ll (\Delta T_0/D_L)_{Ni-based}$  as compared to  $G/R < (\Delta T_0/D_L)_{SS-316L}$ , thus dendritic solidification mode is observed in EB-PBF Ni-based alloys while cellular growth is seen in EB-PBF SS-316L.

For EB-PBF of Ti-6Al-4V alloy, the solidification modes are unable to be identified despite the fact that columnar grain structure is observed [31-34]. The microstructure has undergone a solid-state phase transformation during solidification. The liquid metal solidifies and forms  $\beta$ -phase columnar grains which then mostly transforms into twinned  $\alpha'$  plates during the EB-PBF progressing. In the end, the  $\alpha'$  plates will completely transform into  $\alpha+\beta$  phase. Thus, the originally solidified microstructure is wiped out and replaced by the final  $\alpha+\beta$  phase which has a lamella appearance.

Regarding the EB-PBF process of Co-Cr alloys, recent studies have been highly focused on the Co-29Cr-6Mo alloy [35-40]. The columnar grain structure is similar to that of EB-PBF of Ni-based alloys. Gaytan et al. [36] illustrated the carbides array distributed along sub-cell boundaries. The same observation was reported by Sun et al. [35]. The observation of the

columnar grains with sub-cellular structures in Figure 18 of Gaytan et al. and Sun et al. [35, 36] may suggest the solidification modes of cellular or dendritic.

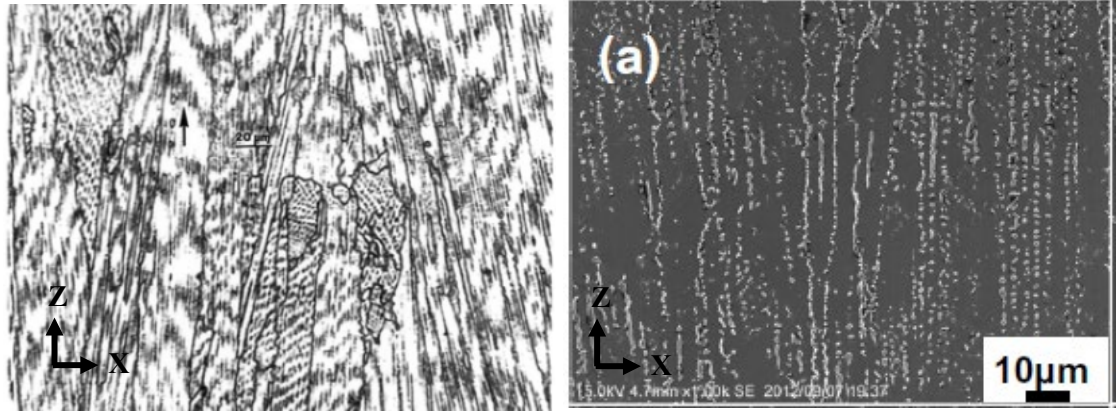


Figure 18. Columnar grains structure with sub-cells observed in EB-PBF Co-29Cr-6Mo alloy [35, 36]

The value of  $D_L$  for Co-Cr alloys is not much available in the literature. However, it can be found  $D_L$  is approximately  $10^{-9}$  m<sup>2</sup>/s for Co-Cr-W alloy [41]. Thus, with an approximation of  $\Delta T_0$  for Co-Cr-W alloy at 88 K [41], the ratio  $\Delta T_0/D_L$  will be approximately  $9 \times 10^{10}$  Ks/m<sup>2</sup>. This ratio is higher than that of SS-316L, however, is lower than that of Ni-based alloys. It is necessary to further investigate the solidified microstructure to clarify  $G$ ,  $R$  and  $\dot{T}$  during EB-PBF of Co-Cr alloys. The correlation between growth morphologies and the potentially estimated  $G$ ,  $R$  and  $\dot{T}$  in EB-PBF of various metallic alloys is important to contribute more to the understanding of solidification during EB-PBF.

### 2.2.2. Melt pool and track formation

The melting of powder particles results in the formation of the melt pool and the scanning tracks. This is an important aspect of PBF-AM. In LB-PBF, many experimental and simulation studies have been done on the influence of the melt pool on mechanical properties [42-45], as-built defects [46-50], crystallographic orientation, and grain growth [44, 51-54].

In EB-PBF process, many simulation studies have been conducted on melt/track formation [55-58], however, experimental observations have been limited. Scharowsky et al. [59] and Riedlbauer et al. [60] used a high-speed camera to investigate the very fast melting and solidification process during EB-PBF of Ti-6V-4Al alloy. The melt pool at a scanning speed of 0.16 m/s has its length estimated to be approximately 1.8 mm and a life time of 11.6 ms. However, the melt pool width was not measured. Moreover, due to the specific solid-state phase transformation of Ti-6V-4Al alloy, traces of melt pool boundaries cannot be observed in metallographic observation.

Price et al. [61] employed a near-infrared thermal imager to measure temperature distribution during EB-PBF process of Ti-6Al-4V alloy. The moving melt pools are captured for increasing values of SFI from 20, 36, 50 and 65 (214-1595 mm/s, respectively). The melt pool length was shown to decrease as increasing the SF values and the building height, as indicated in Figure 19a. However, it can be seen the influence of the building height is not significant for SF50 and SF65 (high  $v$ ). In contrast, the melt pool width is approximately 1 mm for SF20 and SF36 and 0.75 mm for SF50 and SF65. The building height seems not to have a significant effect on the melt pool width. Increasing the beam diameters from 0.55 mm to 0.65 mm results in a reduction from 2.5 mm to 1.8 mm in melt pool length while the melt pool width just slightly increases at around 0.65 mm to 0.7 mm, as shown in Figure 19b. The beam diameters were experimentally obtained, however, the authors did not provide details of FO values used.

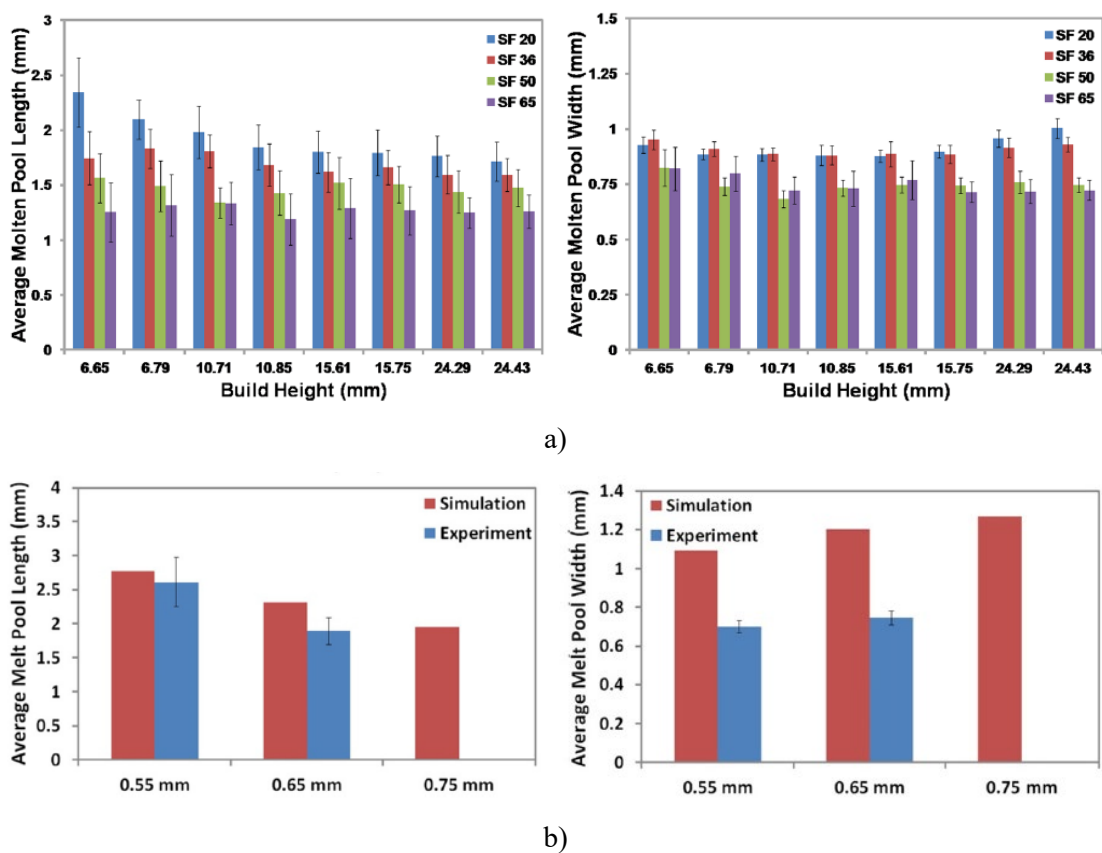
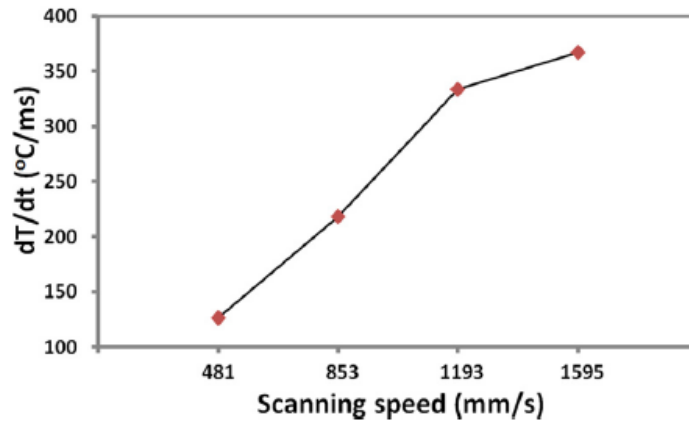
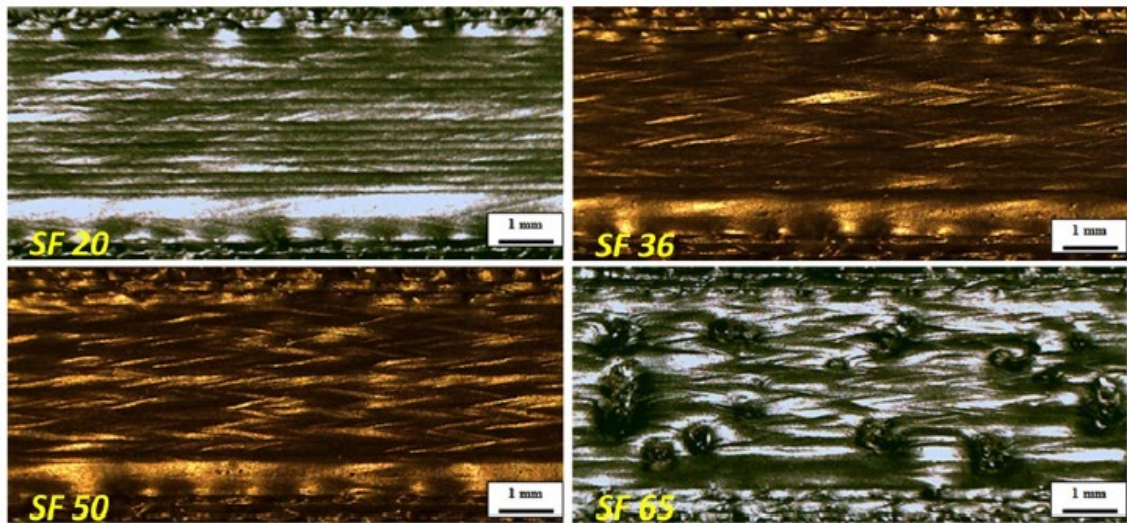


Figure 19. Effect of (a). Scanning speed (via SF values) and (b). Beam diameters on the melt pool length and width in EB-PBF of Ti-6V-4Al alloy [61]

Price et al. [61] also showed that increasing of SF (20 to 65) will increase the cooling rate ( $1.25 \times 10^5$  °C/s to  $3.5 \times 10^5$  °C/ms) in EB-PBF, as shown in Figure 20a. Moreover, in Figure 20b, it can be seen that the higher SF values, the clearer tear-drop ripples can be observed.



a)



b)

Figure 20. (a). The increasing the cooling rate in EB-PBF Ti-6Al-4V as increasing SF values; (b). Features of tear-drop ripples observed on samples fabricated with different SF values [61]

Gong et al. [62] observed the as-built defects as the results of track formation in EB-PBF of Ti-6V-4Al alloy. Alteration of the beam focus offset results in different melt pool geometries, as illustrated in Figure 21a. The change in melt pool depth and width affects the overlapping area which can result in different primary dendrite arms spacing  $\lambda_1$  and  $\dot{T}$ , as pointed out before in the work of Karimi et al. [23]. Moreover, if the overlapping depth is smaller than the layer thickness, this may generate trapped un-melted powders between layers. In Figure 21b, it can be seen that regardless of the focus offset, the tear-drop ripples cannot be observed as in the work of Price et al. [61] (Figure 20b) although Gong et al. used higher SF (of 98) in their study. Thus, it is unclear how the melt pool formed during EB-PBF of Ti-6Al-4V in the work of Gong et al. [62] and why it is different to that of Price et al.'s study [61].

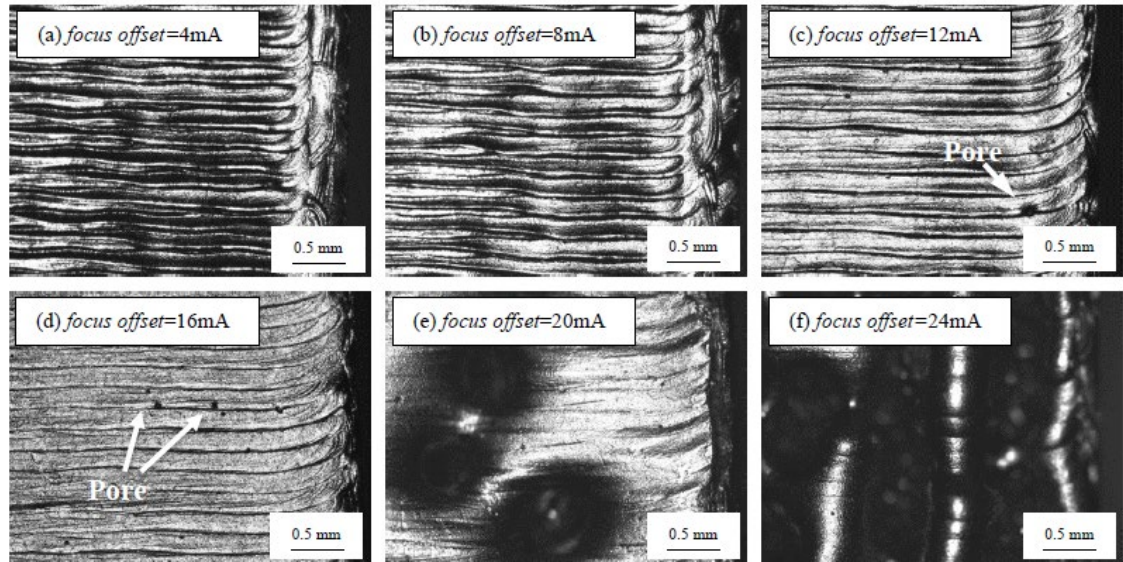
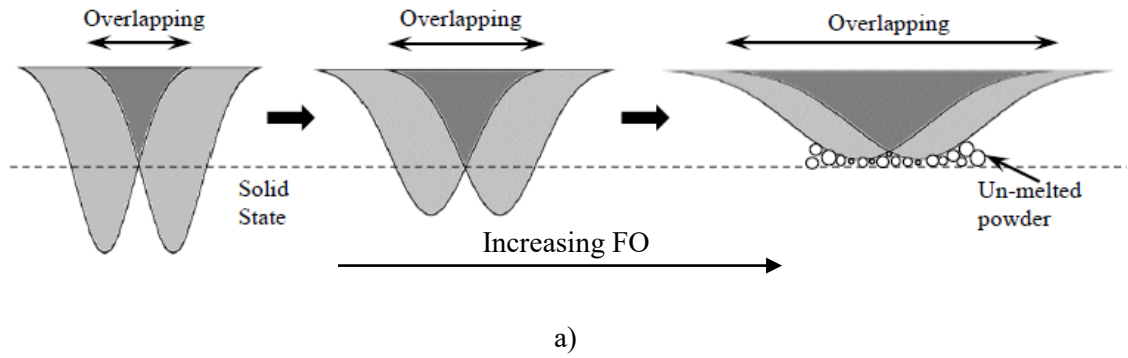


Figure 21. (a). Influence of beam offset on melt pool shape and the overlapping area between two adjacent melt pools and (b). Solidified top surface of EB-PBF samples fabricated by different focus offset values at SF98 [62].

Karimi et al. [23] studied the influence of successive thermal cycling on microstructure evolution in EB-PBF IN-718 alloy. In the study, single as well as multiple tracks were scanned with fixed volume energy  $E_{vol}$  of  $36 \text{ J/mm}^3$  to replicate the hatching process. By increasing the number of scanned tracks, the increasing accumulation of heat energy results in changes of track geometries in both width and penetration depth, from  $312 \mu\text{m}$  (single track) to  $294 \mu\text{m}$  (seven tracks) and from  $40 \mu\text{m}$  (single track) to  $110 \mu\text{m}$  (seven tracks), respectively (Figure 22). The change in melt/track aspect ratio ( $AR = \text{width/depth}$ ) will affect both the heat flux direction and solidification growth rate  $R$ . At high  $AR$ , the melt/track boundary is less curvature leading to more aligned heat flux directions to the build direction. In addition, the angle  $\varphi = \vec{R} \wedge \vec{v}$  will be closer to  $90^\circ$  that causes  $R$  reduced. Although Karimi et al. [23] did not elucidate the relationship between melt/track  $AR$  and solidification conditions, the authors, however, showed that increase in the number of scanned tracks leads to a reduction in cooling rate  $\dot{T}$  from  $2.6 \times 10^5 \text{ K/s}$  to  $0.8 \times 10^5 \text{ K/s}$ . However, increasing in the number of scanned tracks reduces the melt/track

$AR$  which expects to increase  $R$ , thus increases  $\dot{T}$ . Therefore, it can be suggested that the thermal gradient  $G$  may also change following the effect of heat accumulation. Although the observation and estimation are based on the 2D cross-sectional melt/track geometry, it can be seen that the melt/track geometry is very important to solidification conditions of EB-PBF.

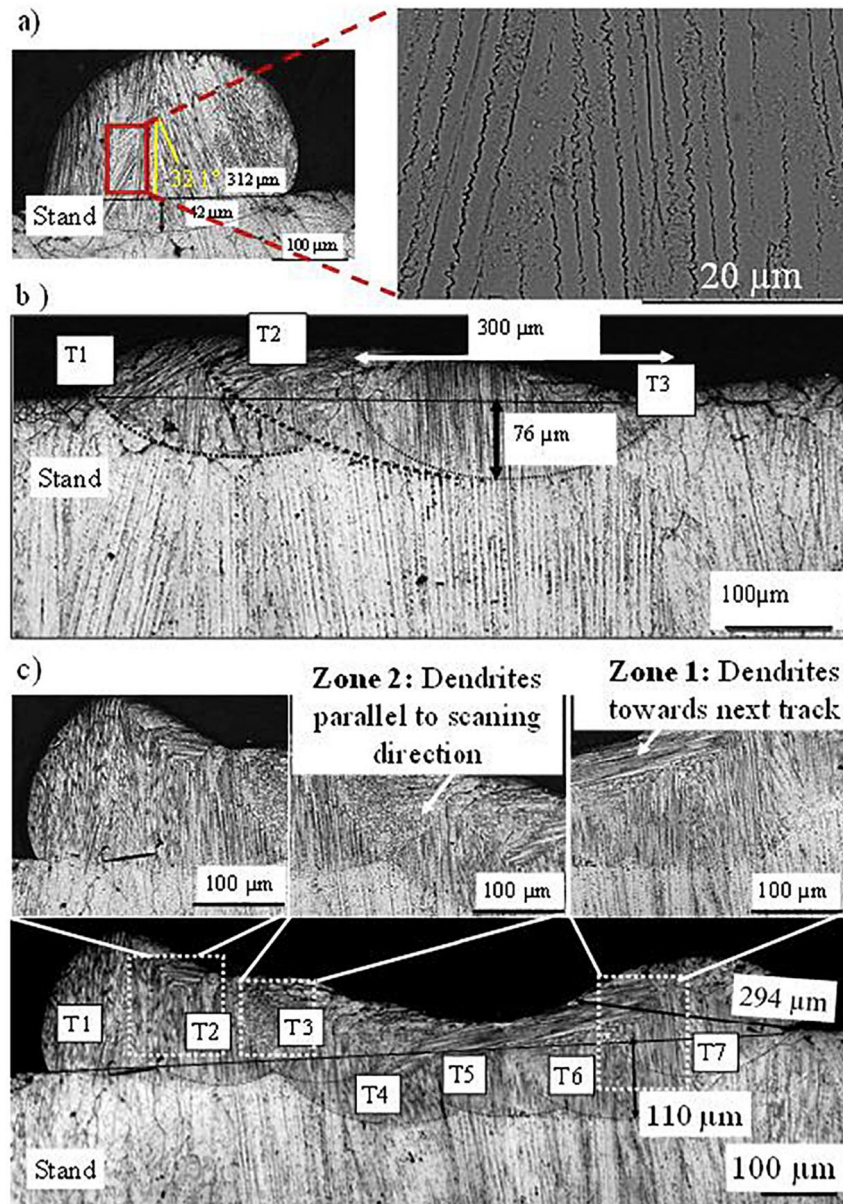


Figure 22. Single track and multiple tracks experiments in [23] showing the effect of heat accumulation on the formation of melt/track geometries

The melt/track formation is EB-PBF parameters (i.e.  $v$ , FO values) dependent. Moreover, the appearance of melt/track and its geometry reflect solidification during EB-PBF. As the typical welding/LB-PBF feature of tear-drop ripples are not usually observed, this may suggest that solidification of the melt in EB-PBF may not be restricted within a melt pool. In addition, the melt/track geometry is shown to be an influential factor to solidification conditions, it is, therefore, crucial to investigate more on how the melt/track formed during EB-PBF.

### 2.2.3. Grain growth directions during solidification

During solidification which is the phase transformation from liquid to solid, the first event to occur is nucleation and then followed by the grain growth. Nucleation involves the clustering of atoms in the liquid metal. The nucleation occurs can be due to the constitutional undercooling or participation of foreign particles [17]. The former is known as homogenous nucleation while the latter is heterogeneous nucleation. In homogenous nucleation, for surviving in the liquid metal, the clusters of atoms need to reach the critical radius  $r^*$  to overcome the critical energy barrier  $\Delta E^*$  (i.e. volume free energy + solid-liquid surface free energy).  $r^*$  and  $\Delta E^*$  decrease as undercooling temperature increases. In contrast, heterogeneous nucleation sides involves foreign particles which are stable at high temperature ( $\geq T_m$ ), thus little or no undercooling is required [63]. In fusion welding, nucleation can occur heterogeneously in different mechanisms such as fragmentation of the dendrite tips, detachment of partially melted grains or via the support of inoculants [64]. Another mechanism is epitaxial nucleation where the new nuclei form at the melt pool boundary and inherent the crystallographic orientation of parents grains. This mechanism is the dominant form of heterogeneous nucleation during welding solidification [63]. As has been stated, the PBF-AM is similar to the fusion welding, hence the dominant form of nucleation is also epitaxial. Epitaxy and microstructure evolution has been thoroughly reviewed by Basak and Das [65] for metal AM of many alloys. Once the nucleation is established, the grain growth occurs which will fully develop the microstructure.

Grain growth is an important aspect from metallurgical perspectives. In addition to solidification modes, how grain grows may determine the overall grain structure. The grain growth has been well investigated during solidification of welding, as thoroughly reviewed in the thesis of Rajamäki [66]. During welding solidification, grain growth occurs in either two directions. The first one is the growth whose direction will follow the heat flux direction. This type of growth direction often occurs at slow growth rates and is normal to the solid-liquid interface, or the fusion line. The second type of growth is strongly affected by the crystallographic characteristics, the so-called easy-growth direction. For the fcc crystallographic structure of Ni or Co-based alloy, the easy-growth direction can follow one of the six  $\langle 001 \rangle$  preferred growth directions. The competitive growth will favor for  $\langle 100 \rangle$  growth direction if it is closely aligned with the heat flux direction, and vice versa, as shown in Figure 23. In this case, heat flux directions act as an influential factor in the growth direction. Körner [3] in her extensive review on EB-PBF of various metallic alloys showed that the process is similar to the fusion welding. Thus, the two growth directions can be applicable.

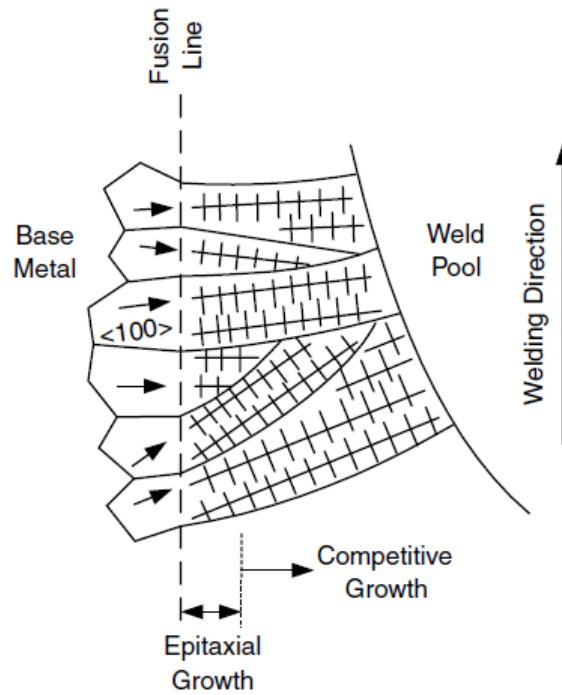


Figure 23. Easy-growth-directions epitaxially follow  $\langle 100 \rangle$  crystallographic directions in welding solidification [67]

The “grain growth directions” term is used to describe the directions along which the grain develops or grows. A single grain of an EB-PBF-built sample comprises of a group of cells/dendrites, as observed in EB-PBF of Ni, Co-based alloy and stainless steel 316L [19-21, 24, 35-40]. However, those grain growth for Ti-6Al-4V alloy is unable to be observed, as previously discussed. The grain growth directions can be expressed in a more exact way as the cells/dendrites-growth directions. The cells/dendrites-growth directions are intensively investigated by Chen et al. [53] for the LB-PBF process of Co-29Cr-6Mo alloy and can be used here to illustrate. The study illustrates that when crossing the track boundary, a grain’s cells/dendrites-growth directions can change  $90^\circ$  from one of  $\langle 001 \rangle$  directions to another  $\langle 001 \rangle$  direction that is most aligned with the new heat flux direction. It is noted that despite the change, this is still epitaxial growth as the grain’s crystallographic orientation remains unchanged. The direction-change location is at the melt pool boundary. Since the scan direction in LB-PBF process rotates  $67^\circ$  by every layer, this also subsequently alters the heat flux directions, which can lead to a disruptive/continuous change in the cells/dendrites-growth directions.

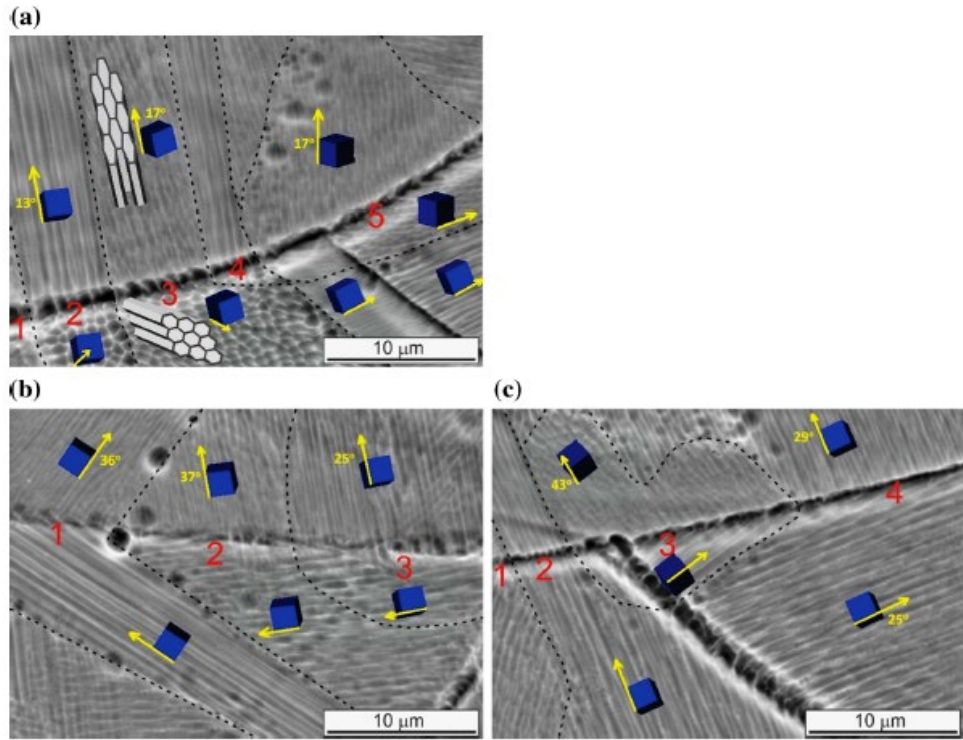
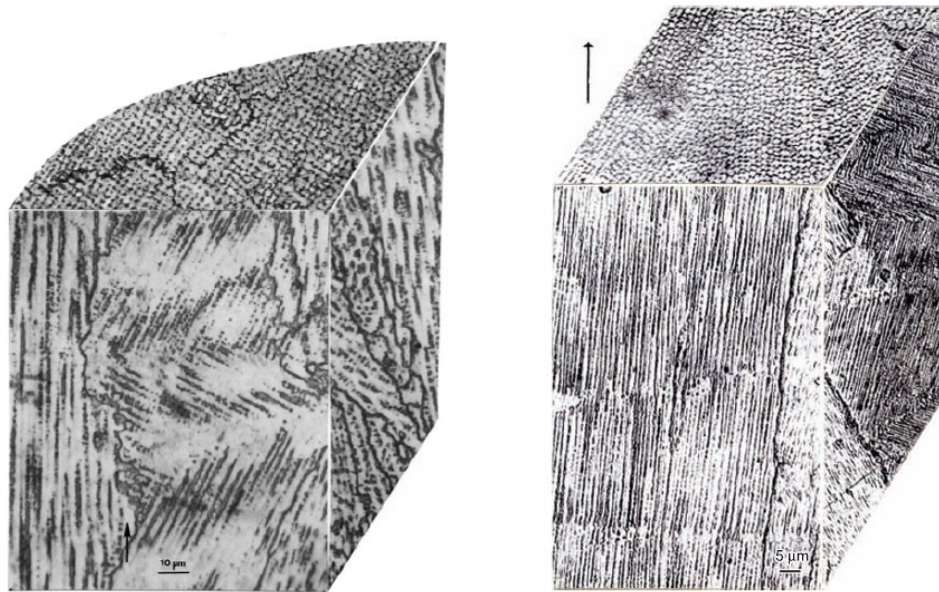


Figure 24. Cells-growth directions at the melt pool boundary and the corresponding crystallographic orientation (of grains) in LB-PBF-fabricated Co-29Cr-6Mo alloy [53]

It can be concluded from Chen et al.'s [53] work that factors affecting the cells/dendrites-growth directions are the melt pool boundary (which determines the heat flux directions), and the crystallographic orientation of the grain from which the cells epitaxially grow. Again, the role of melt/track boundary as discussed in the previous section is shown to be even more crucial.

Gaytan et al. [36] presented an OM image of the EB-PBF-built Co-29Cr-6Mo alloy. A similar observation was reported for EB-PBF high-purity copper by Murr et al. [68]. In Figure 25a, it can be seen that a grains' cells change their growth directions 90° alternatively along the build direction. However, no further descriptions, as well as discussions, were made by the authors on this special feature. It can be seen that the grain with cells growth direction change has to compete with the left one, which may be a preferred  $\langle 001 \rangle$  growth direction (seemingly aligned with the dominant heat flux along the build direction). As the next layer deposited, the right grain may not continue to grow as it is stopped by the left one. However, the heat flux directions (as a result of melt/track boundary) may be aligned with another  $\langle 001 \rangle$  crystallographic direction of the grain, thus the grain continues to grow by changing its direction 90°. This suggestion is consistent with the observation of Chen et al. [53], excepting that melt/track boundary cannot be observed in Figure 25.

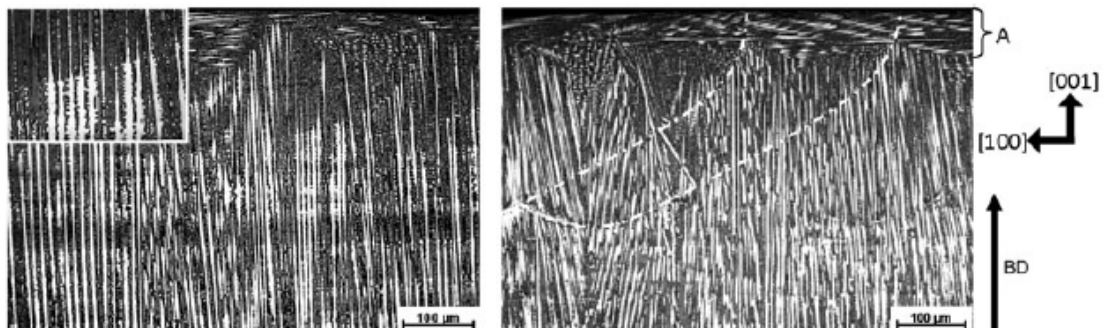


a)

b)

Figure 25. (a). EB-PBF-built of Co-29Cr-6Mo alloy [36] and (b). EB-PBF of high-purity copper showing 90° alternating cells/dendrites-growth directions [68]

Helmer et al. [21] evaluated the microstructure in their EB-PBF of IN718 Ni-based alloy. The grain structures observed are strongly affected by the melt pool shapes which were directly governed by the beam spot sizes. The FO values were not mentioned. Instead, a focused beam of 400 μm and a defocused beam of 500 μm were used (at same  $v = 200$  mm/s and  $P = 200$  W). The melt pool geometries are demonstrated by good cross-sectional micrographs, as shown in Figure 26. A horizontal growth direction can be seen in both melt pool shapes. The feature seems continuous from track to track in the case of the focused beam. The authors suggested that this feature is the development of secondary dendrite arms as the direction of thermal gradient and solidification orientation change during solidification progresses. No further analytical evidence relating to this was provided. Therefore, this growth phenomenon has not been fully understood.



a)

b)

Figure 26. Optical micrographs illustrate the influence of (a). A defocused beam of 500  $\mu\text{m}$  and (b). A focused beam of 400  $\mu\text{m}$  on the melt pool shape in EB-PBF of IN718 Ni-based alloy [21]

Karimi et al. [23] also observed a 90° change in the dendritic growth directions during their multi-tracks experiment of EB-PBF of IN-718 alloy, as shown in Figure 27. The authors suggested that this change is due to the severe change in thermal gradient/heat flux direction during solidification. This suggestion is similar to that made by Helmer et al. [21], which lack of detailed analytical evidence to clarify. In both studies [21, 23], it can be observed that the melt/track boundary may play a crucial role. In Figure 22b [23], no change in cells growth directions is observed for those melt/tracks that have high  $AR$  (width/depth). This high  $AR$  melt/track's boundary is less curvature that leads to the more aligned heat flux directions to the build direction. Consequently, this may not be favorable for the 90° change of cells growth direction.

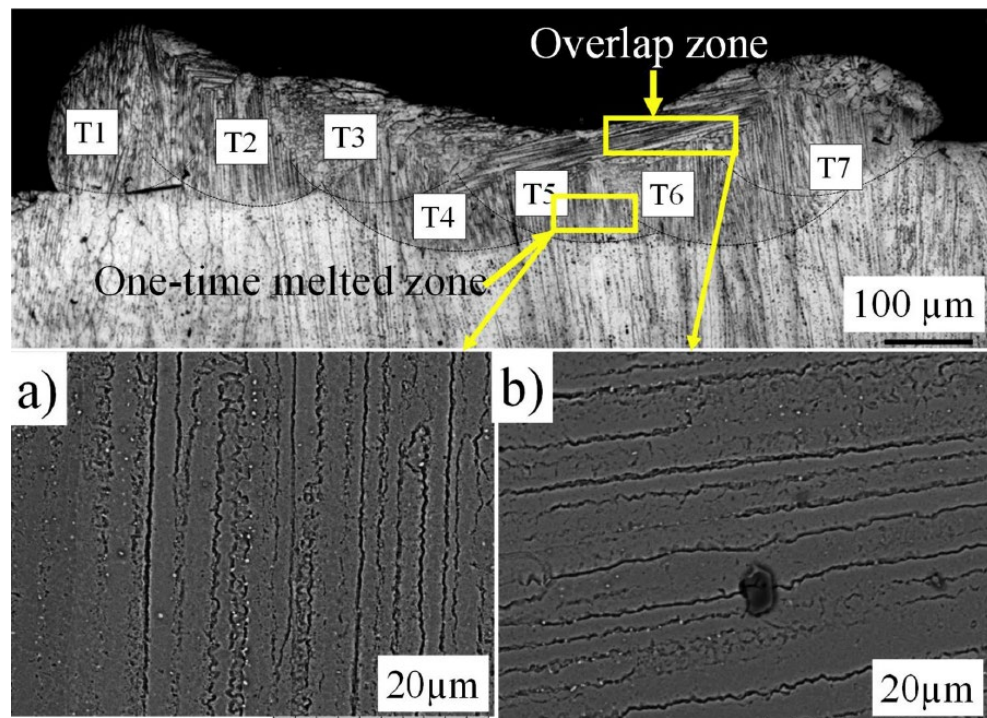


Figure 27. Observation of a 90° change in cells growth direction in Karimi et al.'s study [23]

The alternation of the cells/dendrites-growth directions can potentially affect mechanical properties. Murr et al. [38] showed anisotropic tensile properties between EB-PBF Co-29Cr-6Mo alloy samples that have the pulling axis parallel (EB-PBF-Z) and perpendicular (EB-PBF-XY) to the build direction. It is noted that the cell-growth directions are also along the build direction. In Figure 28, the results show that for the EB-PBF-Z sample, the yield stress (YS) is at 0.5 GPa and the ultimate tensile strength (UTS) is at about 1.5 GPa. For the EB-PBF-XY sample, the YS is higher at  $\sim 0.75$  GPa while the UTS is lower at 0.8 GPa. The elongation is not

significantly different between the two samples. In contrast, the EB-PBF Ti-6Al-4V samples experience similar tensile properties regardless of the pulling axis.

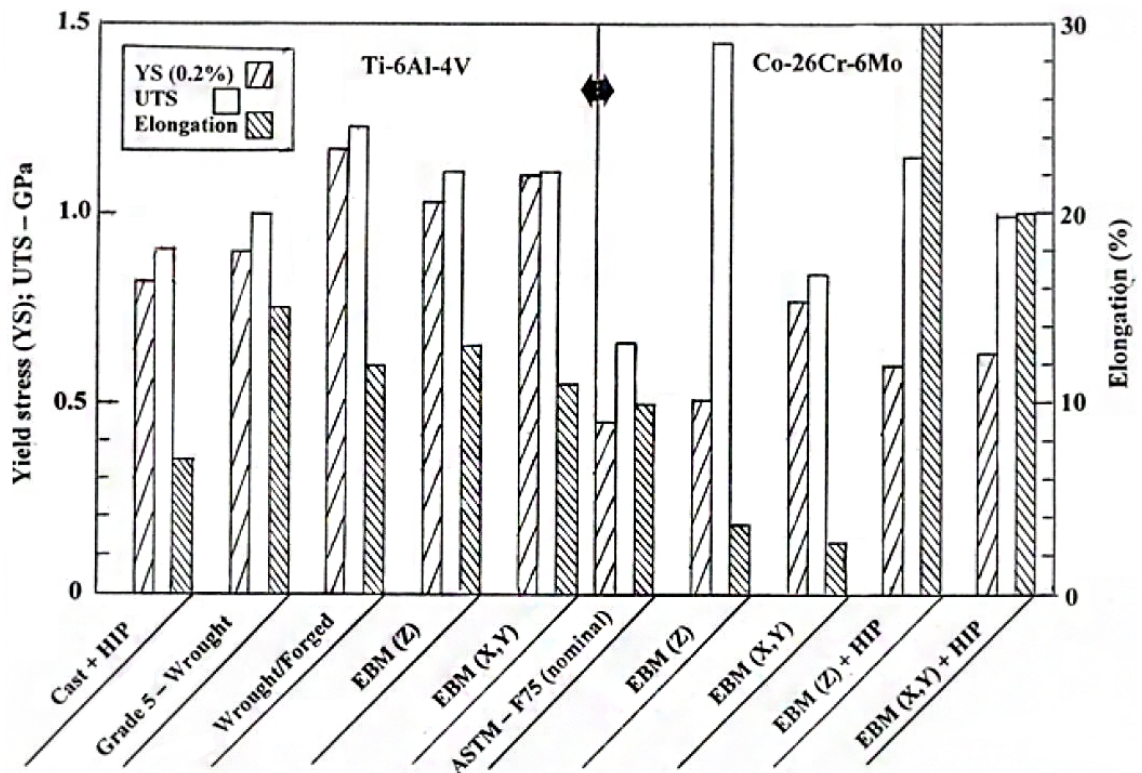


Figure 28. Tensile properties for Ti-6Al-4V and Co-29Cr-6Mo alloy. YS stands for yield stress at 0.2% engineering offset and UTS stands for ultimate tensile strength [38]

Gaytan et al. [36] and Murr et al. [68] illustrated how precipitates formed in their EB-PBF Co-29Cr-6Mo alloy and high-purity copper. The precipitates distribute along the columnar grain boundaries and cells' boundaries which orientate along the build direction. For alloy such as Co-29Cr-6Mo alloy, the carbides act as one of the most important strengthening mechanisms [6, 69]. The change in cells/dendrites-growth directions can affect the arrangement of precipitates/carbides networks, which may result in different mechanical properties in different loading directions. Sun et al. [35] confirmed this statement since they report that the carbides array orientation is one of the influential factors affecting the high-temperature tensile properties of their EB-PBF Co-29Cr-6Mo samples. For the case of Ti-6Al-4V alloy, the cells growth directions cannot be observed and no precipitation strengthening of carbides exists, thus the tensile properties are isotropic. Therefore, understanding of how grains/cells grow with respect to the melt/track geometries, is important. Moreover, the possibilities of modifying the typical columnar grain structure of EB-PBF process by changing the cells/dendrites-growth directions can be desirable since it can alter the carbides array orientation, which possibly mitigates the anisotropic mechanical properties.

### 2.3. Observation and characterization of cracking in PBF-AM processes

The PBF-AM processes are basically similar to the fusion welding process. Thus, a brief summary of understanding on major cracking issues in welding including hot cracking and solid-state cracking will first be given. This is then followed by a critical review of the limited works of PBF-AM processes that have observed or reported on the cracking defect. Research gaps related to the cracking problem in PBF-AM processes will be pointed out and linked to the current cracking problem observed in EB-PBF of Co-29Cr-10Ni-7W alloy.

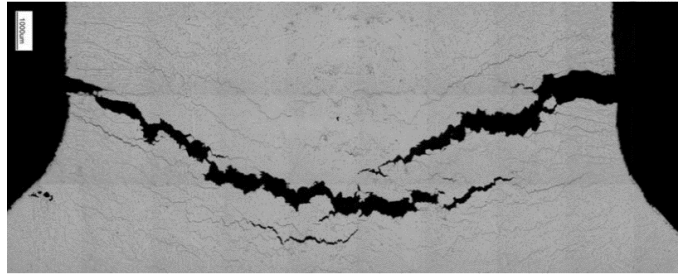
#### 2.3.1. Hot tearing/Solidification cracking

Hot tearing has been a well-known studied subject in the casting of aluminum alloys and steels. Eskin et al. [70] comprehensively review the hot tearing and mechanical properties in the semi-solid state of aluminum alloys which covers a period of 50 years in the literature. For binary aluminum alloys such as Al-Si, Al-Cu, Al-Mg, Al-Fe, Al-Mn and Al-Zn, the hot tearing tendency is shown to have a lambda ( $\Lambda$ ) curve. This tendency reaches to its peak (of the  $\Lambda$  curve) as the alloying elements increase which causes the widening of solidification freezing range. Further increasing of the alloying will result in eutectic solidification and cause a reduction in hot tearing tendency. Similar hot tearing tendency is also applicable to ternary aluminum alloys such as Al-Cu-Mg, Al-Cu-Si, Al-Fe-Si, Al-mg-Si and Al-Cu-Li. For commercial aluminum alloys, hot tearing is also reported for the three series, namely AA2XXX (Al-Cu-Mg), AA6XXX (Al-Mg-Si) and AA7XXX (Al-Zn-Mg). Regarding hot tearing in cast steel, Chojecki et al. [71] point out the influence of carbon and sulfur elements on the hot tearing tendency. While carbon affects the upper temperature of brittleness range, sulfur has been shown to mainly control the range of temperature in which hot cracks can form. However, no  $\Lambda$  curve was shown as in the case of aluminum alloys.

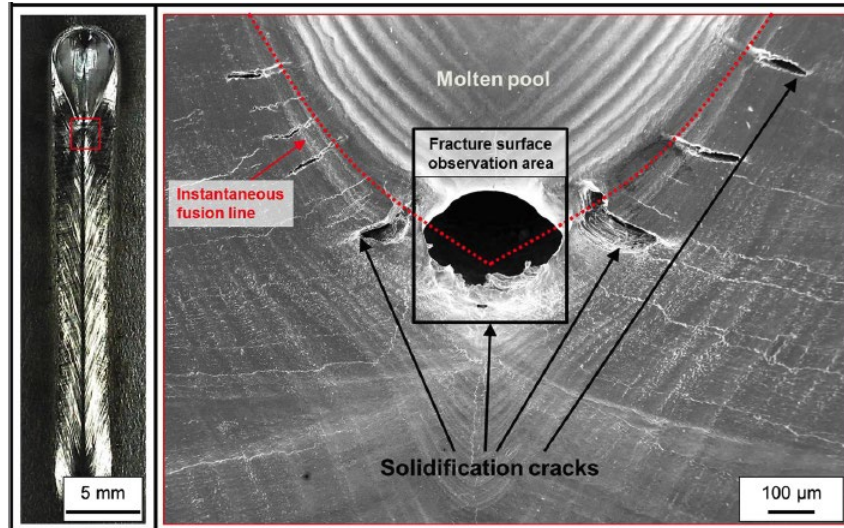
In fusion welding, the crack has been reported to be able to occur both in liquid-state (hot cracking) and in solid-state (referred to as cold cracking). The hot cracking issue is known as solidification cracking and occurs along the solidification grain boundaries, mainly in the fusion zone [63]. The hot cracking in welding includes solidification cracking and liquation cracking. Solidification cracking has been shown to have similar characteristics to the hot tearing phenomena in casting. According to Campbell [16], the hot tearing can be identified by some characteristics:

- The crack is ragged with branching cracks
- The main tear often has many offshoots and follows intergranular boundaries.
- The failure surface reveals dendritic morphology
- The hot tear is highly specific to certain alloys while others may be free from this problem.

Figure 29 illustrates the hot tearing and solidification cracking that occurs in casting and welding, respectively. The solidification cracking normally occurs at the weld bead center-line since this is the place solidification terminates, as shown in Figure 29b (the left image). Factors that contribute to hot tearing/solidification cracking can be listed as thermal effects together with casting/welding restraint and the influence of chemical compositions [72, 73]. Hot tearing/solidification cracking has been observed to occur when solidification processes reach the final stage at which the solid fraction is about 85-95% [70].



a)



b)

Figure 29. (a). Hot tearing in the casting of M206 aluminum alloy [74] and (b). Solidification cracking in laser welding stainless steel 316FR [75]

Figure 30 shows the solidification process. In the beginning, dendrites nucleate and grow from the solid-liquid interface toward liquid metal, as the opposite direction of heat flux. The whole dendrite length is measured from the interface to the dendritic tip, which depends on the alloy's **solidification freezing range ( $\Delta T^*$ )** and can be divided into three areas according to the solid fraction  $f_s$ . The first area, from  $f_s = 0$  to  $f_s = 0.70$ , in which the interdendritic region is relatively wide, together with high permeability of the solidified structure, allows the flow of liquid metal into the region. This backfilling effect can immediately heal any potential cracks or pores that occur at this phase [76]. The second area, from  $f_s = 0.82$  to  $f_s = 0.94$ , is considered as a susceptible region to crack formation. At this stage of solidification, dendrites grow in width and start to interlock each other. Increasing amounts of solid fraction cause a reduction in the structure's permeability. As a result, liquid metal is prevented to flow into interdendritic regions causing traps of thin liquid films. The semi-solid structure (solid + thin liquid film) is very weak to withstand the induced internal and external stresses, which may consequently lead to cracking. Internal stresses can be volume shrinkage or/and thermal contraction and external ones can be the restraint of workpiece with outside mold or fixture. Further increases in solid fraction can create isolated liquid pockets (that originally is a liquid film) which may eventually lead to pore

formation and act as cracking nucleation. The final area shows where the fraction of solid reaches almost 100% ( $f_s \sim 1.0$ ), the material will majorly possess a solids' mechanical properties and is able to withstand induced stresses.

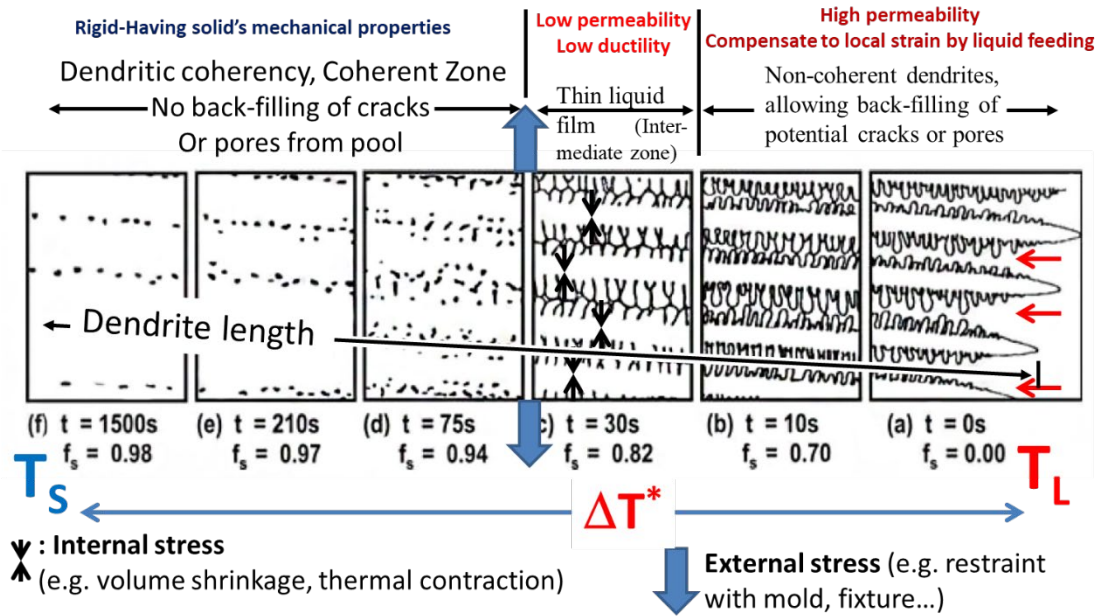


Figure 30. Schematic illustration of hot tearing/solidification cracking mechanism. Larger  $\Delta T^*$  results in longer the inter-dendritic liquid film. (image adapted and modified from [76])

As can be seen from Figure 30, hot cracking susceptibility can be evaluated based on a sensitive liquid film which depends on the intrinsic nature of the material ( $\Delta T^*$ ) and the processes' thermal gradient ( $G$ ), which can be written out as:

$$l_{\text{film}} = \frac{\Delta T^*}{G} = \Delta T^* \cdot \frac{dy}{dT}$$

Eq. 11

The longer the inter-dendritic liquid film is, the more susceptible to hot cracking. By changing alloy compositions,  $\Delta T^*$  can be wider or narrower [71, 77]; and alternating process conditions can influence  $G$ . Moreover, the influence of restraint on cracking susceptibility has been well established [70, 72, 78-84]. Common criteria are employed in these models and be listed as stress-based, strain-based and strain-rate-based which are intensively reviewed in [70].

In the stress-based criteria, the liquid film trapped between grain boundaries is considered as a weak point. If the induced tensile stresses (i.e. thermal contraction, solidification shrinkage) exceed the withstanding limit of the liquid film, then the stresses are sufficient to separate the two grains which result in a fracture. The schematic illustration of the model is shown in Figure 31. The relationship between the induced tensile stresses and the liquid metal film can be simply expressed by Eq. 11, as originally proposed by Novikov [82] and Dickhaus et al. [85]

$$\sigma_{fr} = \frac{2\gamma}{b} \quad \text{Eq. 12}$$

where  $\sigma_{fr}$  is the fracture stress,  $\gamma$  is the surface tension and  $b$  is the film thickness. The Eq. 12 assumes that the liquid is uniformly distributed between grains, thus the effect of liquid film length is neglected. More advanced models can be found in later works of Lahaie and Bouchard [86] with consideration of solid fraction, strain  $\varepsilon$  and microstructure parameter (i.e. equiaxed or columnar grains), or fracture mechanics approach proposed by Williams and Singer [87].

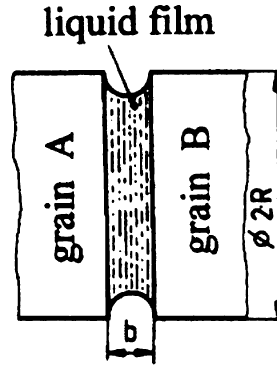


Figure 31. Model of two grains separated by a uniform liquid metal film in the assumption of complete wetting between grains and melts [70] (original from the work of Dickhaus et al. [85])

Regarding the strain-based criteria, Novikov [82] proposed a characteristic called “reserve of plasticity in the solidification range” –  $p_r$  that employs the ductility of the semi-solid material. The value of  $p_r$  is the difference between the average integrated value of the elongation to failure  $\varepsilon_p$  and the linear shrinkage/contraction  $\varepsilon_{sh}$  in the brittle temperature range  $\Delta T_{br}$  [70]. The hot tearing susceptibility is then given by:

$$p_r = \frac{S}{\Delta T_{br}} \quad \text{Eq. 13}$$

where  $S$  is the area between  $\varepsilon_p$  and  $\varepsilon_{sh}$  curves in the brittle temperature range  $\Delta T_{br}$ , as shown in Figure 32. If the  $\varepsilon_{sh}$  curve intersects the  $\varepsilon_p$  then Eq. 13 becomes:

$$p_r = \frac{S_1 - S_2}{\Delta T_{br}} \quad \text{Eq. 14}$$

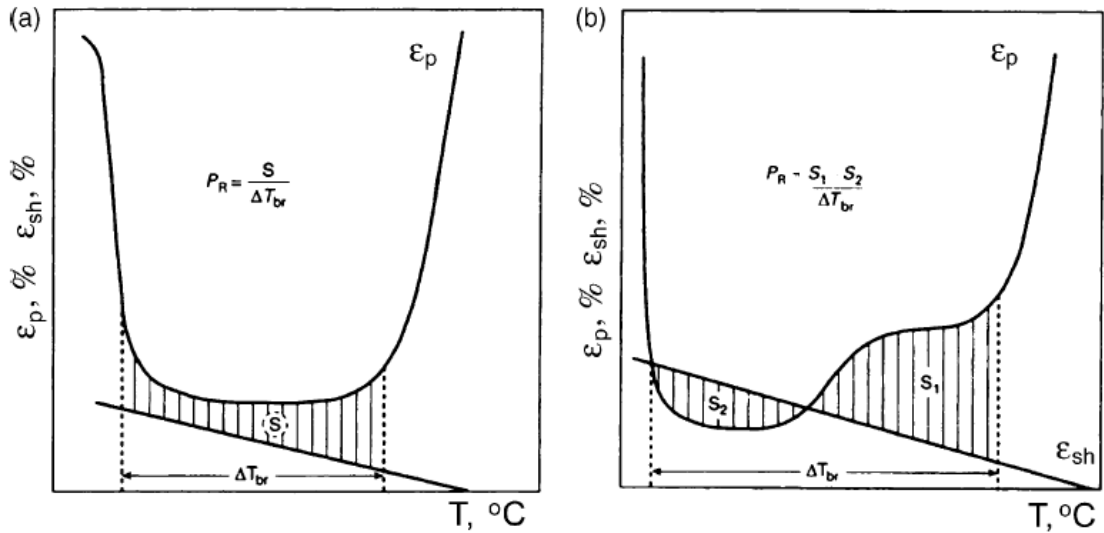


Figure 32. Two types of the temperature dependence of elongation to failure ( $\epsilon_p$ ) and linear shrinkage  $\epsilon_{sh}$  in the semi-solid brittle temperature range [70]

The last hot tearing criteria is the strain-rate based proposed by Prokhorov [88] which considers both the semi-solid material's ductility and the geometrical configuration of the solidifying body. It also differs from the work of Novikov [82] as the strain rate is used instead of strain for measuring the hot tearing tendency. Rappaz et al. [83] based on the strain-rate to develop the widely used hot tearing criterion named as RDG criterion. In this model, cavity formation is considered as hot tear initiation. In addition, the model is derived for columnar dendrites. The hot cracking sensitivity (HCS) is described as:

$$HCS = 1/\dot{\epsilon}_p^{max} \quad \text{Eq. 15}$$

where  $\dot{\epsilon}_p^{max}$  is the critical deformation rate.

### 2.3.2. Liquation cracking

Liquation cracking is classified as hot cracking since it occurs above the solidus temperature. While solidification cracking can happen in both casting (referred to as hot tearing) and welding, liquation cracking is just in welding, specifically located in the partially melted zone (PMZ) of the weld. Different weld zones are shown in Figure 33 with a corresponding temperature range from the phase diagram [89].

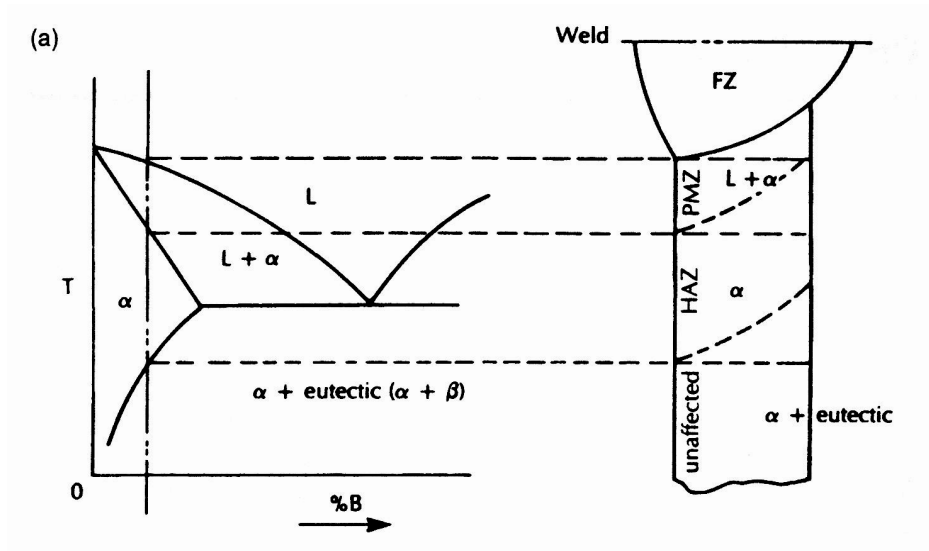


Figure 33. Schematic illustration showing a correlation between various zones in a fusion weld in an alloy and the corresponding equilibrium diagram [89]

Liquation cracks are also observed at intergranular boundaries. Liquation cracking takes place in base metal outside of the fusion zone and is caused by remelting of eutectic structure which has a low melting temperature. Figure 34 illustrates liquation cracking in the PMZ.

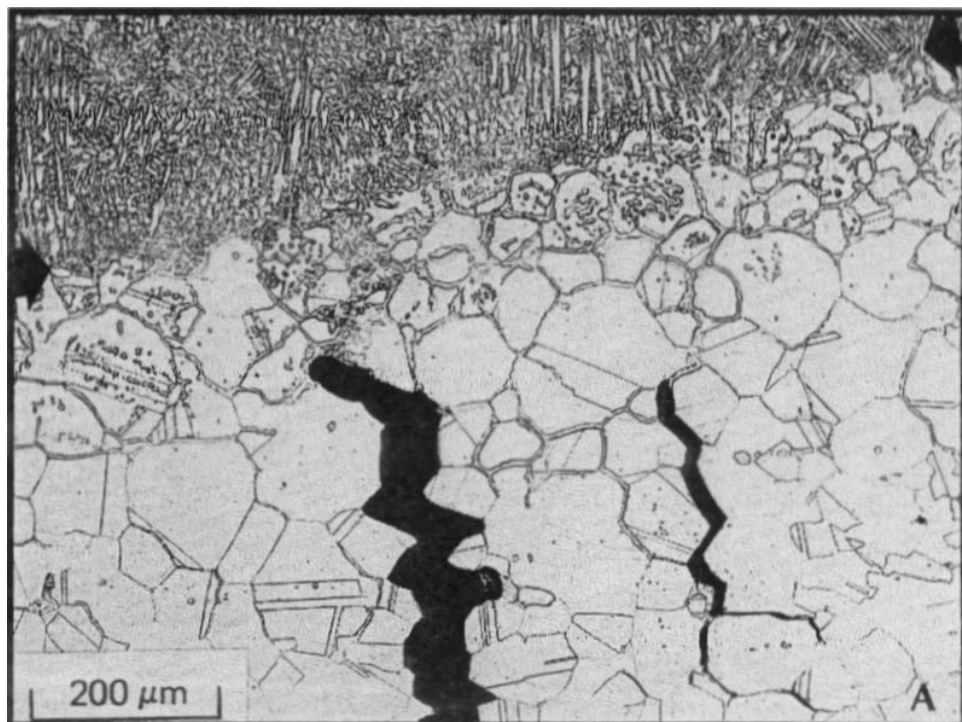


Figure 34. Liquation cracking in the PMZ. The darker area is the fusion zone [90]

There will be two simultaneous solidification processes occurring during welding. The first region is the weld metal or the fusion zone in which metal is completely melted, as illustrated in Figure 33. In this region, the solidified structure will have dendritic or cellular morphologies dependent on temperature gradient and welding speed. The PMZ region comprises of well-

developed grains and low-melting temperature elements at grain boundaries such as eutectic phases formed by segregation process [73, 91]. Those low-melting temperature elements under heat induced from the weld metal will be remelted back and cause grain boundary liquation. The liquation cracking will result from solidification competition between the weld metal and the PMZ. If the weld metal solidifies faster than the PMZ, or in another word, the solid fraction of the weld metal at a point of time is higher than that of the PMZ, there is a considerable tensile force from the weld metal. Solidification shrinkage, as well as thermal contraction from the weld metal, is greater than the tensile strength of the semi-solid structure of the PMZ; therefore, the PMZ will be separated along grain boundaries and cause liquation cracking (Figure 35a). In a reverse way, if the solid fraction of the PMZ is higher than that of the weld metal, there will be a less tensile force from the weld metal and the PMZ structure can accommodate this stress without any cracking happens (Figure 35b).

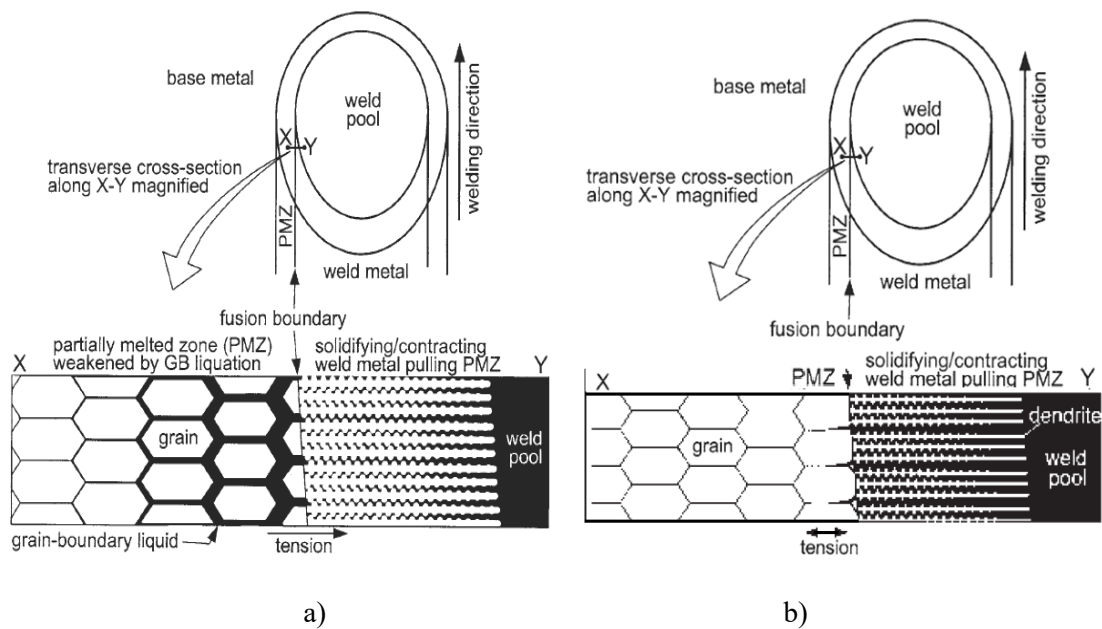


Figure 35. Illustration of liquation cracking mechanism in welding [73, 91]

### 2.3.3. Ductility-dip cracking

Ductility-dip cracking (DDC) phenomenon is determined as solid-state cracking as it normally occurs at an intermediate temperature which is around  $0.6T_s - 0.9T_s$ , as shown in Figure 36 [92]. In literature, DDC phenomenon has been widely studying on Ni-based superalloys in multi-pass welding condition [93-102].

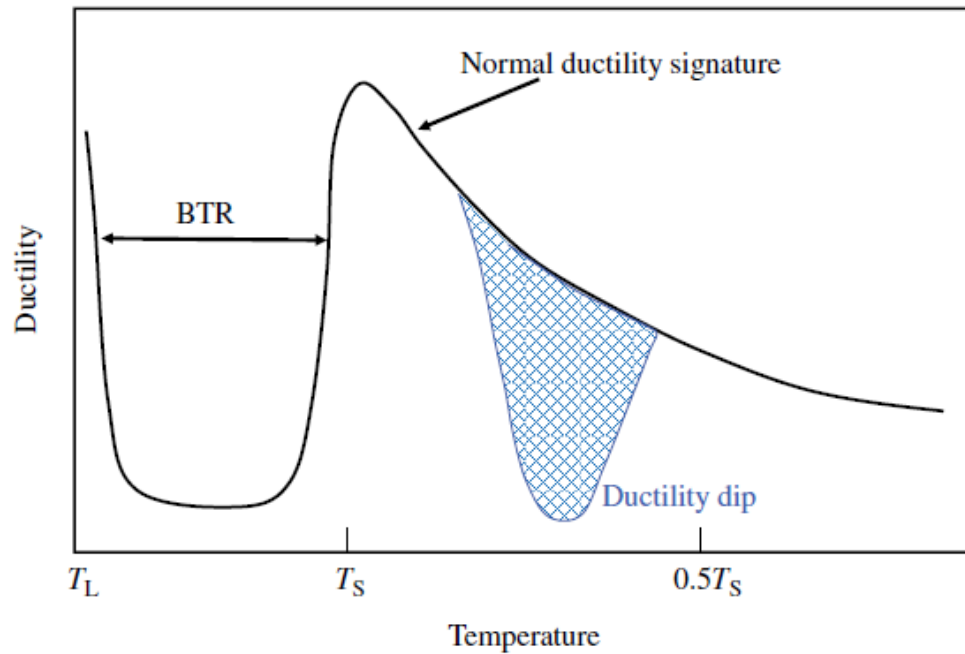


Figure 36. Sensitive temperature range to ductility-dip cracking [63]

Regarding the mechanism of DDC, the so-called grain boundaries sliding (GBS) mechanism has been studied and received most agreement by many researchers [94-99, 101, 103-107]. Nissley and Lippold [103] developed a test method named “Strain to Fracture” (STF) to simulate conditions that promote DDC and to distinguish DDC from liquation cracking. As DDC phenomena usually happen in multi-pass weldments or such conditions in that materials experience many cycles of reheating and cooling. During these cycles, materials experience internal stresses which tend to cause grain boundaries sliding that can promote DDC. Normally, DDC happens at migrated grain boundaries (MGB) which are straight and easy to slide. Migrated grain boundaries is an atomic crossing the boundaries between different grains with net energy gain [108]. MGBs are straight and provide an ideal condition for GBS to occur. Figure 37 shows a solidification grain boundary and a DDC occurs at MGB.

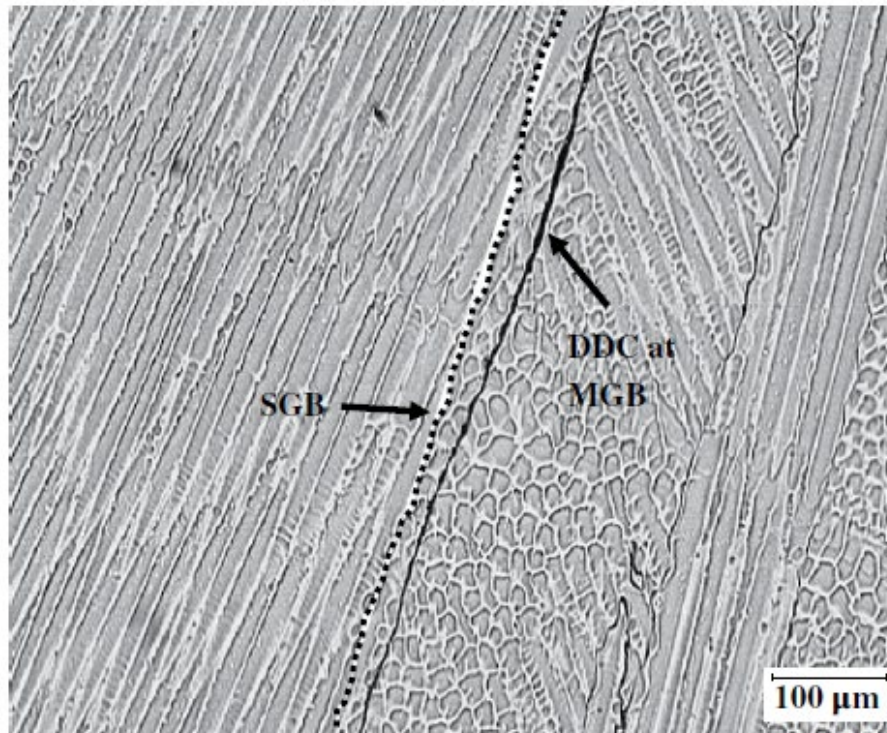


Figure 37. (a). Solidification grain boundaries (SGB) and Migrated grain boundaries (MGB).  
DDC occurs at MGB [92]

The presence of carbides/precipitates is beneficial to prevent DDC. Figure 38 shows that pure Ni-200 alloy has no precipitates observed which have high DDC susceptibility [101]. The carbide precipitates at MGBs can inhibit the mobility of GBs leading to more tortuous GBs instead of straight ones. This pinning or locking effect strengthens grain boundaries so that DDC finds its way very difficult to propagate. These effects depend on carbide types, size, carbides-matrix relationship and the fraction of precipitates on grain boundaries [105]. For example,  $M_7C_3$  carbide forming at GBs showed its overwhelming influence than  $M_{23}C_6$  type. However,  $M_7C_3$  forming elements such as Nb or Ti should be carefully controlled as excessive content will increase the alloy's solidification freezing range which leads to higher liquation cracking susceptibility [96].

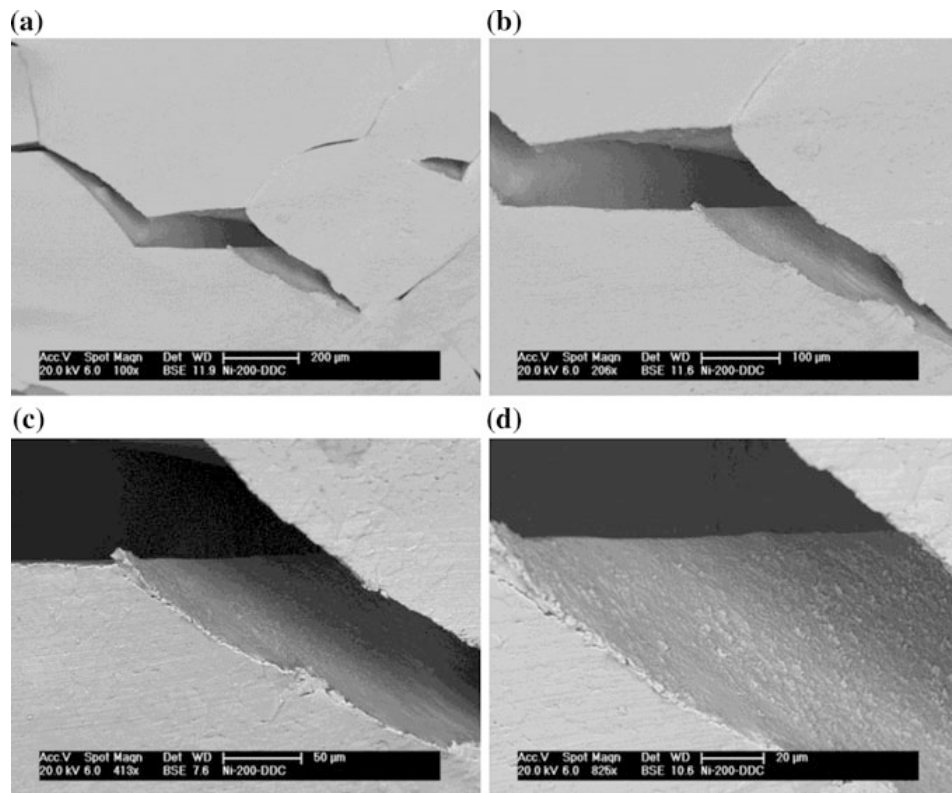


Figure 38. Pure Ni-200 alloy fracture morphology shows a smooth inter-granular DDC. Pure Ni-200 alloy has no precipitates which increase DDC susceptibility [101]

#### 2.3.4. Reheat cracking and strain-age cracking

Reheat cracking and strain-age cracking occur during post weld heat treatment (PWHT) or stress relief heat treatment after welding [63]. In multi-pass welding, these cracking issues also occur because subsequent weld passes cause “re-heating” conditions which is similar to PWHT conditions. As the temperature ranges of PWHT is at around  $0.5T_s$ , thus these forms of cracking are classified as solid-state cracking.

In welding, reheat cracking is common in low-alloy steels with secondary carbide formers (i.e. Cr, Mo or V) while strain-age cracking has been reported for precipitation-strengthened Ni-based alloys. Figure 39 illustrates the mechanisms of reheat cracking at different stages of PMZ and PWHT for low-alloy steels. For strain-age cracking, a similar mechanism is seen as the role of precipitation-strengthening of  $\gamma'$  is identical to the role of secondary carbides in low-alloy steels.

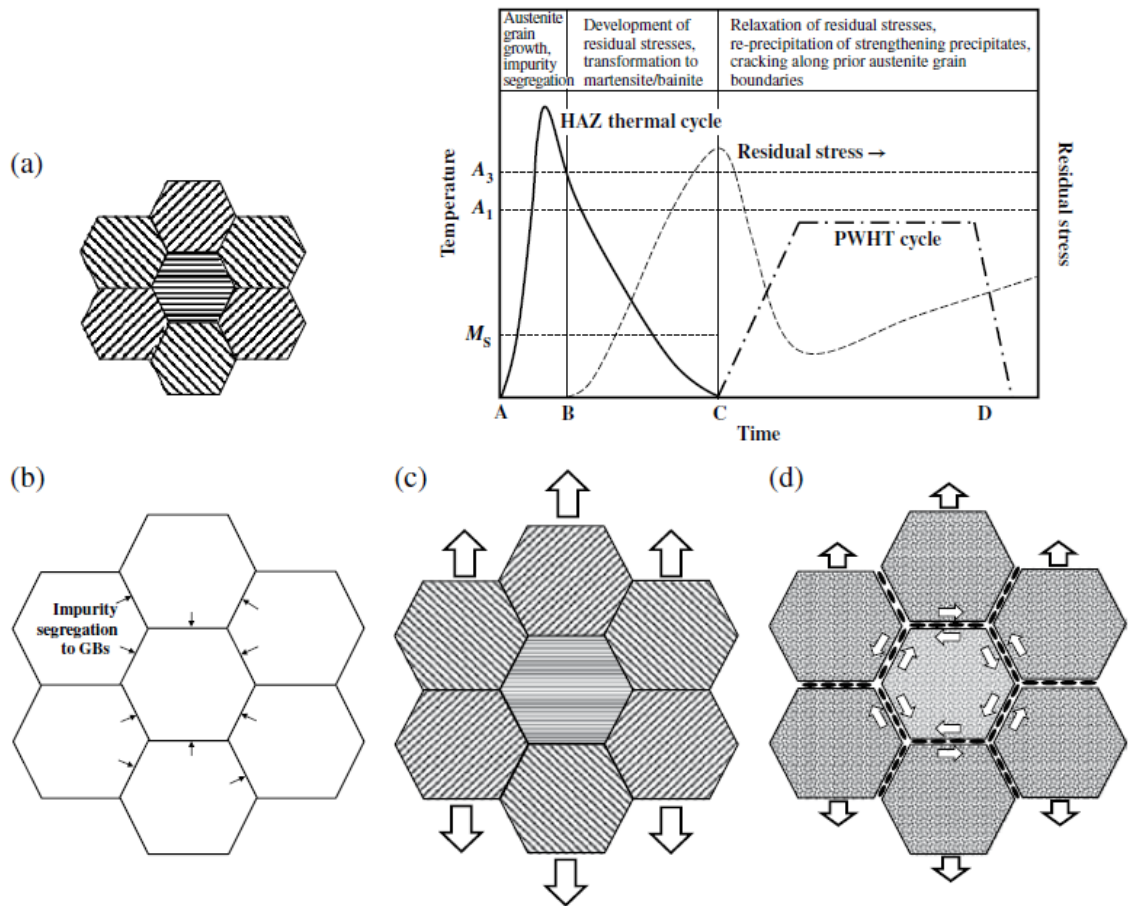


Figure 39. Schematic illustration of thermal cycle associated with reheat cracking in low-alloy steels: (a). Grains in PMZ before welding; (b). Coarser grains due to heat affected by welding; (c). Development of residual stresses incorporating with martensite/bainite transformation; (d). Relaxation of stresses, re-precipitation of strengthening precipitates, cracking along grain boundaries [63]

As indicated in Figure 39, during the welding cycle, grains in PMZ are heated and become coarser. Carbides at grain boundaries if any will be dissolved thus leading to a reduction in hardness. A PWHT then is required to temper the martensitic microstructure. During PWHT, secondary carbides are re-precipitate in combination with the stress relaxation will lead to cracking along the prior austenite grain boundaries of the coarsening grains in PMZ.

### 2.3.5. Identification of hot cracking and solid-state cracking

Accurately identifying the form of cracking is crucial for examining and investigating the causes and mechanisms. Lippold [63] has provided instruction on identifying cracking that possibly occurs during fusion welding. Cross-sectional SEM images can be useful in distinguishing solidification cracking from liquation cracking, reheat cracking and strain-age cracking as one occurs in the fusion zone and the others are in PMZ and HAZ. However, in EB-PBF process, it is difficult to point out the fusion zone, PMZ, and HAZ. Therefore, fracture

surface examination is the most ideal method to provide an accurate interpretation of the cracking characteristics.

For solidification cracking, the fracture surface appears in smooth and rounded features indicating the dendritic morphologies has been separated at the terminal stage of solidification. Figure 40 demonstrates examples of solidification cracks surface as shown by Lippold [63].

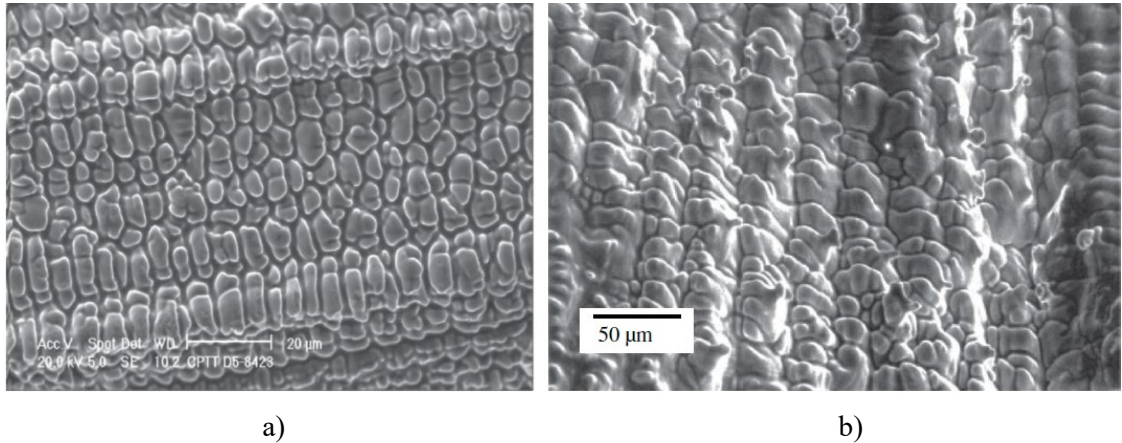


Figure 40. Solidification crack's the fractured surface of (a). Ni-based alloy and (b). Duplex stainless steel [63]

For liquation cracking, it is easy to distinguish from solidification cracking in welding as the microstructures in the fusion zone and PMZ/HAZ is distinctive. However, it is challenged to identify the liquation cracking and other forms of solid-state cracking since they both occur in PMZ and HAZ and along the grain boundaries. In welding, liquation cracking is observed close to the fusion boundary. The liquation crack's fracture surface appears smooth and wavy indicating the presence of liquid film at one time. In addition, no traces of dendritic features make it different from solidification cracking. Figure 41 illustrates the fracture surface of liquation cracking, as obtained by Lippold [63].

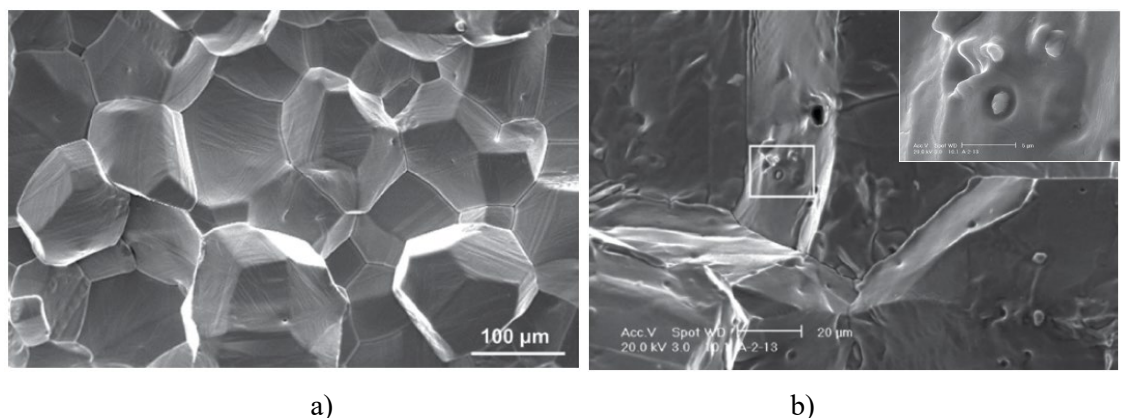


Figure 41. Liquation crack's fracture surface of (a). Low-alloy steel HY-100 [109] and (b). Ni-based alloy (Waspaloy) [110] (obtained by Lippold [63])

Regarding DDC, the examination of fracture surface as discussed in [63] is not significantly different from liquation cracking. The fracture surfaces of DDC of type 310 stainless steel at various testing temperature are shown in Figure 42. It can be seen that the surface is flat at low temperature (750 °C) and becomes wavier as temperature increases (950 °C, 1100 °C). The wavy pattern, however, results in confusion when DDC is compared to liquation cracking. Therefore, other factors should be considered for appropriate identification between DDC and liquation cracking. These factors include the fact that DDC always occurs at MGBs and requires neither formation of strengthening precipitates nor grain boundaries impurity segregation [111].

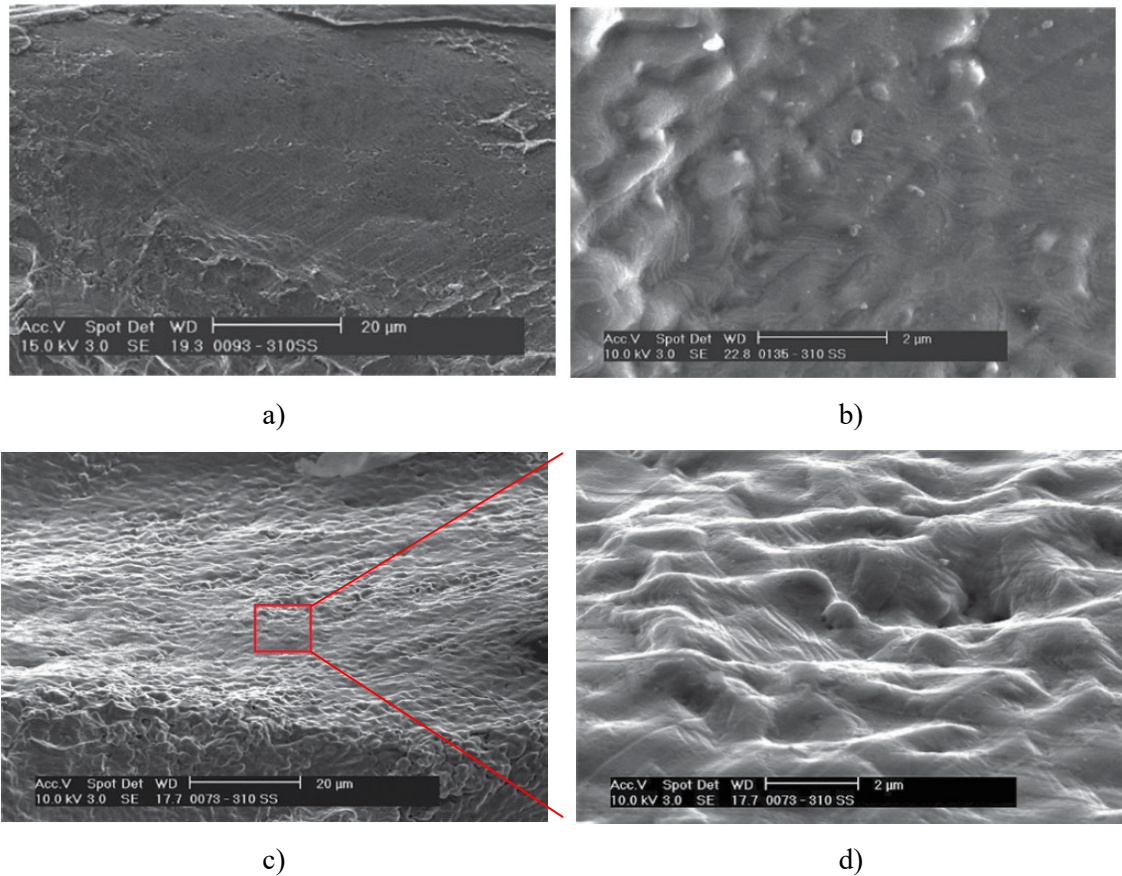


Figure 42. DDC fracture surface in Type 310 stainless steel at (a). 750 °C; (b). 950 °C and (c). 1100 °C; (d). Higher magnification of selected location in (c) [63]

For reheating and strain-age cracking, fracture surface is also observed along the grain boundaries of the PMZ and appears flat, featureless or clearly reveals evidence of microductility. No wavy surface indicative for the presence of liquid film is observed. Figure 43 shows the strain-age cracking fracture surface of Ni-based alloy 718.

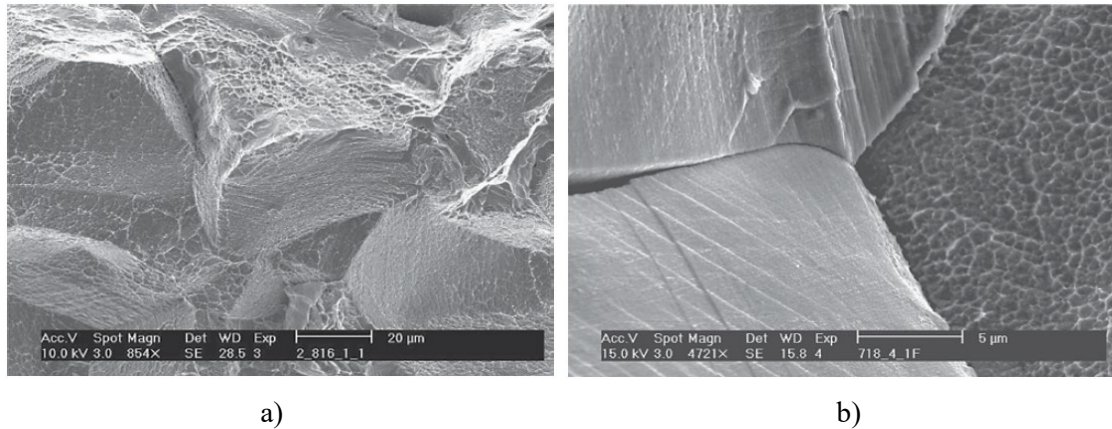


Figure 43. The fracture surface of strain-age cracking in Ni-based alloy 718. (a). Ductile intergranular and (b). Mixed flat and ductile intergranular [63]

## 2.4. Current understanding of cracking in PBF-AM processes

### 2.4.1. Cracking during EB-PBF

Cracking is usually observed in non-weldable metallic alloys such as Hastelloy-X, CMSX-4, CM247LC or IN738 Ni-based superalloys [112-116]. Similar to welding, EB-PBF process has typical characteristics that are susceptible to the hot-cracking formation. The solidification of a single scanning tracks results in solidification cracking while the remelting from successive scans on the preceding tracks/layers can cause liquation cracking to happen. The fundamentals are quite well known in welding; however, still ambiguous in the literature when applying to EB-PBF process. The typical columnar grains microstructure, with long and straight grain boundaries, is favorable for hot-cracking propagation.

Rutter et al. [117] observed large macroscopic cracks throughout the entire cross-sectional surface in the EB-PBF CMSX-4 Ni-based alloy when applying low line energies  $E_{line} = 0.190\sim 0.205$  J/mm. At high line energy  $E_{line} = 0.6\sim 0.72$  J/mm, crack-free samples were achieved. The cracks appear along the columnar grain boundaries, as shown in Figure 44. These cracks are 400-800 μm in length and very severe. The authors suggested that cracks occur due to thermally induced residual stresses, as described by Harison et al. [115] for LB-PBF process. However, in EB-PBF experiment done by Rutter et al. [117], the start plate was preheated to 950 °C. Thus the thermally induced residual stresses are expected to be substantially lower than LB-PBF. In addition, no further analytical evidence supports for the suggestion was done by the authors. Therefore, it is unclear in the work of Rutter et al. [117] which is the mode of cracking. In addition, the effect of high line energies  $E_{line}$  (0.6~0.72 J/mm) on the crack-free sample has not been further analyzed. According to Eq. 11 on the length of liquid film  $l_{film} = \Delta T^*/G$ , increasing the  $E_{line}$  can cause the local temperature of the melt increase. Since the start plate

temperature was kept unchanged at 950 °C, this then increases the thermal gradient  $G$ . Higher of  $G$  will reduce the  $l_{film}$ , thus possibly reducing the cracking susceptibility.

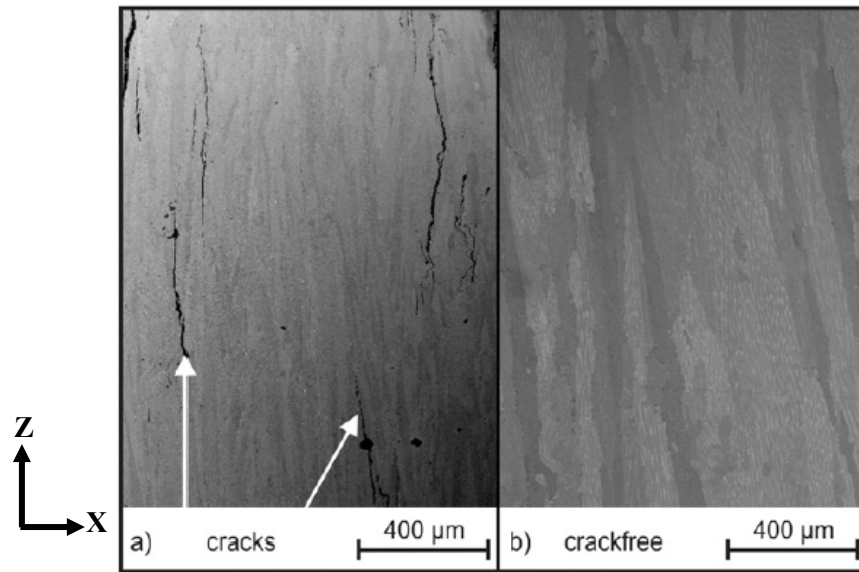


Figure 44. EB-PBF as-built microstructure (along build direction): a) specimens with  $E_{line}$  from 0.19~0.205 J/mm. b) Crack-free specimens built with  $E_{line}$  from 0.6~0.72 J/mm [117]

In a similar study, Ramsperger et al. [118] reported the effect of the preheat temperature on cracking in their EB-PBF CMSX-4 Ni-based alloy. By using a sample with pyramid geometry, at lower preheat temperature of 940 °C cracks occurred, while at a higher temperature of 1040 °C, no cracks were observed. In addition, cubic samples were built with a preheat temperature of 1040 °C and high  $E_{line}$ , as shown in Figure 45b resulted in the crack-free microstructure. Cracks are observed as short cracks (approx. 100-150  $\mu\text{m}$ ) and co-exist with binding faults as the result of lack of fusion, as demonstrated in Figure 45a. The authors believed that very high temperatures are pre-requisite condition for crack-free processing. However, no further analytical works have been done to clarify this suggestion. As the influence of  $E_{line}$  has been shown previously with respect to  $G$  and then  $l_{film}$ , the role of preheat temperature is still unclear. Increasing of the preheat temperature may reduce the thermally induced stresses, however, it possibly decreases thermal gradient  $G$ , thus increases the length of liquid film  $l_{film}$ . The crack-free result of using 1040 °C compared to 940 °C preheat temperature may suggest that the degree of releasing stresses overcomes the risk of increasing the length of liquid film  $l_{film}$ . Therefore, a detailed analysis of the compromise between stress relief and exaggerating the liquid film when increasing preheat temperature needs to be investigated.

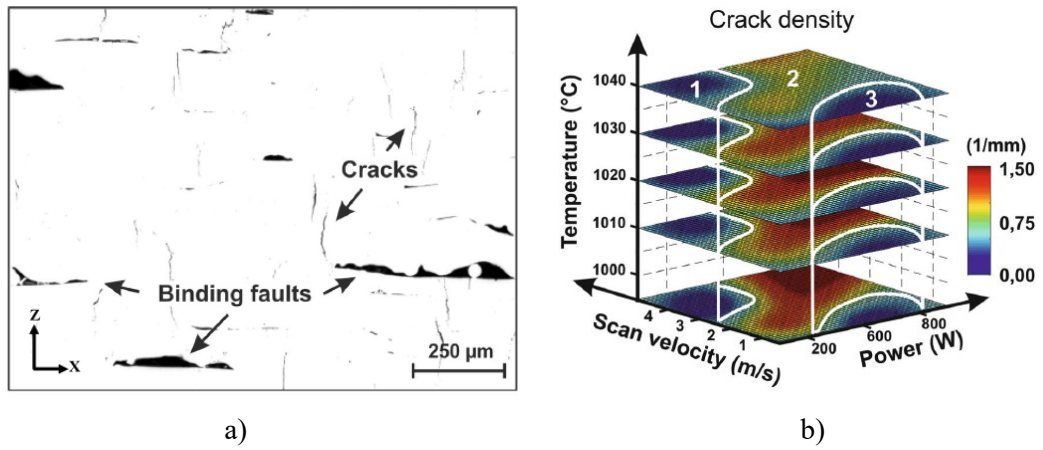


Figure 45. (a) Cracks observed and (b). Relationship between crack density and EB-PBF parameters [118]

Chauvet et al. [113] reported a comprehensible description on hot-cracking in EB-PBF of a non-weldable Ni-based superalloy. In Figure 46, cracks are shown in XZ cross-section (with Z as the build direction). With the sample's height is 30mm, cracks are observed mostly at Z = 12-30 mm. There are no cracks occurred at Z= 0-12 mm. In addition, cracks were found at grain boundaries that have misorientation angles larger than 15° (defined as high angle grain boundaries - HAGBs).

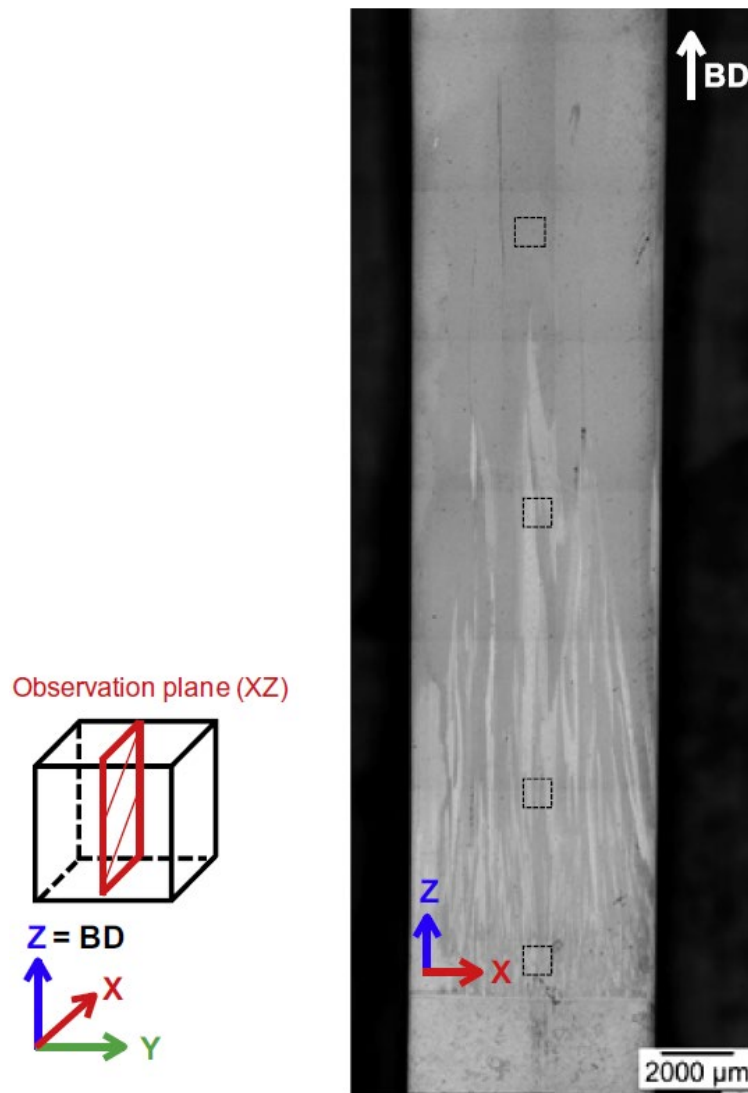


Figure 46. Microstructure of an as-built specimen observed in the central part on an XZ cross-section showing cracks of several millimeters [113]

Regarding cracking mechanism, solid-state cracking is excluded since evidence of liquid film in the form of wetting dendritic morphologies was observed at the fracture surface. The traces of liquid film were indicated to be constructed by various types of boride as the effect of boron enrichment at the grain boundaries. In addition, it was shown that the boron enrichment occurred during the critical temperature range  $\Delta T_{CTR}$  at  $\sim 350$  °C (at a solid fraction from 0.95 to 1). However, Chauvet et al. [113] were unable to discriminate whether the hot cracks are solidification or liquation cracking or a combination of two events. The high distribution of cracks at HAGBs is explained by using the theoretical model of Rappaz et al. [119] on attractive and repulsive grain boundaries. As illustrated in Figure 47, HAGBs promote the stability of the liquid film, thus decreasing the coalescence temperature  $T_{coalescence}^{HAGB}$ . In contrast, dendrite arms are easy to bridge to each other at low angle grain boundaries (LAGBs). In the model, the liquid film length  $l_{film}$  can be seen as proportional to the critical coalescence undercooling  $\Delta T_{CC}$ .

However, how significantly  $\Delta T_{CC}$  relates to the liquid film length  $l_{film}$  was not presented. Furthermore, with  $\Delta T_{CTR} = 350$  °C and the numerically predicted thermal gradient  $G$  for EB-PBF is  $10^5$  K/m [28-30], the liquid film length  $l_{film}$  can be up to  $\sim 3.5$  mm (according to Eq. 11). This liquid film length is significantly longer if compared to the melt pool penetration depths (not larger than 0.3mm) have been reviewed for EB-PBF in chapter 2.2.3. Therefore, liquation may extend to outside the melt/track fusion zones, thus implying the possibility of liquation cracking. Furthermore, cracks are seen extensively crossing many layers. How cracks propagated during EB-PBF process has not been presented by Chauvet et al. [113]. Moreover, the triggering thermal stresses to hot cracking were not discussed with respect to track-by-track and layer-by-layer manufacturing conditions of EB-PBF.

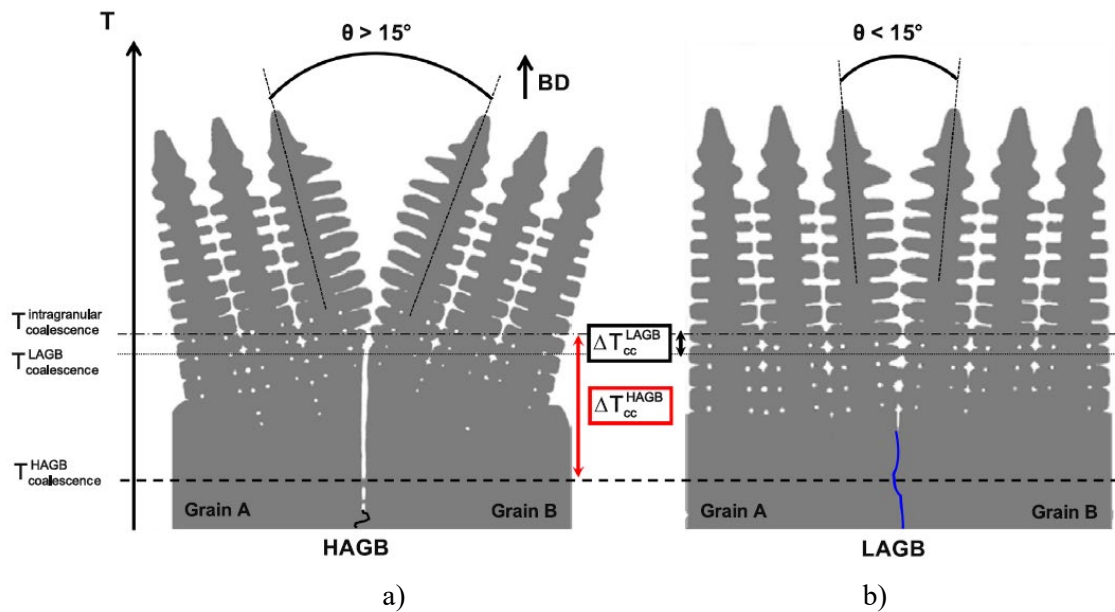


Figure 47. Schematic illustration of the last stage of columnar dendritic solidification. (a). “Repulsive” HAGB and (b). “Attractive” LAGB. The liquid is colored white, solid is grey [113]

Another study on non-weldable Ni-based alloy was conducted by Chauvet et al. [120] related to the production of single crystal microstructure via EB-PBF process. Different line energies  $E_{line}$  from 0.3 to 0.6 J/mm were used. Microstructure characterization shows that cracks are extensively observed in most of the samples, excepting those were built with the highest energy of 0.6 J/mm, as shown in Figure 48. At the highest  $E_{line} = 0.6$  J/mm, the microstructure experienced a transition from polycrystal to the nearly single crystal that consequently reduced grain boundaries misorientation significantly. The measured angles only range from  $2^\circ$  to  $15^\circ$ . Thus, the crack-free sample confirms the findings in the previous study of the authors [113]. Apart from that, the authors did not present an analysis to elucidate the cracking mechanisms.

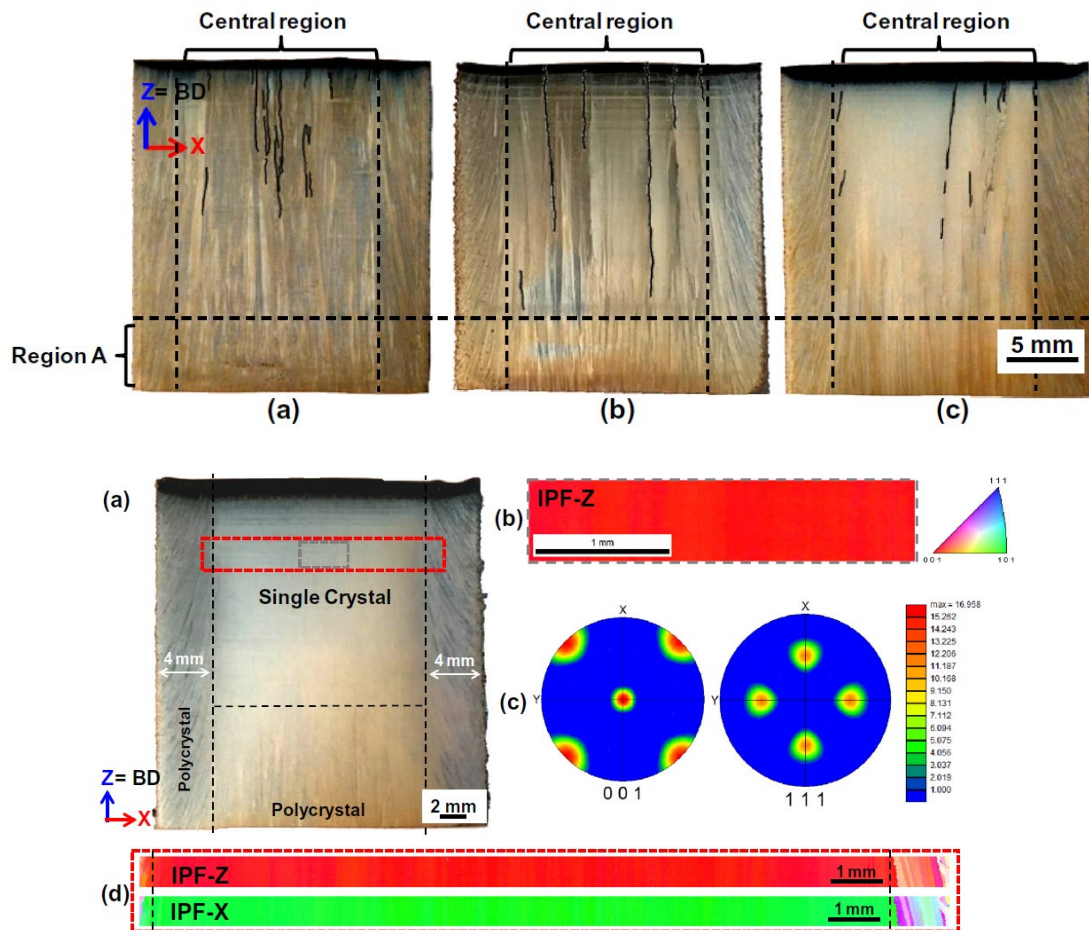


Figure 48. Hot cracking observed of various linear energies in EB-PBF non-weldable Ni-based alloy. A single crystal structure was produced and the crack-free sample was achieved [120] Peng et al. [121] observed similar cracking behavior in their EB-PBF of DZ125 Ni-based alloy, as shown in Figure 49. Cracks are found to be very severe and can last more than a hundred layers regardless of coarse or fine columnar grain structures. Fractography examination of cracks' surface reveals smooth surfaces with rounded features. This suggests that the solidification and/or liquation cracking was the governed mechanisms. However, as similar as Chauvet et al. [113], the authors have difficulty in distinguishing the exact hot cracking mechanisms. The authors stated that incorporation between the liquid film, the solidification shrinkage and thermal contraction in the solid, mainly contributes to the hot cracking. However, no further analytical evidence was provided to support the statement. Moreover, how cracks propagated through many layers has not been considered. Therefore, the hot cracking reported by Peng et al. [121] is just observation.

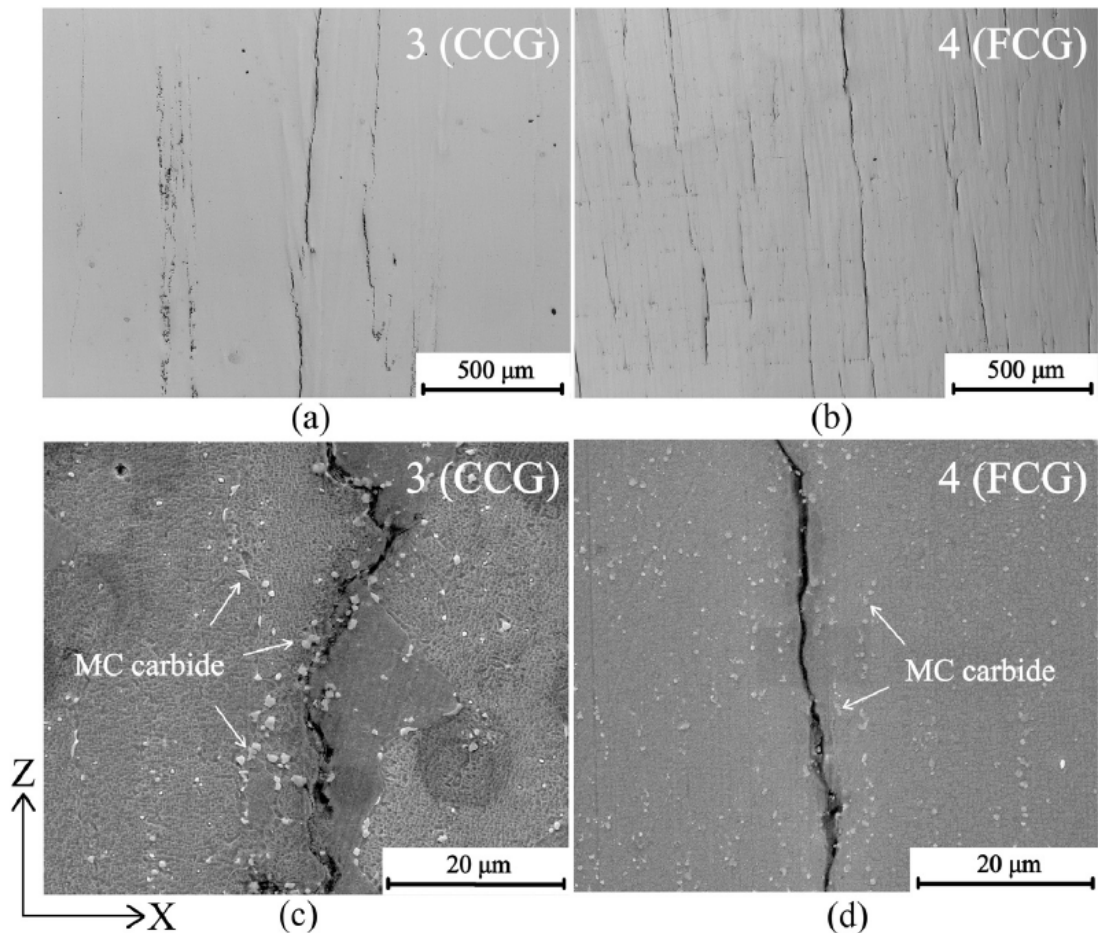
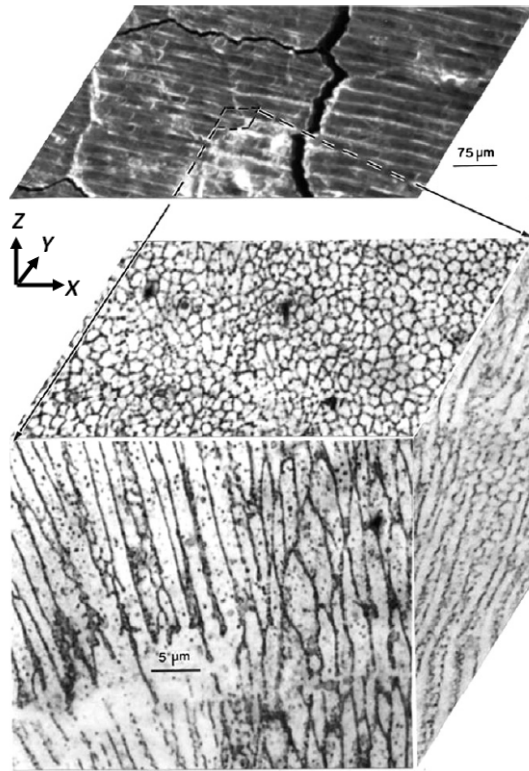
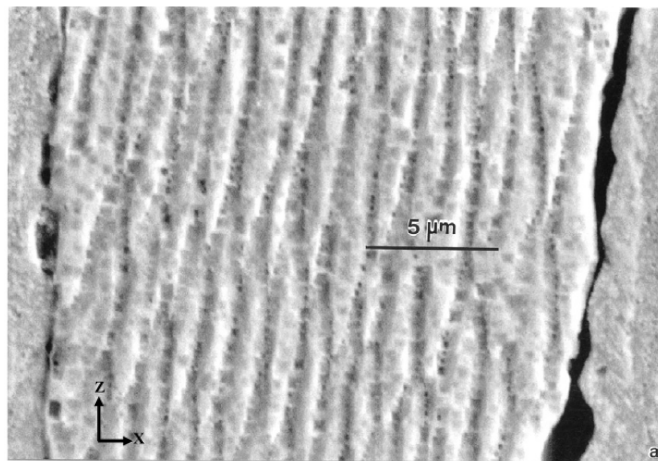


Figure 49. Hot cracking in EB-PBF of DZ125 Ni-based alloy. CCG and FCG stand for coarse columnar grain and fine columnar grain structures [121]

Ramirez et al. [122] observed cracks in their EB-PBF copper. Columnar grains comprise groups of cells. Precipitates arrays are observed distributing along with grains and cells' boundaries. Cracks were seen at the sample's top surface and along the grain boundaries, as shown in Figure 50. There was no further discussion on the cracks presented by the authors. In Figure 50a, it can be seen that surface cracks look more severe when they are perpendicular to the scan directions. This may indicate that stresses can occur more preferentially along the scan direction. Moreover, as observed from the top surface (XY view), cracks can be seen in two-directions (i.e. normal or parallel to scan direction) instead of one-direction (ZX view - along the build direction) as they are usually observed in other works [113, 117, 118, 120, 121]. This shows that crack propagation is not only from layer to layer but also from track to track. Therefore, in order to investigate how crack propagated during EB-PBF, the typical observation from ZX cross-section is not sufficient.



a)



b)

Figure 50. Cracks appear at the top surface in the work of Ramirez et al. [122] showing more severity for the orientation that is normal to the scan direction

Based on the observation from the work of Ramirez et al. [122], the candidate has made an effort to review on crack orientations in the relevant literature of EB-PBF process. However, most of the studies' characterizations were conducted on the ZX cross-sectional images only. The cracking mechanism comprises of crack initiation and propagation, and strongly depends on the thermal stress from the EB-PBF process. As the scan direction alternatively changes 90° every layer, the stresses direction may be altered as well. Therefore, it is important to understand not only how the cracks initiate, but also how they grow in relation to the stresses

direction resulting from every layer deposition. As a result, conventional ZX cross-sectional images are not sufficient to provide good characterizations of the cracking networks develop during the EB-PBF process. Therefore, it is required to have a new way in characterizing the cracking network, in order to have a better examination of the cracks' propagation mechanism.

Chauhan [123] in his master thesis on EB-PBF of ASTM F75 Co-based alloy observed cracks in some EB-PBF-built samples (Figure 51). Specifically, cracks were only seen on those samples of high carbon content (0.15 %wt). Those that were built from low and medium carbon (0.05 %wt and 0.1 %wt, respectively) showed no cracks in the optical micrographs. The author claimed that the amount of carbon content affects the degree of precipitation at the grain boundaries during solidification, which in turn may affect the cracking susceptibility. For low and medium carbon content, there are only sub-cells' boundaries' precipitations while at high carbon content, there were considerable precipitates at the grains boundaries. Unfortunately, the author just purely observed the cracking since no further analysis or discussion was carried out. Therefore, it is unclear what forms of crack occurred. Regarding EB-PBF of Co-29Cr-6Mo alloys [35-40], there have not been any reports related to the hot cracking. Despite that there is a difference in the chemical compositions between Co-29Cr-6Mo alloys and Co-29Cr-10Ni-7W alloys, it is interesting that the former witnesses no cracking problem while the later experiences extensively and severely. Thus, it is motivated to use Co-29Cr-6Mo alloy as reference material for Co-29Cr-10Ni-7W alloys in comparison on cracking susceptibility during EB-PBF process.

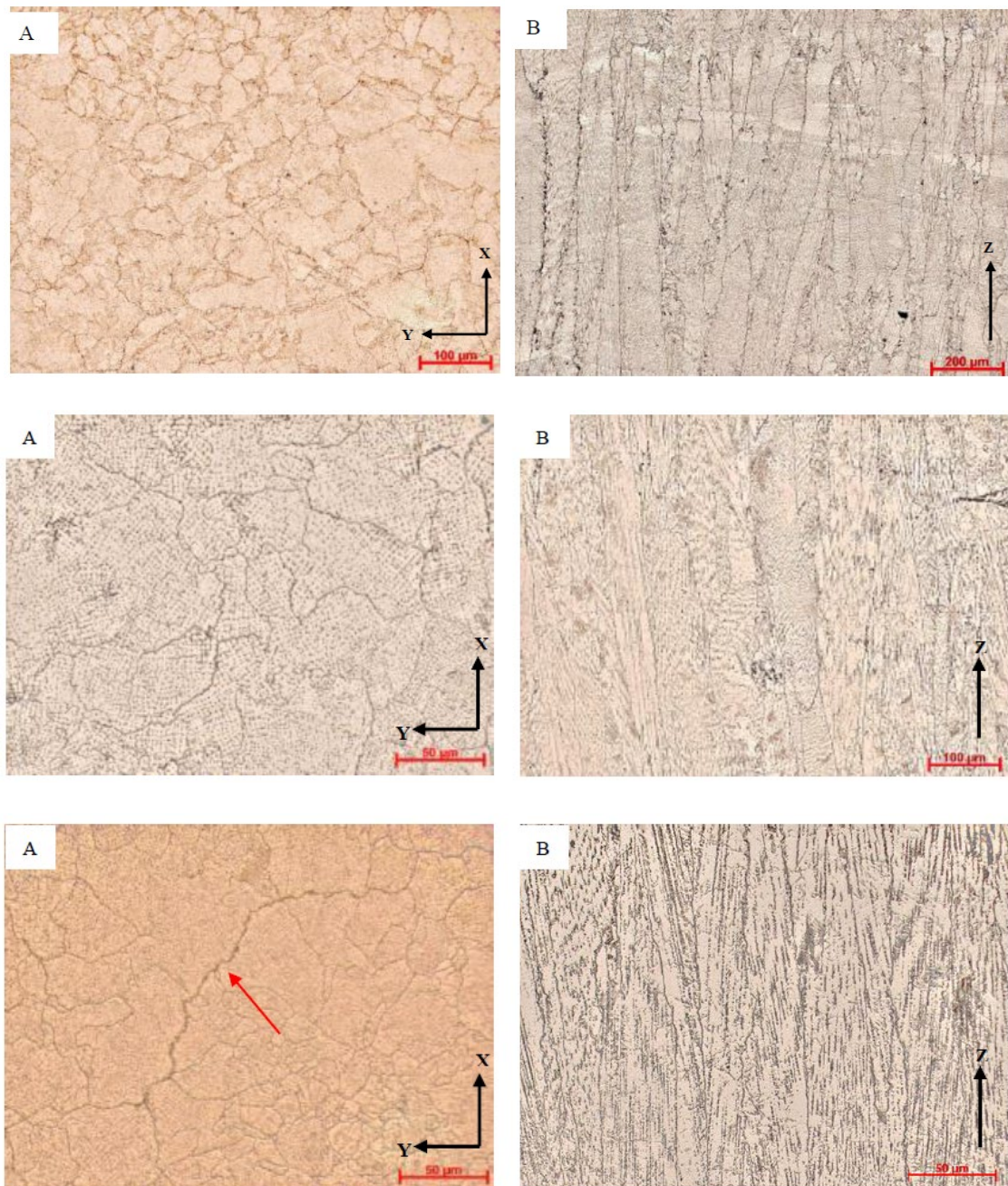


Figure 51. Optical images of EB-PBF build Co-29Cr-6Mo F75 alloys with (a). 0.05 %wt C; (b). 0.1 %wt C and (c). 0.15 %wt C. Crack is shown by red arrows in (c).

#### 2.4.2. Cracking reported in other PBF-AM processes

The literature review is now expanded to cracking reported during the other PBF-AM processes to have a better view. Carter et al. [116] reported different types of cracks in their LB-PBF CM247LC Ni-based samples, as shown in Figure 52. Cracks appear jaggedly, with clearly protruding dendritic structures, and are claimed as solidification cracks (Figure 52a). In contrast, grain boundary cracks are observed with clean and smooth edges and are suggested to form during solid state (Figure 52b). The authors suggested three potential cracking mechanisms as

liquation cracking, strain-aged cracking, and ductility-dip cracking. However, in the scope of the investigation, they were unable to eliminate or prove which one is the governed mechanism.

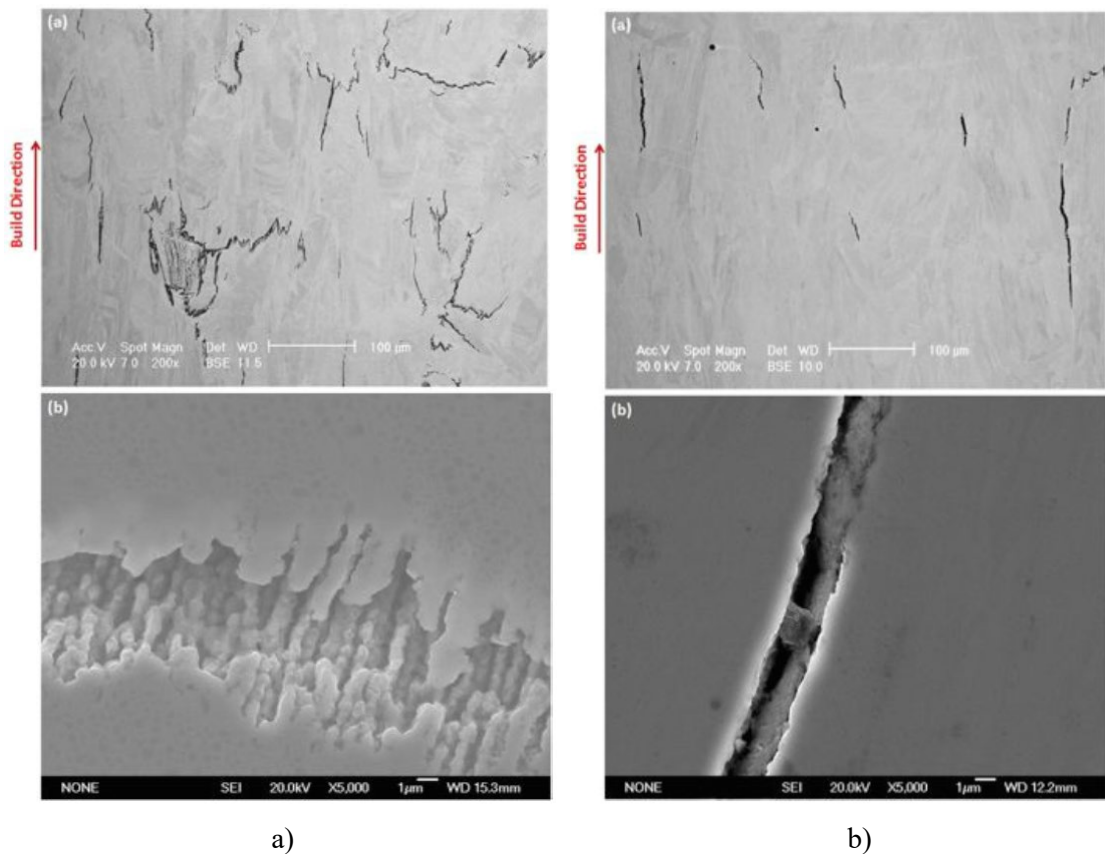


Figure 52. The cracking problem in LB-PBF CM247LC Ni-based samples: (a). Suggested solidification cracking and (b). Suggested solid-state cracking [116]

Sistiaga et al. [124] observed hot-cracks at the grain boundaries in the Al7075 alloy samples fabricated by LB-PBF, as shown in Figure 53. Increasing additional Si content from 1 %wt to 4 %wt resulted in lower cracking susceptibility and eventually crack-free. By adding more Si content, the melting temperature  $T_m$  was reduced 17°C. Moreover, from 2 wt% to 4 wt% Si addition, there is a second eutectic formation at  $T_{E2} = 524$  °C, apart from the main one at  $T_{E1} = 552$  °C. The additional Si content also results in the grain refinement which leads to an increase in total grain boundary density. High grain boundary density will toughen the matrix which increases the intergranular cracking resistance. Although the melting point was reduced, the formation of the second eutectic at  $T_{E2} = 524$  °C does not provide any reduction in the alloy's solidification freezing range  $\Delta T = T_m - T_{E2}$ . Thus, the liquid film length  $l_{film} = \Delta T/G$  will not be shorter, but even longer. The authors suggested that the formation of second eutectic results in the backfill effect which healed the cracks. However, no metallurgical evidence was shown to support the statement. Therefore, it is unclear if the formation of second eutectic or the grain refinement is the main cracking prevention.

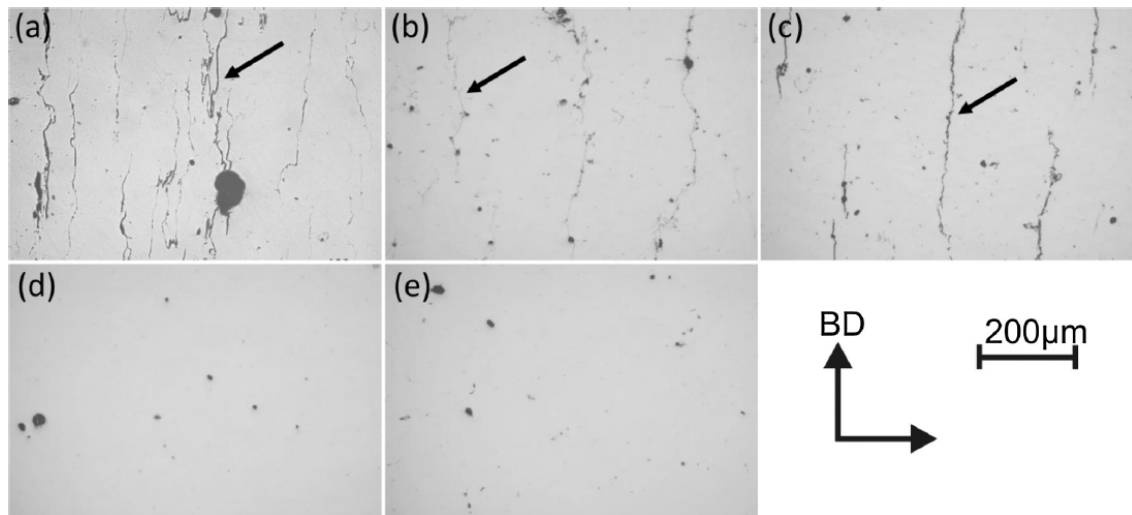
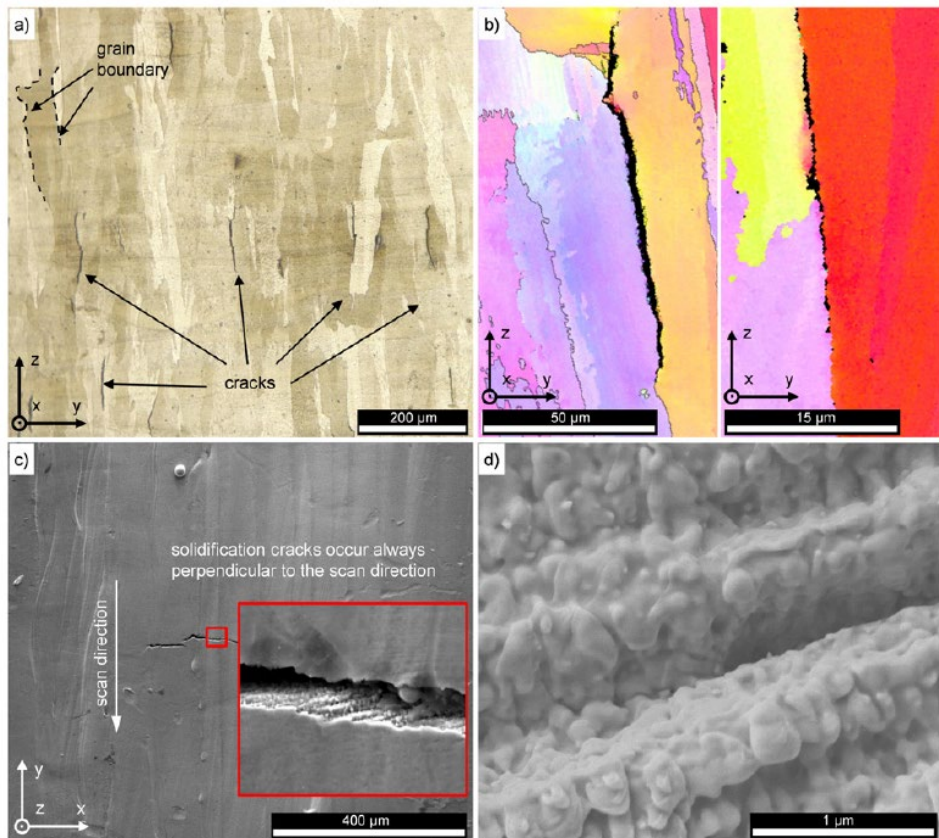
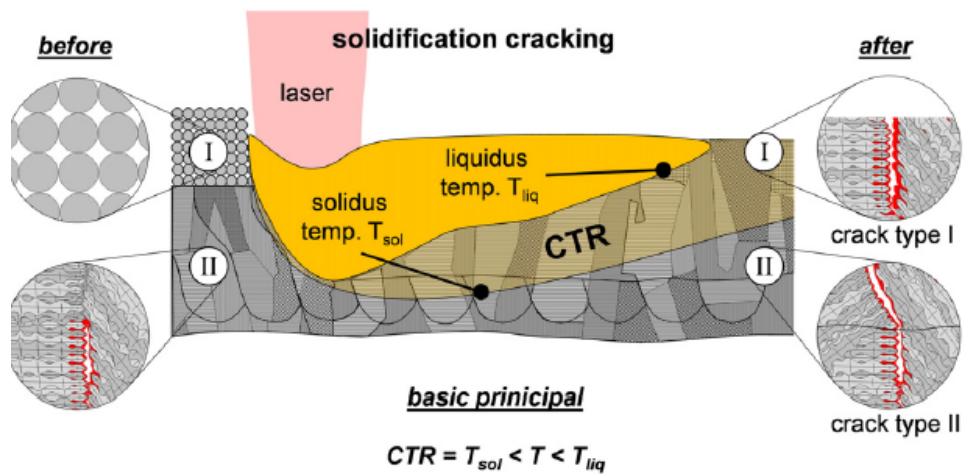


Figure 53. Cracking observed in LB-PBF Al7075 alloy samples with various addition of Si content: (a). 0wt%, (b). 1wt%, (c). 2wt%, (d). 3wt% and (e). 4wt%. Cracks are shown by the arrows [124]

Cloots et al. [112] observed cracks in their investigation on the IN738LC samples fabricated by LB-PBF. Cracks that appear on the top surface are always perpendicular to the scan direction. This is identical to that observed in the EB-PBF copper by Ramirez [122]. The authors separately conducted a series of experiment in which the scan directions were kept in one direction for all layers and the same cracks' orientation was observed on the top surface (Figure 54a). However, the detailed analysis of this feature was not published in the current work. The cracks' surface examination shows wetting dendritic characteristics, thus they were identified as solidification cracks. In addition, grain boundary cracks were seen along the build direction. The authors suggested two scenarios for the hot cracking mechanism, as illustrated in Figure 54b. The first one perceived as solidification cracks occurs during solidification of grains. The second one is the possibility of pre-existing solidification cracks that are partially remelted and act as a nucleus for continuing crack growth. The high concentration of zirconium and potential boron element were detected at the grain boundaries, which are claimed as the main factors for the liquid film formation. The authors showed that the alloy has a very large critical temperature range  $CTR = 696\text{ }^{\circ}\text{C}$ , which is identical to the solidification freezing range  $\Delta T$ . However, the propensity of the liquid film length in regards to the CTR and the LB-PBF thermal conditions has not been discussed. Moreover, the proposed cracking scenarios are simple. Since cracks are observed always perpendicular to the scan direction, further analysis needs to be considered on how cracks networked to each other and propagated with respect to the scan direction change every layer.



a)



- liquid film with high concentration of Zr (red region in image) covers dendrites at grain boundaries
- liquid film cannot absorb solidification shrinkage (→ strains)
- separation of grain boundaries

b)

Figure 54. Suggested scenarios for the hot cracking mechanisms in LB-PBF IN738LC [112]

Harrison et al. [115] in their study of LB-PBF of Hastelloy-X Ni-based superalloy excluded the influence of segregation of low melting elements to grain boundaries on the cracking susceptibility. Thermal Gradient Mechanism (TGM) and examination of the cool-down phase of

the molten top layer proposed by Mercelis and Kruth [125] were employed to explain the cracking mechanism. The authors emphasized that this is a solid-state cracking mechanism although no fractography examination on the crack's surface was provided. Micro-cracking formation was considered as a consequence of induced tensile/compressive stresses caused by rapid solidification of LB-PBF process. Energy Dispersive Spectroscopy (EDS) analysis was conducted at a crack location to evaluate elements distribution. Since the Si element is not seen significantly increased and other matrix elements (Ni, Cr and Fe) are not seen depleted, the authors confirmed their suggestion and excluded the possibility of cracking by metallurgical effects as suggested by Tomus et al. [114] for the same alloy. However, the spatial and depth resolution of an EDS in the SEM is on the order of a few microns. Thus, the scan may include surround elements as the crack is relatively small (width < 1  $\mu\text{m}$ ). Therefore, it is inappropriate to rely on the EDS result to exclude the micro-segregation of elements at the grain boundaries.

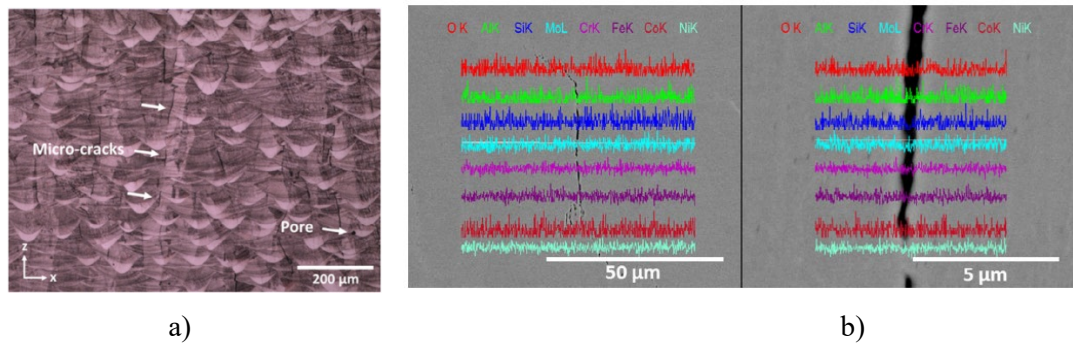


Figure 55. (a). Micro-cracks in as-built LB-PBF of Hastelloy-X. (b). EDS line scans of a crack at medium and high magnification [115]

Chen et al. [126] reported of a liquation cracking problem in their experiments of laser deposited manufacturing (LAM) of IN718 alloy. As shown in Figure 56, no cracks were observed in the first two depositions. Starting from the 3<sup>rd</sup> layer, the crack was seen occurring near the 1<sup>st</sup>-2<sup>nd</sup> layer interface, implying it is a liquation crack as a result of heat affected from the 3<sup>rd</sup> layer. Once formed, the liquation crack will then acts as an initiation point. Stresses will be concentrated at the crack tip and the crack keeps propagating through many layers. Traces of liquated Laves phase were observed at the crack surface (Figure 57). No carbide precipitates were observed and reported. The effect of heat accumulation from the successive depositions can cause grain boundary liquation to occur at previously deposited layers. In addition, high angle grain boundary ( $> 15^\circ$ ) was shown to be favorable for crack growth. While the LAM process is simply one-direction scanning every layer, the cracking mechanism in terms of initiation and propagation can be easily be identified and analyzed. However, it will be more complicated for the LB-PBF as well as EB-PBF processes as the scan directions change every layer. Most of the studies reviewed so far on PBF-AM processes characterize the hot cracking by using 2D vertical cross-sectional images, which clearly cannot reveal the actual 3D cracking

network. If the 3D cracking network can be revealed, the relationship between layers' scan directions and how cracks initiated and propagated can be better investigated.

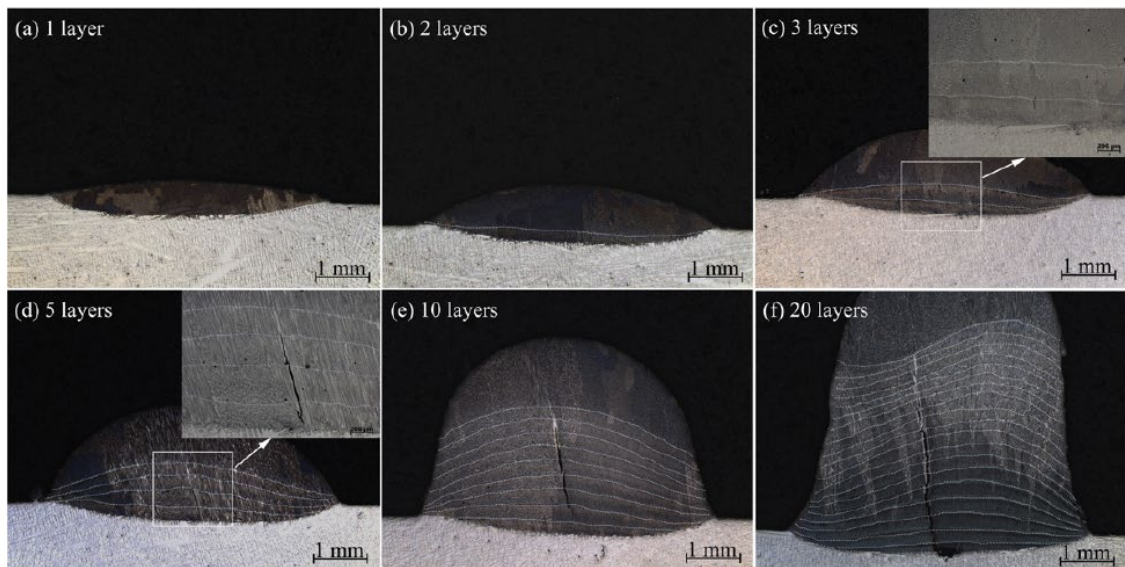


Figure 56. Liquation cracking in LAM process showing the initiation of liquation crack started at the 2<sup>nd</sup> layer after the 3<sup>rd</sup> deposited [126]

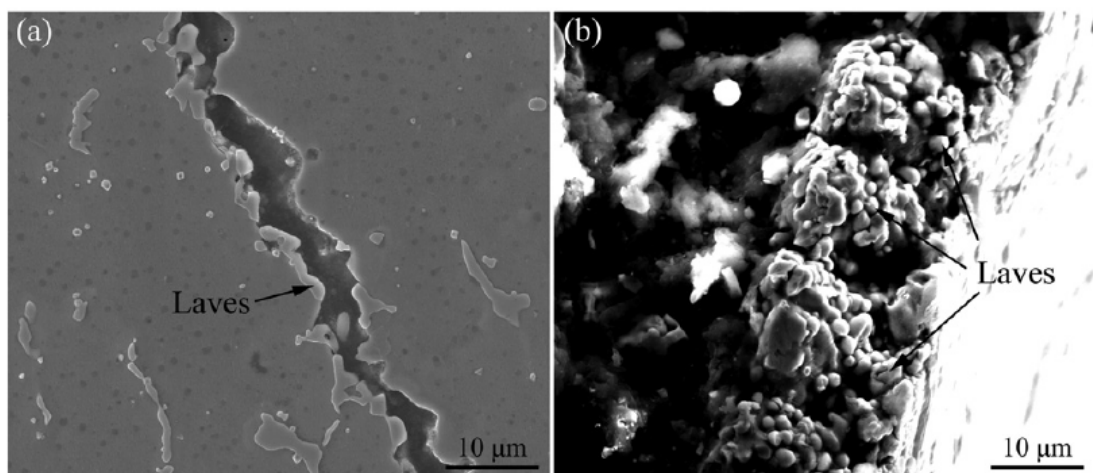


Figure 57. Traces of liquated Laves phase at the crack surface [126]

## 2.5. Summary of the literature review

The cracking occurred when applying EB-PBF process to the Co-29Cr-10Ni-7W alloy has been targeted and aspects related to solidification and cracking during EB-PBF has been reviewed. In summary, several main gaps are pointed out along with the proposed research questions:

- Phase transition temperatures of Co-29Cr-10Ni-7W alloy during melting/solidifying has been insufficiently reported in the literature. This has resulted in the uncertainty of solidification freezing range  $\Delta T_0$  of the alloy.

- The ratio  $\Delta T_0 / D_L$  of Co-Cr alloys has been estimated at around  $9 \times 10^{10}$  K.s/m<sup>2</sup>. However, the ratio  $G/R$  of EB-PBF has not been experimentally estimated. Thus, it is unclear about the growth morphologies for EB-PBF Co-Cr alloys as compared to the fully dendritic ( $\sim 10^{16}$  K.s/m<sup>2</sup>) and fully cellular ( $\sim 10^9$  K.s/m<sup>2</sup>) modes observed in EB-PBF Ni-based alloys and stainless steel SS-316L, respectively.
- The EB-PBF parameters, specifically the focus offset may affect the formation of melt/track. However, the typical tear-drop shape or melt pool ripples has rarely been observed. This has caused a lack of information on how melt/track has formed during EB-PBF.
- The melt/track geometry is the determining factor of the heat flux direction. Grain growth has been observed to be heat flux direction dependent. In EB-PBF, grain structure has been observed to have grains changing their growth direction 90°. The observation, however, has not been clarified, especially with respect to the effect of melt/track geometry.
- Cracking has been reported in many studies in EB-PBF and LB-PBF. However, there has been a disagreement in literature since solid-state cracking and hot cracking are both asserted for the problem. Despite a few studies that have shown evidence of hot cracking, details on the governed mechanism have been unclear whether it is solidification cracking or liquation cracking.
- In EB-PBF, cracks are observed as separated intergranular cracks along the build direction. In addition, cracks are seen to be normal to the scan direction. This suggests that cracks may link or network to each other. However, cross-sections along the build direction are normally used for microstructure characterization. This has been shown to be not possible to fully reveal how cracks may have grown during EB-PBF.
- Cracks observed tends to be perpendicular to the scan direction. Thus, cracking orientation may relate to the scan direction. Cracking is known to be a result of thermal stress. Therefore, the scan direction may affect the stress direction. This relationship, however, has not been clarified for EB-PBF.

### ***Research questions and issues***

- The phase transitions temperature of the alloy needs to be investigated so that the solidification freezing range  $\Delta T_0$  can be clarified. (Chapter 4)
- What is the typical thermal condition in solidification front during EB-PBF and what is the growth morphology of EB-PBF Co-29Cr-10Ni-7W alloy in relation to  $G$  and  $R$ ? (Chapter 4 and Chapter 6)
- How does the electron beam size which is related to focus offset affect the melt/track geometry and grain growth direction? Is it possible to modify the melt/track geometry

via EB-PBF parameters so that grain growth direction and structure can be controlled? (Chapter 4)

- Is cracking during EB-PBF solid-state cracking or liquid state cracking? If it is liquid cracking, does liquation cracking contribute to the cracking process? (Chapter 5 & Chapter 6)
- How do cracks initiate and grow layer after layer? What are the influential factors to cracking during EB-PBF? (Chapter 6)

In summary, the objectives of the thesis study are:

- Identifying/clarifying the Co-29Cr-10Ni-7W alloy's phase transition temperatures. The objective can be achieved by using thermal analysis techniques.
- Investigating solidification modes, the formation melt/track geometry and its effect on grain growth directions during EB-PBF of Co-29Cr-10Ni-7W alloy. The solidified microstructure can be observed and can be used to estimate the EB-PBF thermal conditions (G, R). The formation of melt/track geometry and its effect on grain structures can be elucidated by investigating different beam diameters (while keeping other parameters constant).
- Identification of the form of cracking during EB-PBF of Co-29Cr-10Ni-7W alloy and the respective cracking mechanisms. Based on distinctive characteristics of hot cracking and solid-state cracking, by examining the crack's surface, not only the form of cracking but also specific cracking mechanisms (i.e. solidification cracking, liquation cracking or DDC) can be distinguished.
- Identification of how a crack initiated with regards to its driven mechanisms. Moreover, characterization of the crack network to understand how cracks have grown with respect to the alteration of scan direction every layer. EB-PBF builds the sample layer upon layer, thus cracks can be characterized in a reverse way as consecutive grinding downward layer-by-layer to reveal the crack network.
- As EB-PBF is similar to fusion welding, single-track samples can be used to clarify how crack initiates. The crack network can serve as a way to trace back the propagation mechanism. Numerical simulation can be employed to investigate how the thermal stresses generated during an electron beam scan. Thus, the reason why cracks tend to be normal to the scan direction can be explained.

## CHAPTER 3: EXPERIMENTAL PROCEDURE

This thesis research started by conducting the preliminary experiments to observe cracking in EB-PBF Co-29Cr-10Ni-7W alloy. Then selective EB-PBF experiments were further conducted to produce samples for solidification microstructure and crack network characterization. To add the understanding of solidification, differential calorimetry thermal analysis and analysis of microstructure were conducted. To identify the crack networks in EB-PBF samples, these samples were carefully sectioned and examined sequentially from the top layer. To understand further how thermal stresses during EB-PBF affect the crack pattern and appearance, simulation of stress during EB-PBF was carried out. The details of the procedures of these experiments, analysis, and simulation were described in this chapter

### 3.1. EB-PBF process

The EB-PBF machine used in this research was the Arcam A1, as shown in Figure 58. The machine equips with a vacuum build chamber that can achieve a maximum build size of 200x200x180 mm. According to the manufacturer's datasheet, the Arcam A1 can achieve accuracy from 3D model to built-part of +/- 0.2 mm and +/- 0.13 mm ( $3\sigma$ ) for long range (100 mm) and short range (10 mm), respectively. The surface roughness can be up to Ra25 for vertical sides and Ra35 for the top surface. The system employs a beam power of 50-3000 W (continuous variable) with a beam spot size ranging from 0.2-1.0 mm. Maximum scanning speed is 8000 m/s.



Figure 58. The EB-PBF Arcam A1 machine

- *EB-PBF start plate temperature and preheat temperature*

Unlike LB-PBF, EB-PBF process requires preheating of the start plate with the beam prior to hatching (fusion of powder particles) in order to achieve a proper sintering state of the powder particles that cover under the plate (as shown in Figure 3). Then, during the hatching stage, another preheating step is also done for the new deposited powder particles before the powder fusion takes place. Therefore, the resultant temperature from the preheating stage/steps may affect the local solidification conditions of the molten melt/track in the hatching stage.

Preheating of the start plate is to sinter the underneath powder in order to avoid the repulsive electrostatic forces to build-up (as known as “smoking” shown in Figure 59). The phenomenon is caused by the electrical charge from the e-beam. The preheat temperature of the start plate varies by materials used. For the ease of discussion, the preheat temperature of the start plate is called start plate temperature. In contrast, preheat temperature is to assign for the preheating step at every new layer.

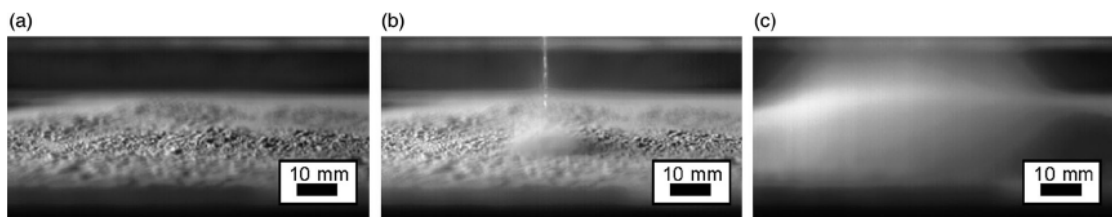


Figure 59. “Smoking” caused by electrostatic repulsion: (a). powder before applying beam, (b). beam-powder interaction and (c). blown-up of powder particles [127] (images originally from the work of Kahnert et al. [128])

The EB-PBF machine measures the start plate temperature by the thermal couple that is mounted underneath the plate. The thermal data is then be stored in the system log file. Sames et al. [129] demonstrated the main steps during a normal build of EB-PBF, as shown in Figure 60. It can be seen that the preheat temperature was at 975 °C at the beginning of ‘Layer melting’ step and increased up to 1000 °C at the end. This is, however, contradictory to the results found by Prabhakar et al. [130] regarding the heat transfer from the layer-to-start plate for EB-PBF of IN718 alloy. The heat transfer model shows that the number of layers is an influential factor on the heat transfer from the currently deposited layer to the start plate. Specifically, as the building-part is higher than the start plate, the highest thermal impact is restricted to the few top layers, thus reducing cyclical temperature influence on the base plate, as shown in Figure 61.

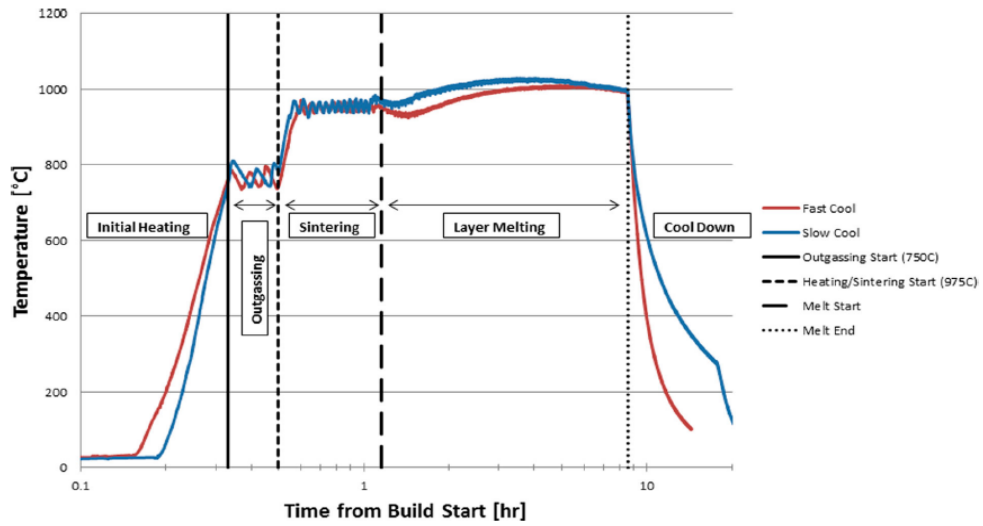


Figure 60. Main steps of a EB-PBF building process [129]

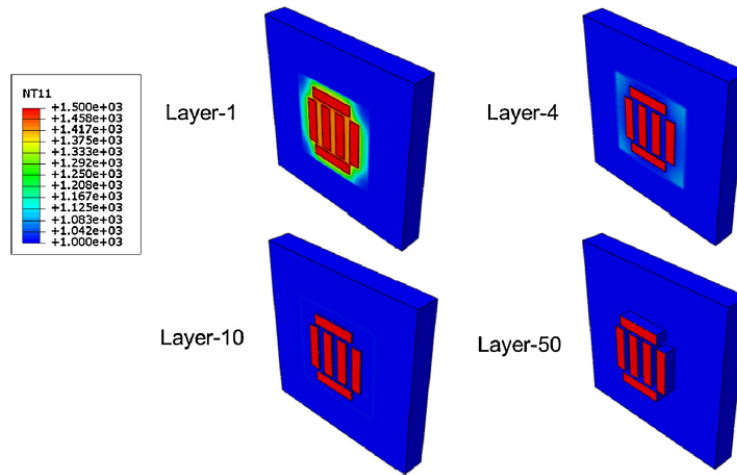


Figure 61. Numerical heat transfer model in EB-PBF of IN718 alloy [130]

Kan et al. [131] demonstrated the temperature history in their EB-PBF of TiAl alloy. The thermal history of the start plate temperature is shown in Figure 62. From the graph, the preheat temperature can be observed gradually decreasing from 1180 °C at the beginning to slightly below 1000 °C toward the end of the hatching state, or stage III. This is in good agreement with the simulated results of Prabhakar et al. [130].

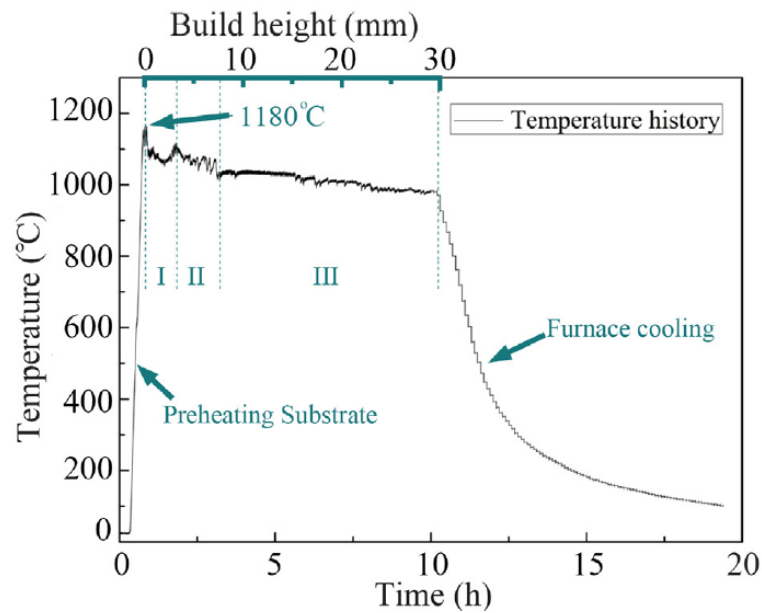


Figure 62. The temperature history of EB-PBF build of TiAl alloy [131]

Smith et al. [132] referred to the preheat function in the Arcam system when conducting a study on the thermal diffusivity and density of Ti-6V-4Al alloy processed EB-PBF. The authors claimed that the Arcam system employs a one-dimensional thermal model to ensure the powder bed is sufficiently sintered. This model analyzes how much energy input ( $E_{line}$ ) is required during preheating and hatching stages. In addition, the required energy input varies as the build progresses higher. The authors had turned off the model and manually applied fixed energy inputs by modifying a parameter so-called as “repetition”. The number of repetitions means the number of passes the beam rasters over the scanned surface in the preheating step. For example, a total energy input applied on a 50x50 mm scanned surface at one-time pass is 325.3 kJ. The value will increase to 1301.4 kJ if the repetition of 4 is used.

Based on the start plate temperature history recorded during EB-PBF from the work of Sames et al. [129], Kan et al. [131], the heat loss simulation by Prabhakar et al. [130], and the mention of repetition number by Smith et al. [132], the EB-PBF system has been shown that it may have specific functions such as extra heating steps for compensating of the heat loss. It can be expected that the heat loss may be more severe in the practical situation since the Prabhakar et al. [130] did not consider heat transfer from the start plate to the surrounding environment (i.e. sintering powder particles).

- *Focus Offset (FO) – Unit of measurement: mA*

As has been mentioned in chapter 1.2., the focus offset (FO) value controls the focus of the beam. In addition, the FO value affects the depth of the melt pool, as illustrated in Figure 63. At a small value (i.e. zero or FO0) the resultant melt pool is very deep and narrow. In contrast, the larger value of FO, the wider and shallower of the melt pool.



Figure 63. Melt pool geometries with different focus offset values

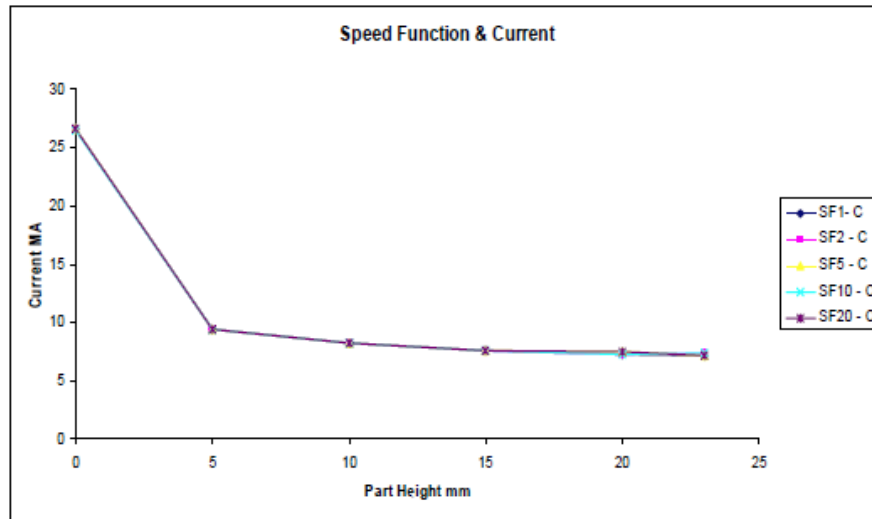
No description of how to correlate between FO values and beam diameters is mentioned by the manufacturer. However, there have been reports on the beam spot size in literature. Galati et al. [133] have mentioned that it is able to focus down to about 0.1 mm despite that specific Arcam system and FO value have not been stated. Fousová [134] has used an Arcam Q10 machine with a spot size of 0.1 mm. However, the respective focus offset value and how the beam size was measured was not mentioned. Schwerdtfeger et al. [5] have used the Arcam A2 in their study on Ti-6V-4Al alloy. They have shown that FO26 (meaning focus offset at 26 mA) corresponding to a beam diameter of 0.15 mm. In addition, a change in the FO in the range of +/- 10mA leads to the beam diameter changes around 0.05 mm. Helmer et al. [21] have used a 400  $\mu\text{m}$  and 500  $\mu\text{m}$  beam spot sizes on an Arcam A2 system in their study. However, they have not mentioned the respective FO values and how the beam spot sizes were obtained.

- *Speed Function Index (SF) – Unit of measurement: N/A*

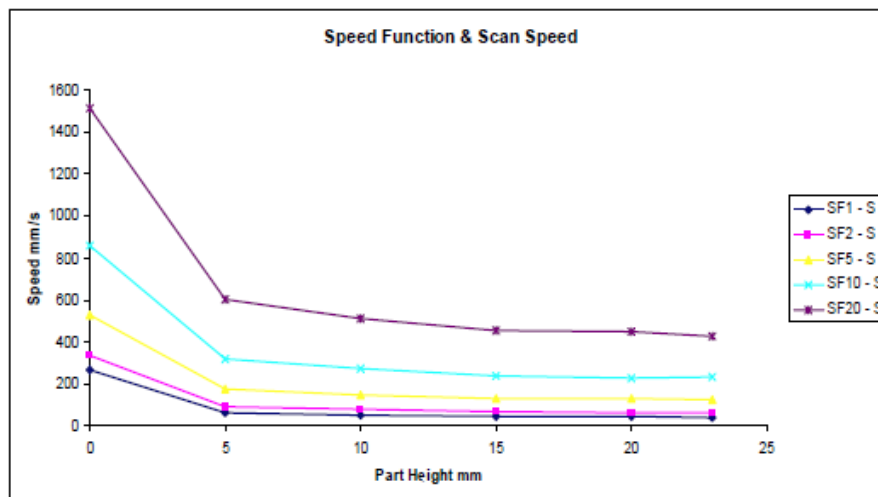
The SF is to simultaneously and automatically control both the beam current  $I$  (mA) and the scanning speed  $v$  (mm/s). The exact algorithm has not been provided by the manufacturer. Price et al. [61] used linear relationships between the actual scanning speeds  $v$  and respective SF values to formulate a regression equation for the scanning speed  $v$  as a function of build height  $H$  and SF values:

$$v = (-0.7343H + 28.554).SF$$

Mahale [135] used the Arcam's EB-PBF Control software to determine the SF parameter of the EB-PBF Arcam S12 machine. It was shown that SF depends on the building height in terms of both  $v$  and  $I$ , as shown in Figure 64. Specifically,  $v$  is around 250 mm/s for SF1 and 1500 mm/s for SF20 at the start of the build. The scanning speeds will dramatically reduce after the building height of 5mm. From there, the scanning speeds are almost unchanged regardless of the building height. The corresponding between the scanning speed and SF values in [135] does not match with the equation proposed by [61]. However, the relationship between the scanning speed, SF values, and the building height is similar. The beam currents  $I$  have the same relationship with the building height as the SF. However, it is observed that the beam currents are the same for all SF values used (SF1, 2, 5, 10 and 20).



a)



b)

Figure 64. The relationship between (a). Beam current and (b). Scan speed of respective SF values and the building height

- *Scanning Strategy*

Scanning strategy in how the beam orientates its scan direction every layer. In the EB-PBF Arcam A1 system, the scanning strategy that is commonly used is the cross-snaking with the scan direction changes 90° every layer. Apart from this, other scanning strategies can be selected such as multi-spots scan, 1-D (unidirectional) scan direction or cross-snaking without 90° rotation of scan direction every layer. Figure 65 also demonstrates all possible scanning strategies provided in the EB-PBF Arcam A1 machine.

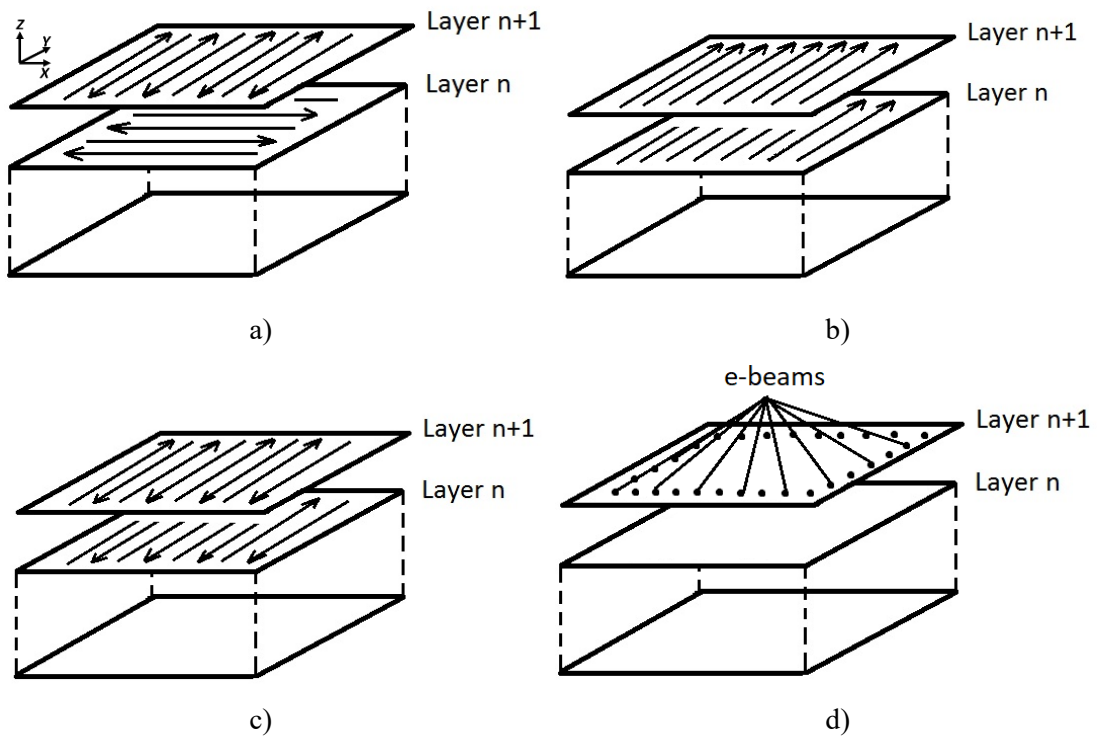


Figure 65. (a). Cross-snacking with the 90° rotation of scan direction every layer and other possible scanning strategies in the EB-PBF Arcam A1 machine (b). 1-D scanning without 90° rotation, (c). Cross-snacking without 90° rotation and (d). Multi-spots scanning

- Powder recycling system (PRS)

The powder recycling system is the device to be used at the end of the EB-PBF process. After the fabricated parts are taken out of the build chamber of the EB-PBF machine, they are brought into the PRS chamber. Here, the PRS uses a high velocity of same powder particles to blow out all non-sintered and sintered powder particles that stick around the parts. At the result, the parts and the start plate on which they were built are the remaining objects. From then, parts can be sectioned out by using hand grinder or further advanced machining technique such as wire electric discharge machining (WEDM). Figure 66 shows a PRS used for EB-PBF process.



Figure 66. Powder recycling system.

### 3.2. Powder materials

The composition of the initial powder of the Co-29Cr-10Ni-7W alloy used in this study is provided in Table 1. The powder was supplied by Metal Spray Supplies Australia (MSSA). For comparison, the composition in the ASM specification is also provided. The powder's compositions were analyzed by the Agilent 730 inductively coupling plasma optical emission spectroscopy (ICP-OES) using hydrofluoric acid setup and Anton Paar Multiwave 3000 microwave digestion unit. The samples were digested in the microwave and the resulting solutions made to a 100 ml volume. After an appropriate dilution to suit the calibration range, the major elements were measured by ICP-OES. Minor elements were measured directly by using matrix-matched calibration standards. In addition, the composition of light elements such as carbon and sulfur were identified using LECO CS600.

The powder particle size was measured by laser diffraction technique using Malvern Mastersizer S. The incident laser beam will be scattered when it gets in touch with the sample cells containing the powder particles. In addition to the scattered light, there are also refracted and back-scattered lights. The scattered lights will then be measured by a multi-element detector while the un-scattered lights are measured by using an obscuration detector. Back-scatter detector is also used for the respective light. Figure 67 schematically illustrates the basic operational principle of the used device Malvern Mastersizer S. The device's measured range is from 0.5 $\mu\text{m}$  to 900 $\mu\text{m}$ . In this work, the powder particles size distribution is  $D_{10} = 55.7 \mu\text{m}$ ,  $D_{50} = 76.2 \mu\text{m}$  and  $D_{90} = 105.7 \mu\text{m}$ . Figure 68 shows the SEM images of the Co-29Cr-10Ni-7W powder particles.

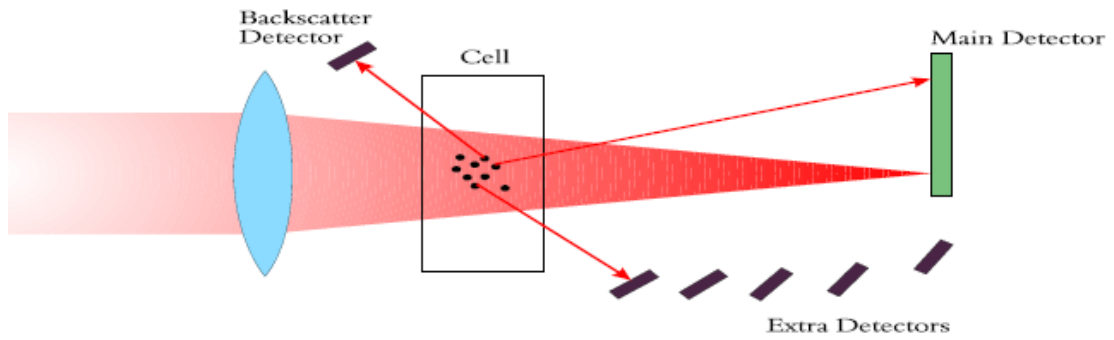


Figure 67. Optical systems of the Malvern Mastersizer S

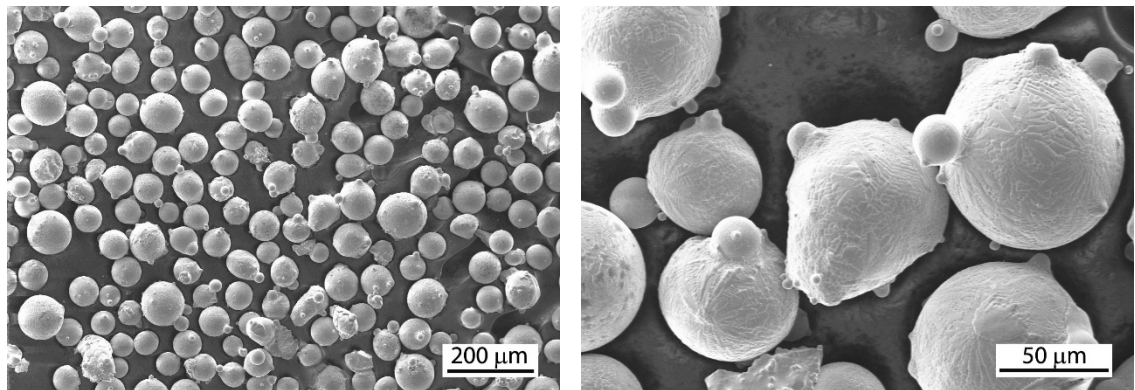


Figure 68. SEM images of the Co-29Cr-10Ni-7W powder particles

Table 1. Composition (wt%) of FSX-414 Co-based alloy

Element	Co	Cr	Ni	W	Fe	Mn	Mo	C	B
This study	Bal.	27.4	10.6	7.3	0.7	0.4	0.1	0.15	0.008
Specification [6]	Bal.	29	10	7.5	1	-	-	0.25	0.01

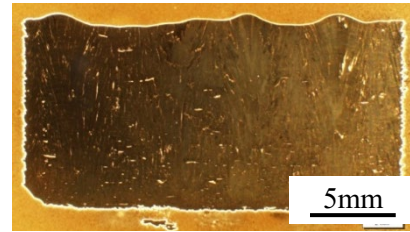
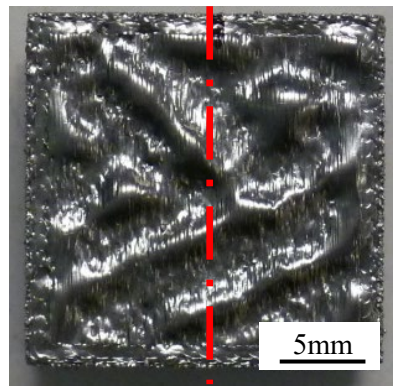
### 3.3. Preliminary design of EB-PBF experiments

The EB-PBF process standards have not been developed and recommended by the Arcam. Thus, the preliminary work had been conducted to study the appropriate processing parameters at CSIRO Clayton, Melbourne, Australia. The process parameters were attempted at various ranges of line offset  $h$  and SF values. Focus offset (FO) was kept unchanged at a value of 22. The start plate was preheated at 800°C. The outcome samples were analyzed in terms of outer appearance as well as microstructural defects. In addition, the sample size was varied for the group of  $h = 0.13$  mm. Sample 1 was purposely reduced in height down to 7 mm. Sample 4 was made in size of 10x10x5 mm. The rest of the samples were made at 20x20x20 mm<sup>3</sup>. These variations are to investigate the effect of sample size on the resultant samples' microstructure. Table 2 displays the conditions used for the respective sample number:

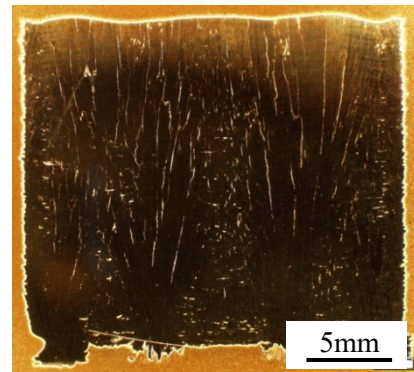
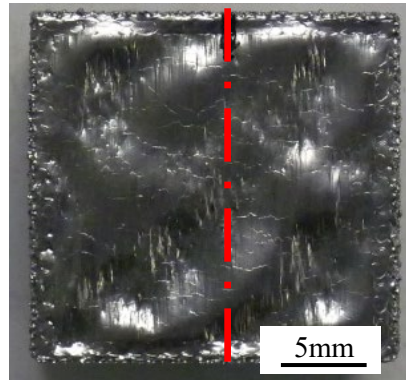
Table 2. EB-PBF parameters used in preliminary work

Sample No.	Line Offset $h$ (mm)	Speed function (SF)
1	0.13	24
2	0.13	50
3	0.13	75
4	0.13	100
5	0.05	24
6	0.05	50
7	0.05	75
8	0.05	100
9	0.0375	24
10	0.0375	50
11	0.0375	75
12	0.0375	100

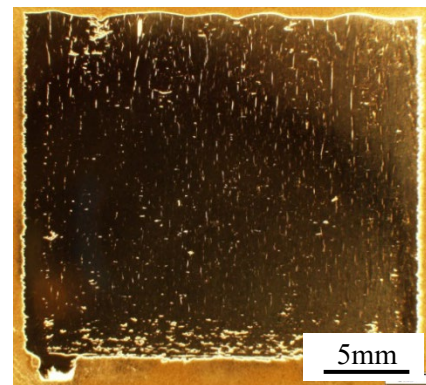
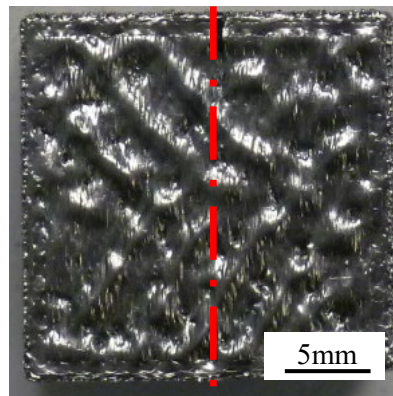
The samples are grouped and compared by their line offset values, as shown in the following Figure 69, Figure 70 and Figure 71. The group of  $h = 0.13$  mm results in rippled/swelling top surfaces of samples. The group of  $h = 0.05$  mm result in smoother surfaces for all evaluated SF values. The group of  $h = 0.0375$  mm results in the smooth and flat top surface, excepting the swelling surface for the fastest speed at SF100. Cracking had been observed on the top surface and normal to the scan direction. Cracks can be simply revealed by cross-sectional optical images. White-color highlighted patterns represent for cracks. Cracks appear as vertically along the build direction. However, in sample 6, 7, 10 and 11, some horizontal cracks appear to connect the vertical ones. In summary, for the evaluated range of preliminary parameters, the extensive cracking problem was observed in combination with the uneven/swelling top surface.



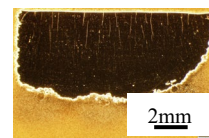
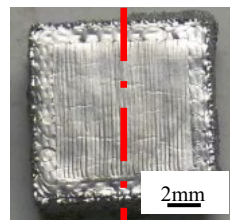
a) Sample 1



b) Sample 2

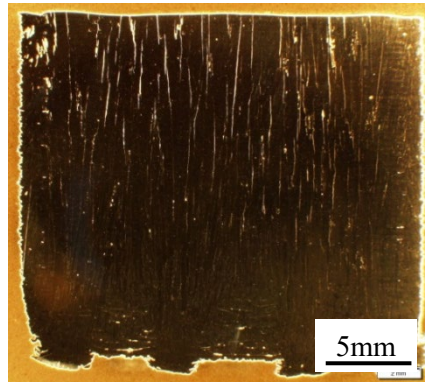
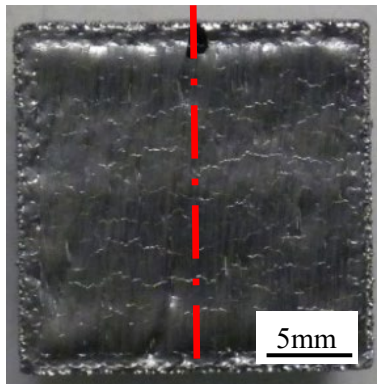


c) Sample 3

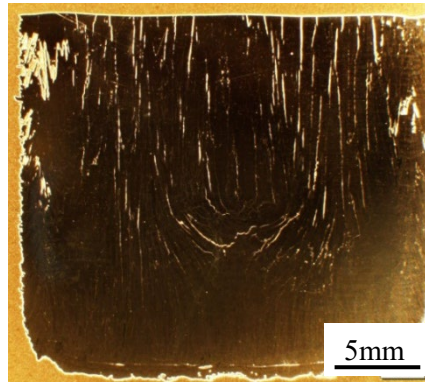
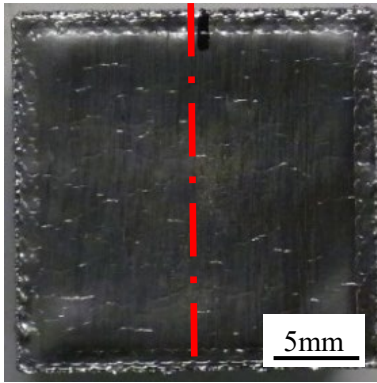


d) Sample 4

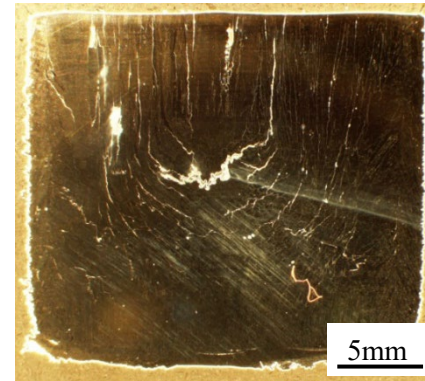
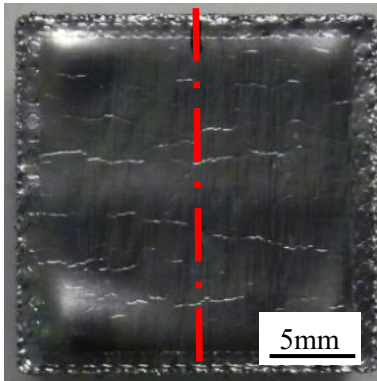
Figure 69. (a) – (d) The top surface and cross-sectional images of samples with constant LO at 0.13 mm. Note that sample 1 and sample 4 are different in size compared to the others. The SF increases from 24 to 100 from left to right.



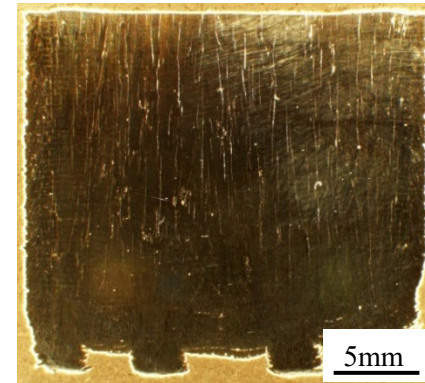
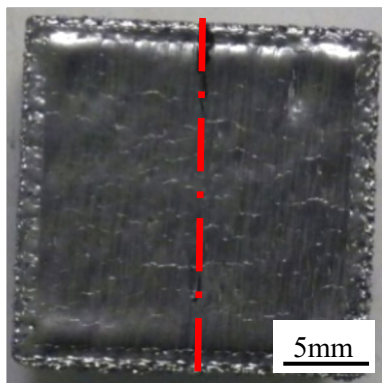
a) Sample 5



b) Sample 6



c) Sample 7



d) Sample 8

Figure 70. (a) – (d) The top surface and cross-sectional images of samples with constant LO at 0.05 mm. The SF increases from 24 to 100 from left to right.

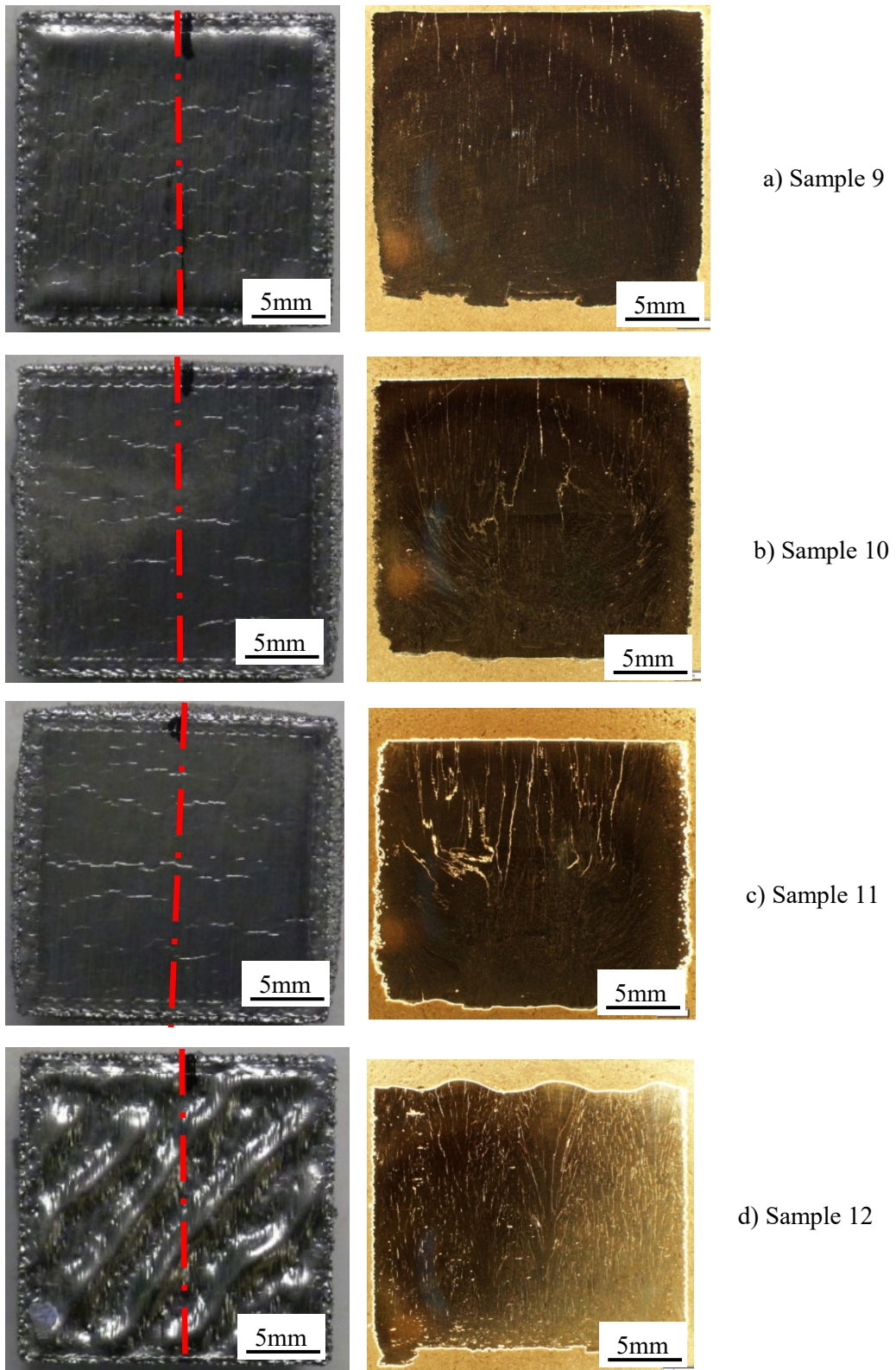


Figure 71. (a) – (d) The top surface of samples and cross-sectional images of samples with constant LO at 0.0375 mm. The SF increases from 24 to 100 from left to right.

### 3.4. Design of EB-PBF experiments

Based on the observation from the preliminary work, further design of EB-PBF experiment was prepared in a way not to repeat the range of preliminary parameters. The new ranges of parameters, therefore, were selected not only to extend the process windows for the EB-PBF Co-29Cr-10Ni-7W alloy but also to aim for investigating the cracking problem arising during the process.

Two new FO values were used as 25 mA and 50 mA. The line offset values were selected at 0.1mm and 0.2mm. The SF values were kept as similar as preliminary work, ranging from 25, 50, 75 and 100. The start plate was preheated at a higher temperature at 950 °C to investigate the effect of preheat temperature on cracking susceptibility. The conditions are shown in Table 3. For the ease of discussion, all samples are specifically coded following their process parameters. The F stands for focus offset, the L stands for line offset and S stands for speed function index. Line offset 0.1 mm and 0.2 mm are coded as L1 and L2, respectively. Focus offset 25 mA and 50 mA is coded as F1 and F2, respectively. Therefore, for the FO of 25 mA (FO25), LO of 0.1 mm (LO0.1) and SF of 25 (SF25), the sample will be coded as F1L1S25. Table 3 also shows the sample name according to their process conditions.

Table 3. EB-PBF parameters used in the new experiment

Focus offset 25mA							
Line offset at 0.1mm				Line offset at 0.2mm			
SF25	SF50	SF75	SF100	SF25	SF50	SF75	SF100
<b>F1L1S25</b>	<b>F1L1S50</b>	<b>F1L1S75</b>	<b>F1L1S100</b>	<b>F1L2S25</b>	<b>F1L2S50</b>	<b>F1L2S75</b>	<b>F1L2S100</b>

Focus offset 50mA							
Line offset at 0.1mm				Line offset at 0.2mm			
SF25	SF50	SF75	SF100	SF25	SF50	SF75	SF100
<b>F2L1S25</b>	<b>F2L1S50</b>	<b>F2L1S75</b>	<b>F2L1S100</b>	<b>F2L2S25</b>	<b>F2L2S50</b>	<b>F2L2S75</b>	<b>F2L2S100</b>

The sample is a cubic shape with a dimension of 20x20x10 mm<sup>3</sup>. The samples were fabricated by two builds at a layer thickness  $t = 70 \mu\text{m}$ . The first build has nine samples from F1L1S25 to F2L1S25 and was arranged in a scanning order as shown in Figure 72. The second build thus has seven samples left. There were additional two samples to fill up the number of nine samples per build. These two samples use the parameters of F1L1S25 sample; however, they differ in scanning strategies. The first sample is coded as F1L1S25Z as it has cross-snaking scanning strategy without 90° rotation in scan direction every layer. The second one is coded as F1L1S25d as it has no 90° rotation in scan direction every layer and no cross-snaking scanning.

The aim of removal the 90° rotation in scan direction every layer is to observe the cracking orientation whether it has any correlation to the scan direction of every layer.

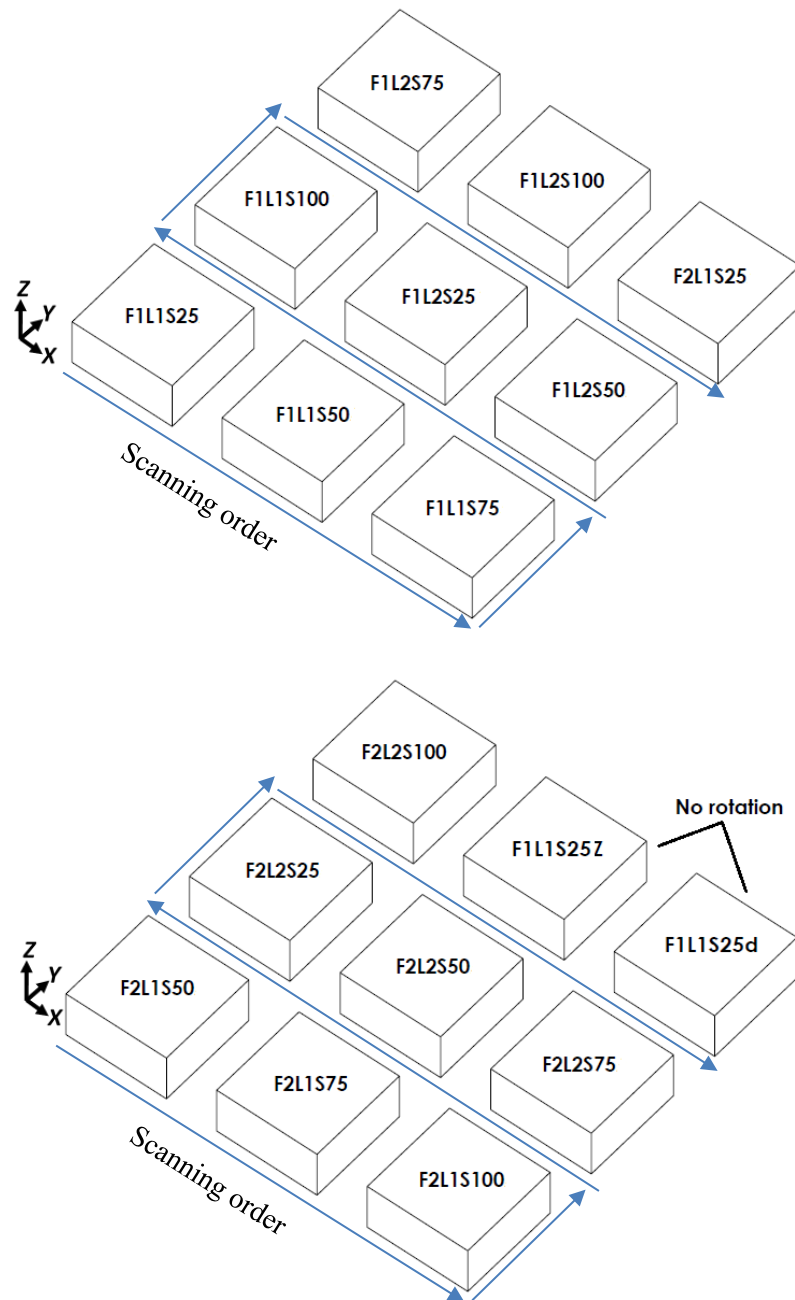
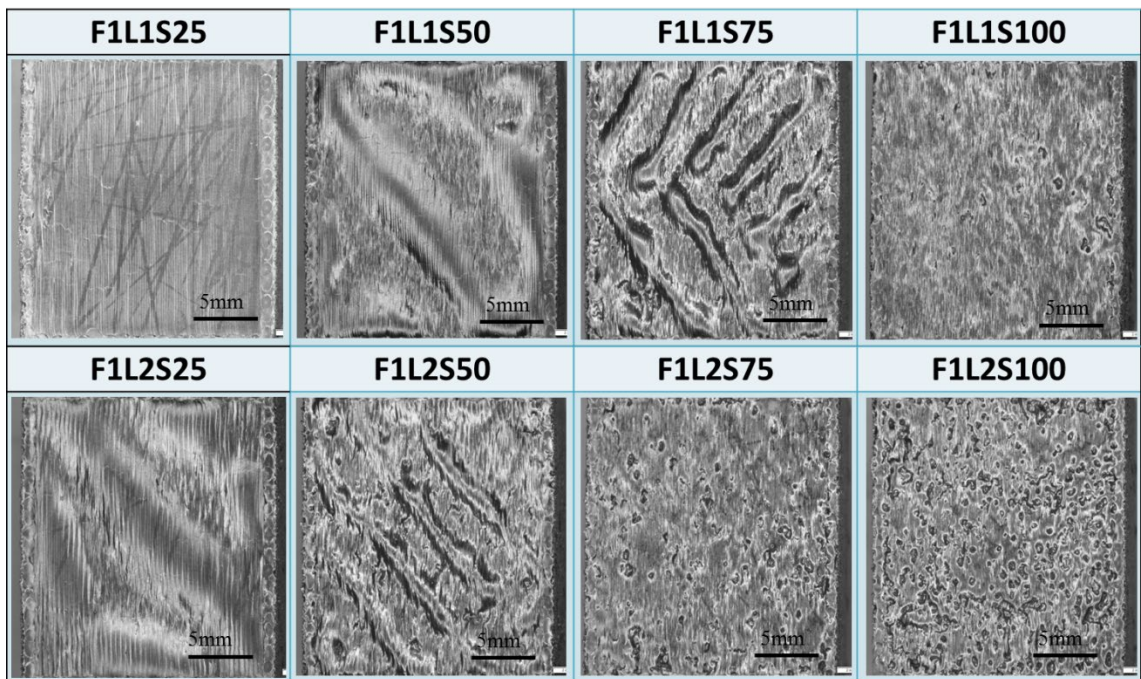


Figure 72. EB-PBF builds and arrangement of samples per build. Scanning order is also illustrated

The as-fabricated samples are shown in Figure 73. As can be seen, for the group of samples that have the same code of focus offset F1 (or FO25), most of them have swelling/rippled surface. Lack of fusion can also be observed for samples with high SF values such as F1L1S100, F1L2S75, and F1L2S100. The best sample achieved is F1L1S25 as the surface appears very smooth and flat although some crack-like feature can be observed. For the group of samples with F2 code (FO50), there is no swelling defect detected. Instead, lack of fusion is observed for

most of the samples, except the F2L1S25. The best sample achieved in this group is the F2L1S25 as the surface has no swelling or lack of fusion. The extensive crack network can be seen on the top surface and looks more severe than the F1L1S25 sample. The remaining two samples F1L1S25Z and F1L1S25d have no swelling/rippled or lack of fusion. This shows a consistency with the F1L1S25 sample. In addition, all samples' cracks' orientation is perpendicular to the scan direction, which shows similarity to the preliminary work. The 90° and no 90° rotation both results in same crack orientation. This suggests that how crack orientates may relate to the scan direction, at least the last layer. Cross-sectional images viewing from XY plane should be observed to further examining the correlation between crack orientation and the scan direction.



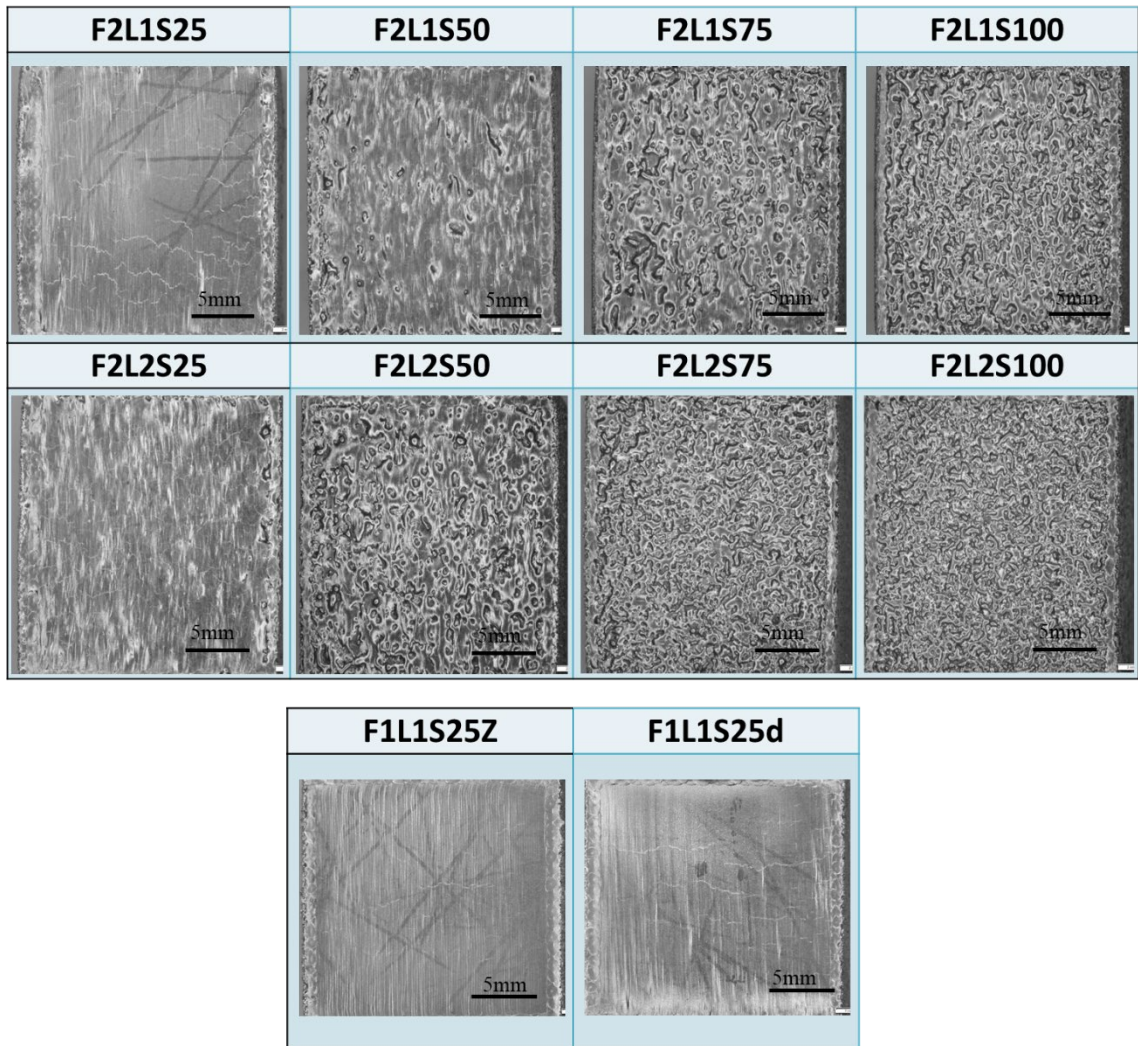


Figure 73. As-fabricated samples from the new EB-PBF experiments.

The F1L1S25 and F2L1S25 were selected for further investigation in terms of cracking problem during solidification in EB-PBF Co-29Cr-10Ni-7W alloy. These two samples have no swelling and lack of fusion that can affect the cracking propensity. Swelling of the surface can affect the next layer raking which causes uneven powder particles distribution. Thus, in the hatching stage, the powder fusion process will be affected. Hollow areas that are full of powder particles may result in lack of energy input since there is highly local powder packing density. In contrast, areas with less powder (i.e. the bulges) may result in severe remelting since there is no powder to cover. As a consequence, the bulges or swellings keep growing leading to the termination of the process or damaging the raking blades. The swelling phenomenon was reported as a combination of the vapor back pressure and the surface tension of solidifying molten metal [3].

Lack of fusion in forms of porosity or pores can inhibit the crack growth path. Moreover, pores or voids in the microstructure can mitigate residual stresses as the materials have enough space for further deformation to release the stresses. As lack of fusion is not observed for the two samples, the porosity density, if any, can be predicted to be the least among all samples.

In Figure 74, the severity of cracks observed on the top surface implies that the FO applied may have significant influence since other parameters are the same. The relationship between the FO values and the beam sizes have not been thoroughly reported in the literature. The difficulties are due to the complex combination of electromagnetic coils in the EB-PBF column as well as no further instruction documents provided by the Arcam GE. Thus, the measurement from the width of the scanning tracks is used to approximate the beam sizes. Based on that, any effects of the FOs will be examined, especially on the cracking problem.

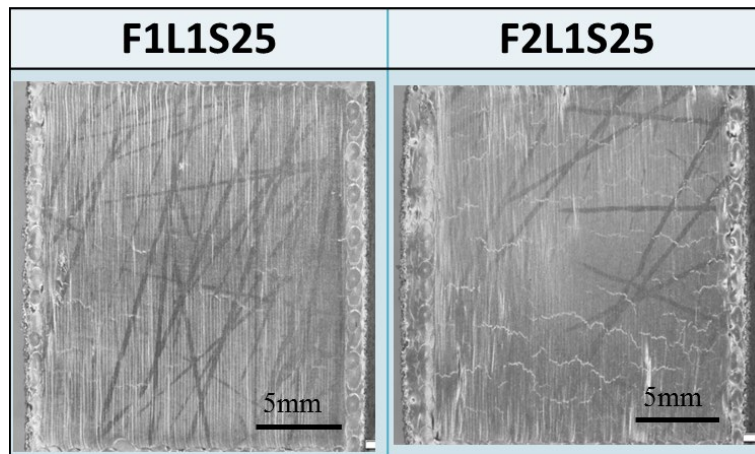


Figure 74. Cracking severity in two selected samples. FO values are different while other parameters remained unchanged

### 3.5. Differential Scanning Calorimetry (DSC):

The thermal analysis technique is employed to examine the phase transition temperatures of the alloy during melting and cooling processes. The temperature difference ( $\Delta T$ ) is measured between the sample and the reference material as both undergo the same heating/cooling program. If there is a heat absorption event in the sample, as known as an endothermic thermal event (i.e. melting), the sample temperature  $T_{sample}$  will be lower than that of the reference  $T_{ref}$ . In contrast, a heat releasing or exothermic thermal event (i.e. solidification), then the  $T_{sample}$  is higher than  $T_{ref}$ . The DTA system will record the  $\Delta T$  against the  $T_{ref}$  and plot out the DTA curves. Figure 75 shows an example of DTA result from melting of pure Ag [136]. It can be seen that the  $T_{ref}$  linearly increases while there is a lag in the  $T_{sample}$  from 1600 s to 1850 s (Figure 75a). In Figure 75, the differential signal  $\Delta T$  can also be seen for the plotted curves of  $T_{sample}$  and  $T_{ref}$ .

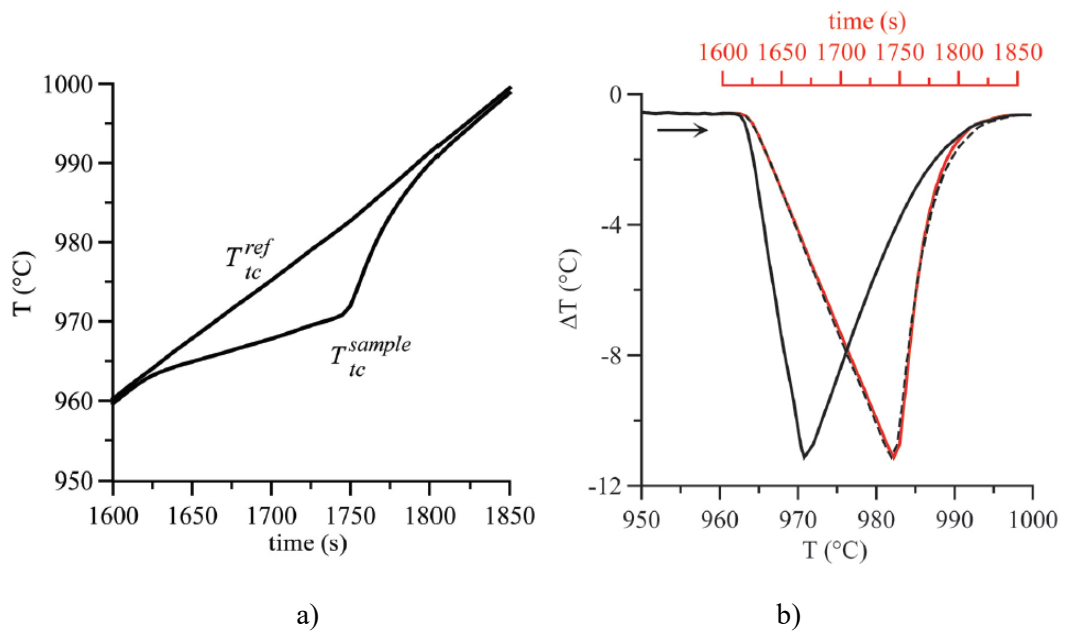


Figure 75. DTA melting of 211.6 mg pure Ag at 10 K/min. (a).  $T_{sample}$  and  $T_{ref}$  versus time and (b). Differential signal  $\Delta T = T_{sample}$  (solid black) –  $T_{ref}$  (dashed black) vs time [136]

Figure 76 illustrates the DTA on-heating and on-cooling curves with denotations of thermal peaks for result interpretation [13]. Based on the indicated exothermic direction, specific thermal events can be translated whether they are endothermic or exothermic events.

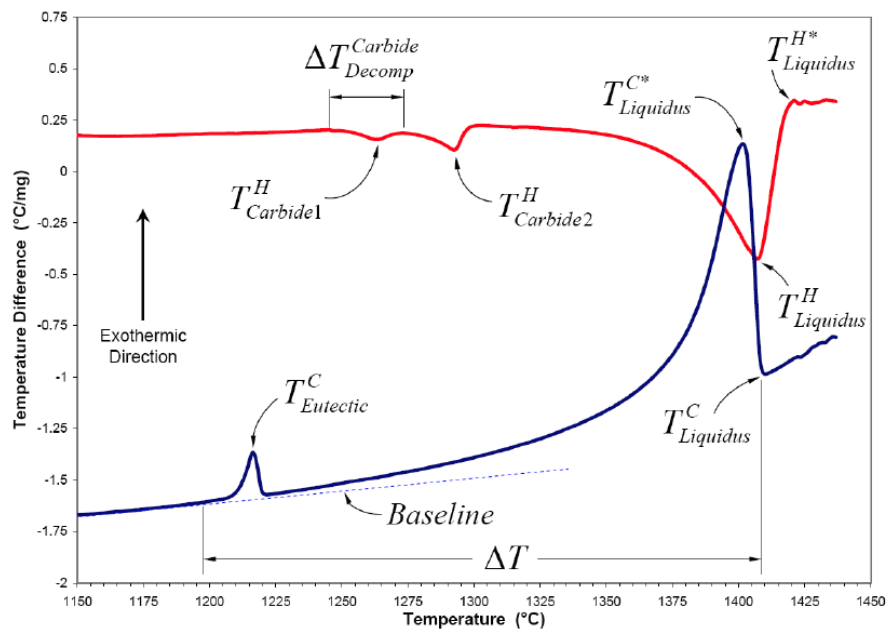


Figure 76. Interpreter of DTA results [13]

- $T_{Liquidus}^C$  Liquidus temperature (on-cooling curve)
- $T_{Liquidus}^{C*}$  Liquidus temperature, alternation definition (on-cooling curve)
- $T_{Liquidus}^H$  Liquidus temperature (on-heating curve)

$T_{Liquidus}^{H*}$	Liquidus temperature, alternation definition (on-heating curve)
$T_{Eutectic}^C$	Eutectic solidification temperature (on-cooling curve)
$T_{Carbide_x}^H$	Carbide decomposition temperature (on-heating curve)
$\Delta T_{Decomp}^{Carbide}$	Range of carbide decomposition

Differential Scanning Calorimetry is one of the methods of differential thermal analysis (DTA). The main difference of DSC from DTA is that it measures the heat flow of energy into or out of the sample as a function of temperature or time [137]. Figure 77 schematically demonstrates a DSC system [138]. The homogeneous temperature field of the furnace will cause equal heat flows into the sample and the inert reference pan that sits on two respective disk-shaped sensors. Similar to DTA, if there is an endothermic or exothermic thermal events occur in the sample, the heat capacities between the sample and the reference will be different. In DSC, the sample and the reference are connected by thermal resistances which are very good thermal conductors. For any discrepancies in temperature, there will be a heat flow between the sample and the reference. The flow directions depend on whether the thermal event is endothermic or exothermic. The sensitive sensors (temperature and heat flux sensors) will record temperature gradients and measure every difference in heat flow quickly and accurately. The temporal deviations will be shown as respective thermal peaks in the DSC differential heat flow curves against a DSC baseline.

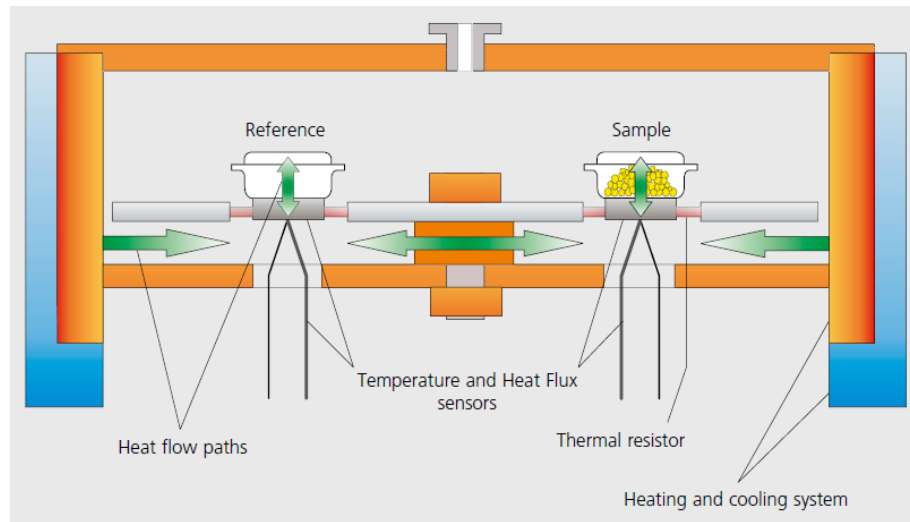


Figure 77. Schematic illustration of a heat-flux DSC furnace

In this work, the DSC experiment was conducted using a Netzsch STA 449 F1 system fitted with a SiC furnace and an S-type DSC sensor, as shown in Figure 78. Sample in the form of powder was put into an Al<sub>2</sub>O<sub>3</sub> pan and was heated to 1500 °C from room temperature and then cooled down to room temperature. The heating and cooling rate used was 10°C/m. The heating stage was conducted under Argon purge gas at 50 cm<sup>3</sup>/min. The cooling stage, however, was

unable to use the same condition as the sample was cooled down by air. The DSC tests were repeated three times to ensure the reliability of the measured data. An initial blank run was carried out at every test to correct the baseline.



Figure 78. DSC Netzsch STA 449 F1 system

### 3.6. Specimen preparation for metallurgical analysis

The cubic specimens were sectioned into smaller sizes of 6x10x10 mm that are used for observation in each viewing direction, XZ, YZ, and XY as illustrated in Figure 79. The specimens were then mounted by the Struers LoboPress-3 metallurgical mounting machine with a heating temperature of 180 °C in 8 minutes at a pressure of 25kN following by cooling in 3 minutes. The mounting resins include a thin layer of Multi-Fast resin at an approximately 1-2 mm thickness from the cross-sectional surface and the rest is covered with Condu-Fast resin whose purpose is for creating good electrical conduction. The Multi-Fast resin layer is to ensure better quality when observing under scanning electron microscopy (SEM) while the Condu-Fast resin is beneficial for the later electrolytic polishing step. The mounted specimen is illustrated in Figure 80.

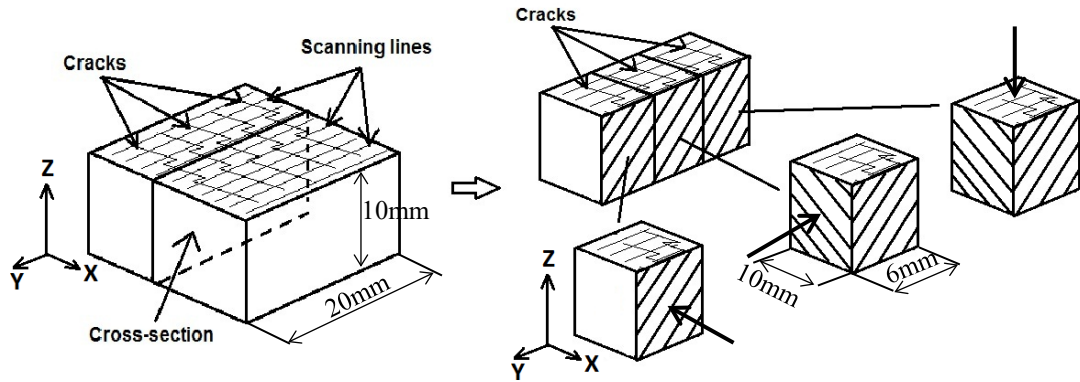


Figure 79. Schematic illustration of sectioning of cubic sample for observation of XZ, YZ, and XY cross-sections.

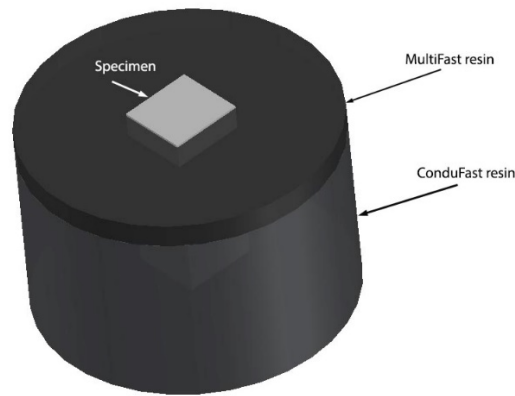


Figure 80. Illustration of the mounted specimen with two different layers of mounting resins

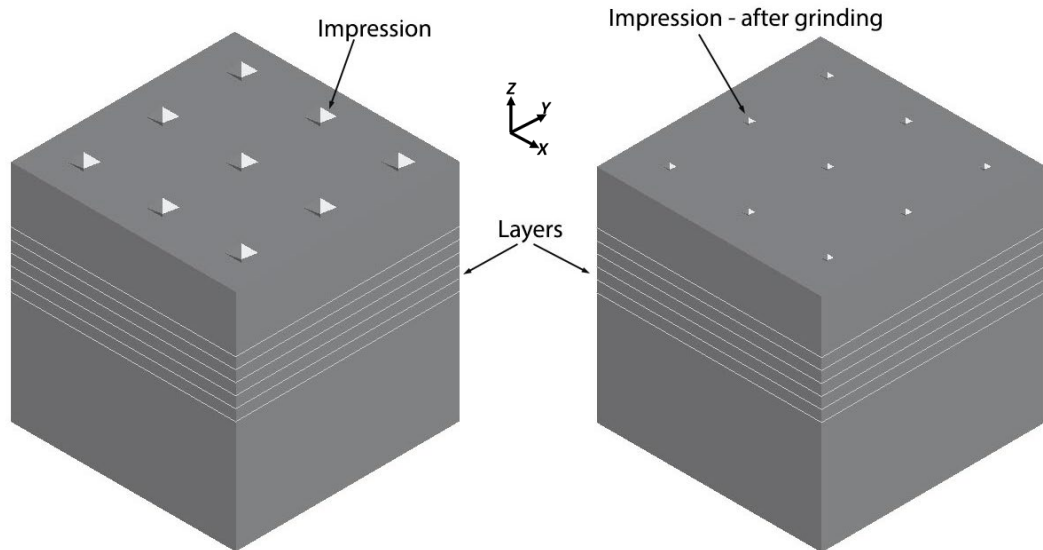
Mounted specimens were then passed through multiple grinding steps with 180, 500, 1200 and 2400 grit SiC papers on a Metaserv rotary grinder. After that, the specimens were finally polished with 6 $\mu$ m diamond suspension (DP) and 1 $\mu$ m standard colloidal silica suspension (OP-S) using the automatically polishing machine Struers TegraPol-21. At this stage, a mirror-like surface was achieved. Finally, electrolytic polishing Struers LectroPol-5 machine was used to polish the specimens to be able for further microstructure characterization. Etchant solution used in the electrolytic polishing is 10% H<sub>2</sub>SO<sub>4</sub> + 90%CH<sub>3</sub>OH. The polishing duration is 7 s for scanning electron microscopic observation and 25s for electron backscatter diffraction analysis.

### 3.7. Specimen preparation for characterizing the crack network

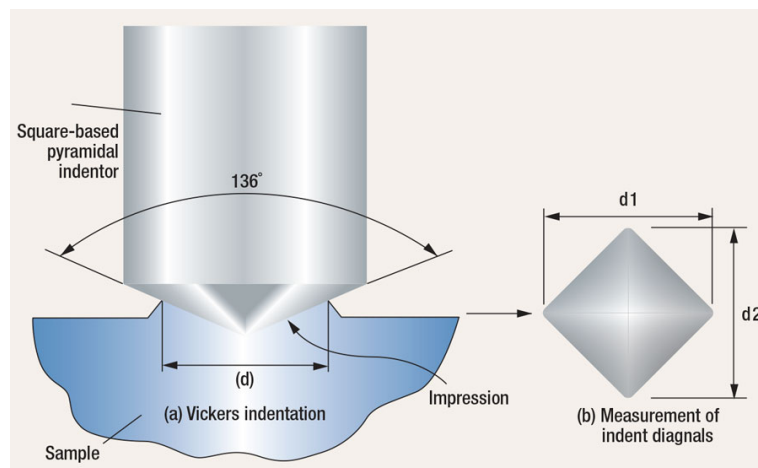
In order to reveal the crack network in a way that is beneficial for better illustration than normal 2-D XZ and YZ cross-sections, the examined specimens were consecutively ground/polished off from the top surface downward (XY cross-section), layer-by-layer. It is important to properly control the amount of material to be ground/polished off. Therefore, micro-indentation was employed using a micro-Vicker hardness tester. The indenter has fixed pyramidal shape with a

known face angle of  $136^\circ$ . The specimens were indented at several locations throughout the surface, as illustrated in Figure 81a. The applied force was selected at 1kg with a dwell-time of 10 s. As illustrated in Figure 81b, the two diagonal dimensions  $d_1$  and  $d_2$  were measured and the impression depth can be geometrically figured out. With the selected force and dwell time, an individual indentation will result in a 15~16  $\mu\text{m}$  impression depth. This depth is then considered as the standard depth that will be used to identify the total distance of removed material during a single grinding. For example, a two-standard depth grinding will remove a total ~32  $\mu\text{m}$  of materials.

The grinding process was strictly controlled and frequently observed under optical microscopy to check if all the indentations disappear. Then, the next series of indentations are carried out until the desired grinding/polishing amount is achieved and the examined layer has been reached. The examined layer will then be passed through a standard specimen preparation for scanning electron microscopy imaging. After that, the process was repeated for the consecutive layers. As the grinding process was done manually, therefore a perfectly even grinding surface is hard to achieve. Nevertheless, the revealed crack network at each layer was able to be revealed and provide good observation for tracing back how cracks have grown during EB-PBF.



a)



b)

Figure 81. (a). Illustration on how micro-Vicker indentation was used to control the ground/polished of the amount of material and (b). Geometrical calculation of the impression depth [139]

### 3.8. Macro and microstructure analytical techniques

Optical microscopy (OM) was used to capture optical images at low magnifications of 50x, 100x, 200x and 1000x. The device used is an Olympus BX51M optical microscope.

Scanning electron microscopy (SEM) was used for microstructure characterization in terms of grain structures, grain boundaries... Two SEM machines were employed. The first one is a Hitachi SU-70 field emission SEM located at Auckland University of Technology in Auckland, New Zealand. The second one is a Zeiss Merlin field emission SEM located at Materials Characterization Group, CSIRO Clayton site in Melbourne, Australia. Figure 82 schematically illustrates an SEM system. An SEM uses a focused beam of electrons to scan a regular pattern

on the specimen's surface. The electrons that come out of the specimen's surface will then be captured by means of electron detectors. Then, a magnified image of the specimen will be created.

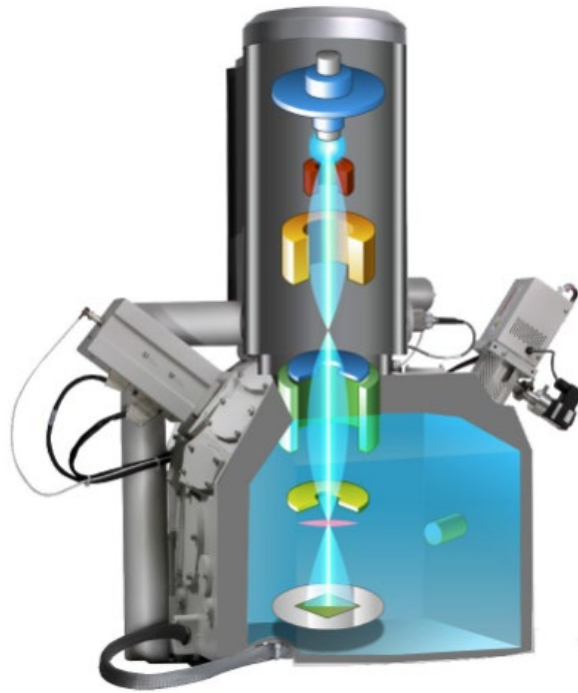


Figure 82. Illustration of an SEM [140]

For surface topography which is mainly used in this work, secondary electron imaging mode is employed. A low voltage of 5 kV was used. The secondary electrons (SE) have low energies ( $\sim 2$  to 50 eV) and are rejected only from the specimen's surface. These SE will be captured by a common type SE detector named as Everhart-Thornley detector [140].

Electron backscatter diffraction (EBSD) is additional characterization technique to an SEM to examine the crystallographic orientation, local texture, and phase identification and distribution of crystalline materials. The EBSD patterns are generated on a phosphor screen by back-scatter diffraction of a stationary beam of high energy electrons. The patterns, as known as Kikuchi pattern is a series of parallel lines projected on the phosphor screen, as shown in Figure 83a. These lines are the result of the back-scatter diffraction the electron beam via the crystallographic planes, as illustrated in Figure 83b. The two diffraction cones form the edges of the Kikuchi band and the center plane between these cones is the geometric projection of the diffracting plane [141]. The width of the Kikuchi band relates to interplanar spacing  $d_{hkl}$ , the Bragg angle  $\theta$  and the x-ray wavelength  $\lambda$ , according to the Bragg's law:

$$n \cdot \lambda = 2d_{hkl} \sin \theta$$

The Kikuchi pattern is bound to the crystallographic structure of the specimen. Thus, when the crystallographic orientation changes, it will lead to the change in the Kikuchi pattern. As a result, positions of Kikuchi bands can be used to calculate the crystallographic orientation.

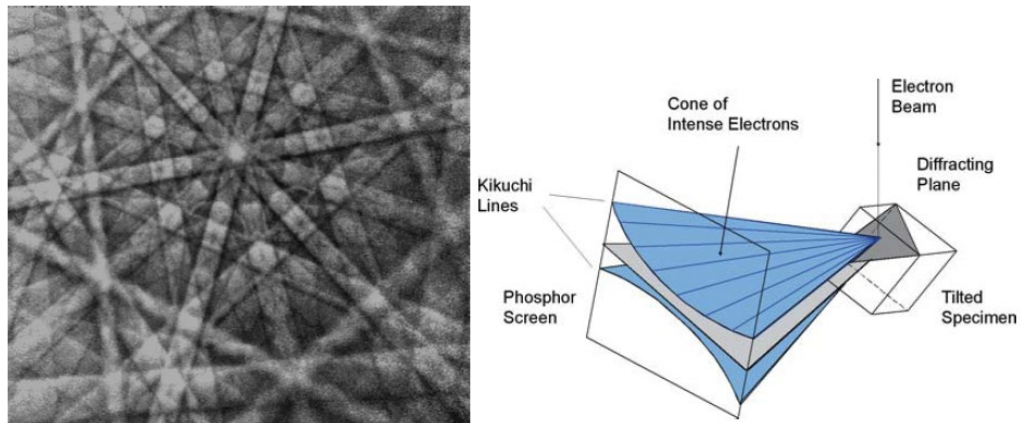


Figure 83. (a). Back-scatter Kikuchi pattern from cadmium at 20 keV acquired by an analog video camera; (b). Schematic illustration of diffracting cones with respect to the reflecting plane, the specimen and the phosphor screen [141]

The EBSD system components are similar to an SEM with an additional EBSD detector. The detector consists of a phosphor screen that is surrounded by forescatter diodes and a camera to capture the Kikuchi band. The interpretation of the Kikuchi band into specifically crystallographic orientation is done by the system's software. Figure 84 illustrates principal components in an EBSD system.

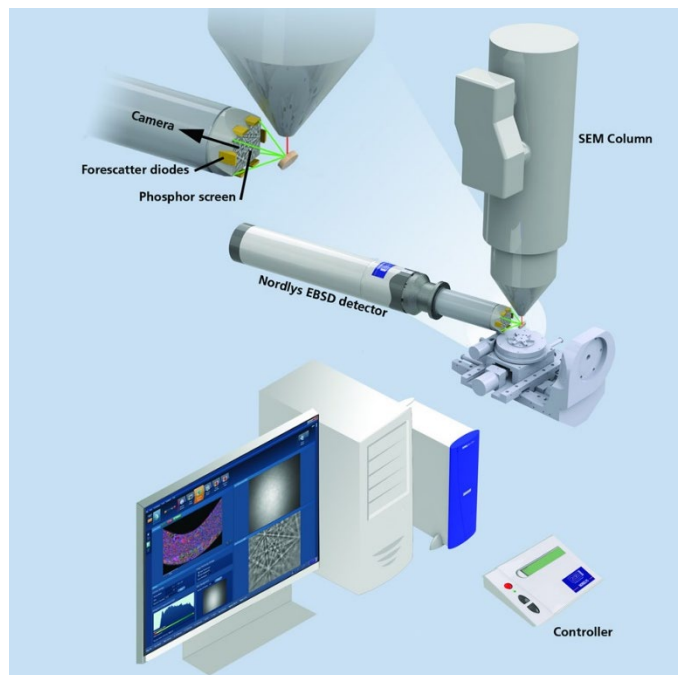


Figure 84. Principal components in an EBSD system [142]

In this study, an acceleration voltage of 20 kV, accompanied with a working distance of 26 mm and a sample tilt angle of 68° was chosen in order to maximize backscattered electron diffraction. In addition, the combination of working distance and the tilt angle is to ensure collision between the sample and the detector will not occur for preventing damaging the EBSD detector. The EBSD process was conducted on an FE Hitachi SU-70 using the fully automated data acquisition programs 'NSSTM' that acquire EBSD patterns from the scan of the sample.

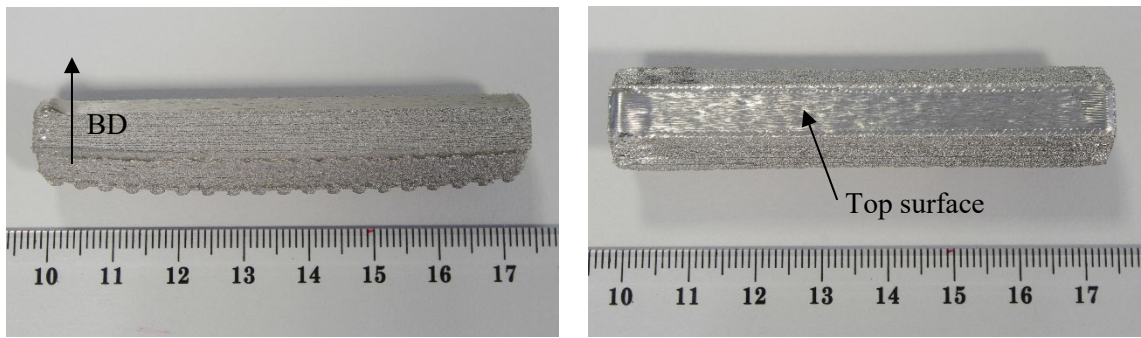
### 3.9. X-ray diffraction analysis

X-ray diffraction (XRD) analysis was used for phase identification of the studied alloys. The analysis was conducted in CSIRO Manufacturing Clayton site in Melbourne, Australia. The powder samples were loaded into a standard sample holder for data collection. A Bruker D8 Advance A25 X-ray Diffractometer operating under  $\text{CuK}\alpha$  radiation (40 kV, 40 mA) equipped with a Lynx Eye XE-T detector was employed to obtain the XRD patterns. The samples were scanned over the  $2\theta$  range from 5° to 130° with a step size of 0.02° and a count time of 1.6 seconds per step, and were spun at 15rpm during data collection.

Analyses were performed on the collected XRD data using the Bruker XRD search match program EVA™ 4.3. Crystalline phases were identified using the ICDD-JCPDS powder diffraction database.

### 3.10. Tensile testing for fracture surface obtaining

The tensile testing experiment aims to observe the fracture surface that is expected to be caused by the internal cracks of the samples. By observing the original cracking surface, identification of crack types whether they are hot cracking or solid-state cracking can be achieved. As can be seen in the preliminary work, cross-sectional optical images reveal extensive cracking along the build direction. Thus, if the pulling axis is perpendicular to the build direction, it is likely that these cracks will be the initiated locations for the fractured failure occurs. The sample for the tensile test was printed as a hexagonal bar whose longitudinal axis is perpendicular to the build direction, as shown in Figure 85. The hexagonal shape is to avoid the overhang structure. In addition, the hexagonal shape is for the ease of the later machining step to make the sample in a dog-bone shape for the tensile test. Figure 85b shows the tensile sample in as-fabricated and as-machined dog-bone shapes.



a)



b)

Figure 85. As-fabricated hexagonal bar and as-machined dog-bone tensile sample

The tensile test was done following ASTM-E8/E 8M-08 standards for tensile testing of metallic materials. The testing machine used is 100 kN Instron 5566 tensile testing machine that is located at CSIRO Clayton site in Melbourne, Australia. The strain rate used is at the upper limit of the standard's recommendation which is 0.5 mm/min to break the sample as fast as possible. The test was conducted at room temperature. Since the aim of the test is for fracture surface observation, no stress-strain curve will be provided.

### 3.11. Numerical simulation by ANSYS ADPL 16.2

As observed from both preliminary work and the new experiments, crack orientation tends to be perpendicular to the scan direction of the last layer. This suggests that the triggered stresses for cracking may orientate along the scan direction. To clarify this, numerical simulation is conducted since this is more convenient and provides better visualization on how thermal and thermal-stress distribute during EB-PBF. The software used is the ANSYS Mechanical APDL v.16.2. Sequential steps have to be defined prior to executing the simulation. The brief description of modeling steps is shown as following:

1. Identification of simulation mode (i.e. thermal or structural): thermal mode is selected.
2. Identification of elemental types: solid.
3. Input the material properties: to define the temperature-dependent material properties.
4. Generation of part model: to construct the 3D model of the specimen on which the simulation will be conducted. Details of the 3D model are shown in Figure 86.

5. Meshing the model: a finite element mesh is generated by selecting the type and size of elements. Mesh size and type can be different for different regions of the part. The meshed model is shown in Figure 86.
6. Solution step: in this step, thermal loads and analysis method are defined. In this study, a 2D Gaussian heat source is applied on a pre-defined path located on the part model. The moving of the heat source represents a moving melt pool. Thermal load is the heat flux from the heat source applied to the scanning area. Transient analysis is applied to analyze the temperature distribution from the heat source to the meshed model. After that, the job will be executed and perform analysis based on all input variables.
7. Results: This step provides a graphical display of the thermal analysis done in step 6. The temperature distribution on the meshed model as well as an individual element can be viewed. The thermal analysis result is then used to be the input for the thermal-stress analysis.

For thermal-stress analysis steps:

1. Simulation mode is selected to be a structural mode.
2. The element type is still solid.
3. Temperature-dependent mechanical properties are defined.
4. The same 3D model is retained.
5. The same meshing method is retained
6. Solution step: the thermo-mechanical load is imported from the thermal analysis result. Addition definition of the mechanical boundary has to be set out. Details on the mechanical boundary condition are shown in Figure 145, in chapter 6.
7. Results: Component stresses in ZX, ZY, XY planes can be viewed. In addition, principal stresses  $\sigma_1$ ,  $\sigma_2$  and  $\sigma_3$  along Z, Y, and X-axis, respectively can be viewed in a form of stress vectors. These stress vectors are crucial since they visualize how stresses orientate with respect to the scan direction.

The simulation model is constructed in an attempt to replicate the actual situation in EB-PBF. The 3D model comprises three volumes, as shown in Figure 86. The first volume is the solid substrate, which represents the already built material. The second volume is the partially deposited solid top layer and the third one is the remaining powder within the same layer. The simulated beam scan is at the boundary between the solid and powder of the top layer. The block model has a dimension of 10x10x5mm. The smaller dimensions are used in order to save the processing time of simulation work. The added layer thickness is 0.07mm. The solid substrate is meshed by 8-nodes tetrahedral-shape and comprises of 30825 elements. The deposited top layer including solid and powder areas are meshed by 8-nodes tetrahedral-shape and hexahedron-shape and comprise of 2718 and 2825 elements, respectively.

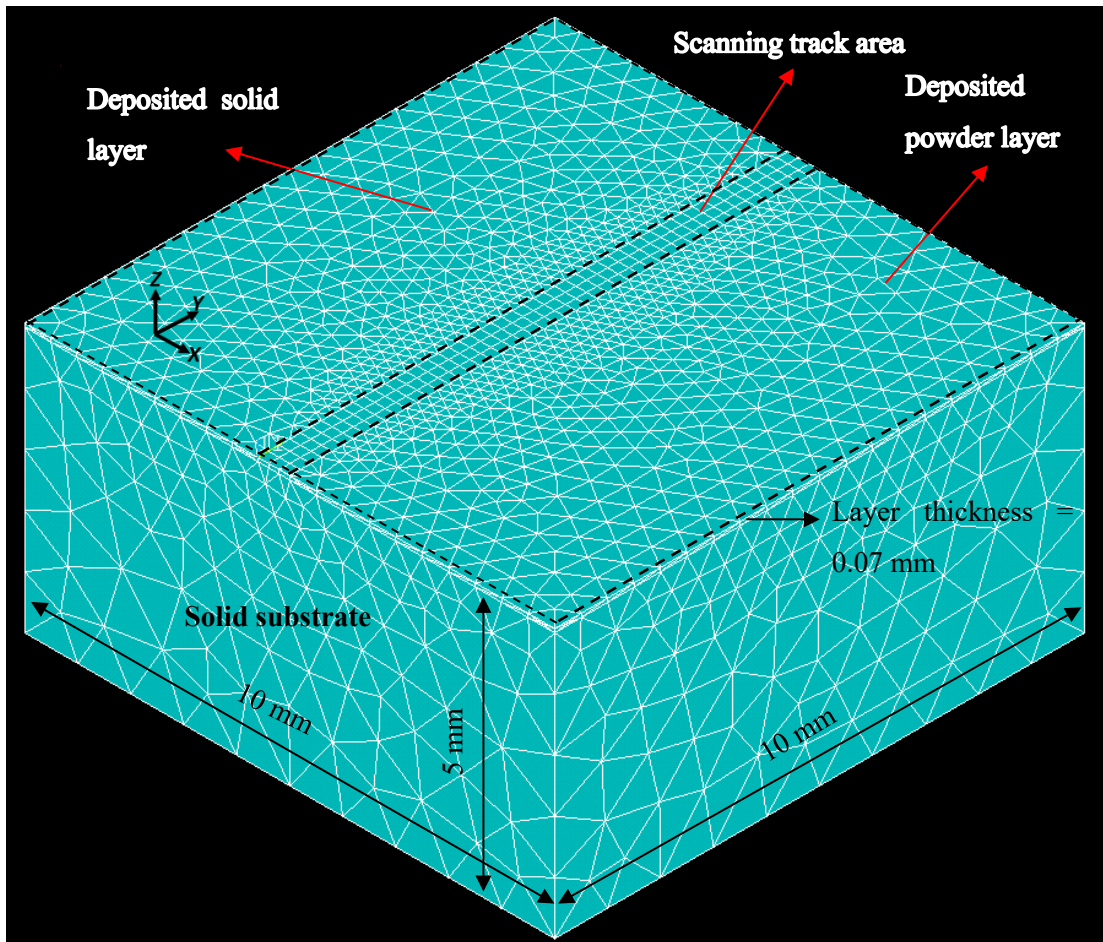


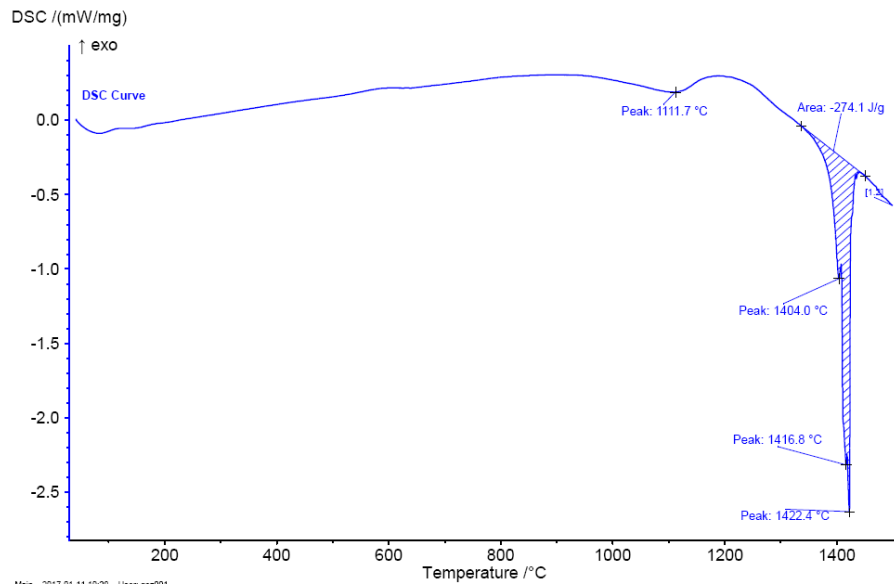
Figure 86. Simulation block model of 10x10x5 mm.

## **CHAPTER 4: SOLIDIFICATION DURING ELECTRON BEAM POWDER BED FUSION**

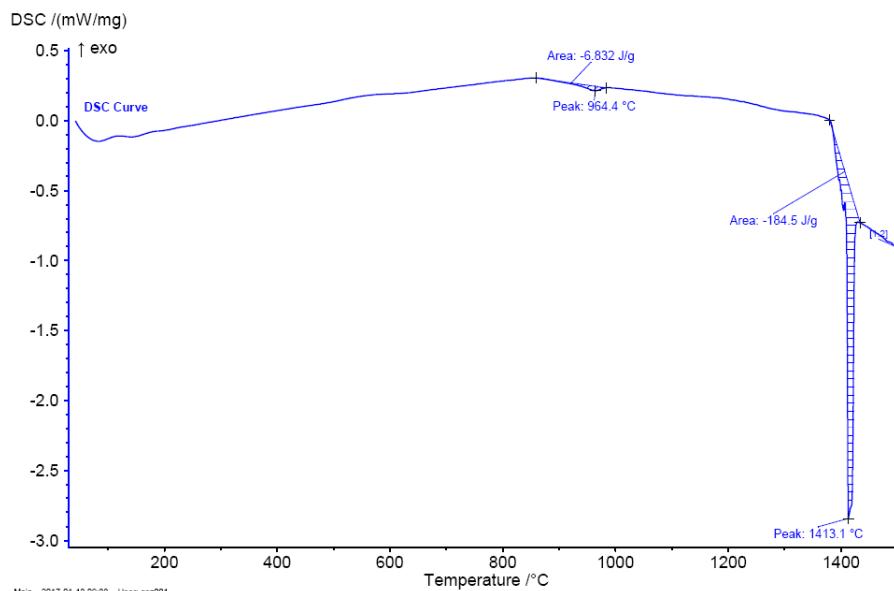
In this chapter, thermal analysis results will first be presented to ascertain the solidification temperature ranges of the relevant alloys used in this research. Then, how tracks appear on the top surface, grain structures and solidified microstructure will be presented for samples built with FO25 and FO50 conditions. An attempt has been made to estimate the thermal quantities that determine solidification mode based on track boundary spacing and dendrite spacing. The focus offset dependent melt/track geometry which directly links to the absence or the presence of horizontal grown dendrites, identified in the present research, will be presented. Based on this newly observed growth feature, possible process control to eliminate the dominance of growth along the build direction will be illustrated and discussed.

### **4.1. Phase transition temperatures during heating and cooling of Co-29Cr-10Ni-7W and Co-29Cr-6Mo alloys**

As aforementioned earlier, EB-PBF Co-29Cr-10Ni-7W alloy resulted in extensive cracking networks but not for Co-29Cr-6Mo alloy. How these two alloys melt/solidify in terms of relevant phase transition temperatures is important to understand their solidification behavior in EB-PBF. Solidification freezing ranges that are one of the most crucial factors affect the hot cracking. Therefore, by using Differential Scanning Calorimetry (DSC), the melting/cooling process of Co-29Cr-10Ni-7W and Co-29Cr-6Mo alloys has been analyzed. At first, the DSC analysis results of powder materials of the two alloys are given. Figure 87 shows the on-heating curves of the two alloys' powders.



a)



b)

Figure 87. The DSC on-heating curves of (a). Co-29Cr-10Ni-7W alloy and (b). Co-29Cr-6Mo alloy

As it can be clearly seen, several peaks are detected during the heating of Co-29Cr-10Ni-7W alloy. Among those, the 1111.7 °C and the 1422.4 °C are noteworthy. Respectively, for Co-29Cr-6Mo alloy, the noted peaks are at 964.4 °C and 1413.1 °C. The highest peaks can be easily figured out as the melting temperatures. In other words, the alloys will fully transform from solid to liquid at those temperatures. On the other hand, the lowest peaks need to be carefully examined because of various thermal activities may occur at this temperature range. Since EB-PBF Co-Cr alloys processes at very high preheat temperature, it is important to understand the

thermal event at those peaks whether they are eutectic melting points or solid-state phase transformation.

It is challenging to distinguish between the eutectic melting points and solid-state phase transformation by the DSC results only. Commonly, the DSC analysis has to be accompanied by other techniques such as XRD analysis and microstructure characterization to provide details of thermal activities happened. Therefore, the XRD technique was employed to identify major phases of the powder materials. Figure 88 illustrates the XRD phase analysis of the respective powders. For Co-Cr alloys, solid-state phase transformation can be  $\epsilon$ -to- $\gamma$  phase transformation or carbides dissolution. Figure 88a shows that there is no  $\epsilon$ -phase detected in the Co-29Cr-10Ni-7W powder, however, the Co-29Cr-6Mo powder contains a considerable amount of the  $\epsilon$ -phase (Figure 88b.). Pure cobalt element has the  $\epsilon \leftrightarrow \gamma$  phase transformation at 423°C [6]. Additions of major elements such as chromium and molybdenum in the Co-29Cr-6Mo are known as the  $\epsilon$ -phase stabilizers. Therefore, it is expected that the  $\epsilon \leftrightarrow \gamma$  phase transformation temperature increases. For the Co-29Cr-10Ni-7W alloy, tungsten is the  $\epsilon$ -phase stabilizer while nickel is the  $\gamma$ -phase stabilizer. According to Figure 89, that is cited from the work of Sims [11], by using the nominal compositions of Co-29Cr-6Mo and Co-29Cr-10Ni-7W alloys, one can estimate the temperature at which  $\epsilon \leftrightarrow \gamma$  phase transformation occurs:

For Co-29Cr-6Mo alloy:

$$T_{\gamma \leftrightarrow \epsilon} = 423^{\circ}\text{C} + 28_{\text{Cr}} \times 0.4 \times 30^{\circ}\text{C} + 6_{\text{Mo}} \times 0.2 \times 35^{\circ}\text{C} = \mathbf{801^{\circ}\text{C}} \quad \text{Eq. 16}$$

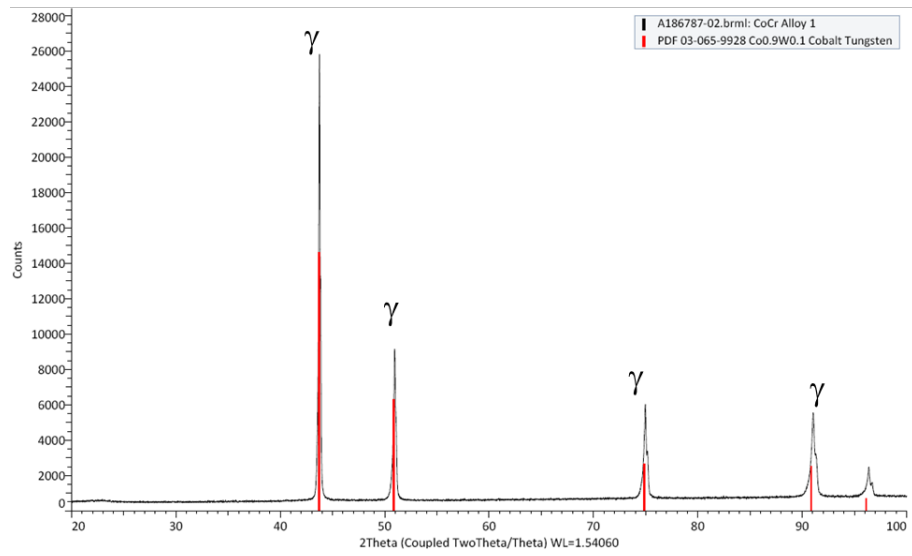
For Co-29Cr-10Ni-7W alloy:

$$T_{\gamma \leftrightarrow \epsilon} = 423^{\circ}\text{C} + 28_{\text{Cr}} \times 0.4 \times 30^{\circ}\text{C} + 7_{\text{W}} \times 0.18 \times 55^{\circ}\text{C} - 11_{\text{Ni}} \times 20^{\circ}\text{C} = \mathbf{608.3^{\circ}\text{C}} \quad \text{Eq. 17}$$

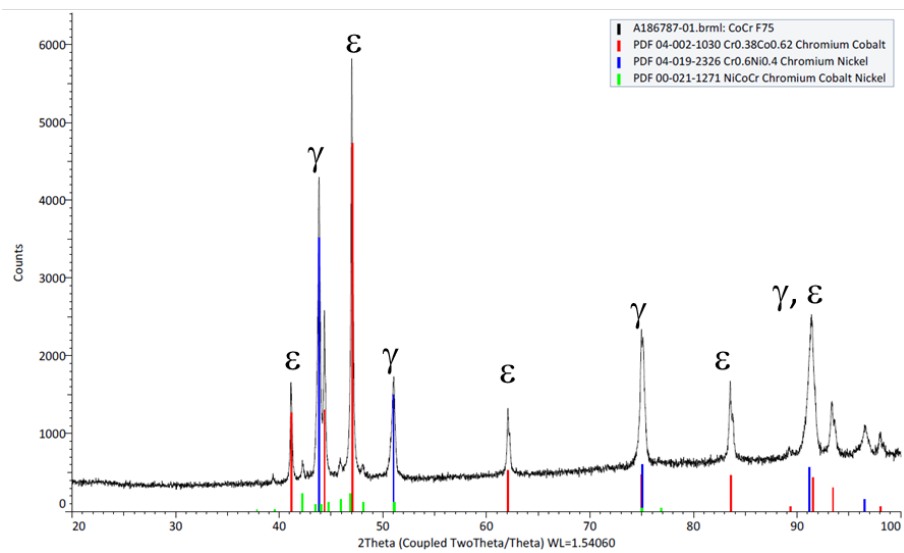
To validate Eq. 16 and Eq. 17, literature related to the phase transition of the two alloys is reviewed. Kurosu et al. [143] study on the isothermal phase transformation of the Co-29Cr-6Mo alloy. The authors based on Thermo-Calc software and the alloy's thermodynamic database to suggest that the  $\epsilon$ -phase transforms to the  $\gamma$ -phase and vice versa at around 900°. Saldivar-Garcia and Lopez [144] observed in their in-situ X-ray diffraction that the FCC-phase when heated over 950°C, there is enough activation energy to promote the transition into stable HCP-phase. Mergulhão and Das Neves [145] also obtained similar DSC result in their LB-PBF-fabricated Co-29Cr-6Mo sample. However, the  $\epsilon \leftrightarrow \gamma$  phase transition is just purely suggestion without any supportive scientific analyses.

The case for Co-29Cr-10Ni-7W alloy is more challenging since there is no recorded data or observation about the  $\epsilon \leftrightarrow \gamma$  phase transformation temperature. However, it is expected that the temperature is lower than that of Co-29Cr-6Mo alloy as shown in Eq. 16. Moreover, there is no

$\epsilon$ -phase observed in Co-29Cr-10Ni-7W powder; therefore,  $\epsilon \leftrightarrow \gamma$  phase transformation can be excluded for the 1111.7°C peak.



a)



b)

Figure 88. XRD analysis of (a). Co-29Cr-10Ni-7W alloy powder and (b). Co-29Cr-6Mo alloy powder

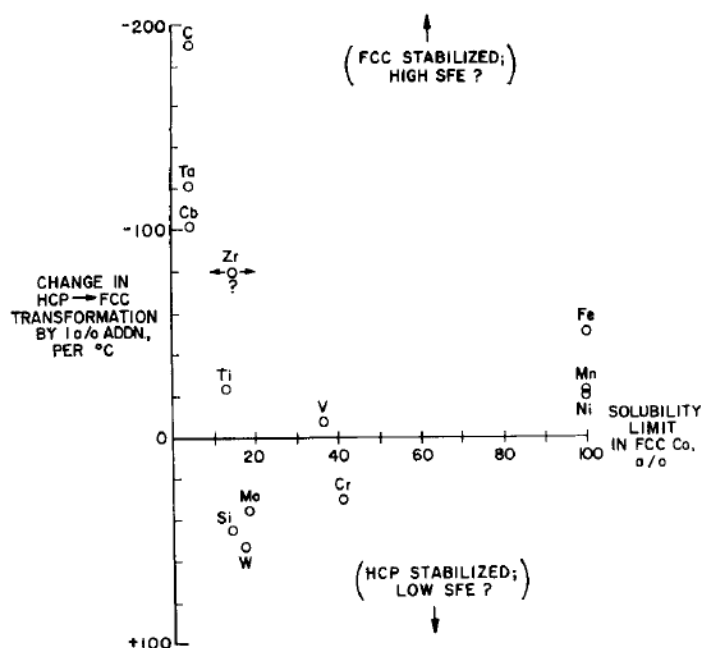


Figure 89. Effect of alloying additions on the HCP-FCC transformation in cobalt as a function of solubility in FCC Co [11].

It has been demonstrated so far that for the Co-29Cr-6Mo alloy, the 964.4°C peak obtained in the DSC result is probably the event of  $\epsilon \leftrightarrow \gamma$  phase transformation, but not for 1111.7°C peak for the Co-29Cr-10Ni-7W alloy. However, it is also noteworthy to figure out whether or not these peaks are possibly the eutectic melting temperatures. Kilerner et al. [146] has showed that as-cast Co-29Cr-6Mo alloy has eutectic mixture at grain boundaries melted at around 1235°C. The mixture consists of  $M_7C_3$ ,  $M_{23}C_6$ , sigma phase and an FCC-cobalt rich phase that easily wets the grain boundaries when heated above 1235°C. Similar report on eutectic melting point at around 1200°C can be found in [147].

In Figure 87b, this eutectic temperature cannot be observed since the DSC curve is almost straight until reaching the fusion temperature at 1413.1°C. The reason can be due to the carbon content used in this study Co-29Cr-6Mo alloy is extremely low (<0.01wt% C) compared to 0.27 wt.% used in [146]. The extremely low carbon content can result in very low amount of eutectic carbides which in turn causing the DSC device unable to detect. The same observation for influence of carbon content on the micro-segregation at grain boundaries was reported in the work of Chauhan [123].

For Co-29Cr-10Ni-7W alloy, as pointed out in chapter 2, the thermal analysis of as-cast samples shows a distinctive peak at around 1300°C for the DTA on-heating curve and 1225°C for the on-cooling curve. These peaks are reported as the eutectic melting temperatures during melting and solidifying, respectively. Clearly, the 1111.7°C peak detected in Figure 87a has not been reported in Literature. According to Beltran [12], the as-cast microstructure of Co-29Cr-10Ni-

7W alloy contains  $M_{23}C_6$  pseudo-eutectic carbide at the interstices of secondary dendrite arms and at grain boundaries. This carbide is a result of the last freezing liquid during solidification process and still stable up to the incipient melting temperature of around 1330°C. Moreover, standard heat treatment procedure of the alloy includes a solution treatment at temperature range 1149-1204°C to dissolve the grain boundaries carbides and homogenize the microstructure, which then followed by the aging process at a lower temperature (760-982°C). At this point, the thermal event at 1111.7°C in Figure 87a can be linked to the first stage of the mentioned heat treatment process at which the coarse carbides are being dissolved. In addition, the endothermic curve after 1111.7°C until the melting point can coincidentally include the eutectic melting peak, which is around 1300°C. In order to clarify this matter, the DSC tests were conducted again for the Co-29Cr-10Ni-7W powder and the as-cast sample. The on-heating curves are illustrated in Figure 90.

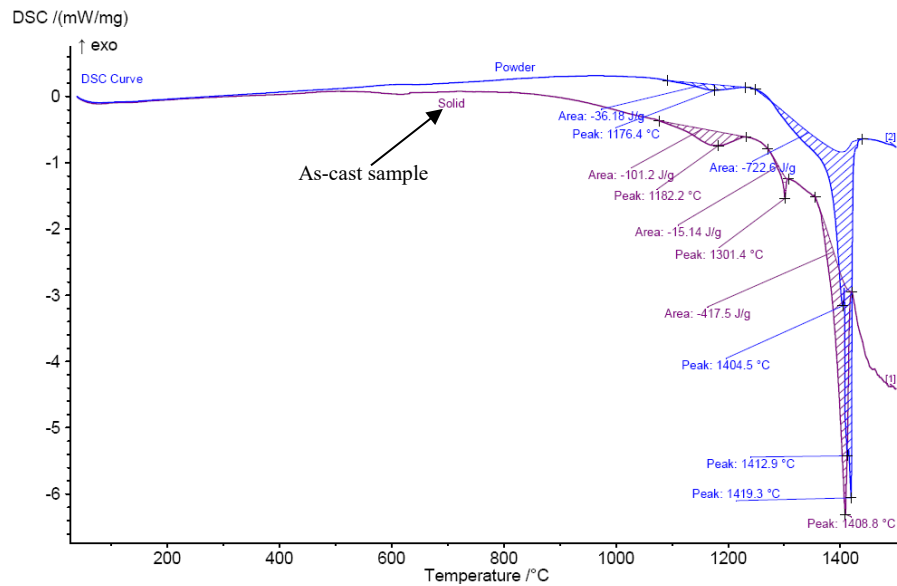


Figure 90. The DSC on-heating curve of powder and as-cast Co-29Cr-10Ni-7W samples

Figure 90 shows the DSC on-heating curves of the solid as-cast specimen and the powder sample. There is a consistent observation for the carbides dissolution peaks at around 1180 °C for both samples. However, the thermal energy consumed for the dissolution in the as-cast sample is almost three times bigger than the powder sample. Regarding the eutectic melting point, for as-cast specimen, it is 1301.4 °C. This is in good agreement with those reported in the literature [13]. In contrast, the DSC curve for powder sample again witnesses a steep slope at temperature range respective to the eutectic melting point. The consumed energy for carbide dissolution is -36.18 J/kg and -101.2 J/kg for powder and solid as-cast samples, respectively. In addition, no eutectic melting point detection in the powder. Further examination of solidified microstructure between as-cast and powder samples was conducted to clarify the reason.

As shown in Figure 91, for the as-cast sample, eutectic carbide islands are obviously observed at the grain boundaries along with finer re-precipitate carbides. On the other hand, for powder particle cross-section in Figure 91b, similar eutectic carbides seem to be absent. Instead, only the tiny phase distributed at boundaries between primary and secondary dendrite arms is observed. Higher magnification (top corner of Figure 91b) of these boundaries shows that the second phases formed at this region are extremely fine which is expected as a result of rapid solidification conditions of the gas-atomized process. Moreover, the analyzed carbon content of the powder sample (0.15 wt%) is quite low compared to that from the nominal compositions recommended for casting. Thus it is expected to result in a lower amount of eutectic carbide formation that leads to undetectable eutectic melting point in DSC analysis.

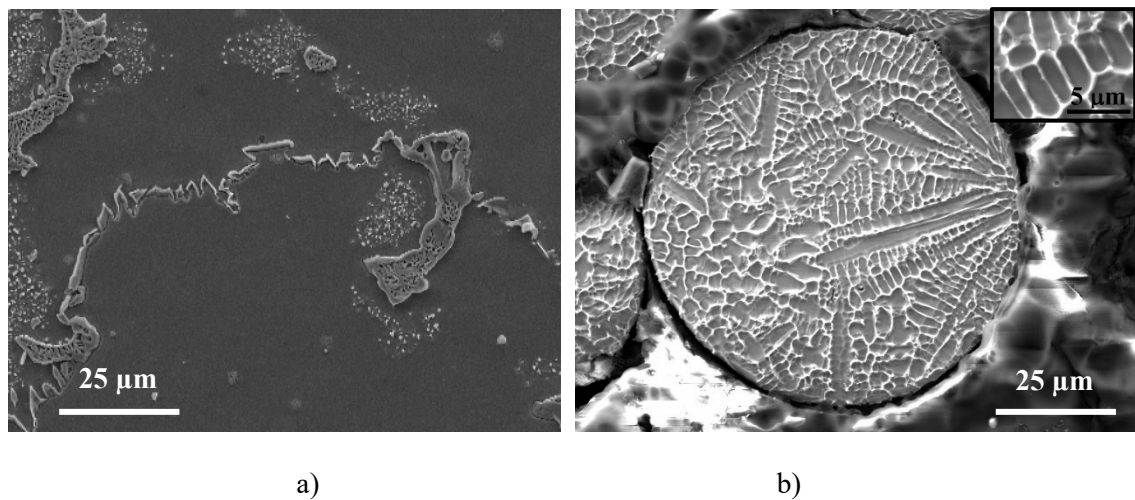
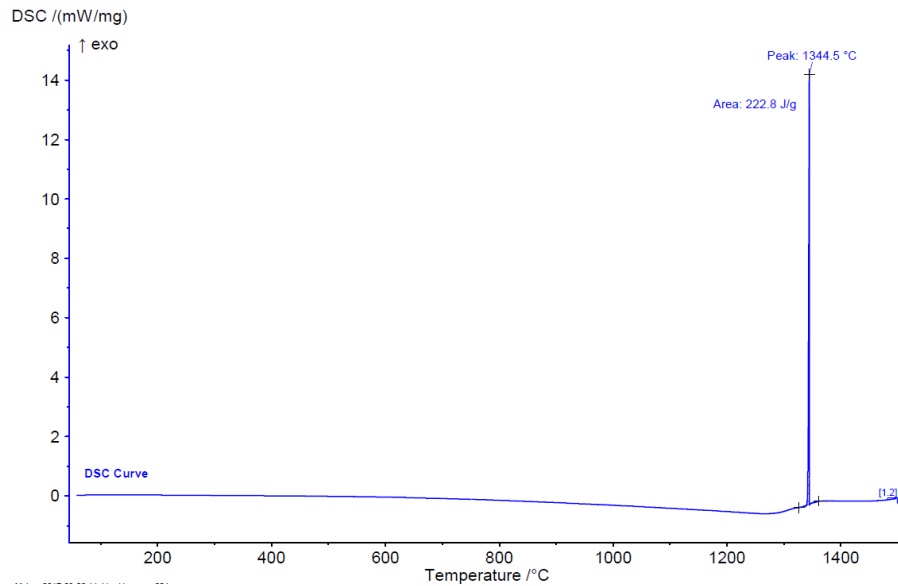
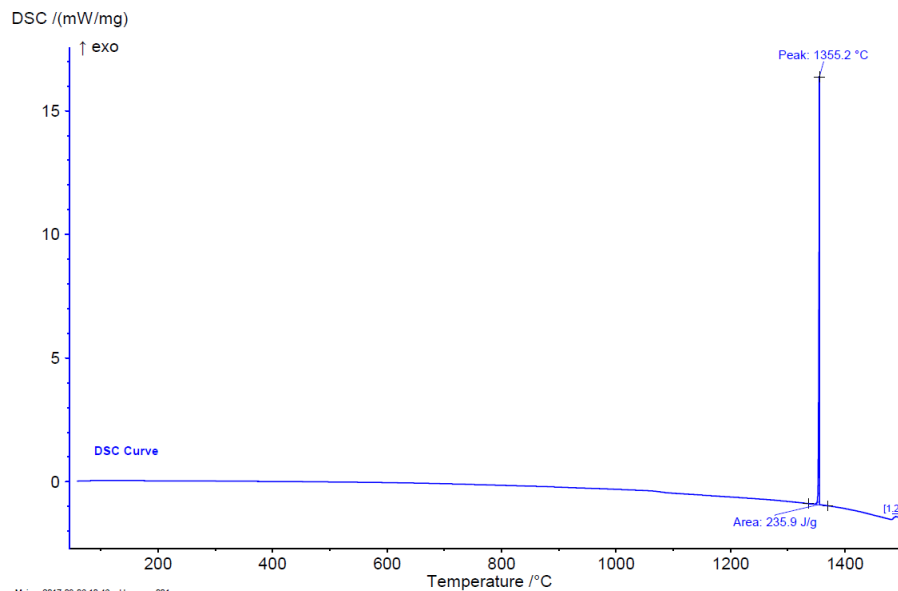


Figure 91. SEM images showing the microstructure of (a) as-cast sample and (b) powder of Co-29Cr-10Ni-7W alloy

So far, thermal analysis together with phase identification suggests that in the Co-29Cr-6Mo powder, during melting there are a  $\epsilon \leftrightarrow \gamma$  phase transformation at 964.4 °C and no eutectic melting point detected. In contrast, for the Co-29Cr-10Ni-7W powder, there is carbides dissolution at around 1111.7 °C and eutectic melting event at ~1300 °C. Regarding the cooling stage, the DSC results do not reflect much information, as shown in Figure 92. The on-cooling curves of both alloys only display the melting temperature. There are no eutectic solidification temperature points detected. The DSC test was re-conducted three times to consider the reliability of the result. However, similar results were still observed.



a)



b)

Figure 92. The DSC on-cooling curves of a) Co-29Cr-10Ni-7W alloy and b) Co-29Cr-6Mo alloy

Ronan [13] conducted the DTA experiments on 21 specimens and only a few of them have the second peak detected for the on-cooling curves. For the current studied Co-29Cr-10Ni-7W alloy and Co-29Cr-6Mo alloy, it is unable to identify the eutectic solidification temperature. Moreover, it shows the same result for all repeated DSC experiments. Since DSC analysis based on the temperature difference between the sample and the reference to calculate the heat flow in and out of the sample, thus improper contact area between the sample and the Al<sub>2</sub>O<sub>3</sub> pan (thus the underneath sensors) may affect the DSC results.

According to Boettinger [136], sample shape is a significant factor in DTA/DSC analysis, especially when information is extracted in the first melting cycle. In addition, the thermal contact area between the sample and the pan will change as the test progresses. In the current study, the specimen used was a powder that promotes the best contact area. Consequently, the DSC thermal sensors detected consistent peaks for the on-heating stage. However, as the liquid metal cooled down, it has possibilities of spheroidal event occurred. This event significantly reduces the contact area.

Figure 93 shows the shapes of two specimens after the DSC test, which suggests the reason for the issue. The low contact area between the specimens and the DSC pan's bottom can lead to poor sensitivity of the heat flux sensor mounted underneath the pan. For the Co-29Cr-10Ni-7W alloy, the specimen's shape is half-spherical, which results in a very poor contact to the DSC pan's bottom. Regarding the Co-29Cr-6Mo sample, its shape is not as same as Co-29Cr-10Ni-7W sample; however, the thermal contact area with the pan is not that much.

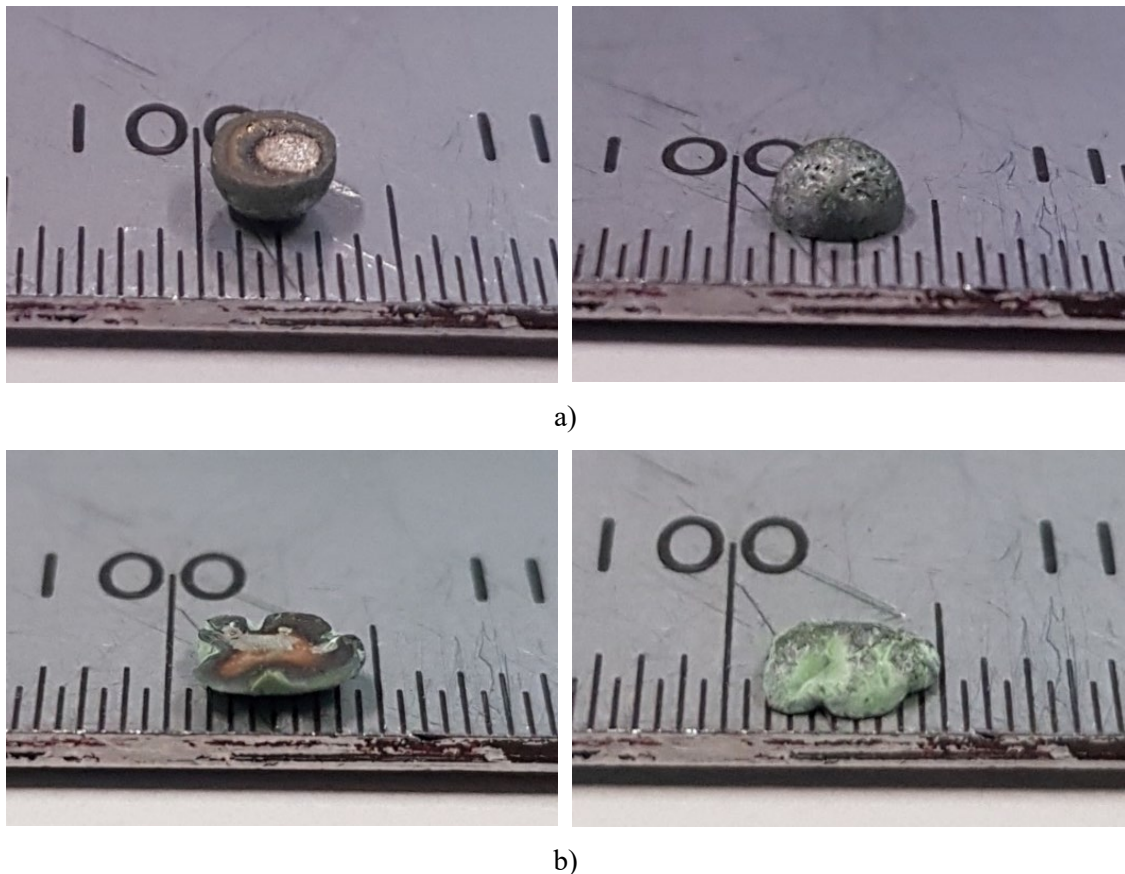


Figure 93. The specimens after DSC test: a) Co-29Cr-10Ni-7W alloy and b) Co-29Cr-6Mo alloy

Identification of solidification freezing range for the DSC on-cooling curves of Co-29Cr-10Ni-7W and Co-29Cr-6Mo alloys are unable to achieve. Therefore, it is reasonable to adapt reported results from the literature. Regarding Co-29Cr-10Ni-7W alloy, since the DTA thermal analysis results of Ronan's work [13] was extensively achieved on large scales of samples and shows

good agreement with another result from Kasala et al.'s work [14], thus the solidification freezing range of this alloy will be adapted from Konan's work [13].

For Co-29Cr-6Mo with low carbon content, it is challenging to acquire results from literature since there are limited works have been found. The carbon content should be considered when reviewing the alloy's solidification freezing range as it is a significantly influential factor, as shown in Table 4 [12].

Table 4. Influence of alloying elements on the melting temperature of Co-Cr alloys

Alloying elements	Melting temperature (°F)
<b>Raise</b>	
Tungsten	+1
<b>Lower</b>	
Nitrogen	-1
Iron	-1
Chromium	-5
Molybdenum	-8
Vanadium	-15
Manganese	-15
Aluminum	-20
Tantalum	-30
Zirconium	-30
Sulfur	-40
Titanium	-65
Columbium	-70
Silicon	-75
Boron	-115
Carbon	-120

Kurosu et al. [143] illustrated the equilibrium phase diagram of a Co-29Cr-6Mo alloy without carbon addition using Thermo-Calc software. It can be extracted from the phase diagram that the solidification freezing range is approximately 25°C. Zhao et al. [148] in their simulation work, the thermal properties of a Co-29Cr-6Mo alloy with 0.05 wt% C show liquidus and solidus temperatures at 1703K and 1623K, respectively. This means that the alloy's freezing range is 80K. Since the investigated Co-29Cr-6Mo alloy has carbon content less than 0.01wt%, it is expected that the solidification freezing range obtained from Kurosu et al.'s work [143] is more appropriate. Therefore, the solidification freezing range for Co-29Cr-10Ni-7W and Co-29Cr-6Mo alloys will be as below:

$$\Delta T'_{Co-Cr-Mo} = \sim 25 \text{ } ^\circ\text{C}$$

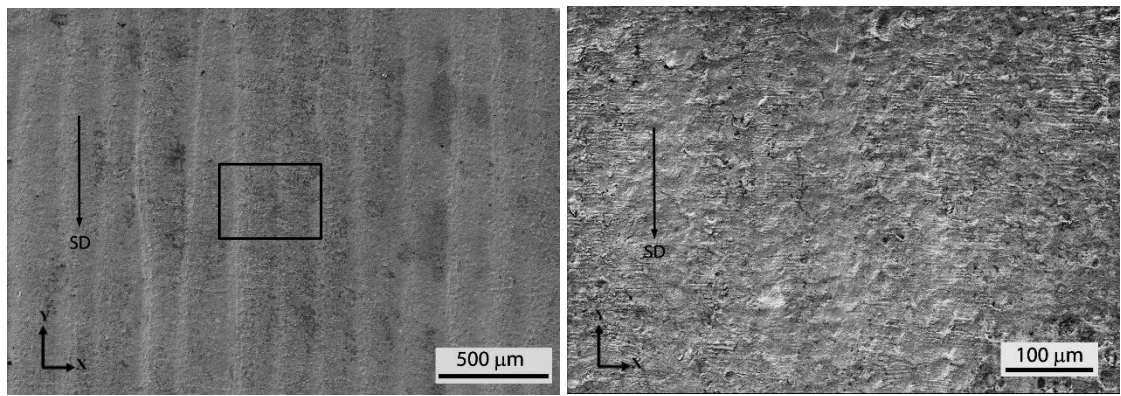
$$\Delta T'_{Co-Cr-Ni-W} = 150 \sim 180 \text{ } ^\circ\text{C}$$

## 4.2. Microstructure characterization of EB-PBF of Co-29Cr-10Ni-7W alloy

Solidification of the investigated alloy during EB-PBF is now presented regarding how process parameters resulted in the formation of scanned tracks, and solidified grain structures. The experimental parameters used were described in Chapter 3.

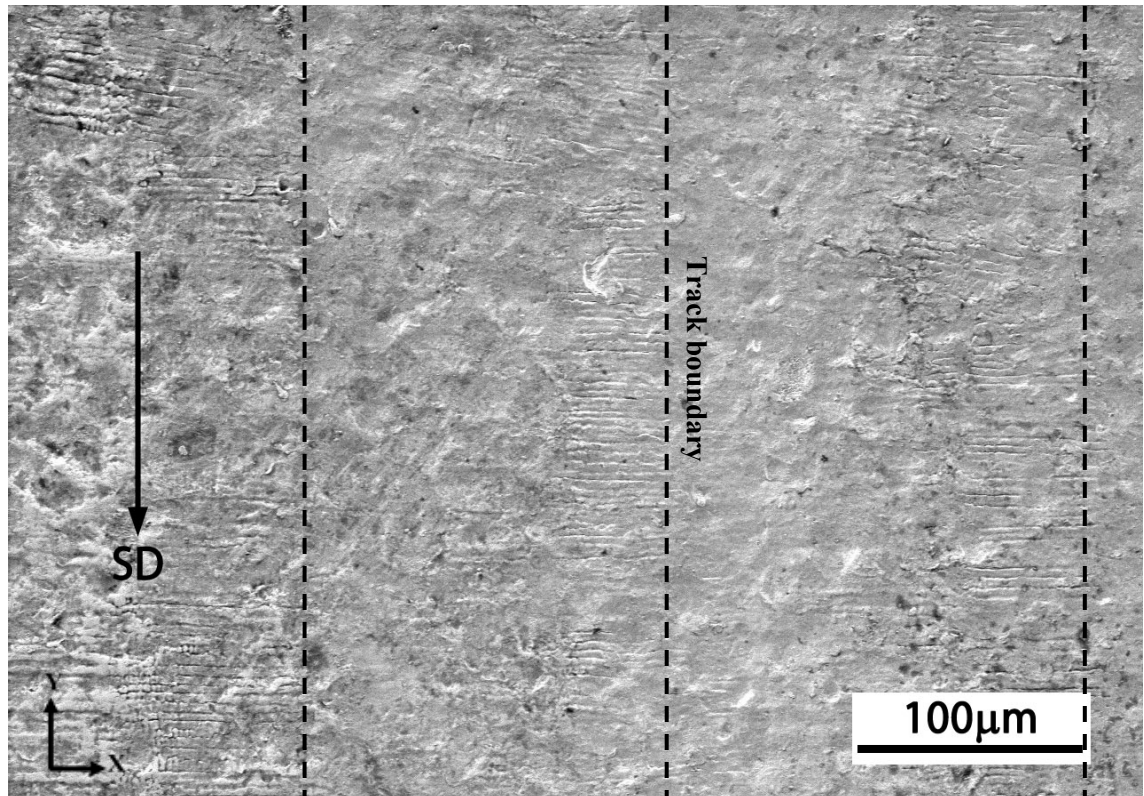
### 4.2.1. Observation of as-built samples

Figure 94 shows the surface of the FO25 sample. The surface image in Figure 94a displays clearly a wave-front appearance, suggesting that the melt is confined within the track being scanned. However, there is not clear tear-drop ripples observed. This suggests that the melt pool is a long melt track. In Figure 94b and Figure 94c, higher magnification of the surface shows that there are uncommon dendrites portion growing normal to the scan direction. These dendrites are only observed close to the track boundaries. During a beam scanning, the previous track can be heat-affected and areas that are in close proximity to track boundaries can be considered as the partial-melted-zone (PMZ). Therefore, the features observed in Figure 94b and Figure 94c may indicate re-melting of low melting phases (i.e. eutectic) at interdendritic regions has occurred. The following re-solidification incorporated with thermal shrinkage and was further exaggerated by EB-PBF rapid cooling rate provokes the interdendritic bridging; hence leaving traces of the re-solidified dendrites as seen in Figure 94c. The length of these dendrites may also indicate the effective length of PMZ within an individual track.



a)

b)



c)

Figure 94. SEM images showing: (a). The surface of FO25 sample; (b) and (c). Higher magnifications of the selected area in (a). Dendrites are seen growing normal to the track boundary

A surface image of a sample made with FO50 is shown in Figure 95. A clear feature is track boundaries (TBs) almost unrecognizable. In fusion welding, a tear-drop shaped melt pool advances thus leaving behind tear-drop ripples after solidification. EB-PBF is also a process of melting followed by solidification. In Figure 95a, ripples neither in the form of tear-drop shaped piled along the scan direction nor wave-front normal to scan direction are absent. This suggests that, locally in a track (n-1 track), the surface remained in liquid-state when the heat source melted the powder next in n track. This means the melt was not confined in the track being

scanned and instead the melt pool was multitrack wide. Moreover, there is no similar dendritic structure observed as the FO25 sample shown in Figure 94b. Higher magnification in Figure 95b shows a very smooth surface without any traces of partially solidified dendrites. This not only indicates the absence of track boundary and PMZ within each track but also shows that no remelting event had occurred as in the FO25 sample.

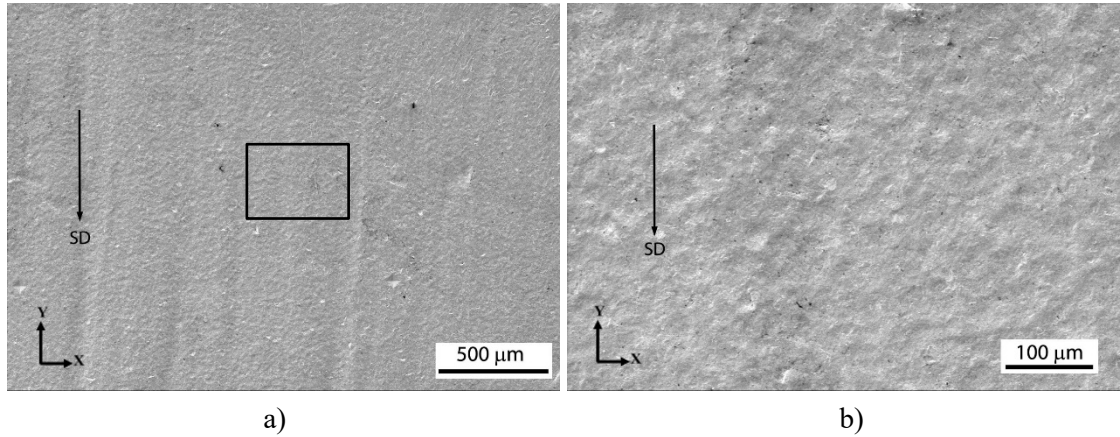
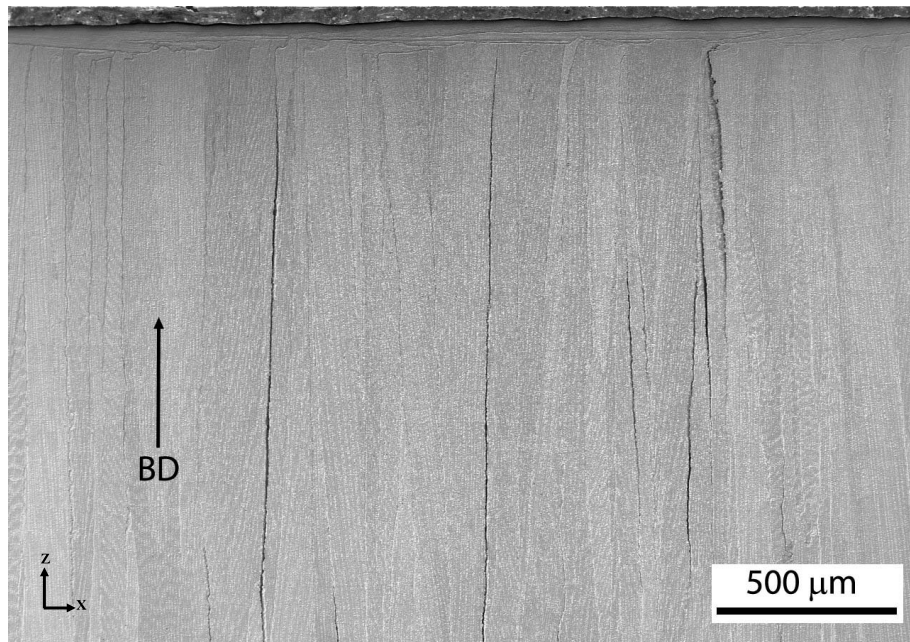


Figure 95. SEM images showing: (a). The surface of FO50 sample, (b). Higher magnification of the selected area in (a)

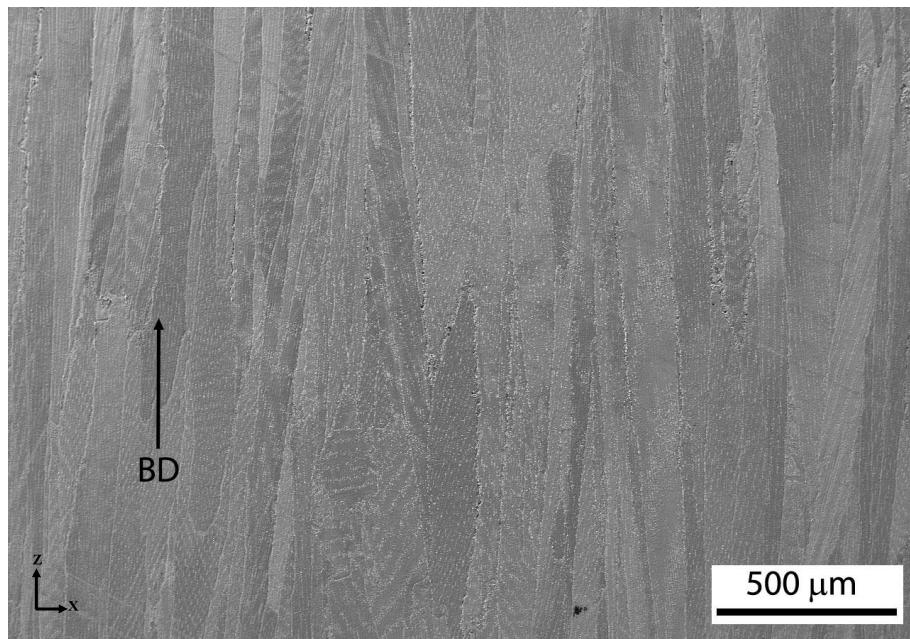
#### 4.2.2. Grain structures

Figure 96 shows cross-sectional SEM images of the FO25 sample from the bottom to the top surface. Typical columnar grains of EB-PBF are observed. There are also columnar grains that grow horizontally to the build direction. This interesting feature has been rarely observed in EB-PBF process. The thickness measured is up to 70  $\mu\text{m}$ , which is considerable as compared to the layer thickness of 70  $\mu\text{m}$ . These uncommon growth directions have a strong relationship to the melt pool geometry, which will be discussed in details in following chapter 4.3. Moreover, the grains structures appear differently along the build direction. Figure 96a and Figure 96b show the grain structure at the height of 1-3 mm from the block bottom and at the top surface, respectively. The grain shapes are observed changing significantly as the building height increasing, from a mixture of short and long columnar grains to almost very long columnar grains. This can be seen via the grain distributing density as 41 grains are counted in Figure 96a while it is 31 grains in Figure 96b.

Also in Figure 96a, cracks observed at columnar grain boundaries crossing many layers. However, all cracks were stopped from reaching to the top surface. The horizontal dendrites are seen as barriers to obstruct these cracks' continuation. On the other hand, it seems that no cracks can be pinpointed in Figure 96b.



a)

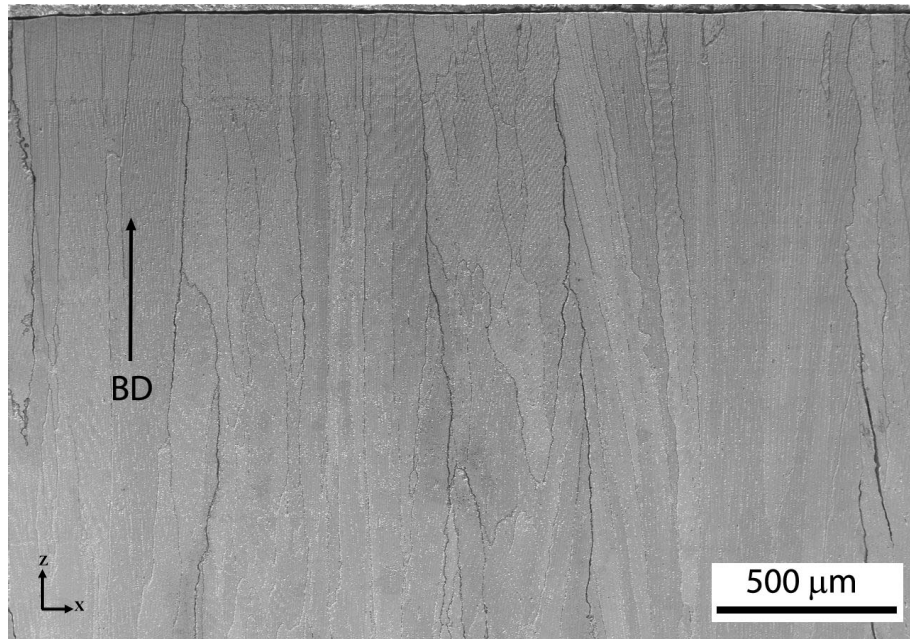


b)

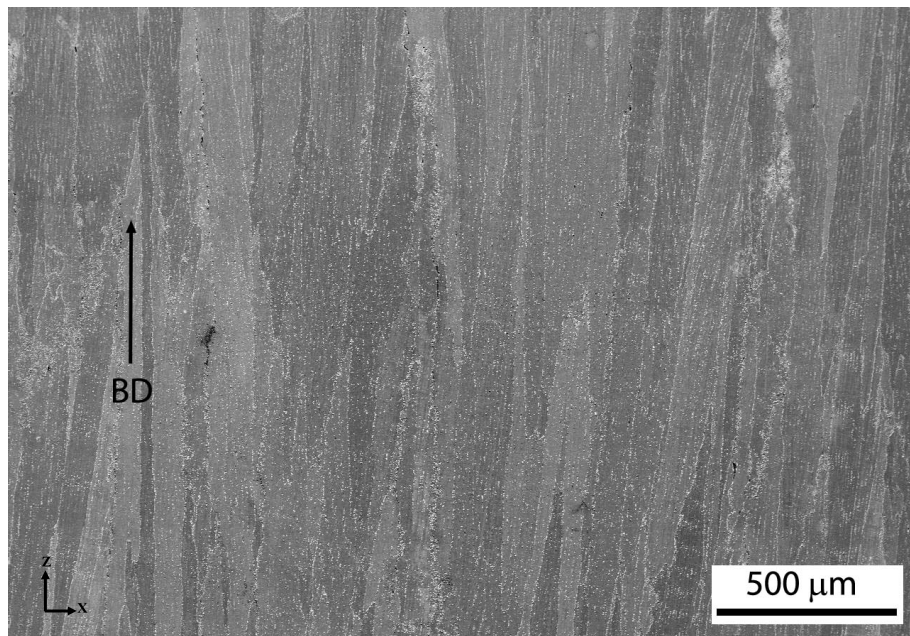
Figure 96. Cross-sectional SEM images showing the FO25 sample at (a). The upper part close to the top surface and (b). 7 mm away top surface downward. Cracks are seen at the upper part

Figure 97 shows the cross-sectional SEM images of the FO50 sample. Typical columnar grains structure is observed. However, horizontal dendrites are absent. In general, the grain structure observed from the top surface region and the bottom part is identical. Grains distributing density are counted as 40 grains and 36 grains, respectively. This is, however, different from that observed in the FO25 samples. The grains shapes in the FO50 sample are more uniform regardless of their locations.

It is also clearly seen that an extensive number of cracks in Figure 97a while they cannot be seen in Figure 97b. Since there are no horizontal dendrites, cracks can freely reach to the top surface. Despite that the two regions have similar grains distributing density, cracks are observed extensively in the upper part. This observation suggests that grain distributing density may not significantly obstruct cracking. Instead, thermal stresses may be less profound in the bottom part (1-3 mm) as compared to the upper part.



a)



b)

Figure 97. Cross-sectional SEM images showing the FO50 sample at (a). The upper part close to the top surface and (b). 7 mm away top surface downward. Cracks are seen at the upper part

#### 4.2.3. Correlation between grain structures and the used EB-PBF conditions

The final grain structures depend on the grain growth directions. These follow one of the <001> preferential crystallographic directions. In EB-PBF, the continuity or termination of grain is determined by how close its <001> crystallographic growth direction is aligned with the heat flux directions. The heat flux directions are normal to the melt/track boundary. This is because the thermal gradient  $G$  is at a maximum in these directions, thus the heat extraction is also at a maximum. However, the degree of heat extraction may not be uniform along the melt/track boundary, since it can be affected by the thermal conditions in EB-PBF. As has been previously demonstrated, the scanning speed  $v$  and the beam current  $I$  change along with the building height as a result of the SF algorithm. Moreover, the start plate temperature during EB-PBF has been shown to reduce as building height increases. Therefore, the thermal conditions during EB-PBF may also change along the build direction. This will be clarified by analyzing the log file of the EB-PBF build. How the EB-PBF thermal conditions change will be then investigated to correlate with the observed grain structures. In addition, observation of un-cracked and cracked regions between the top and bottom of parts will be discussed.

The process data were recorded by the machine log files. It shows that the scanning speed  $v$  and the beam current  $I$  are same for the FO25 and the FO50 samples as the same SF value of 25mA was used. The line energy  $E_{line}$  is restated again:

$$E_{line} = U.I / v$$

The  $E_{line}$  was used to evaluate the effect of EB-PBF parameters.  $U$  is the accelerated voltage of 60 kV,  $I$  is the beam current and  $v$  is the scanning speed. The block starts building after 3mm of support above the start plate. Figure 98 plots out the change in scanning speed  $v$ , beam power  $I$  and line energy  $E_{line}$  with respect to the blocks' height (from 3 mm to 13 mm). The beam velocity was around 1981 mm/s at the building height of 3mm and slowed down to approximately 500 mm/s at the final layer at 13mm height. In contrast, the line energy curve starts at approximately 0.2 J/mm and increases to 0.8 J/mm, respectively. Both scanning speed  $v$  and line energy are observed to be more stable from a 6mm height. As can be seen, the change in line energy and scanning speed is coincident with the change in grains structure (for the FO25 sample) and the un-cracked/cracked regions (for both samples).

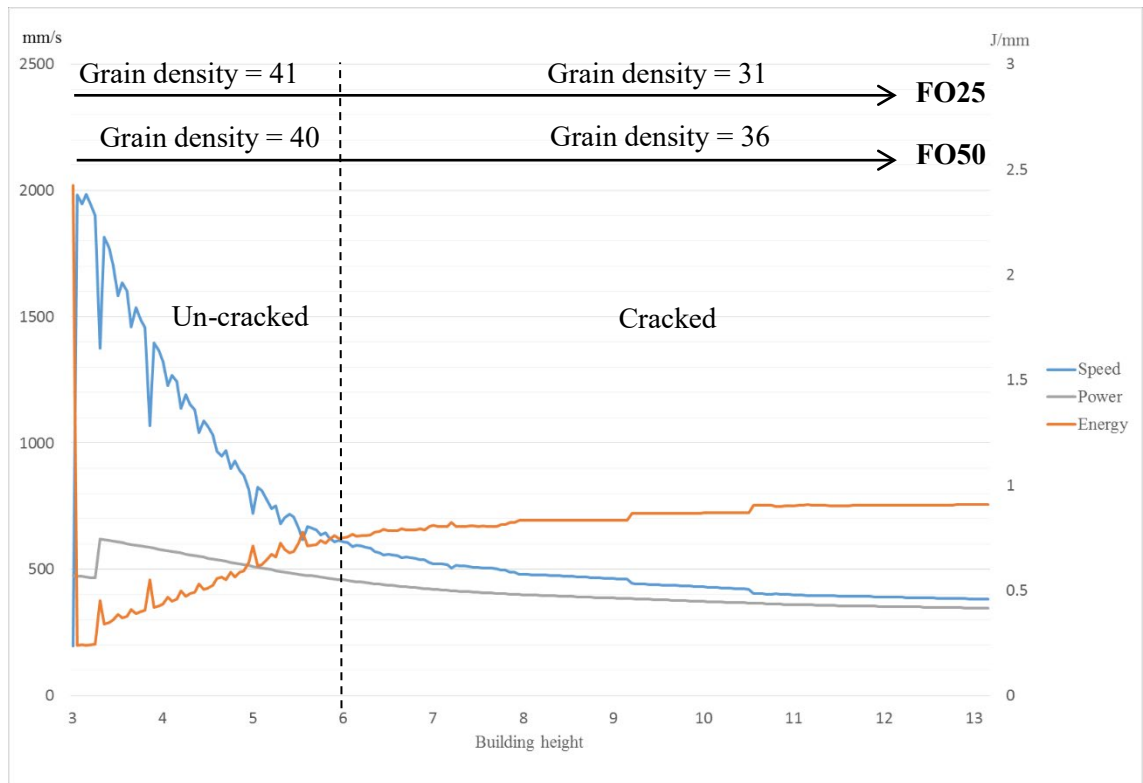


Figure 98. Recorded data of  $v$ ,  $I$  and the calculated  $E_{line}$  along the build direction

The temperature history of the start plate of the build is also demonstrated in Figure 99. The start plate was at the highest temperature of around 950 °C when the build started and slightly reduced to 790 °C at the end of the build (13mm height). As has been previously described in chapter 1.2, EB-PBF process has one preheat stage at the very beginning to heat up the start plate and a preheat step during every layer hatching. These two preheat stage and step employs a defocused beam which rasters at very high speed for a number of times (so-called repetition number). Smith et al. [132] showed that alteration of the repetition number can affect the preheat energies, which may affect start plate temperature. The initial preheat temperature has significance in establishing heat conduction into the bed and getting all components hot. However, the preheat step at every layer can be changed during building. Therefore, the log files have been checked regarding the repetition numbers during the preheat steps. However, it is unable to obtain the data as the log files show no record. The system shows only one default value of repetitions that had been preset throughout the process. Thus, it is unable to clarify whether or not the Arcam A1 system has any temperature compensation function. As the start plate temperature drops from 950 °C to 790 °C during EB-PBF, it is suggested that there may not have extra heating steps, otherwise, it is not so effective.

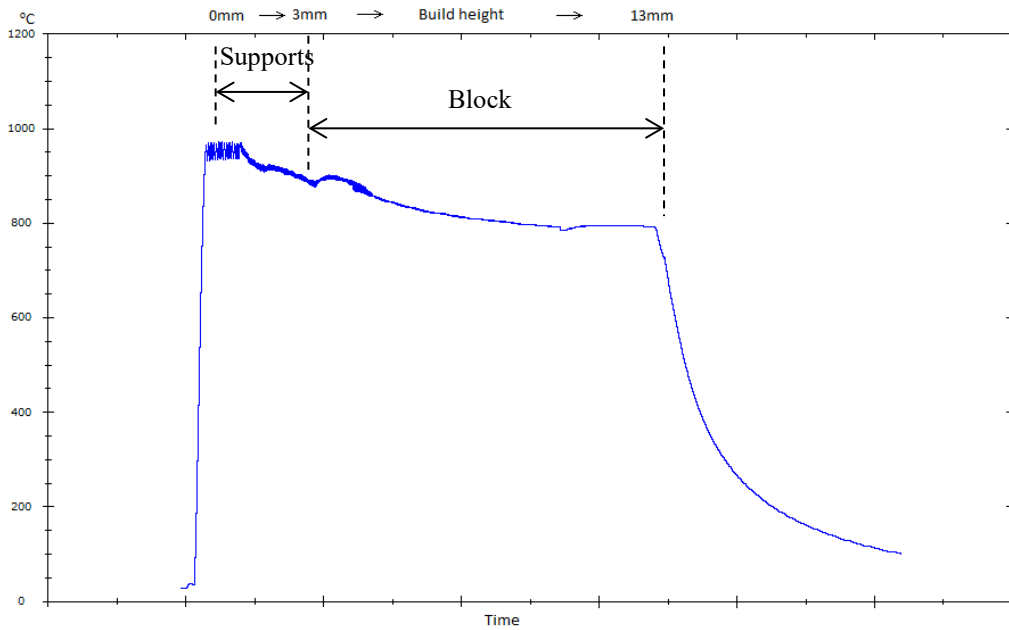


Figure 99. The temperature history of the start plate versus the building height

The grains structure also depends on the heat flux directions which are normal to the melt/track boundary. Therefore, the melt/track boundary in FO25 and the FO50 samples will be traced back to visualize how this occurs. Figure 100 illustrates the melt/track geometries in ZX cross-sections of FO25 and the FO50 samples obtained at the last layer of melting by using the optical microscopy (OM) images. The light reflection of the OM reveals the overlapped track boundaries from which the rest of the melt boundary is extrapolated.

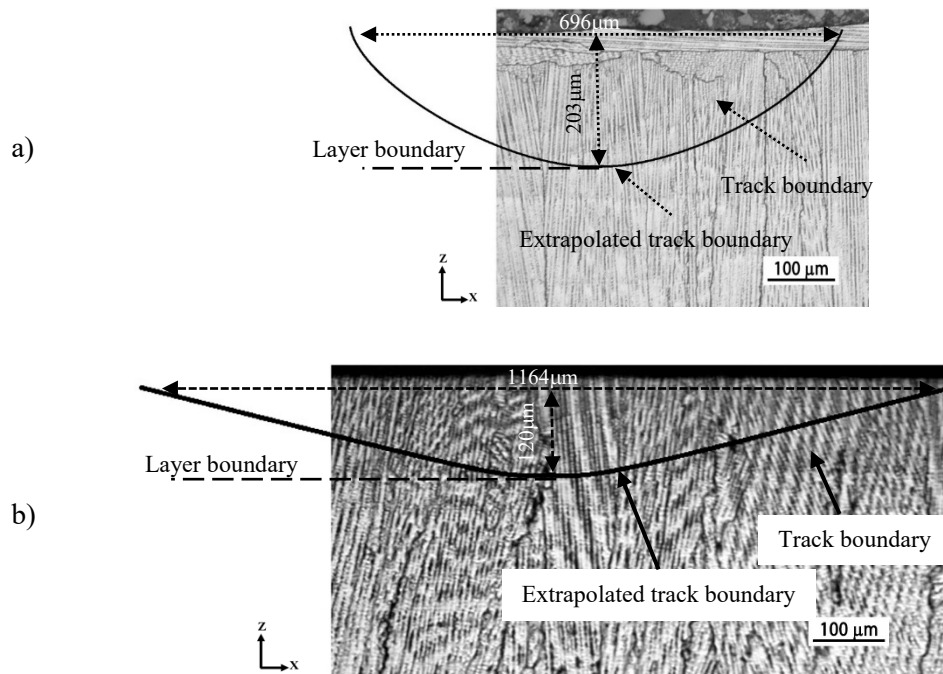


Figure 100. Extrapolated melt/track geometries of (a). the FO25 sample and (b). the FO50 sample. Layer boundary can also be identified

The aspect ratio  $AR = width/depth$  is again used to evaluate the melt/track boundaries obtained from the two samples. For the FO25 sample, the  $AR \approx 3.4$  while it is 9.7 for the FO50 sample. Clearly, the melt/track of FO25 can be seen to be deeper and narrower than that of the FO50 samples. Higher  $AR$  means the melt/track boundary of the FO50 sample is less curved, which leads to the heat flux directions being more aligned to the build direction (Z-axis).

The change of line energy  $E_{line}$  and the drop of start plate temperature ( $T_{start-plate}$ ) during the build can affect the domination of heat flux directions. Figure 101 schematically illustrates how all of the factors including  $E_{line}$ ,  $T_{start-plate}$  and the melt/track  $AR$  affect the heat flux directions, and then the grain growth during an EB-PBF build.

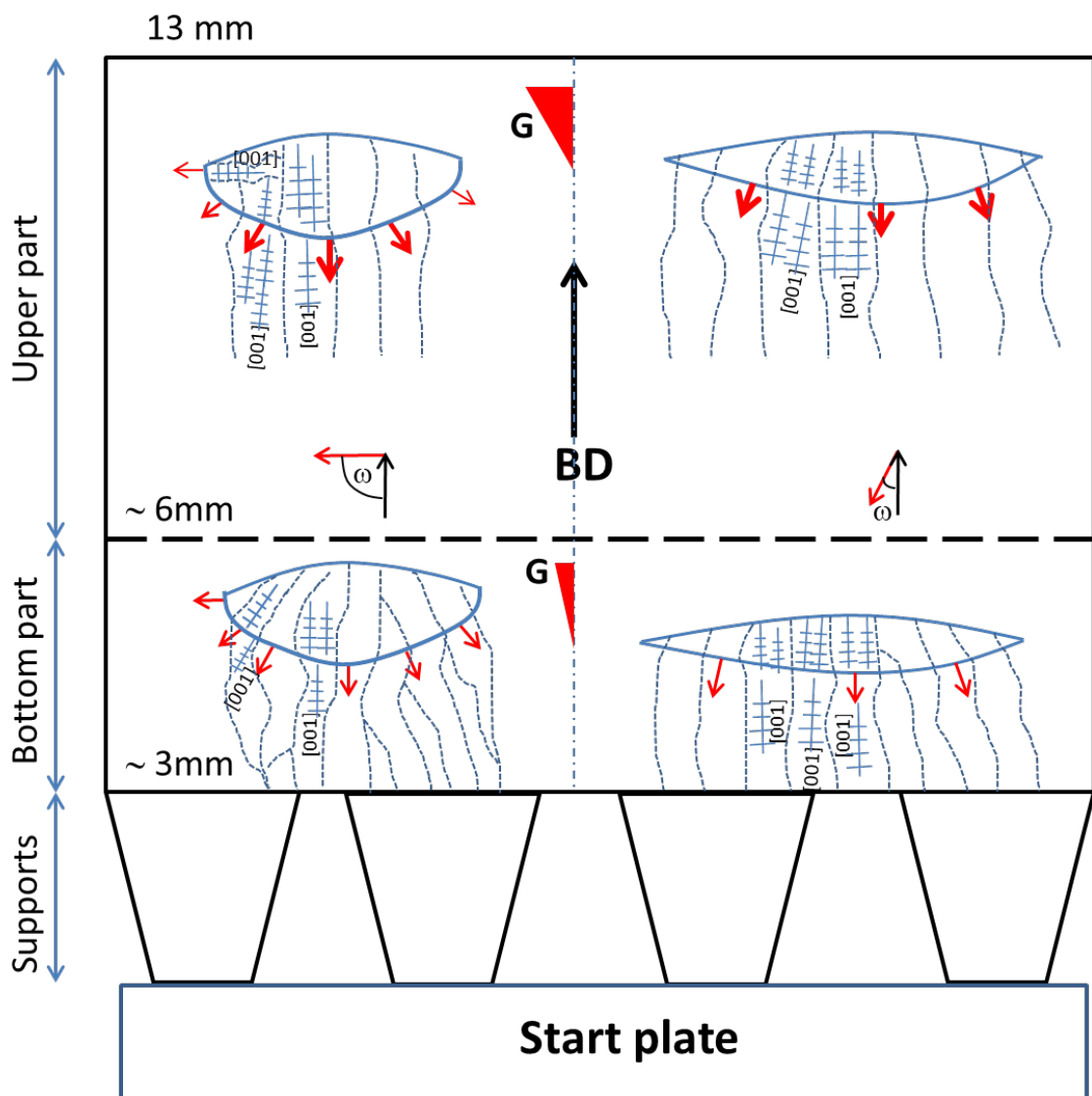


Figure 101. Schematic illustration of the change in grains structure following the change in the thermal gradient along the build direction. Melt/track geometries can be seen to have a significant effect on heat flux directions.

At the bottom part 3mm to 6mm, the high  $T_{start-plate}$  (900~950 °C) and the low  $E_{line}$  (0.2~0.6 J/mm) resulted in a small thermal gradient  $G$ , as illustrated in Figure 101. This small  $G$  leads to the heat transfer around the melt pool being more uniform, and the heat flux is identical in all directions. Grain growth will follow the <001> crystallographic direction that is closely aligned with the heat flux directions. As the FO25 sample has low melt/track  $AR$ , the angle  $\omega$  (defined by the heat flux direction and build direction) can range from  $0^\circ$  (aligned with build direction)  $< \omega < 90^\circ$  (horizontal heat flux direction). For the FO50 sample, the range of  $\omega$  is much lower, ranging from  $0^\circ < \omega < 20^\circ$  since the melt/track  $AR$  is much higher as compared to the FO25 sample. Therefore, within the first 3mm, grains are able to grow in a range of directions in FO25 compared with the FO50 sample.

As the building height increases from 6mm to 13mm,  $T_{start-plate}$  drops gradually to 790°C (at 13mm) while  $E_{line}$  increases to 0.8J/mm. This results in an increased thermal gradient which consequently enhances heat flux along the build direction. Thus, for the FO25 sample with a wide range of  $\omega$ , grain growth will start to favor those heat flux that is more aligned with the build direction. In contrast, the shallower and wider melt pool of the FO50 sample results in heat flux directions more or less aligned with the build direction regardless of the building height and thus the thermal gradient degree. Therefore, grains structure observed in the FO50 sample is identical throughout the building height.

The difference in grain structure along the build direction was observed by Chauvet et al. [113, 120] and shown in Figure 46 and Figure 48. In their study [113], the authors showed that the grains are small in size (grain width from 30~150  $\mu\text{m}$ ) with a random orientation at the first 10mm build height. Then, for the final 20mm, grains increase in size and become more oriented along the build direction. In their study [120], the authors aimed to achieve a single crystal structure by using several  $E_{line}$  from 0.3 to 0.6 J/m. At  $E_{line} = 0.3$  J/mm, grains are identical in width  $\approx 100$   $\mu\text{m}$  throughout the building height. In contrast, at  $E_{line} = 0.45$  J/m, grains' width is small at the bottom (0~5 mm) and increases up to several millimeters at the upper part (5~20 mm). This observation by Chauvet et al. shows that the effect of  $E_{line}$  is in good agreement with the analysis made in this study. Increasing of  $E_{line}$  and a potential drop in  $T_{start-plate}$  will impose larger thermal gradient  $G$  which may enhance the heat flux along with the build directions. Furthermore, the thermal conditions can be used to explain why cracks are not observed at the bottom part. The low  $G$  will result in lower thermal stresses. In addition, higher grain boundary density at the bottom part increases the cracking resistance. Again, Chauvet et al. [113, 120] observed similar cracking in their EB-PBF Ni-based alloys. Cracks are shown to appear in the upper part while no cracks are observed at the bottom part.

### 4.3. Solidification microstructure and cells/dendrites-growth directions in EB-PBF of Co-29Cr-10Ni-7W alloy

#### 4.3.1. Solidification microstructure

Figure 102 demonstrates the microstructures observed in the last layer of FO25 and the FO50 samples. This is the region to last solidify and receive the least homogenization effect in EB-PBF. Thus, the microstructure analyses can reflect more the actual situation of the solidification process. The examined locations will be at the layer boundary, the middle and near the top surface. Horizontal dendrites can be seen for the FO25 sample. This distinctive feature will then be discussed in the following sub-sections. The layer boundary is identified by comparing the same location under optical microscopy (as in Figure 100 of the previous section) and highlighted by the dash lines. Higher magnification SEM images of related locations are also presented in Figure 103 and Figure 104.

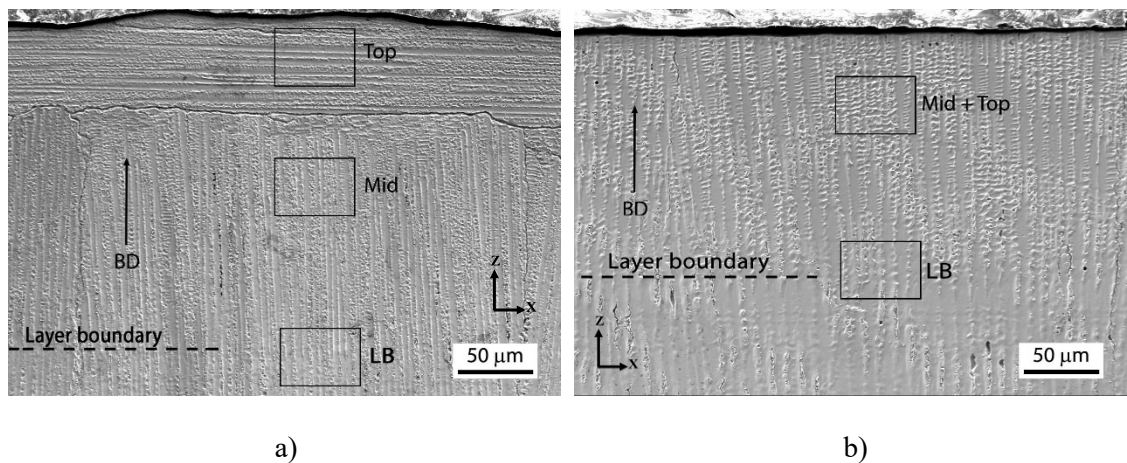
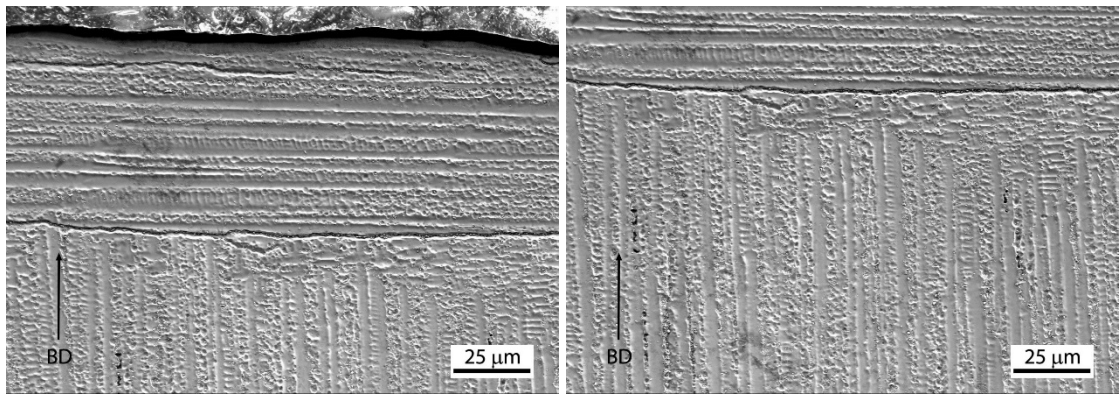


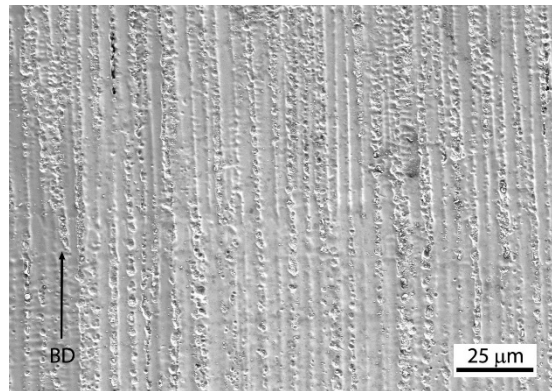
Figure 102. SEM images showing solidification microstructure in the last layer of (a). FO25 sample and (b). FO50 sample. Locations are selected for further examination.

Epitaxial grain growth can be observed at the layer boundary in both samples. The solidification morphology is cellular and dendritic growth for the FO25 sample while it is columnar-dendritic for the FO50 sample. As can be seen in Figure 103 for the FO25 sample, the cellular growth starts to branch out the secondary dendrite arms at the middle of the layer up to the horizontal grain where it is difficult to identify the solidification modes (Figure 103a and Figure 103b). However, evidence of secondary dendrite arms can be traced although they may be confused with the artificial over-etched features. For the FO50 sample, the secondary dendrite arms are clearer in shape as growing further away from the layer boundary to the top surface (Figure 104a). Moreover, the branching direction is observed toward to the left which is the direction of track scanning.



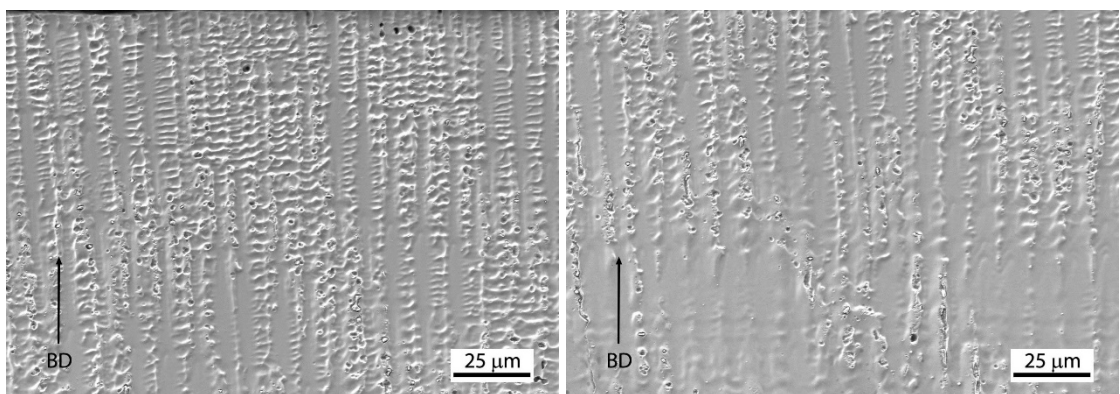
a)

b)



c)

Figure 103. SEM images showing higher magnifications of selected areas in Figure 102a: (a). Top, (b). Mid and (c). Layer boundary



a)

b)

Figure 104. SEM images showing higher magnifications of selected areas Figure 102b: (a). Top and (b). Layer boundary

The observation on cellular-dendritic to more dendritic growth morphologies from the layer boundary to the top surface can be suggested due to the change in local thermal conditions. The ratio  $G/R$  (thermal gradient/growth rate) determines the growth morphologies. At the start of solidification, due to the difference between the previously built solid and liquid temperature ( $\sim 900\text{ }^{\circ}\text{C}$  and  $\sim 1400\text{ }^{\circ}\text{C}$ , respectively); the local thermal gradient will be at the maximum value

and the solid-liquid interface velocity will be at the slowest. Consequently, this high G/R ratio favors for cellular growth. Toward the end of solidification, as the heat has been evenly distributed throughout the solidified solid, the thermal gradient will reduce and the growth rate increases. This low G/R ratio then promotes more dendritic growth morphology.

An attempt to estimate a link between the observed solidification modes to thermal conditions during EB-PBF process is now made. The FO50 sample has been selected for conducting the estimation due to its crystallographic orientation being highly <001> oriented (Figure 105). The primary dendrite trunks are observed to be closely aligned with the heat flux direction, which is normal to the melt pool boundary. Therefore, it is reasonable to apply Eq. 9 which derived by Kurz and Fisher [17] on the relationship between primary arm spacing, thermal gradient (G) and solidification rate (R):

$$\lambda_1 = 4.3 \frac{(\Delta T_0 \cdot D_L I)^{0.25}}{k^{0.25} R^{0.25} G^{0.5}}$$

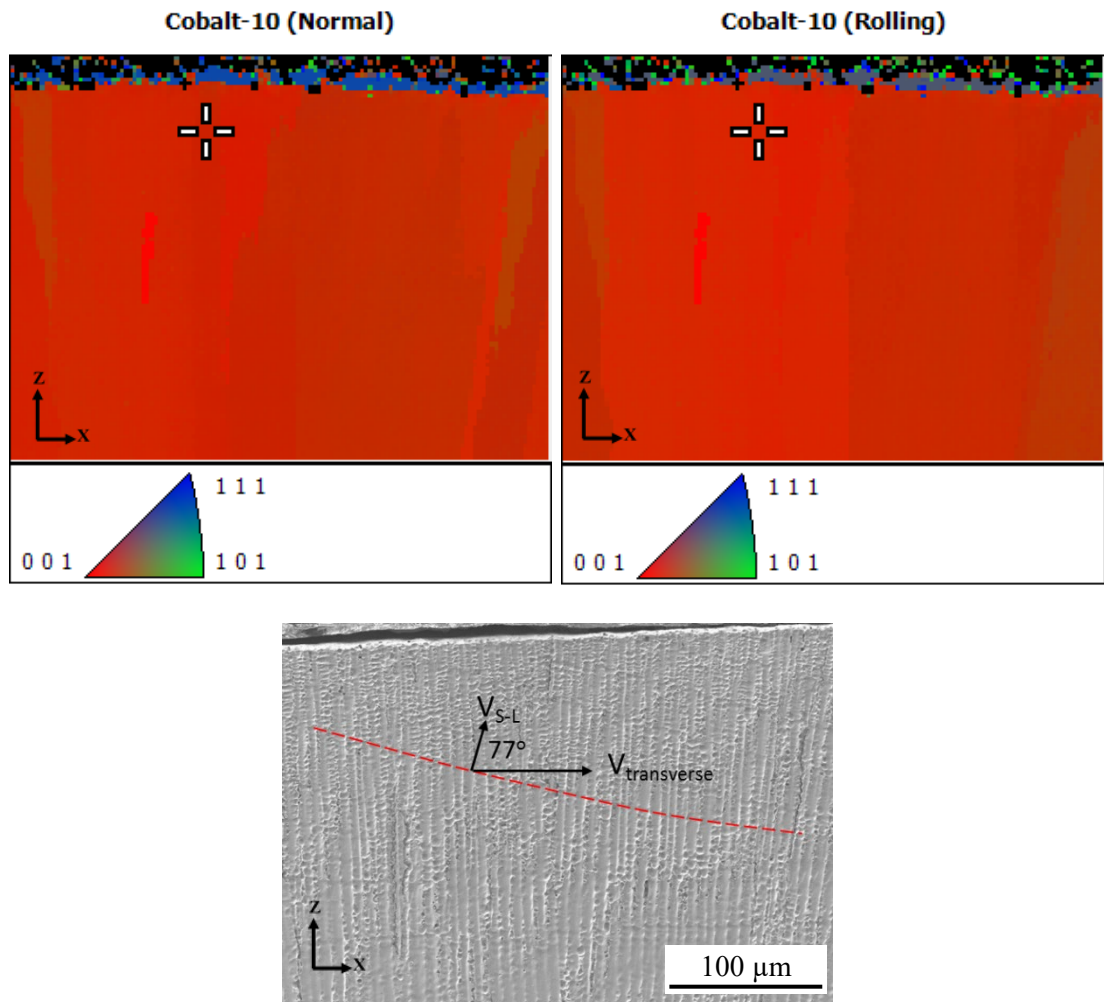


Figure 105. EBSD map and corresponding SEM image showing crystallographic orientation near the top surface of the FO50 sample. The images were obtained in the XZ cross-sections

As previously suggested in chapter 4.2.1 for the FO50 sample, the surface of the track (n-1) may remain in liquid-state when the beam scans track n. Thus, the melt pool is multitrack wide. This results in the velocity of the solid-liquid interface will depend on the transverse velocity, as shown in Figure 105. The sample width is 20 mm. The line offset value is 0.1 mm. The track width is approximated at 1.2 mm from the extrapolated melt pool geometry in Figure 100. The hatching time for the last layer is 9.74 s obtained from the EB-PBF log files. Thus, the number of tracks of one layer, time to finish one track (for the last layer) and the transverse velocity can be figured out:

$$\text{The number of tracks/layer: } \frac{20\text{mm} - 1.2\text{mm} - 0.1\text{mm}}{0.1\text{mm}} = 187 \text{ tracks}$$

$$\text{Time to finish one track} = 9.74\text{s} / 187\text{tracks} = 0.052\text{s}$$

$$V_{\text{transverse}} = 0.1\text{mm} / 0.052\text{s} = 1.923 \text{ mm/s}$$

$$\text{Thus, } V_{\text{S-L}} = V_{\text{transverse}} \cdot \cos 77^\circ = 0.433 \text{ mm/s}$$

The estimation of  $V_{\text{transverse}}$  is made over the line offset distance = 0.1 mm. This means when track n is scanned, the solid-liquid interface has moved a distance of 0.1 mm in track (n-1). However, in a practical situation, it is unknown how far the solid-liquid interface has advanced in track (n-1) when the track n is scanned. The difficulty, but still possible in identifying the track boundaries in the FO50 sample suggests that the solid-liquid interface did advance more than the distance of line offset = 0.1 mm. Therefore, the estimated value of  $V_{\text{S-L}}$  can be larger.

The primary dendrite arms spacing  $\lambda_l$  is measured by using XY cross-sectional SEM images (Figure 106). The respective EBSD images are obtained to ensure the measured dendrite trunks are most aligned with [001] crystallographic orientation. This is important since unaligned dendrite trunks to [001] direction can result in elongated dendrite trunks' cross-section that leads to improper measurement of  $\lambda_l$ . The primary arms appear as in round-shapes with a few of those are slightly elongated. In order to ensure the minimum of artificial errors caused by the measurement, 27 locations were selected for the measurement. Each location comprises of a row of six to eleven primary arms. The average  $\lambda_l$  measured is 5.471  $\mu\text{m}$ .

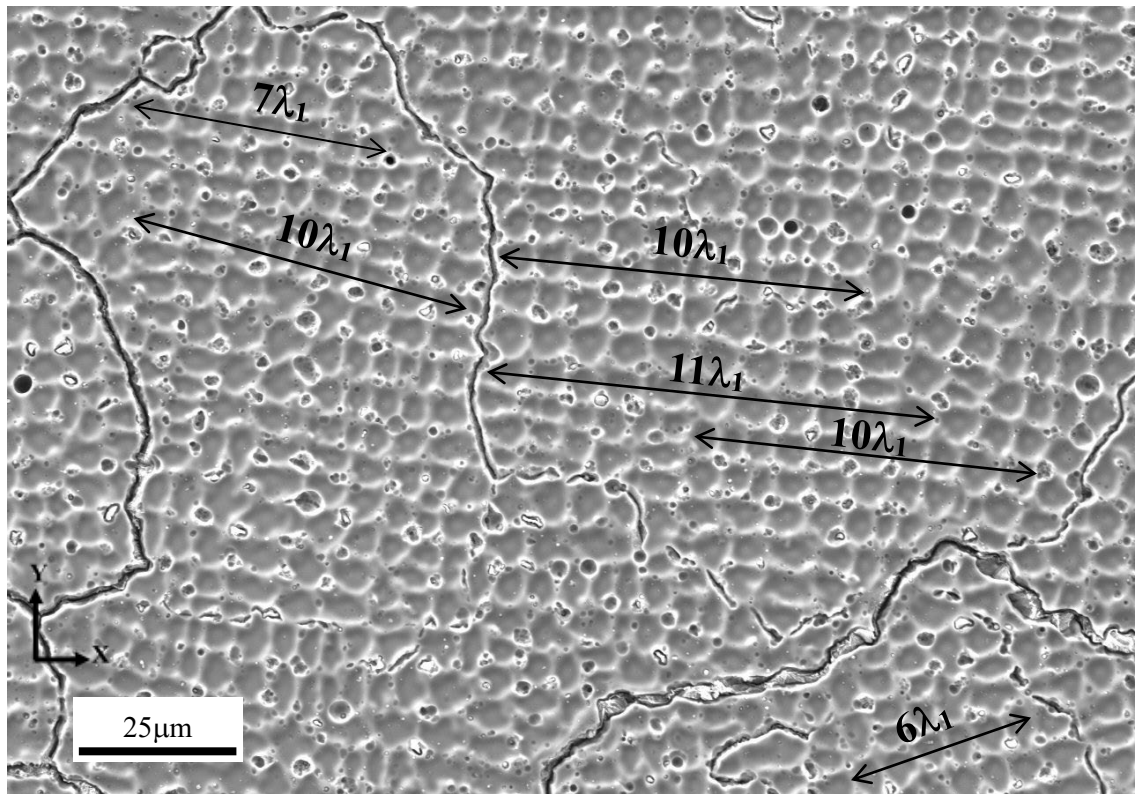


Figure 106. Illustration of how the average value of  $\lambda_1$  is obtained by using SEM image in XY cross-section

Since it is unknown for Co-29Cr-10Ni-7W alloy related to other variables required in Eq. 9, thus these variables are adapted from [41] for a Co-Cr alloy and shown as below:

Non-equilibrium solidification freezing range	$\Delta T_o = 180\text{K}$ [13]
Equilibrium partition coefficient:	$k \sim 0.808$
Gibbs-Thompson coefficient:	$\Gamma = 2.10^{-7} \text{ mK}$
Liquid diffusivity:	$D_L = 10^{-9} \text{ m}^2\text{s}^{-1}$

Eq. 9 thus will be:

$$5.471 \times 10^{-6} = 4.3 \left( \frac{180^\circ\text{C} \cdot 10^{-9} \text{ m}^2/\text{s} \cdot 2 \times 10^{-7} \text{ Km}}{0.808} \right)^{0.25} (4.33 \times 10^{-4})^{-0.25} \cdot G^{-0.5}$$

Thermal gradient  $G = 6.26 \times 10^6 \text{ K/m}$

Cooling rate  $\dot{T} = G.R = 6.26 \times 10^6 \text{ K/m} \times 4.33 \times 10^{-4} \text{ m/s} = 2710.58 \text{ K/s}$

As previously discussed,  $V_{S-L}$  or  $R$  is assumed to be at the minimum value as compared to a real situation. Therefore, the value of  $G$  and  $\dot{T}$  can be considered as an overestimation. This means that, in a practical situation,  $R$  can be larger, thus  $G$  should be lower. The estimation of  $G$  will be experimentally achieved later then in chapter 6.

Since  $G$  and  $R$  are now estimated, the relationship between  $G$ ,  $R$  and the solidification modes observed in EB-PBF Co-29Cr-10Ni-7W alloy is now clarified by using Eq. 10 (conditions for cellular/dendritic growth):

$$\frac{G}{R} < \frac{\Delta T_0}{D_L}$$

Thus:

$$\frac{6.26 \times 10^6 K/m}{4.33 \times 10^{-4} m/s} < \frac{180 K}{10^{-9} m^2 s^{-1}}$$

$$\Rightarrow 1.44 \times 10^{10} K.s/m^2 < 1.8 \times 10^{11} K.s/m^2$$

The Eq. 10 is satisfied. This is also confirmed by the dendritic growth observed previously. Therefore, the estimated values of  $G$  and  $R$  during EB-PBF Co-29Cr-10Ni-7W are reasonable. In addition,  $G$ ,  $R$  and  $\dot{T}$  are compared to the solidification map adapted from literature. Chen et al. [149] conducted a study on solidification of LB-PBF Co-29Cr-6Mo alloy. The authors estimated the  $G$  and  $\dot{T}$  of the LB-PBF process and correlated the results with the observed fine cellular solidification mode. The solidification map from the work of Chen et al. [149] is illustrated in Figure 107. The  $G$  and  $R$  during EB-PBF Co-29Cr-10Ni-7W fall into columnar dendrites region. As  $G$  and  $R$  are overestimated and underestimated, respectively, thus it is expected that solidification conditions during EB-PBF will orientate more toward the columnar dendrites region, as indicated by the red arrow in Figure 107.

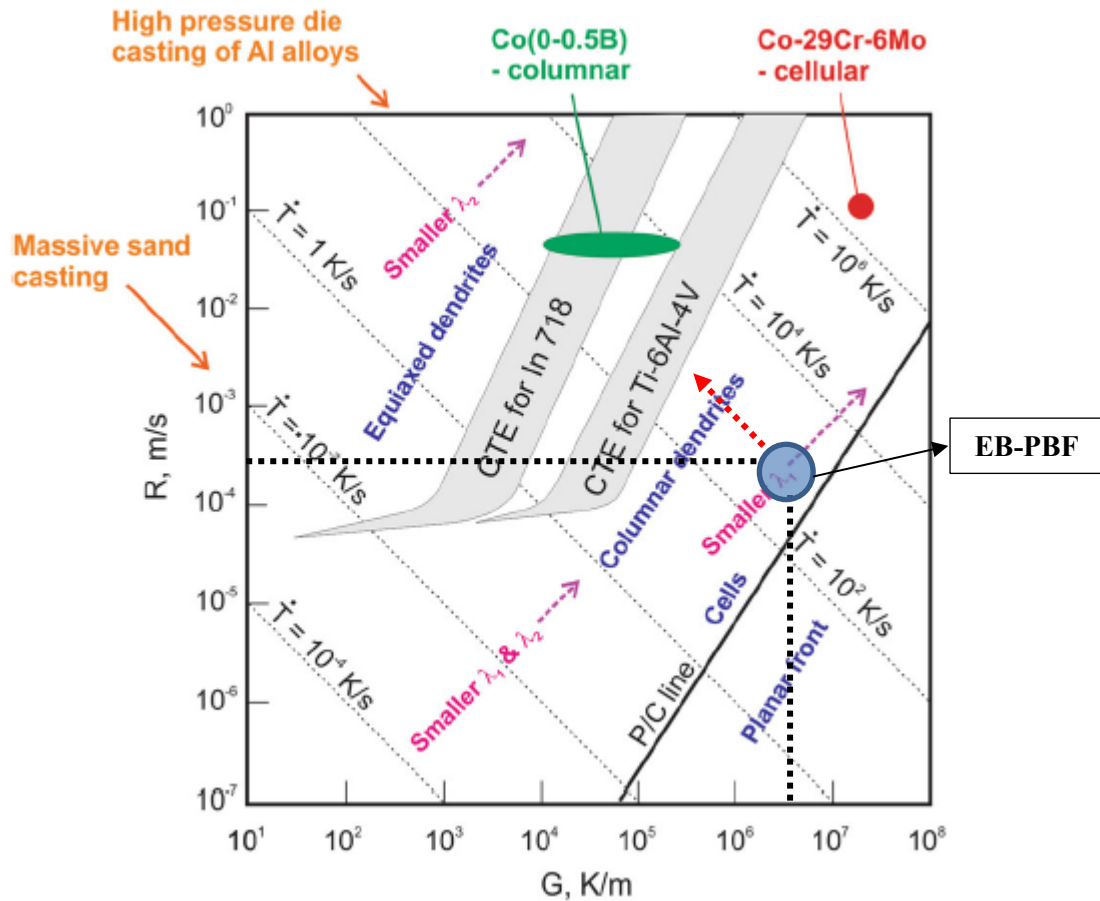


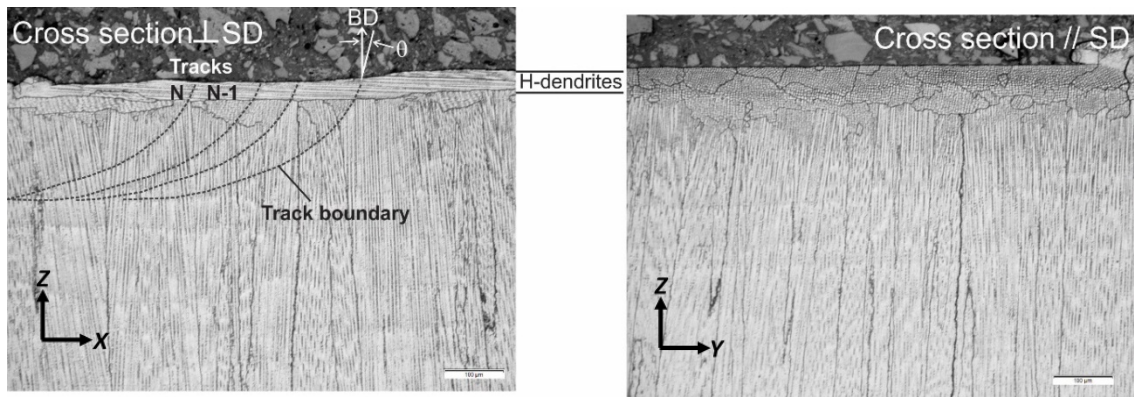
Figure 107. Solidification map for LB-PBF Co-29Cr-6Mo alloy and several metallic alloys (adapted from [149])

#### 4.3.2. Effect of focus offset values on formation and geometry of the scanned track

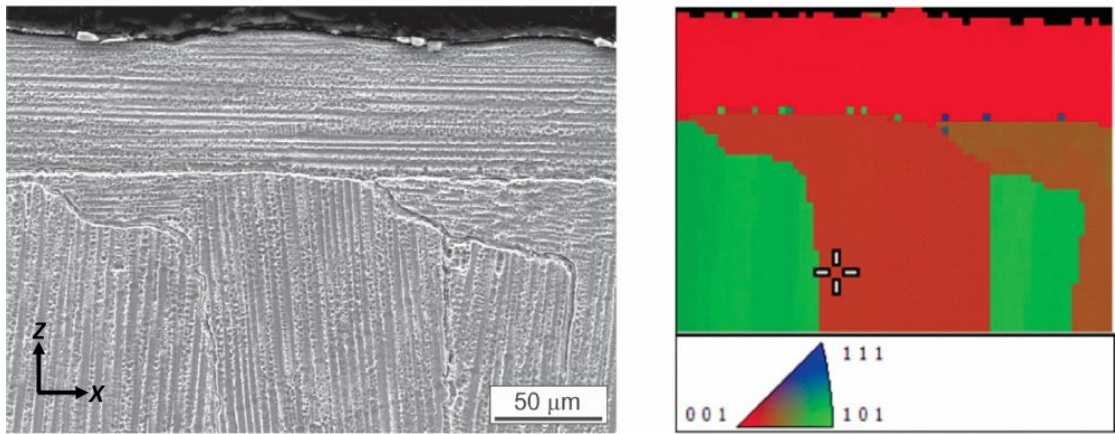
As previously discussed in chapter 2, grain growth directions changing was observed in many studies on EB-PBF metallic alloys [23, 36, 68]. Specifically, Helmer et al. [21] observed an additional feature of grain growth normal to the build direction and in the top region. However, no further analytical evidence relating to this was provided. The feature's thickness is 50  $\mu\text{m}$  is significant as compared to the EB-PBF layer thickness of 50~70  $\mu\text{m}$ . Surprisingly, in the comprehensive reviews of EB-PBF, the referred growth feature has not been noted and discussed. In this study, the horizontal growth feature is also observed and shown in chapter 4.3.1. The following section will be dedicated to analyze and discuss more in-depth in regards to this growth feature.

Figure 108 shows the cross-section OM images and crystallographic orientations near the top surface of the FO25 sample. Track boundaries (TBs) are highlighted by dashed lines in Figure 108a, curving considerably towards the surface. Hereby, the  $\theta$  angle is defined as the angle between build direction and the tangent line to the track boundary at the meet point with the top surface. In Figure 108a,  $\theta$  is measured at approximately 15°. This low  $\theta$  value must be the result

of a lateral heat transfer dominant. Consistent with this are the dendrites in the top layer of 50-80  $\mu\text{m}$  grown largely horizontally. Figure 108b clearly shows the horizontal dendrite (H-dendrite) layer in a complete different  $\langle 100 \rangle$  direction to all the vertically grown dendrites below.



a)



b)

Figure 108. a) Optical micrograph of cross-sectional view and (b) SEM image and EBSD orientation map showing the horizontal dendrite layer up to  $\sim 80 \mu\text{m}$ .

A cross-sectional image of the FO50 sample is shown in Figure 109. In this image, TBs can hardly be recognized. In the same view under a microscope in a slightly out of focus condition, TBs can be identified and are indicated in Figure 109. The boundaries extending all the way to the surface are in a high angle ( $\theta \approx 80^\circ$ ) with respect to the build direction. Thus, columnar growth along the build direction was favorable even in and near the edge of the melt pool. This is because even at the surface location, TB is close to the direction normal to the build direction meaning that heat transfer should be dominantly in a direction directly opposite to the build direction. The crystal orientation of dendrite trunks is a  $\langle 100 \rangle$ . If  $\theta$  is not too small, the continuation of dendritic growth in the same  $\langle 100 \rangle$  direction should be favorable all the way to the track surface.

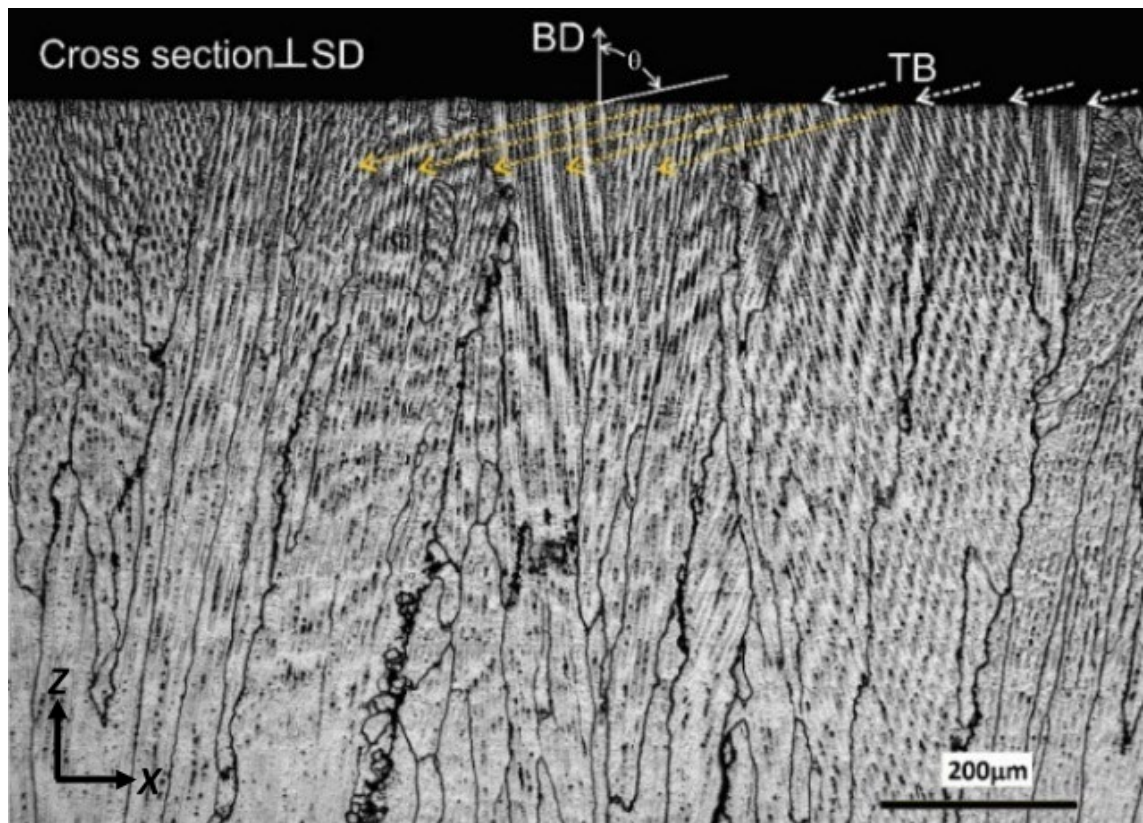


Figure 109. Optical micrograph of cross-sectional view displaying columnar dendrites grown completely along the build direction. Track boundaries are indicated.

#### 4.3.3. Melt/track geometries dependent cells/dendrites-growth direction

Further discussion can be made with the aid of an illustration in Figure 110. A track (track  $n$ ) overlaps the one before (track  $n-1$ ) considerably representing the actual tracks depositing shown in Figure 108a and Figure 109. This overlapping may be necessary for preventing a lack of fusion. As has been explained, the whole track  $n$  is in liquid-state. Track  $n-1$  can also be still in liquid-state during track  $n$  scanning, depending on EB-PBF condition. If track  $n-1$  is still in liquid form when the beam scans back during track  $n$  scanning, the overlap of tracks is a liquid mixture. The subsequent solidification should then leave almost no ripple on the surface. This is FO50 in Figure 109, represented as a wide and high  $\theta$  melt track in Figure 110 (lower left). For FO25, track  $n-1$  has solidified when the beam scans back in track  $n$ . The movement of the liquid in track  $n$  behind the beam as a wave rippling sideways and solidification of track  $n$  thus leaves the mark as a wave-front ripple. The growth of H-dendrites, same as vertically grown dendrites (V-dendrites), started at each TB as epitaxial growth. Near the surface region, low  $\theta$  means heat transferred out largely in the horizontal direction ( $Q_H$ ), as in Figure 110 (lower right), and epitaxial growth with a  $\langle 100 \rangle$  largely horizontally. This growth repeats track after track and thus long H-dendrites can be seen.

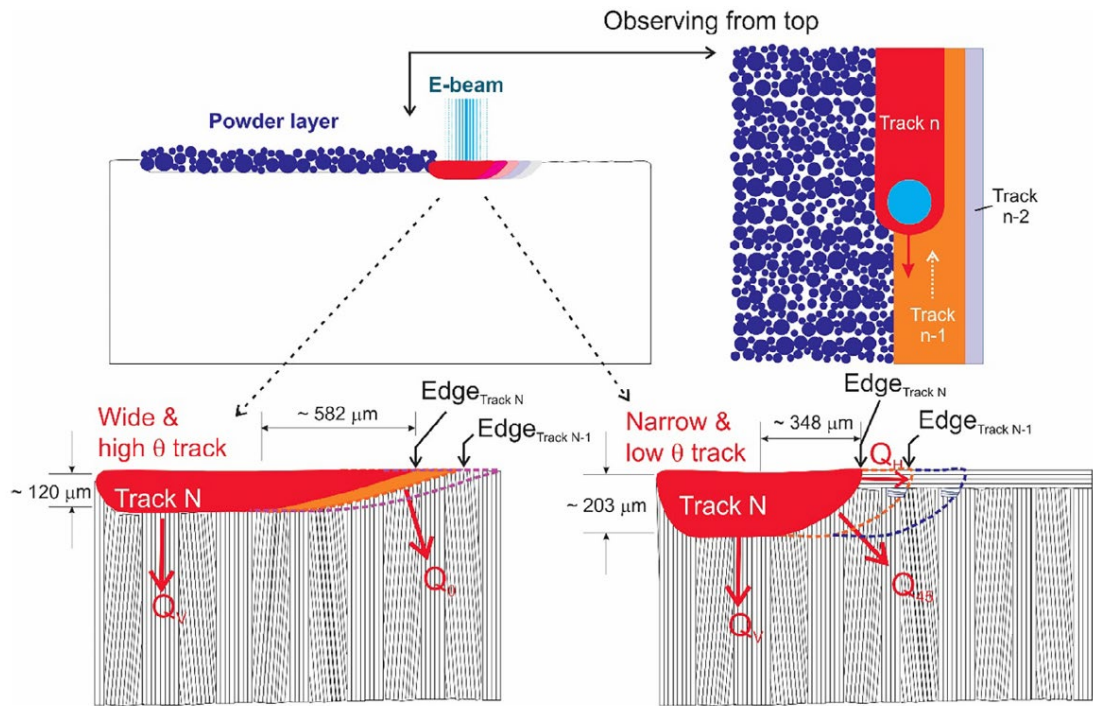


Figure 110. Schematic illustration of a melt track, colored red, during EB-PBF with heat flow direction normal to track boundary indicated.

With the same values of both speed function,  $SF$  and line offset  $h$ , samples built with FO25 and FO50 should be the same in beam energy. The difference is the used focus offset. The beam diameter of FO50 should be significantly larger than that of FO25. The less focused beam may still melt largely the same volume but the material to be melted is wider and thinner, meaning a larger aspect ratio ( $AR = 9.7$ ). On the other hand, a more focused beam should result in a deeper and narrower melt, meaning a more U-shaped track. The thickness of an H-dendrite layer up to  $80 \mu\text{m}$  is significant as EB-PBF layer thickness is  $70 \mu\text{m}$ . A melt pool/track of a more U-shape should result in a large portion of H-dendrites. The simple difference in focus offset and the resulting differences as illustrated in Figure 110 have suggested that grain growth control to avoid columnar growth dominantly in the build direction is possible. It is suggested that a highly focused beam to result in a small AR should result in a large portion of grain growth in direction considerably different to the build direction.

#### 4.3.4. Controlling/maintaining horizontal dendrites growth structure

With the observation of H-dendrites, it is indicative that the dominant columnar grain structure highly oriented to build direction can be altered. Thus in this research, a further attempt has been made to manipulate the grains structure of alternatively vertical and horizontal columnar grains. The practical significance of this is a possible route to stop crack growth. To achieve this, parameters were modified to investigate the workable values. The prerequisite feature is that the track profile has to be U-shape and H-dendrites are not to be remelted completely in the

successive layer hatching. This is to ensure that grains can epitaxially grow from H-dendrites in the next layer. Then, at first, the condition of the FO25 sample was selected. Next, layer thickness needs to be adjusted to maintain the existence of H-dendrites.

To ensure that H-dendrites are maintained, the track's penetration depth ( $P_{Tk}$ ) of the topmost layer (i.e. melt pool depth) cannot exceed the layer thickness  $t$ , as illustrated in Figure 111. In addition, it should be considered the consolidation mechanism of powder particles in EB-PBF process. As the powder particles are melted and then consolidate, the melt pool surface will be lower than the deposited powder surface. Therefore, the condition for maintaining H-dendrites through many layers will be:

$$P_{tk} < t \quad \text{Eq. 18}$$

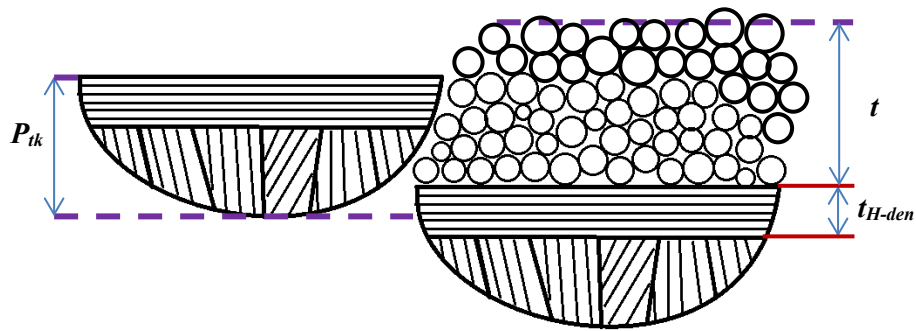


Figure 111. Illustration of layer thickness selection for maintaining H-dendrites

The currently applied layer thickness is  $70\mu\text{m}$  and the measured  $P_{tk}$  of the FO25 sample (Figure 100a) is  $203\mu\text{m}$ . Thus,  $P_{tk}$  and  $t$  obtained from the FO25 do not satisfy Eq. 18. Therefore, the layer thickness needs to be modified for the Eq. 18 to be satisfied.

At this stage, the volumetric energy density  $E_{vol}$  defined previously in chapter 1.2 is employed. The use of  $E_{vol}$  is due to its inclusion of multiple EB-PBF parameters such as layer thickness  $t$  and line offset  $h$ . The role of layer thickness  $t$  has been discussed earlier. As increasing of  $t$  will decrease  $E_{vol}$  which may result in lack of fusion. Thus, line offset  $h$  can be used as an adjusting parameter to ensure the sufficiency of  $E_{vol}$ .  $U$  is the accelerated voltage fixed at  $60\text{kV}$ ,  $I$  and  $v$  are the beam current and scanning speed which are controlled by an unchanged SF25. The Eq. 2 for  $E_{vol}$  then is shown again:

$$E_{vol} = \frac{U \cdot I}{v \cdot t \cdot h}$$

Based on the measurements of  $P_{tk}$  of the FO25 sample, then  $t$  should be larger than  $203\mu\text{m}$ . The layer thickness  $t$  was then selected as  $300\mu\text{m}$ . However, only one parameter is changed at one time to evaluate how the resultant  $E_{vol}$  affect the microstructure. Therefore, line offset  $h$  was still kept as  $0.1\text{mm}$ . Figure 112 demonstrates a significant change in the microstructure. The dominant columnar grains along the build direction are no longer seen. Instead, shorter

vertical columnar grains appear with a distance of one to two layer thicknesses (0.3~0.6 mm) and epitaxially grow on top of the horizontal grains. In addition, equiaxed-like grains, which are horizontal grains viewed from other direction, can be pointed out. Lack of fusion as a result of the reduction of  $E_{vol}$  can be observed. This is expected since the line offset  $h$  was not changed.

The  $E_{vol-1}$  is the original energy used in the FO25 sample with  $t_1 = 70 \mu\text{m}$  and  $h = 0.1 \text{ mm}$ .

$$E_{vol-1} = \frac{U \cdot I}{v \cdot t_1 \cdot h} = \frac{U \cdot I}{v \cdot 70 \mu\text{m} \cdot h}$$

The  $E_{vol-2}$  comprises of a change in  $t_2 = 300 \mu\text{m}$  while  $h = 0.1 \text{ mm}$ .

$$E_{vol-2} = \frac{U \cdot I}{v \cdot t_2 \cdot h} = \frac{U \cdot I}{v \cdot 300 \mu\text{m} \cdot h}$$

Thus, the reduction in energy of  $E_{vol-2}$  as compared to  $E_{vol-1}$  is:

$$E_{vol-2} = \frac{E_{vol-1}}{4.2}$$

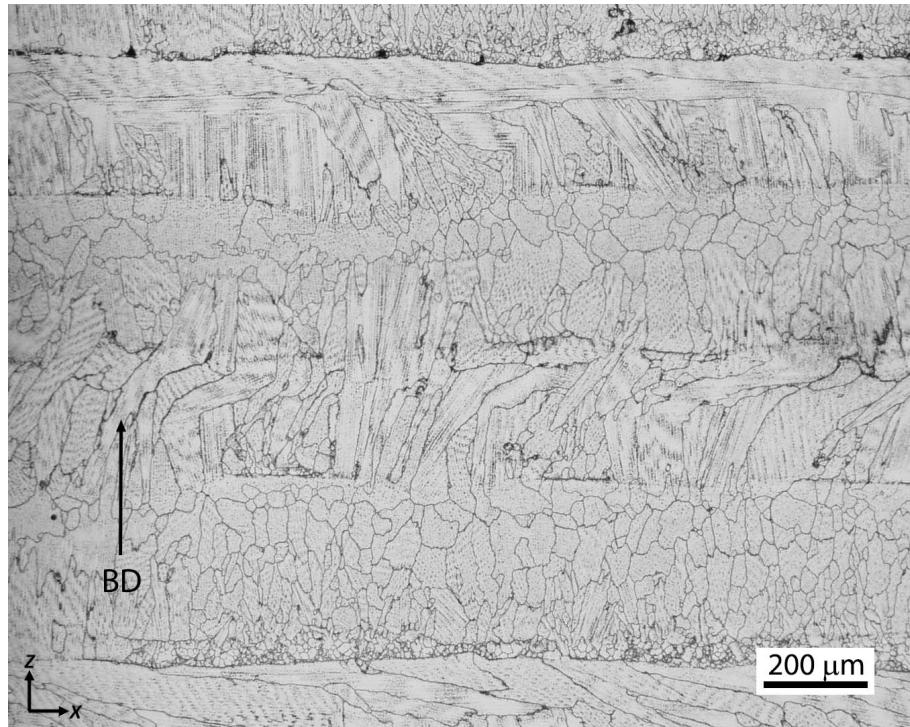


Figure 112. Optical micrograph showing the microstructure of EB-PBF fabricated sample using FO25 conditions with layer thickness  $300 \mu\text{m}$  and line offset  $0.1 \text{ mm}$

The microstructure observed in Figure 112 shows that H-dendrites were successfully retained. However, the lack of fusion is observed. This indicates that a slightly increasing in  $E_{vol}$  will generate the desired microstructure of fully dense with alternatively H-dendrites and V-dendrites. Therefore, the  $E_{vol-3}$  was obtained by reducing the line offset  $h$  from  $0.1 \text{ mm}$  to  $0.05 \text{ mm}$  while layer thickness was kept at  $300 \mu\text{m}$ . As compared to  $E_{vol-1}$  and  $E_{vol-2}$ , one can have:

$$E_{vol-1} = \frac{U.I}{v.t_1.h} = \frac{U.I}{v.70\mu m.h}$$

$$E_{vol-2} = \frac{U.I}{v.t_2.h} = \frac{U.I}{v.300\mu m.h}$$

$$E_{vol-3} = \frac{U.I}{v.t_2.h} = \frac{U.I}{v.300\mu m.\frac{h}{2}}$$

Thus:

$$E_{vol-3} = 2.E_{vol-2} = \frac{E_{vol-1}}{2.1}$$

Figure 113 shows a fully dense microstructure without lack of fusion was achieved for the  $E_{vol-3}$ . H-dendrites are successfully maintained. During any new layer hatching, there is only a portion of H-dendrites are remelted. Then columnar grains will epitaxially grow from these H-dendrites long the build direction. These vertical grains will again be stopped by the current layer's H-dendrites. The grain growth cycles keep repeating and the growth direction changes every layer.

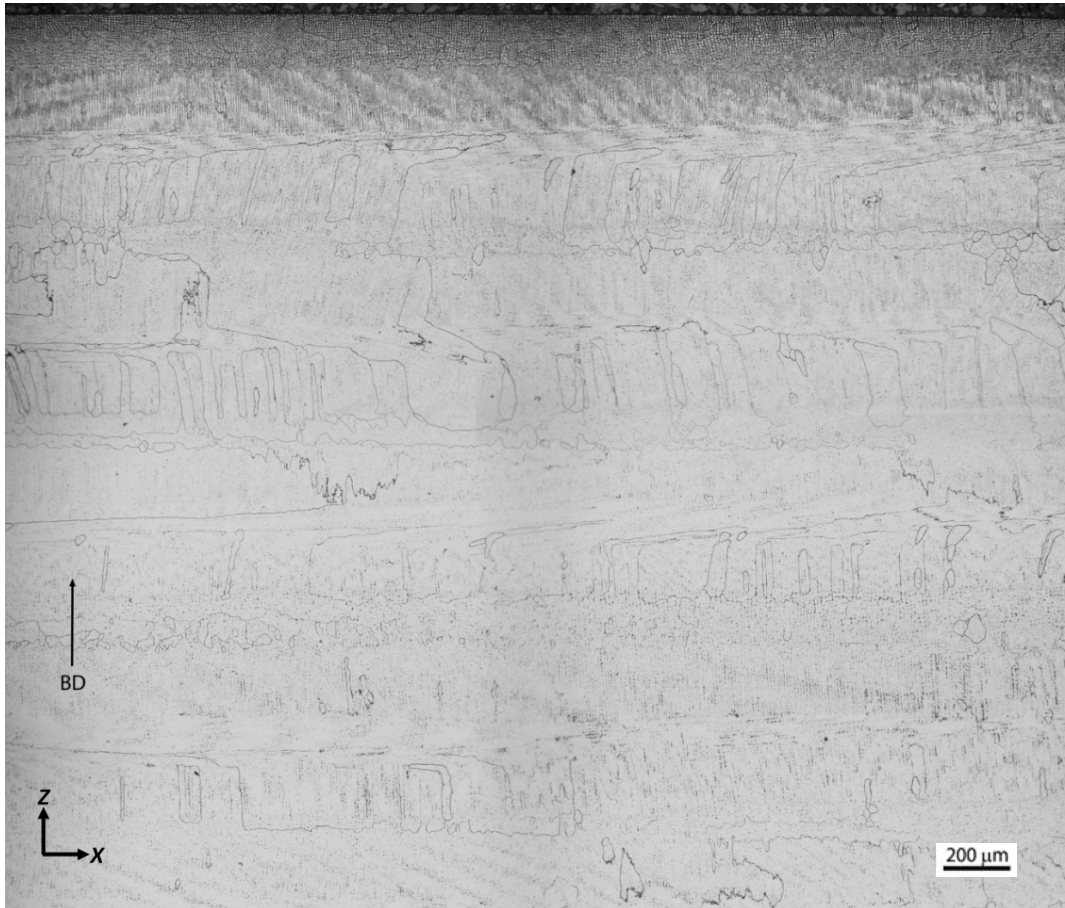


Figure 113. Optical micrograph showing the microstructure of EB-PBF fabricated sample using FO25 conditions with layer thickness 300 μm and line offset 0.05 mm

The change in grain growth directions prevents cracking in the as-fabricated sample. Horizontal grains as seen in Figure 113 replace the dominant vertical columnar grains. The change in grain growth direction results in the unfavorably straight path of grain boundaries for crack propagation. This novel grain structure may also benefit the mechanical properties. For the typical EB-PBF grain structures, the tensile strength along the build direction is higher than along the horizontal direction (normal to build direction). This is because of the highly oriented columnar grains along the build direction. In addition, carbides distribution at grain boundaries plays a crucial role. If the tensile axis is aligned with the carbides array, it is highly possible that sliding and voids formation is prevented during loading. In contrast, the tensile axis perpendicular to the carbides array is easier to form voids around the precipitates, which reduces the tensile strength. The dependence of mechanical properties on build direction was investigated by Shun et al. on EB-PBF Co-29Cr-6Mo alloy [35]. They found that the sample perpendicular to the loading axis has the lowest ultimate tensile strength value.

Figure 114 illustrates how the novel grain structure looks like in a 3D perspective. Within the individual layer, there are H-dendrites at the top region and V-dendrites at the bottom. As aforementioned, V-dendrites epitaxially grow from H-dendrites of the previous layer. The TBs and layer boundaries are displayed by dotted and dash lines, respectively in Figure 114. Different grains are represented by different colors (as similar as crystallographic orientation map). It can be seen that grains are no more vertically columnar. Instead, they appear as horizontally columnar grains. Moreover, the novelty of this grain structure is that grain can epitaxially grow in a way as illustrated by the blue grain in Figure 114. The V-dendrites in layer (n+1) epitaxially grow from H-dendrites of layer n. In layer (n+1), secondary arms of V-dendrites can horizontally branch out, which then develop into new H-dendrites. Then, V-dendrites of layer (n+2) epitaxially grow from these H-dendrites of layer (n+1). This cycle of epitaxial growth keeps continuing which finally results in the irregular-shaped grain (blue color). As a result, the overall grain structure will compile of irregular-shaped grains that interlock each other, which may mitigate the anisotropic mechanical properties.

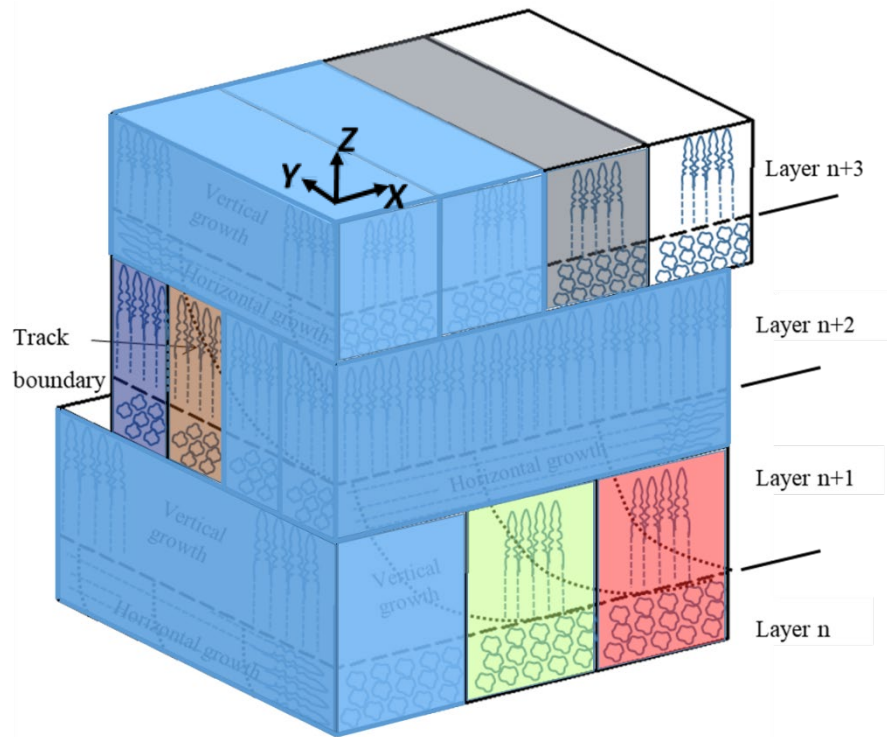


Figure 114. 3D illustration of the novel grain structure obtained showed in Figure 113. Track boundary, layer and dendrites growth direction is indicated. The blue grain can be seen to have an irregular shape.

#### Summary of the chapter:

The thermal analysis has shown that the studied Co-29Cr-10Ni-7W alloy has a wide solidification freezing range of approximately around 180 °C suggesting that the alloy is susceptible to hot cracking. Track shape has been shown to be focus offset dependent. The track boundary spacing and dendrite arm spacing determined have been used to estimate  $G$  to be  $6 \times 10^6$  K/m and  $\dot{T}$  to be  $\sim 2710$  K/s. These are upper bound (overestimated) values. This thermal condition is consistent with the columnar dendrite growth of the alloy during EB-PBF. The use of the more focused beam has resulted in a more U-shape melt/track geometry which promotes the lateral heat transfer. Thus, dendrites have grown horizontally in the top region with a considerable thickness of up to  $80\mu\text{m}$ . The defocused beam results in much less U-shape melt/track geometry that promotes vertical heat transfer. Thus, no horizontal grains are observed. Further process modifications have been made to have successfully manipulated the grains structure that results in a crack-free EB-PBF of the crack-prone alloy.

## CHAPTER 5: CHARACTERIZATION OF HOT-CRACKING NETWORKS

In this chapter, first, the form of intergranular cracks being liquid-state (hot) cracking and not solid-state cracking during EB-PBF will first be clarified through the observation of fractured surfaces of samples. Horizontal dendrites preventing the crack network extending to the surface will be briefly demonstrated, including the possible relationship between the rarely observed horizontal dendrite associated small cracks to the crack network below. Then, crack networks in relation to how they appear in the sample surface and to the scan direction in every layer during EB-PBF will be shown in detail. The relationship will be demonstrated to be applied to both focus off-set conditions.

### 5.1. Observation of cracks

Figure 115a and Figure 115b show the stereo-optical micrographs of FO25 and the FO50 samples, respectively. As can be seen, the top surfaces of the two samples are observed with extensive cracking. However, the severity in the FO25 sample is much less than the FO50 sample. The cracking density measured for the FO25 sample is 15 cracks while the figure for the FO50 sample is 75 cracks over the surface area. Furthermore, it is noted that cracks tend to be perpendicular to the tracks' scan direction. A location on each sample is selected (boxes) for higher magnification observation by SEM.

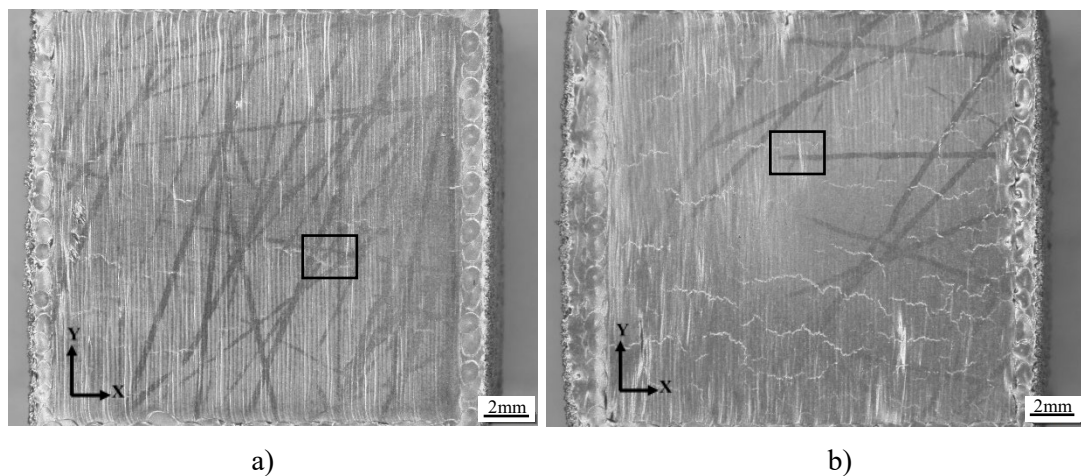


Figure 115. Stereo-optical microscopy images showing the top surface of (a). FO25 and (b). the FO50 samples

Figure 116 shows higher magnification OM and SEM images of selected locations in Figure 115. The “crack-like” that appears in Figure 116a is not a crack. This “crack-like” feature is actually a groove on the surface. The reflection from the stereo-optical microscopy light has caused the groove to appear as similar to a crack while under SEM, there is no light reflection. Other “cracked” locations on the FO25 sample’s surface were SEM observed and show a

similar feature. Instead, short and straight cracks as shown in Figure 116c were detected. However, the number of these real cracks is only five over the surface area.

Figure 116b and Figure 116d show a real crack, not a groove caused by light reflection as seen for the FO25 sample. The crack appears to be rugged as opposed to straight and short crack in the FO25 sample. It can be seen that the groove is also rugged. This may suggest the grooves in the FO25 sample may be a crack, however, did not reach the top surface.

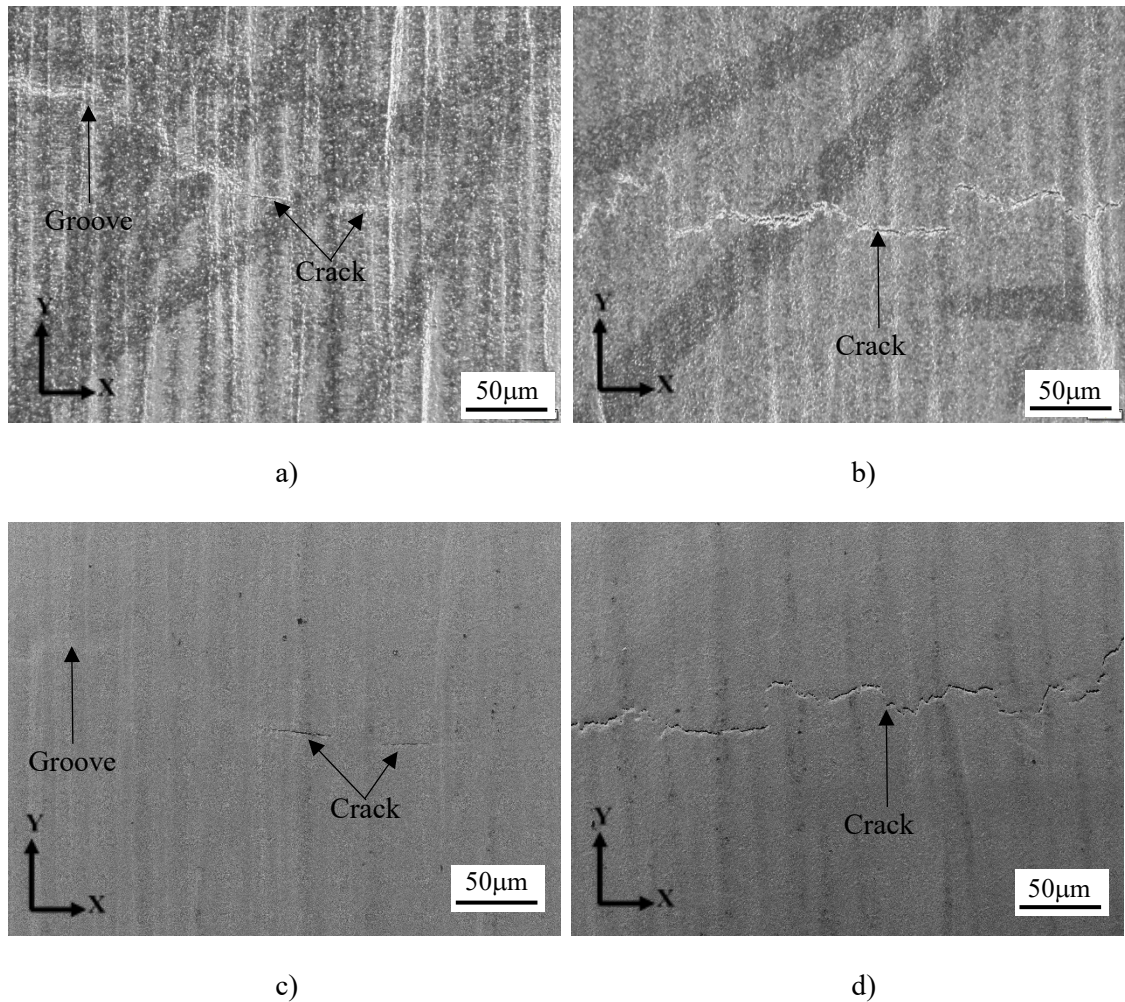


Figure 116. (a) & (c). OM and SEM images showing groove and cracks in the FO25 sample and (b) & (d). OM and SEM images showing rugged cracks in the FO50 sample. It is noted that a groove as pointed by the arrow is not easy, but still able to be observed on the FO25 sample's surface

Longitudinal cross-sections along the build direction are shown for both samples in Figure 117. Cracks are the clear and common feature observed. Moreover, the cracks are clearly the result of cracking along the inter-columnar grain boundaries along the build direction. Clearly, there are no inter-columnar grain boundaries for cracks to continue to the surface in the horizontal dendrite layer for the FO25 sample. As has already been explained, the thickness of the horizontal dendrites is 50-80 µm. The subsequent remelting of these dendrites means they have

in effect not affected the overall growth of cracks grown vertically. It is noted that the attempt made as presented in the last section of the last chapter (4.3.4) aimed not to completely melt this H-dendrite layer and thus to stop the crack growth beyond one layer.

For the FO50 sample, there are no H-dendrites to cover the cracks. Thus, cracks have grown to the surface. In Figure 117, the cracks appearing in both XZ and YZ cross-sections are similar because inter-columnar grain boundaries should appear similar when samples are sectioned parallel to the build direction. However, as pointed to previously, the cracks orientate somewhat normal to the scan direction on the sample surface. During EB-PBF, as in the experiments and as it is commonly used, the scan direction changes by  $90^\circ$  after every layer. Thus, if there is a directional preference of cracking due to the directional preference of stress relating to the scan direction, crack growth direction should be alternating in the same manner.

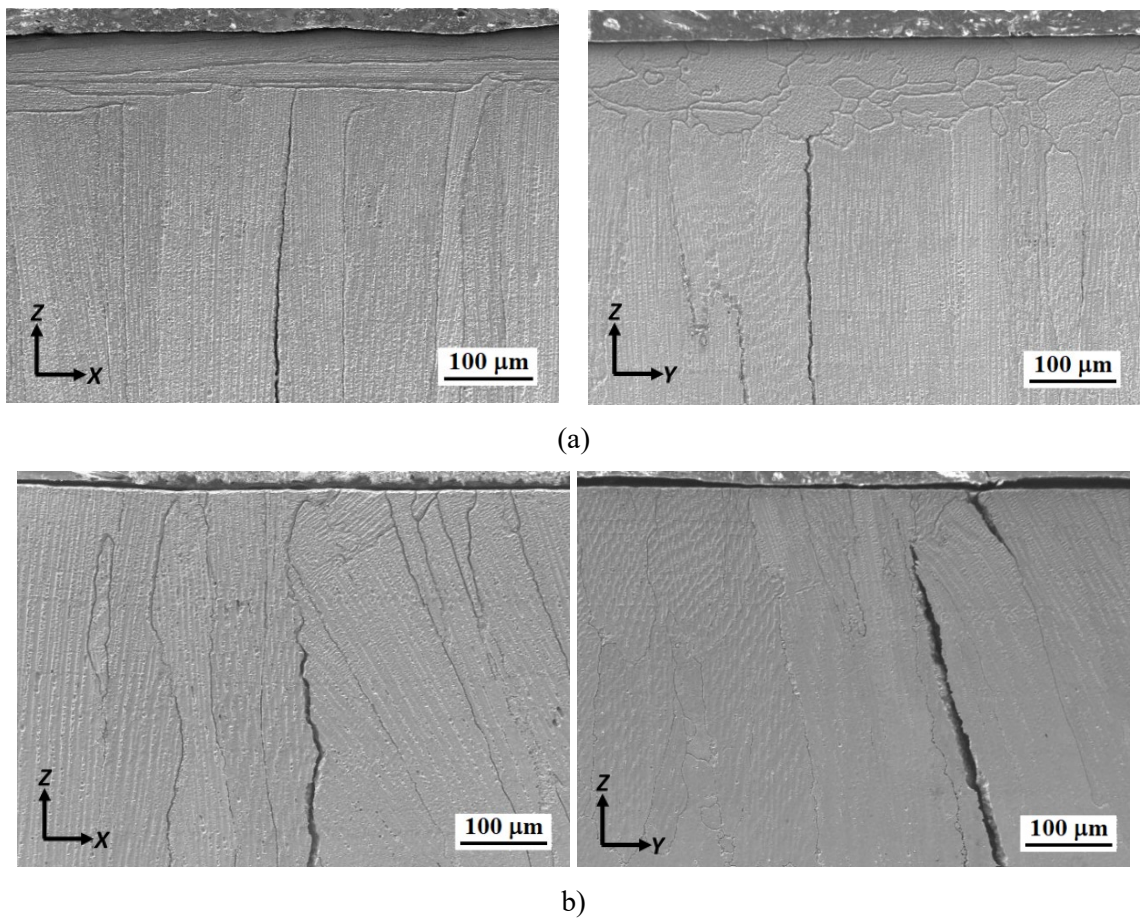


Figure 117. XZ and YZ cross-sectional SEM images showing the topmost layers of (a). FO25 sample and (b). FO50 sample

## 5.2. Examination of cracks' surface morphologies

Cracking has been reported in many studies in EB-PBF and LB-PBF processes. However, there has been disagreement since solid-state cracking and liquid-state cracking (or hot cracking) are both claimed for the form of cracking. Thus, an investigation was conducted and is presented here to verify if it is solid-state or hot cracking. This is done by examination of the crack surface in its as-built condition without passing through the specimen preparation process. The cracks on the samples' top surfaces are directly observed by using SEM. However, the grain boundaries crack observation needs further preparation for fractographs observation, which was described in chapter 3.

Cracks on top surfaces of both samples are closely examined by higher magnification SEM images, as shown in Figure 118. In Figure 118a, the crack can be seen occurred between the H-dendrites. The dendrites with features of secondary arms can be clearly observed. The crack's surface shows a very smooth morphology that indicates the evidence of liquid film was existing at one time. Crack's surface examination for the FO50 sample in Figure 118b shows similar features. The rounded feature and "egg-grate" surface indicate the dendritic morphology. However, it can be seen that the crack occurred between vertical dendrites along the build direction.

Definition of hot tear by Campbell [16] is now again stated. A hot tear (or solidification crack) will have a number of characteristics:

- Ragged form, branching crack
- Main tear with numerous offshoots following intergranular paths.
- The failure surface reveals a dendritic morphology

Therefore, it can be seen that the cracks in both samples have the characteristics of being ragged, cracking along the intergranular paths and dendritic appearance. The missing feature of the branching/tearing offshoots can be because of the rapid solidification in EB-PBF as compared to casting. As shown in Figure 107, solidification conditions during EB-PBF promote columnar dendrites. In contrast, the conditions in casting promote for equiaxed dendrites. The less development of secondary dendrite arms during solidification in EB-PBF thus limits the pathway for branching/tearing offshoots.

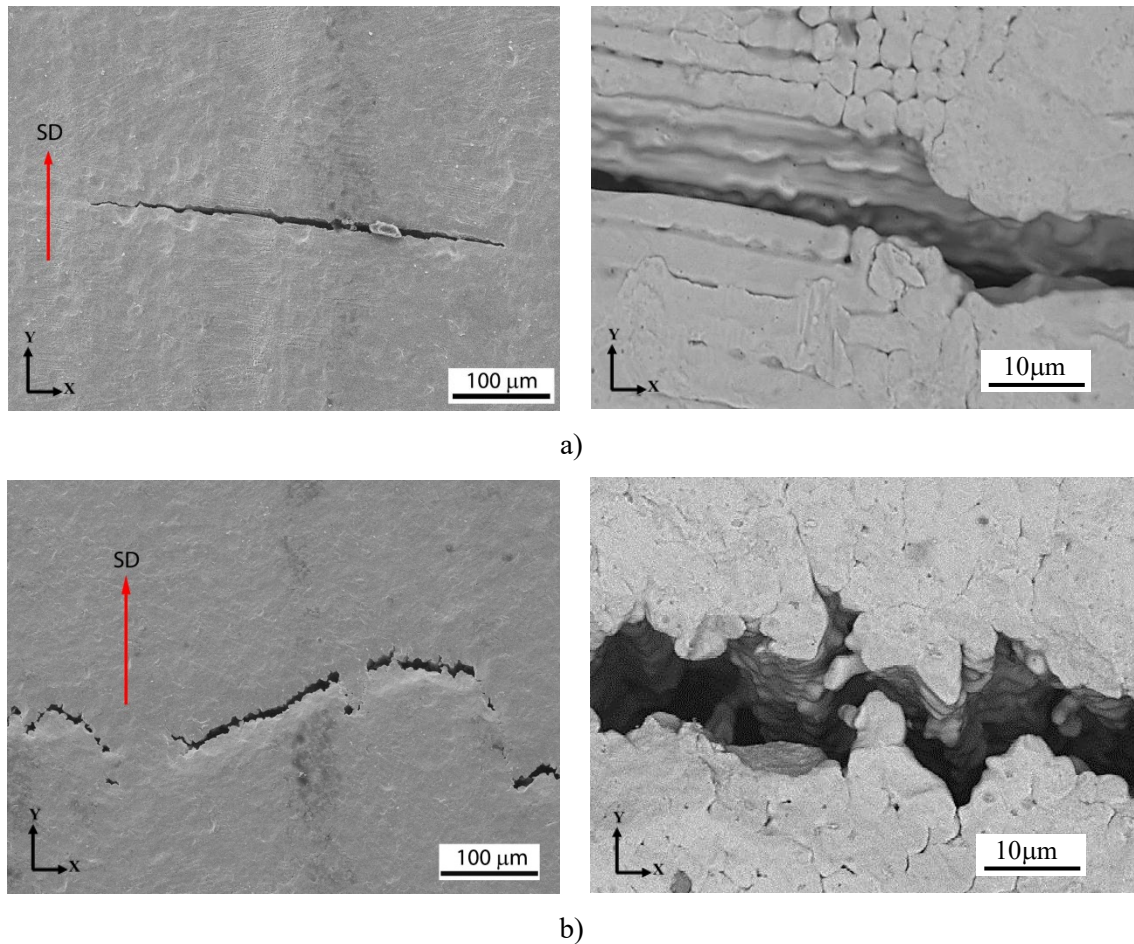


Figure 118. SEM images at low and high magnification showing hot tears identified as the cracking mechanism for the surface cracks in (a). FO25 sample and (b). FO50 sample

Solidification cracking has been identified for those cracks appear on the samples' top surface. However, previously presented SEM images on intergranular cracks along the build direction cannot provide details regarding what forms of the crack. This is due to the examined specimens were sectioned and passed through the preparation procedure (i.e. grinding, electrolytic polishing). This results in the intergranular cracks observed are not in the as-built condition as similar to the cracks on the top surface. Therefore, to examine the as-built intergranular cracks surface, tensile test was employed. The sample was built with horizontally in a shape of the hexagonal bar. Then, it was machined into the ASTM-standard dog-bone shape for tensile testing. Details about the experiment can be viewed in chapter 3.10. The pulling axis (along Y-axis) is perpendicular to the build direction (Z-axis), thus normal to the orientation of the intergranular cracks. Therefore, the EB-PBF as-built intergranular cracks are expected to be the initiating points to fracture. Figure 119 shows the fracture surface of the tensile tested sample under stereo OM and SEM.

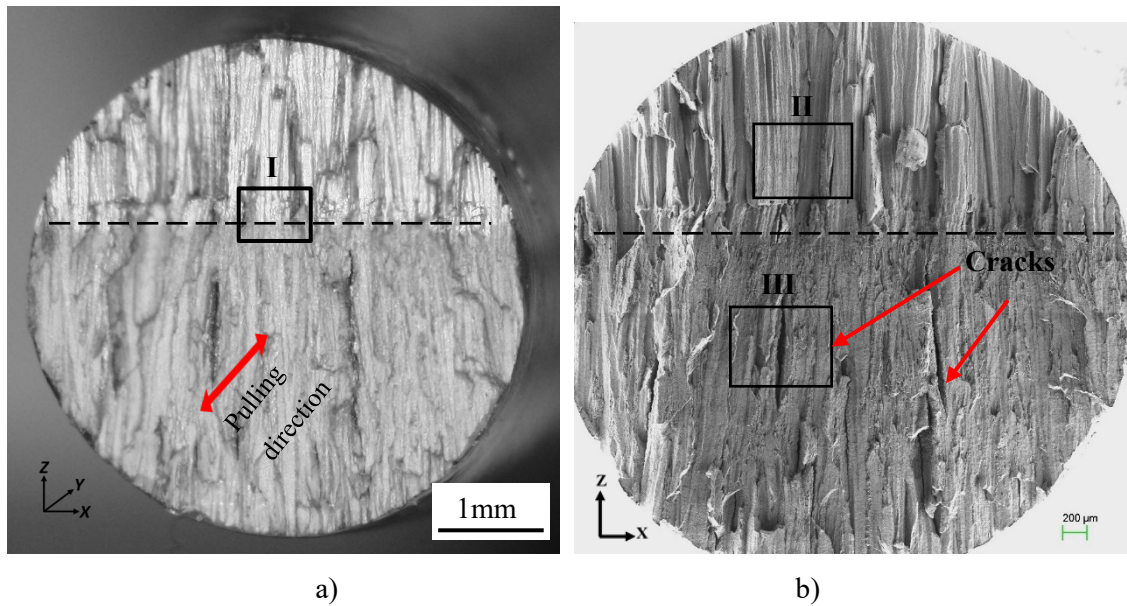


Figure 119. (a). Stereo OM image and (b). SEM image showing the fracture surface of the tensile tested sample.

It can be seen that the fracture surface appears differently under stereo OM, as shown in Figure 119a. The bright and grey appearance indicate that different light reflections of these two areas. This suggests that they may have different roughness. To clarify this, location I at the areas' boundary (illustrated by the dashed line) is selected for further examination. In addition, location II (of the bright area) and location III (of a grey area) containing an opened crack are selected to be examined regarding the identification of form of intergranular cracks. The crack's opening direction (along X-axis) can be seen perpendicular to the tension axis (Y-axis). Further observation on the crack surface will provide insight on whether it is EB-PBF as-built intergranular cracks or fracture caused by the tensile test.

Figure 120 shows a high magnification SEM image of the location I in Figure 119a. The upper area appears to be smoother than the bottom one. In addition, it can be seen that the bottom area surface having a dimple-like feature indicating that deformation may have occurred.

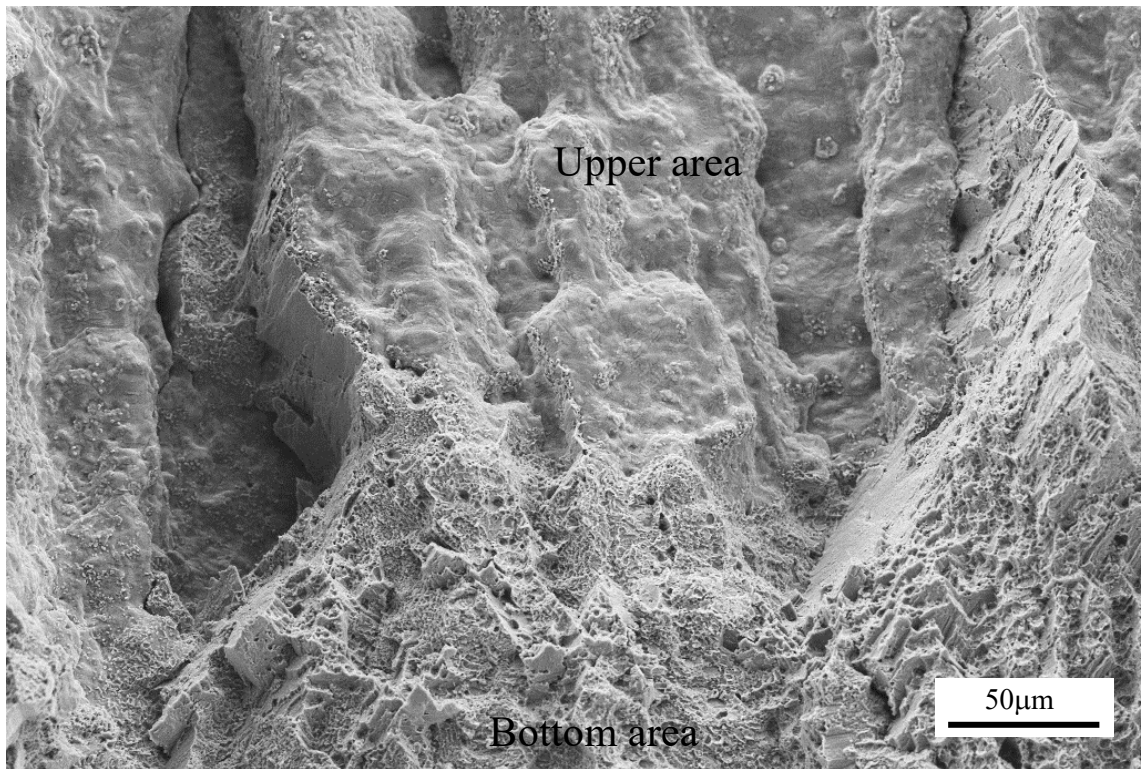


Figure 120. SEM image showing high magnification of location I in Figure 119a. The relatively smooth surface in the upper area indicates that no deformation may have occurred.

In Figure 121a, the surface is relatively smooth showing no typical fracture characteristics like dimples or cleavage. The smooth surface is shown in the location I explain why the upper area appears in the bright color under stereo OM. The smooth surface is also observed for the crack surface in Figure 121b. Small particles can be seen distributed along the surface which may be the precipitates at grain boundaries. Since no evidence shows that deformation may have occurred, this indicates that the observed surface at the location I may be the EB-PBF as-built intergranular cracks surface.

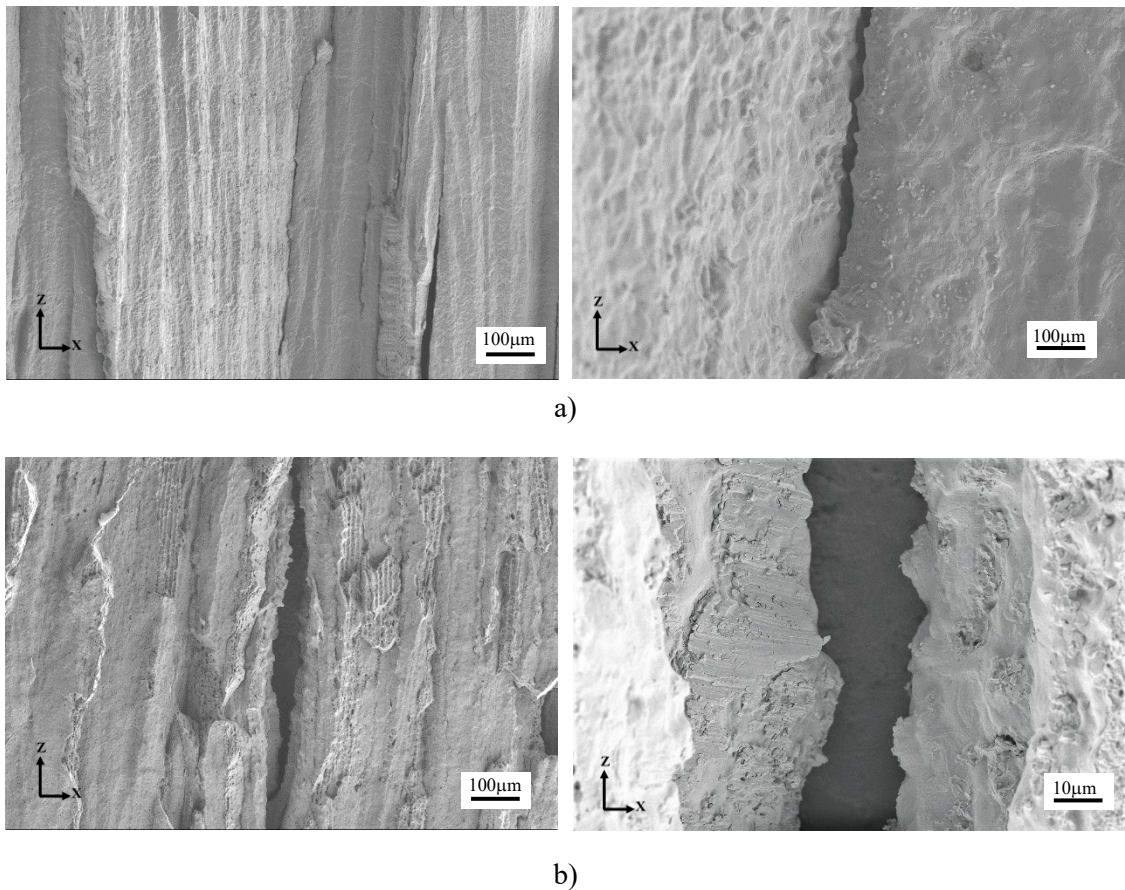


Figure 121. SEM images showing cracks observed from the fracture surface at (a). Location II and (b). Location III, as depicted in Figure 119b.

The surface observed in the location I and inside the crack at location II as shown in Figure 121 implies that it is the intergranular crack surface. Thus, the next step is to identify the form of the intergranular cracks. As has been discussed earlier in chapter 2.3.5, different forms of crack can be distinguished by examination of the crack surface. In Figure 121a, the surface shows no evidence of micro-ductility feature. This, together with the observation on precipitate particles on the surface, therefore, can exclude the reheat/strain-age cracking. This form of crack normally has a flat and featureless crack surface.

It is challenging to distinguish whether the intergranular crack is DDC or hot cracking. This is still difficult in welding where the fusion zone and the PMZ/HAZ can be easily distinguished. In EB-PBF, the specific zones as in welding cannot be traced. Since DDC always occurs at MGBs which requires no precipitates or impurity segregation at the grain boundaries [111]; therefore a cross-sectional SEM image of the FO25 sample is employed to examine the microstructure. As can be clearly seen in Figure 122, the grain boundaries are heavily decorated by chains of carbides/precipitates. In addition, the second phase can be pointed out at the cell boundaries. This indicates that micro-segregation has occurred during solidification in EB-PBF process. Moreover, the observation of carbides/precipitates at grain boundaries shown in Figure 122 is

consistent with the observation of precipitates on the intergranular crack surface in Figure 121. Therefore, it is unfavorable for DDC to occur and the form of crack can be identified as hot cracking. The smooth surface with less feature of secondary dendrites arms observed can indicate for liquation cracking. However, further investigation is needed on how to clarify these two mechanisms of hot cracking.

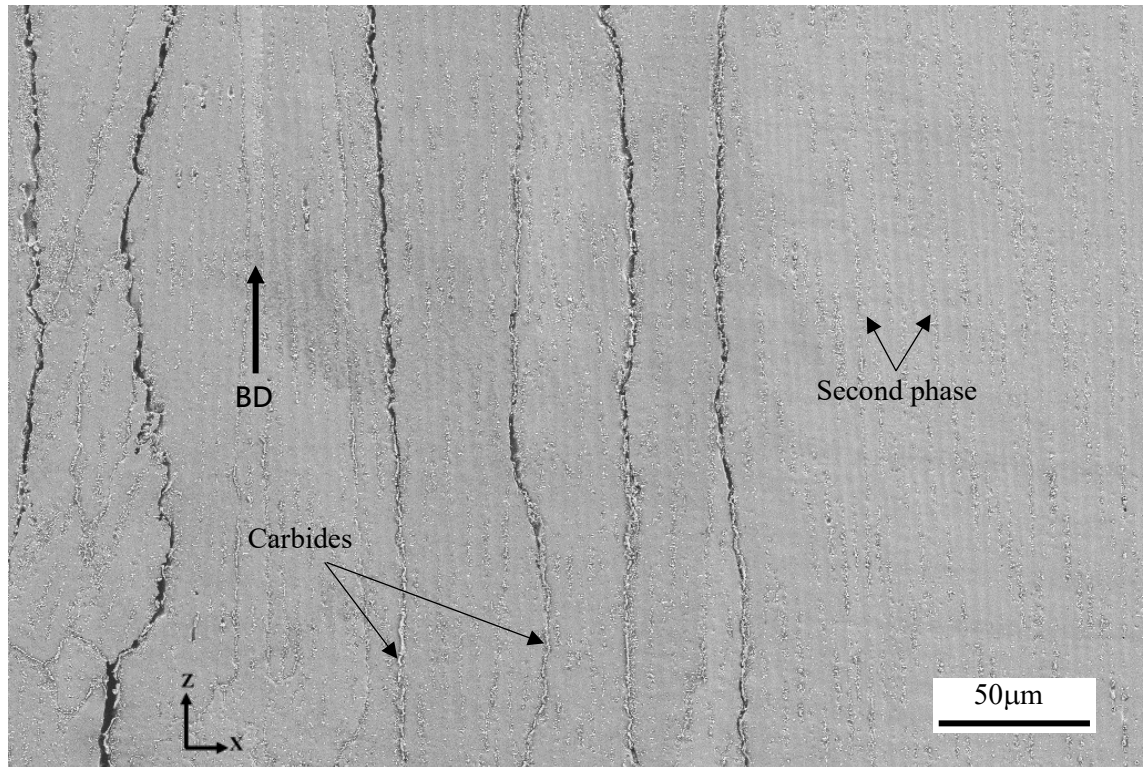


Figure 122. Cross-sectional SEM images showing intergranular cracks and grain boundaries decorated with carbides/precipitates in the FO25 sample

### 5.3. Crack network along build direction

The hot cracking identified comprises of solidification cracking and possible liquation cracking mechanisms. Longitudinal cross-sections are only able to view the hot cracks propagation through many layers along the build direction. However, as can be seen on the surface of the sample, cracks also propagate from track to track horizontally and are always normal to the scan direction. The change of 90° in scan direction would affect directions of thermal stresses that is a necessary condition to alternate hot cracks every layer. In the studies where cracking was observed, both in EB-PBF [113, 121, 122] and LB-PBF [112, 115, 116, 124], how hot cracking networks develop and propagate have not been well demonstrated. Therefore, the following section will present the characterized crack network obtained from the progressively grinding off layer-by-layer downward along the build direction, starting from the top surface of FO25 and the FO50 samples.

### 5.3.1. Crack network mapping for the FO25 sample

Crack network for the FO25 sample is now presented in the order of the last layer downward until the next two layers. Hereafter, the last layer is named as Layer 1<sup>st</sup>, which includes the top surface and has the thickness of the track's penetration depth. For the FO25 sample, the last layer's thickness is approximately 203  $\mu\text{m}$ , as measured previously in chapter 4. From then on, the next layers will be named as Layer 2<sup>nd</sup> and Layer 3<sup>rd</sup>. The thickness of Layer 2<sup>nd</sup> onward is 70  $\mu\text{m}$  that is exactly the layer thickness used in EB-PBF experimental setup. Figure 123 again displays the top surface in a larger area. Track boundaries in the form of wave-front ripples can be observed. No rugged cracks are seen. The two straight and sharp cracks are observed at the bottom right corner of the image. These are named as Crack-1 and Crack-2 for the ease of further discussion.

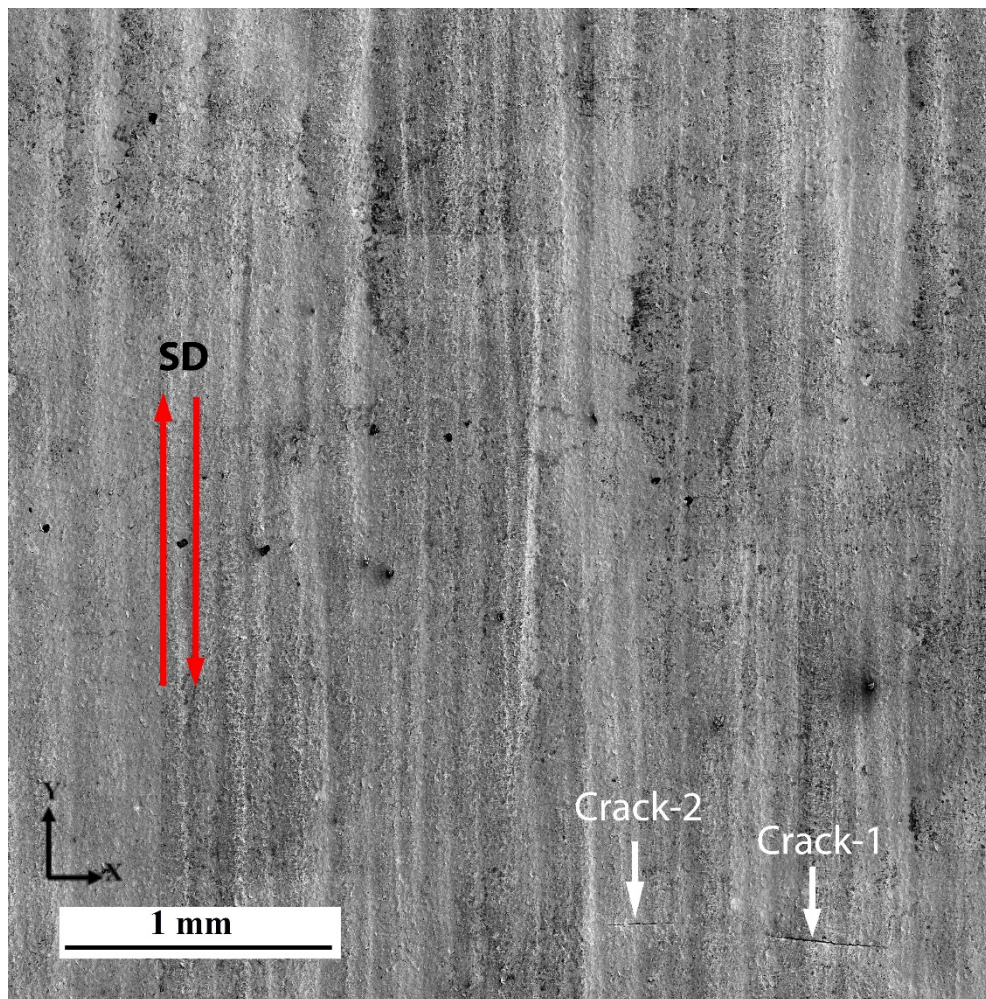


Figure 123. SEM image showing the top surface of the FO25 sample contains Crack-1 and Crack-2

Figure 124 shows the cross-sectional images after conducting the first time and second time grinding. The first time grinding removed one-standard depth ( $\sim 16 \mu\text{m}$ ) and the second time

grinding removed two-standard depth ( $\sim 32 \mu\text{m}$ ) of material. The standard depth was previously defined in chapter 3.7 as the impression depth calculated for one single indentation. Figure 124a shows the cross-sectional image of  $16\mu\text{m}$  underneath the top surface after the first grinding. Since there was not much material to be ground off, traces of tracks from the top surface can still be seen. Moreover, H-dendrites start to appear. Figure 124b shows the cross-sectional image after an additional  $32\mu\text{m}$  layer of material was ground off. Thus, the total grinding distance is  $48 \mu\text{m}$  ( $\sim$  three-standard depth) from the top surface. The microstructure reveals the H-dendrites clearly because it is still within the H-dendrites layer. Traces of scanned tracks on the top surface are no more observed.

Figure 125 superimposes Crack-1 and Crack-2 from Figure 123 onto Figure 124a. Crack-1 disappears after  $15 \mu\text{m}$  ground off and two new cracks appear, named as Crack-1a and Crack-1b. These two cracks are different in orientation and not aligned with Crack-1. In contrast, Crack-2 still remains after  $15 \mu\text{m}$  ground off and in the same orientation, as shown in Figure 125. In Figure 124b, Crack-1b disappears after another additional  $32 \mu\text{m}$  ground off while Crack-1a and Crack 2 remains visible. However, the length of Crack-2 gradually reduces and is expected to be gone after subsequent grindings.

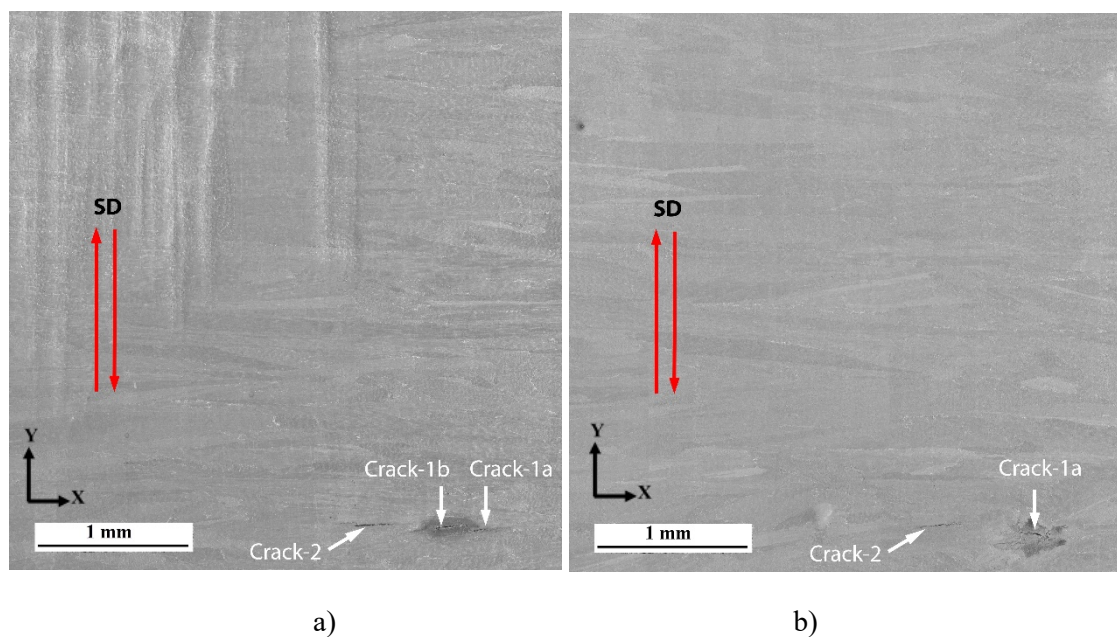


Figure 124. Cross-sectional SEM images showing (a). after a first  $16\mu\text{m}$  ground off and (b). after an additional  $32\mu\text{m}$  ground off from the second time grinding

The appearance of Crack-1a and Crack-1b can suggest these two cracks may have connected to Crack 1. The propagation of Crack-1a and Crack-1b may be impeded by the new grains (from which Crack 1 will occur). Because of the impediment, the induced stresses to cause Crack-1a and Crack-1b may concentrate on the new grain boundaries which will trigger Crack 1 to occur later. It is difficult to trace whether Crack 1 connects to Crack-1a and Crack-1b just based on the

superimposed image shown in Figure 125. However, these three cracks are in close proximity and direct to each other, thus it is reasonable to suggest that Crack-1a and Crack-1b may favor for the initiation of Crack 1.

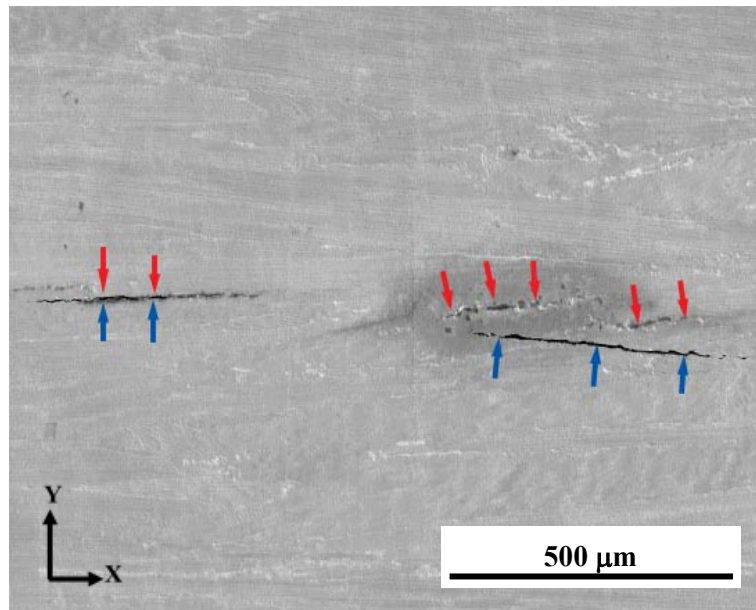


Figure 125. SEM image showing a superimpose of cracks in Figure 123 onto Figure 125a. Red arrows are cracks in Figure 125a and blue arrows are cracks in Figure 123

Since the H-dendrite layer's thickness is shown to be up to  $80\mu\text{m}$ , thus the third time grinding was conducted at three-standard depth ( $\sim 48\mu\text{m}$ ) to remove the H-dendrite and expose the underneath microstructure. However, after grinding, there is a small portion of the horizontal grains still remaining. The vertical columnar grains, which are in the same direction as the build direction, begin to be seen and appear as equiaxed grains in the viewing cross-section. This can be seen in Figure 126 and Figure 127. In Figure 126, numerous cracks underneath the H-dendrite layer can be observed. The emerged cracks run along grain boundaries and mostly perpendicular to the Layer 1<sup>st</sup> scan direction (so-call  $SD_{\text{Final}}$ ). It is different from those cracks on the top surface since the cracks appear to be rugged. Moreover, these vertical intergranular cracks are clearly stopped by the H-dendrite layer as none of those are seen in Figure 124b.

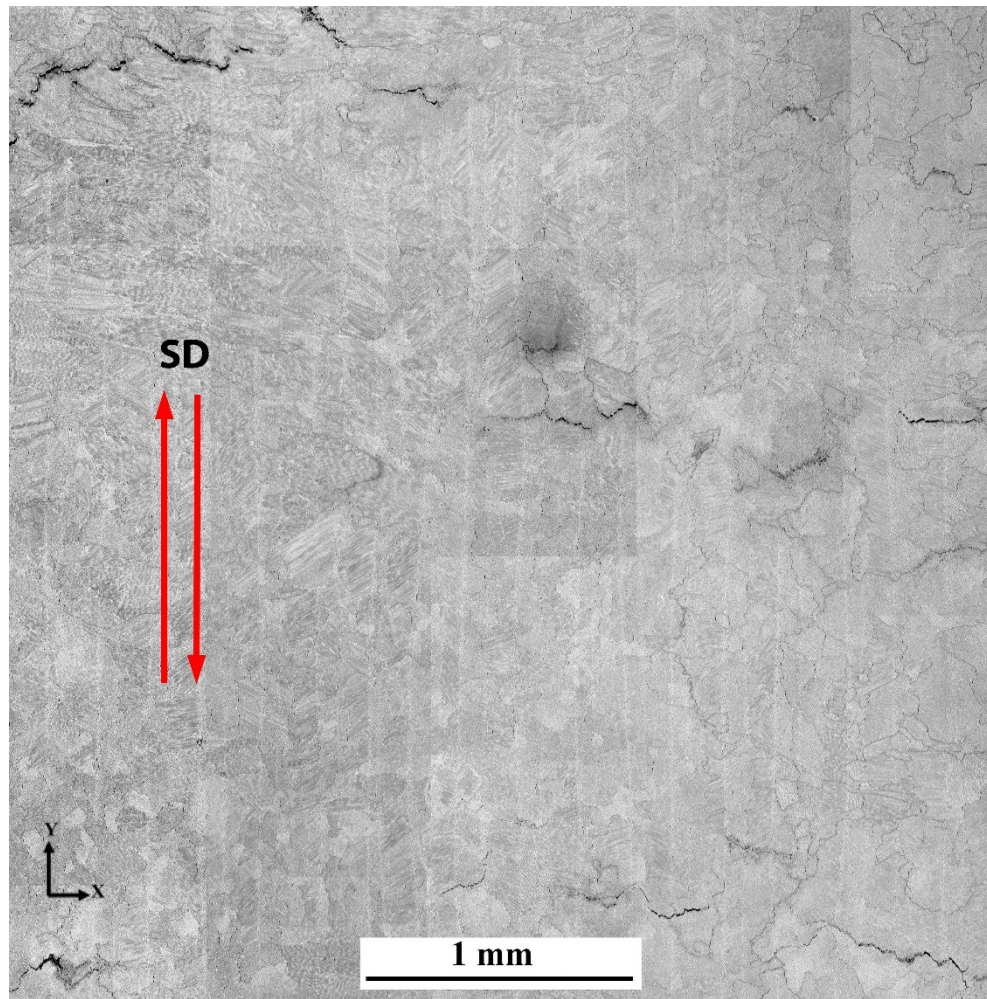


Figure 126. Cross-sectional image after 95 $\mu$ m ground off from the top surface. H-dendrites layer is no longer be seen. Crack network starts to show up

In Figure 127, a superimposed image between the cross-sections in Figure 124b and Figure 126 was done to correlate the Crack-1a and the new crack at the same location. Blue and red arrows illustrate the Crack-1a in Figure 124b and the new crack in Figure 126, respectively. It can be seen that these cracks are not aligned with each other. The Crack-1a occurred within H-dendrites may or may not connect to the underneath crack. During solidification of a single melt pool, as the vertical cracks propagate along the build direction, the H-dendrites may have fully grown, solidified and covered the top surface. Then, the propagation of vertical cracks is obstructed by H-dendrites. This is due to the U-shape melt track of the FO25 sample that favors for lateral heat flux, thus for H-dendrites growth, as discussed previously in chapter 4.3.2. The vertical cracks are stopped, however, they can induce the stress onto the H-dendrite boundaries, in a similar mechanism to that described earlier for Figure 125. Depending on the stress intensity, H-dendrites boundary can be cracked or un-cracked. However, the induced stress from vertical cracks may not be significant since numerous cracks are seen in Figure 126 but no cracks in H-dendrite layer at corresponding locations are seen in Figure 124b.

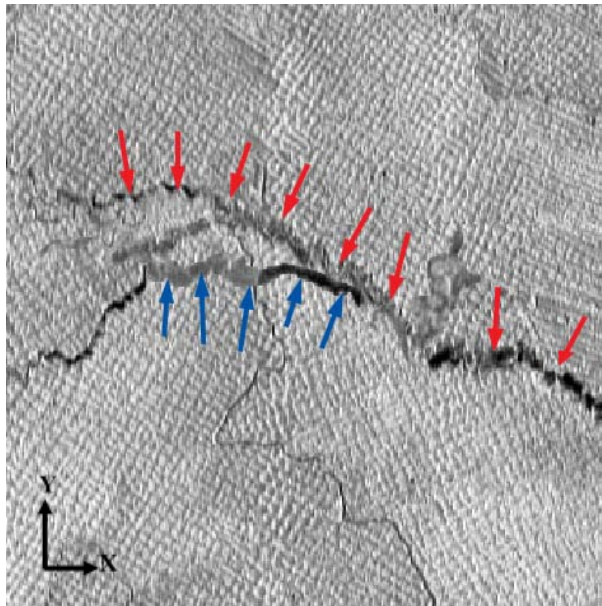


Figure 127. Superimpose of Crack-1a (blue arrows) onto the underneath cracks (red arrows) of the respective location

The following Figure 128a, Figure 128b, and Figure 128c represent for the last portion of Layer 1<sup>st</sup>, the next Layer 2<sup>nd</sup> and Layer 3<sup>rd</sup>, respectively. Optical micrographs (right-hand side) corresponding to SEM images (left-hand side) of each layer are also illustrated. Traces of track boundaries can be seen which indicates the scan direction of each layer. The crack network is observed clearly growing extensively in both size and number of cracks. The cracks appear also in irregular form and mostly orientate normal to the  $SD_{Final}$ , even for those in Layer 2<sup>nd</sup> and 3<sup>rd</sup>. In the areas 1 and 2 outlined in Figure 128, cracks start to be seen as although they are not observed in Figure 126. The area 1 and 2 cracks become more severe from Layer 2<sup>nd</sup> to Layer 3<sup>rd</sup>. In addition, these emerged cracks orientate differently, which are aligned more with the  $SD_{Final}$ .

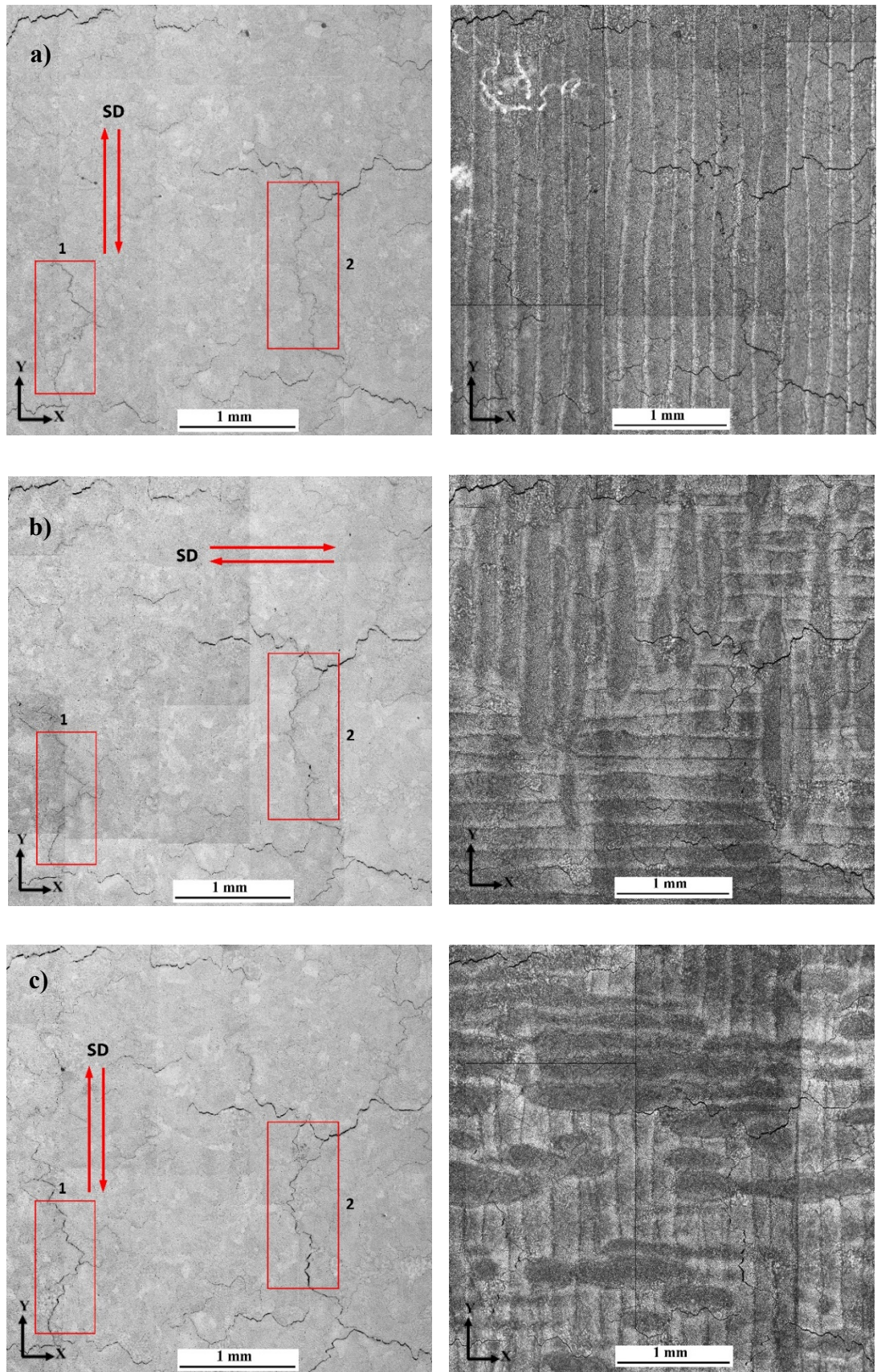


Figure 128. Cross-sectional SEM images (left) and OM images (right) of (a). Last portion of Layer 1<sup>st</sup>, (b). Layer 2<sup>nd</sup> and (c). Layer 3<sup>rd</sup>

Figure 129 illustrates area 2 outlined in Figure 128. In the middle of Layer 1<sup>st</sup> (96 $\mu$ m from top surface), the grain boundaries are observed un-cracked and orientate largely parallel to the scan direction. Coming to the last portion of Layer 1<sup>st</sup> (bottom of the layer), the grain boundaries appear darker and clearer compared to surrounding ones. As the Layer 2<sup>nd</sup> is revealed, the grain boundaries are seen to be cracked, however discontinuously. The cracked grain boundaries become continuous and clearer when coming down to Layer 3<sup>rd</sup>. Thus, before Layer 1<sup>st</sup> deposited, the crack may exist along the examined grain boundaries in Layer 3<sup>rd</sup> and possibly in Layer 2<sup>nd</sup>. The observation in Figure 129 can suggest how intergranular cracks have propagated along the build direction during EB-PBF. In addition, the un-cracked grain boundaries observed in the middle of Layer 1<sup>st</sup> poses a question on how the cracks are stopped. Further analysis of the propagation mechanism will be discussed later in the next chapter.

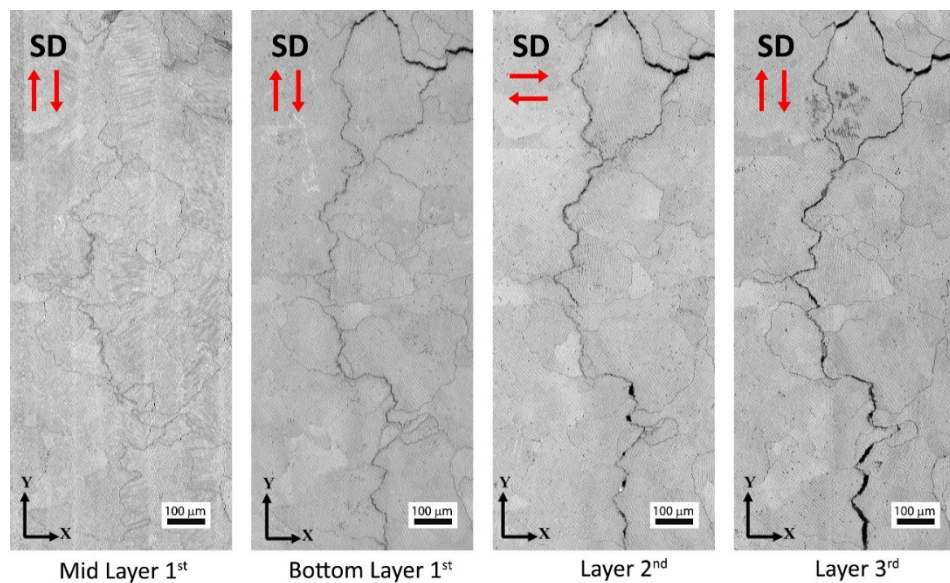


Figure 129. High magnification SEM images showing the outlined area 2 in Figure 128, demonstrated cracks start to be seen as consecutive grinding downward from Layers 1<sup>st</sup>-3<sup>rd</sup>

The layer-by-layer grinding and examination of the FO25 sample show that the hot tears appear on the top surface do not connect to the underneath rugged crack network. The H-dendrites act as barriers to prevent crack growth to the top surface. In addition, the crack network development strongly relates to the layer's scan direction. Cracks' severity is observed increasing as getting further away from the top surface, downward. Also, as grinding down to Layer 2<sup>nd</sup> and 3<sup>rd</sup>, some un-cracked grain boundaries in Layer 1<sup>st</sup> that orientate along the SD<sub>Final</sub> start to be cracked and link to the existing cracks to form the crack network.

### 5.3.2. Crack network mapping for the FO50 sample

Characterization of the crack network for the FO50 sample is now presented. The Layer 1<sup>st</sup> thickness was measured at about 120  $\mu$ m, as aforementioned in chapter 4. The sample was

ground off until the Layer 5<sup>th</sup>. This will provide more insight into the cracking propagation since crack growth is observed in more layers. The rugged crack network observed in the FO25 sample from the last portion of Layer 1<sup>st</sup> appears similar to that of the FO50 sample's surface. In addition, the FO50 sample has no H-dendrite layer as observed in the FO25 sample.

Figure 130 shows the top surface of the FO50 sample. The scan directions and numbers of cracks are highlighted by the red and white arrows, respectively. The observed rugged cracks have their orientation somewhat normal to the scan directions. This is consistent with the observation from the FO25 sample. Further consecutive grinding to downward layers is illustrated by SEM images in Figure 131.

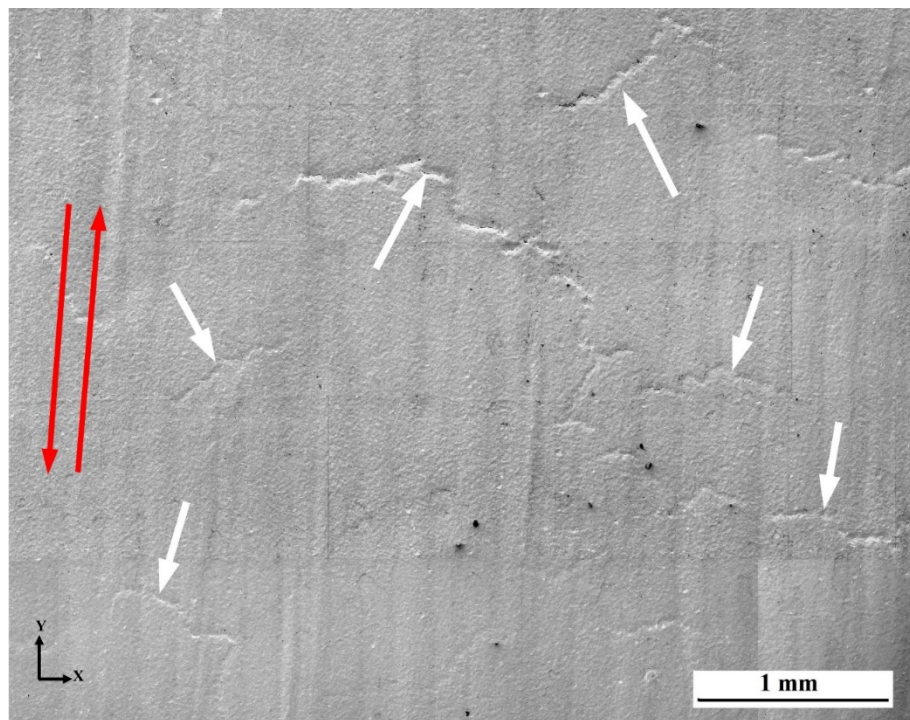
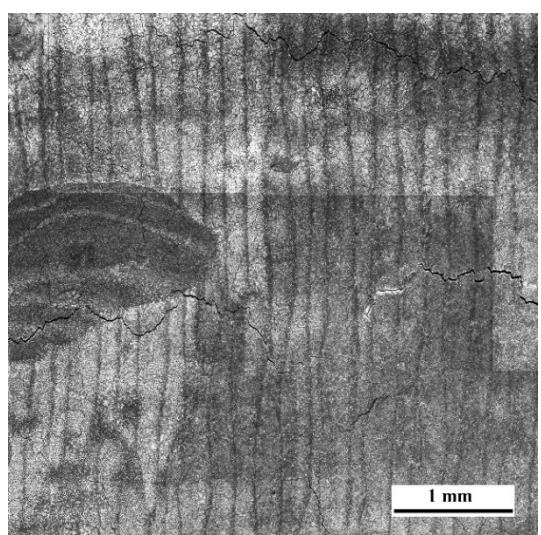
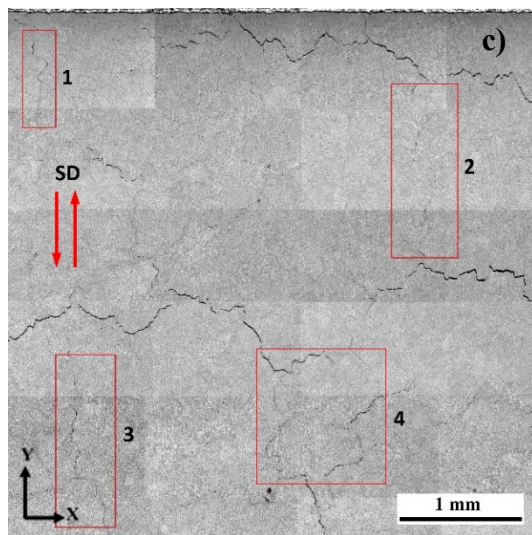
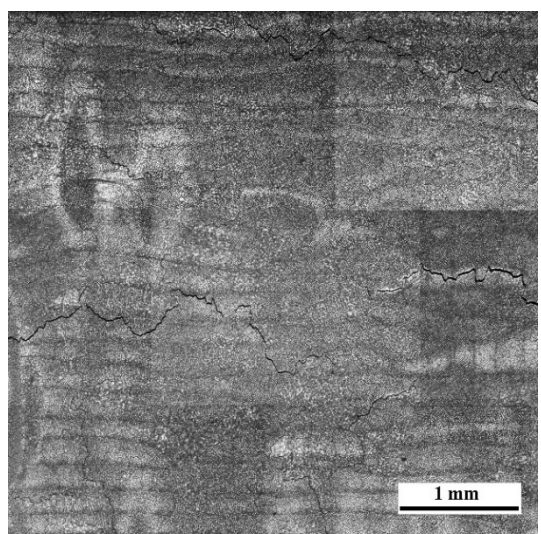
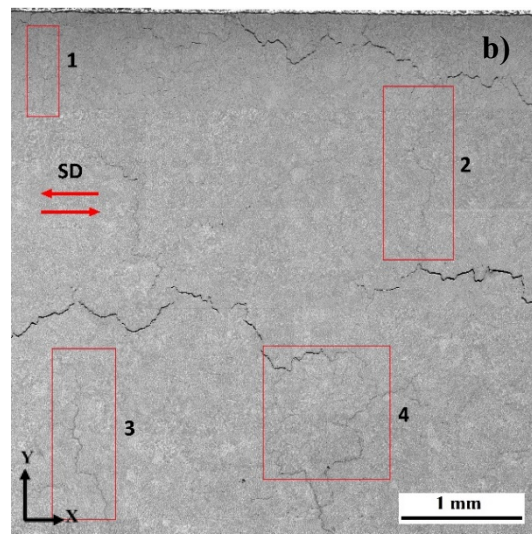
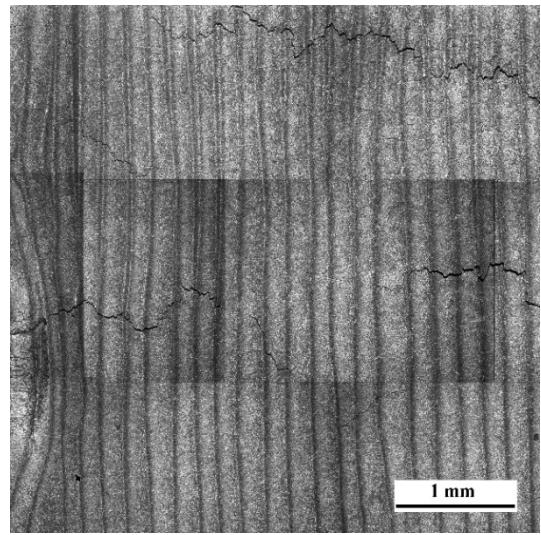
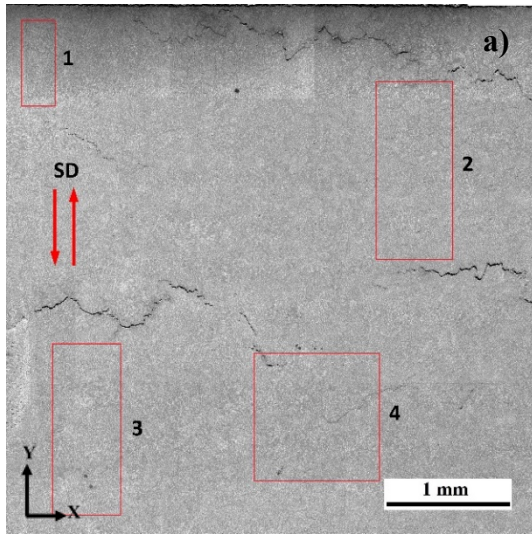


Figure 130. SEM image showing the top surface of the FO50 sample with highlighted cracks (white arrows) and the scan direction (red arrows)

In the low magnification images (Figure 131), the rugged cracks orientated more in the direction normal to  $SD_{Final}$  (similar to those appearing in Figure 130) are clearly seen in each layer. This means cracks observed in Layer 1<sup>st</sup> are cracks grown from many layers below. Observations on these cross sections have revealed the similar feature of cracks as in the FO25 sample. The irregular cracks orientated more aligned with  $SD_{Final}$  are revealed in lower and lower layers. To illustrate this, areas 1-4 are outlined in Figure 131. In each of these outlined areas, cracks that are not or not fully present along the grain boundaries orientating more parallel to  $SD_{Final}$  in the first or even second layer are seen in the subsequent layers below.



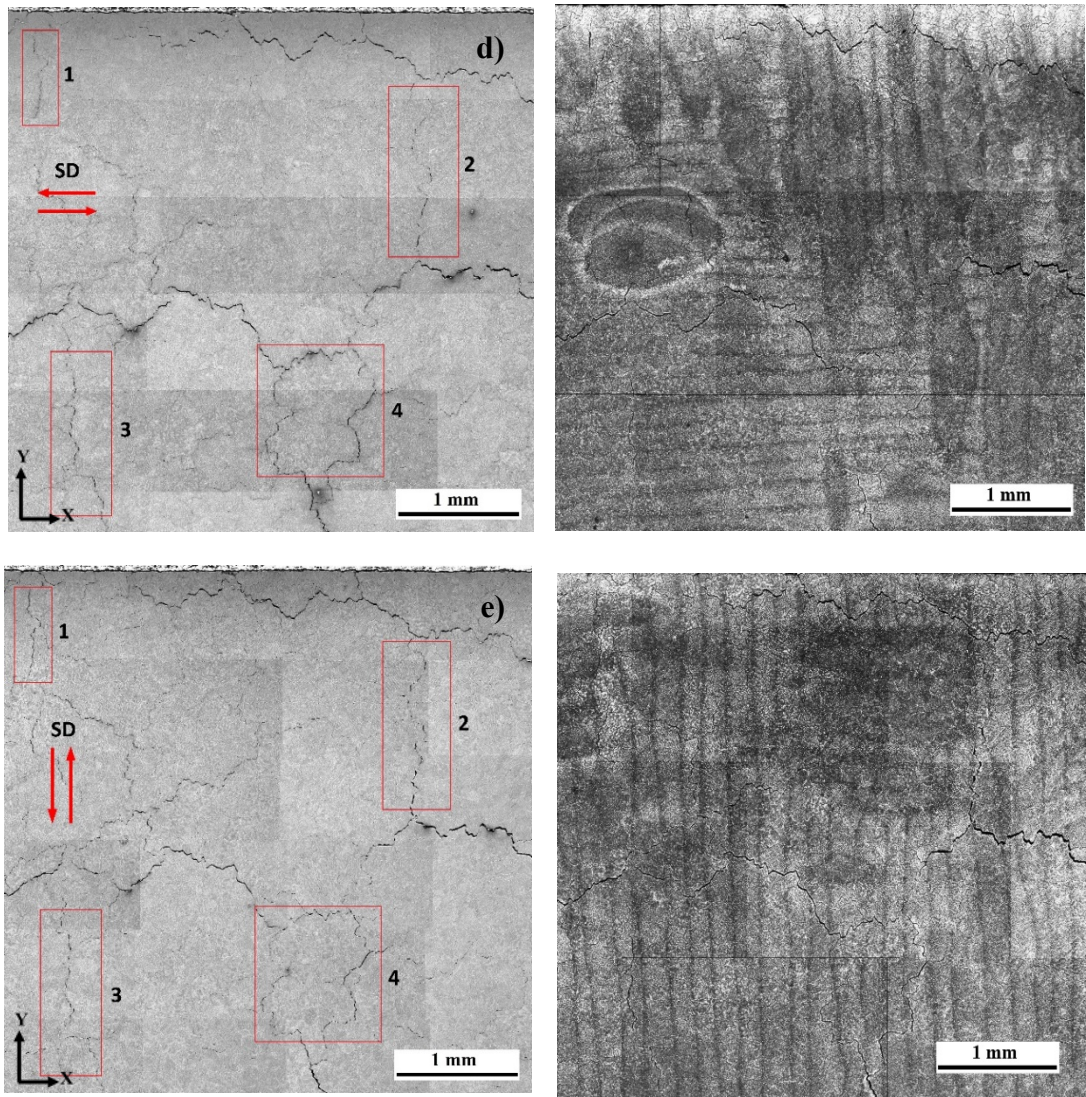


Figure 131. Cross-sectional SEM images (left) and OM images (right) of (a). Layer 1<sup>st</sup>, (b). Layer 2<sup>nd</sup> and (c). Layer 3<sup>rd</sup>, (d). Layer 4<sup>th</sup> and (e). Layer 5<sup>th</sup>

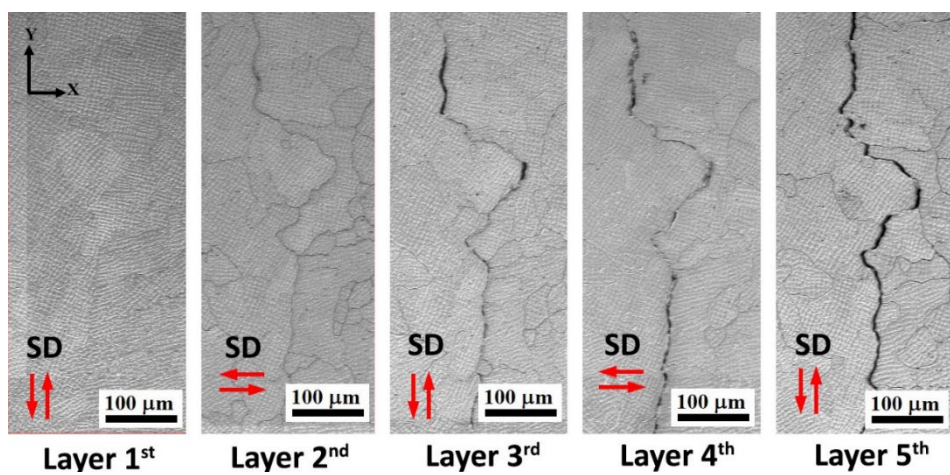


Figure 132. High magnification SEM images showing the outlined area 1 of five layers obtained in Figure 131, demonstrated cracks start to be seen as consecutive grinding downward

An example of gradually more revealing of a crack being closely aligned to  $SD_{Final}$  is illustrated in higher magnification in Figure 132 for area 1 in Figure 131. In the top layer (Layer 1<sup>st</sup> in Figure 130), as XY cross-section is viewed, grains can be seen but no crack is observed in this small area (area 1). In Layer 2<sup>nd</sup>, cracks are still largely absent. In Layer 3<sup>rd</sup>, a crack which may not be fully continuous can be seen. The crack is clearer in Layer 4<sup>th</sup> and in Layer 5<sup>th</sup> the crack is fully continuous. It is very clear that the crack follows the columnar grain boundaries. Viewing the current cross-sections in Figure 132, the grains are largely equiaxed and thus grain boundaries are irregular (rugged). Thus, although the crack in area 1 after the top two layers is more aligned with  $SD_{Final}$ , it also appears irregular. This is also the reason that cracks appear in the sample surface quite irregular, as observed in Figure 130. The observation in Figure 132 is similar to that observed in Figure 129 for the FO25 sample. The difference is that in the FO50 sample, the crack in area 1 starts to be seen from Layer 3<sup>rd</sup>. This suggests that crack may have existed in Layer 4<sup>th</sup> downward and possibly in Layer 3<sup>rd</sup>.

The observation from the crack networks of the FO25 and FO50 samples indicates that the last layer scan direction  $SD_{Final}$  may have an effect on stopping cracks growth. Cracks that are more aligned with the  $SD_{Final}$  are seen to be stopped growing toward the last layer. In addition, the observation of crack in area 1 of the FO50 samples poses questions on why and how the crack is stopped when reaching to Layer 2<sup>nd</sup>. Therefore, the next chapter will deal with further analysis to clarify how the crack network has developed in such a way observed in the FO25 and FO50 samples.

Summary of the chapter:

Cracks occurred during EB-PBF FO25 and FO50 samples have been shown to be hot cracking, meaning cracking associated with the presence of the liquid film. Cracks, as seen on the top surface, have been identified as solidification cracking (hot tear) but in two different forms. Short and straight cracks are rare but exist when solidification of the top surface is columnar growth horizontally under FO25 condition. The other form is in irregular shape although they tend to be normal to scan direction. These cracks are abundant and are the result of crack networks grown to the surface for FO50 condition. The two different forms of cracks may possibly be related. Long crack networks along the build direction have been identified for both EB-PBF conditions. The networks in the last three layers appear peculiarly as the cracks have been shown to be predominantly present normal to the scan direction.

## CHAPTER 6: THE HOT-CRACKING MECHANISM

In the previous chapter, the crack surface was examined and networks of cracks for the FO25 and the FO50 samples were characterized. In this chapter, first, further effort is made to clarify how hot cracks have initiated by examining the single-track sample. Then, how hot cracks have propagated and how grain boundary liquation has contributed to cracking will be demonstrated based on the crack network sequentially observed. In addition, the influential factors affecting the propensity of liquation as well as solidification cracking subsequently during solidification within the track will be discussed. The estimated length of grain boundary liquation is used to predict the thermal gradient during EB-PBF and compare to the previously estimated result and the available estimates in the literature. Furthermore, the effect of grain boundary misorientations on promoting/impeding crack growth will be discussed. Simulation results of thermal stresses during EB-PBF will then be presented. This will be used to explain the orientation of cracks observed.

### 6.1. Formulating hot cracking mechanism

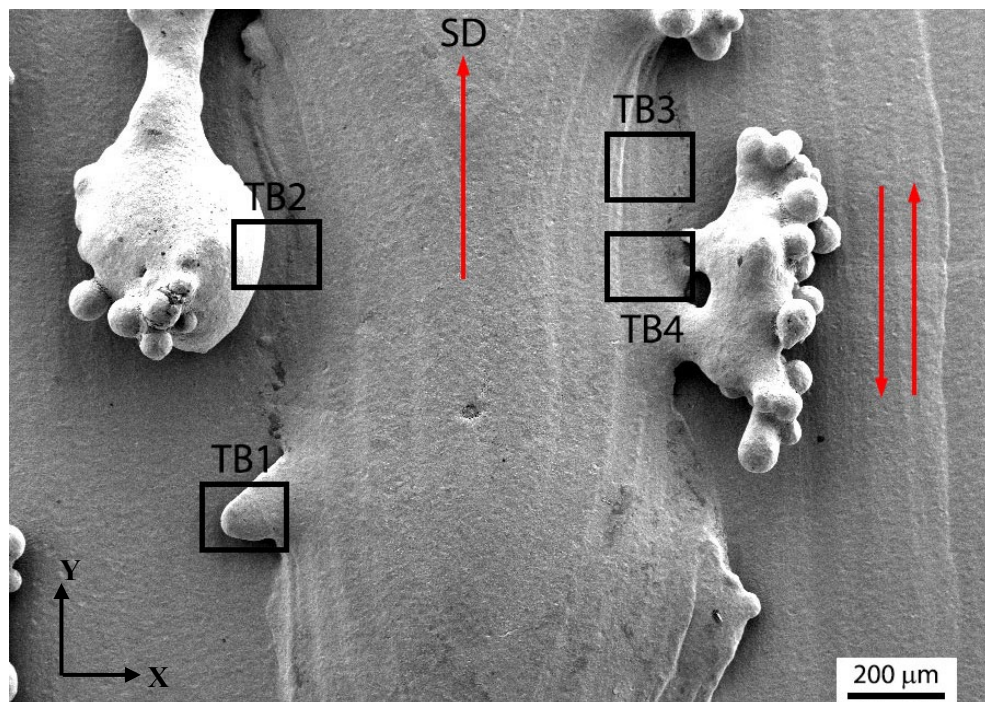
#### 6.1.1. Cracks initiation

In chapter 5, the fracture surfaces of the as-built sample were examined showing typical characteristics of the hot cracking phenomenon. However, distinguishing between liquation crack and solidification crack in EB-PBF is challenging. Chauvet et al. [113] and Peng et al. [121] were unable to identify whether their hot cracks initiated due to liquation cracking or solidification cracking. Since in EB-PBF, the partially melted zones (PMZ) and the fusion zones (FZ) are identical. Both of the regions are columnar grains. This is unlike the fusion welding where FZ and PMZ's microstructure are completely distinguishable. Chen et al. [126] in their experiments on laser cladding of IN718 observed liquation cracks initiated in the first two layers when the third one deposited. The possibility of running individual builds at a different number of layers helps the authors to investigate when and where the cracks started. In contrast, EB-PBF build of a sample comprises of thousands of layers, thus, it is impossible to replicate the experiments as Chen et al. [126] to trace where cracks initiated. Therefore, an alternative method to investigate how hot cracks initiate is needed and is presented here.

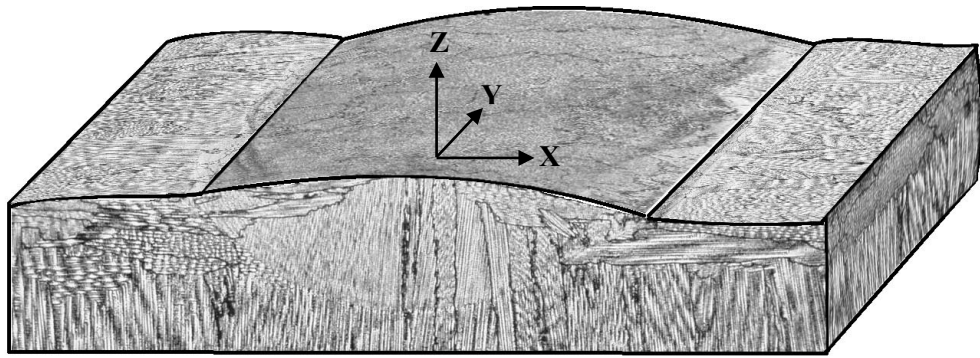
Since the H-dendrites were discovered in the FO25 sample and has been described in chapter 4, this special feature serves to formulate a method to study how hot cracks initiate in EB-PBF process. Figure 133a shows a single-track scanned on the top surface of the FO25 sample with four locations TB1 to TB4 are selected to be examined. The sample is then ground off from top until the H-dendrites layer to obtain the XY cross-section. Additional cross-sections from ZX and ZY views are also obtained. These three cross-sections are then OM imaged and

constructed into a 3D image to provide a perspective view of the sample's microstructure, as shown in Figure 133b.

The single-track experiment is effective in a single bead-on-plate weld. After the FO25 block's last layer being built, a new powder layer was raked and preheated and then the single track was scanned with a scanning speed of 600 mm/s using FO25. The region within the track is the fusion zone. The block sample on which the track was scanned acts as the substrate. Both scan directions of the single-track and the surface layer are shown as red arrows in Figure 133a. In Figure 133b, H-dendrites from the top surface of the FO25 sample can be seen growing normal to the track's scan direction. The microstructure in the track's FZ epitaxially evolved from the FO25 sample's microstructure (the substrate). As has been well described in the last chapter, cracks occurred intergranular along the build direction. However, in H-dendrite layer, cracks are rarely seen and have no connecting to the crack network below. Thus, the examination of the FS/PMZ boundary in H-dendrites layer can suggest how the heat from the single track affects the PMZ's microstructure with respect to cracking formation. In addition, characteristics of H-dendrites in terms of heat transfer are similar to V-dendrites, as has been discussed in chapter 4. Therefore, the observation on hot cracks formation from H-dendrites can reflect the initiation mechanism at one time along the build direction during EB-PBF process.



a)



b)

Figure 133. (a). SEM image showing the top surface of the single track sample and selected locations for examination and (b). OM image showing 3D views of the sample's microstructure

Figure 134 shows high magnification SEM images of selected locations shown in Figure 133a. Dashed lines illustrate the track boundary, which distinguishes the FZ and the PMZ. Grain structures in the PMZ correspond to the H-dendrites which orientate normal to track boundary, thus they are closely aligned with the heat flux directions (red arrows). Consequently, this may cause high susceptibility in grain boundary liquation.

In Figure 134, several cracks can be seen crossing from PMZ to FZ. These four locations from TB1 to TB4 appear as no cracks on the top surface (Figure 133a). This suggests that the solidification cracks can be excluded from those cracks. Thus, the observed cracks can be the defect caused by the single-track scanning. As can be seen clearly, the cracks' tips located in PMZ are decorated with re-solidified microstructure. This indicates that the low melting temperature eutectic structure at grain boundaries have been remelted and re-solidified. In addition, in Figure 134b, there is a crack located away and not crossing the track boundary. This suggests that the crack may be partially healed by the backfill of molten metal from the FZ.

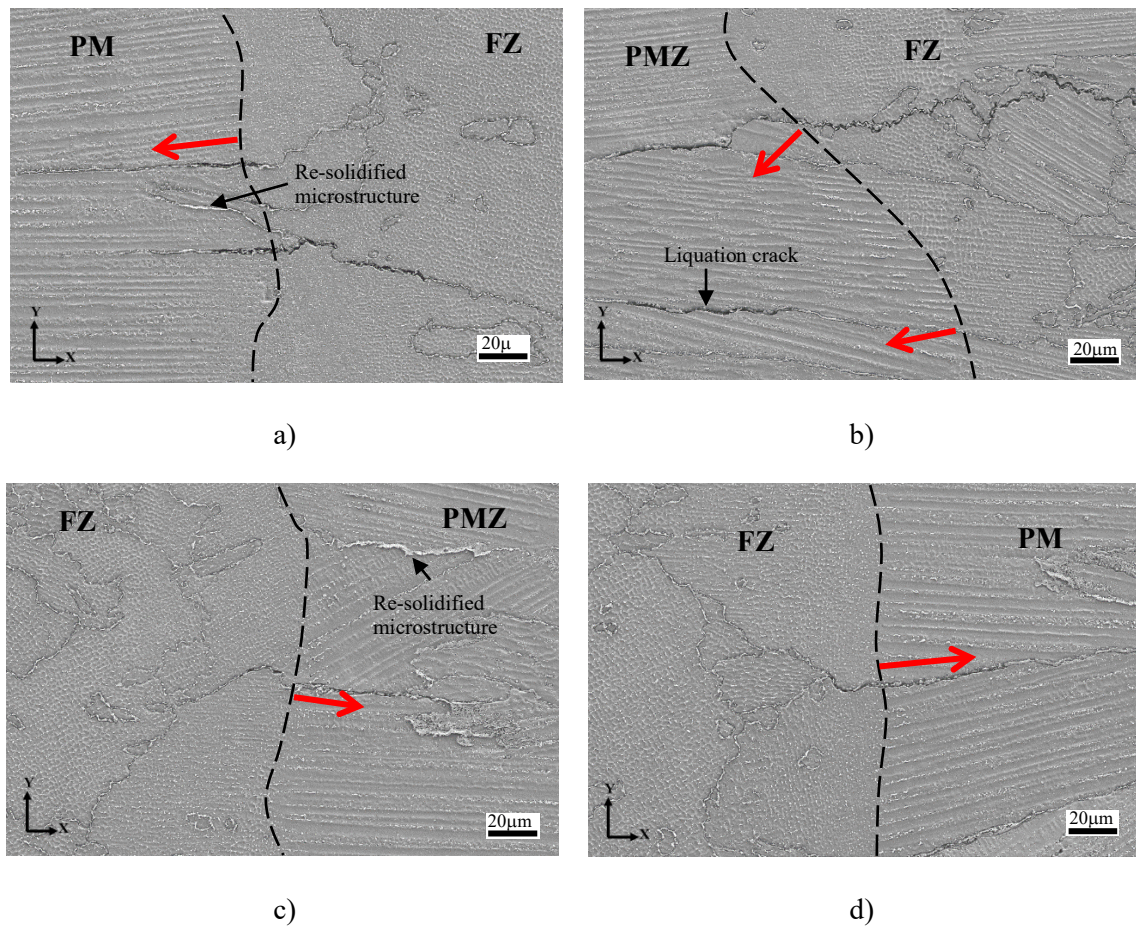


Figure 134. SEM images showing examined locations TB1 to TB4 outlined in Figure 133a, (a) to (d) respectively. Red arrows represent heat flux directions. Evidence of grain boundary liquation, re-solidified microstructure, and liquation cracking can be observed and pointed out by black arrows

The single-track experiment has demonstrated that liquation cracking did occur. However, it is not possible to identify where these cracks initiated in a bulk sample due to multiple thermal cycles. It can be suggested that grain boundary liquation and then solidification cracking occur during each layer hatching. As illustrated in Figure 135a, grain boundary liquation always occurs during layer hatching in EB-PBF. As long as the build height  $H < H'$ , there will be not liquation cracking occurs as the triggered thermal stresses are not sufficient. This has been suggested and discussed previously in chapter 4.2.3 as the effect of changing thermal conditions along the build direction during EB-PBF. When  $H > H'$ , the change in thermal conditions result in increasing induced thermal stresses that sufficiently trigger liquation cracks, as demonstrated in Figure 135b. The value of  $H'$  depends on the specific EB-PBF parameters used as well as the sample's geometry. The liquation cracks will keep propagating along the build direction. How these cracks have grown and formed the crack network, as observed in Chapter 5 will then be analyzed and discussed in the next section.

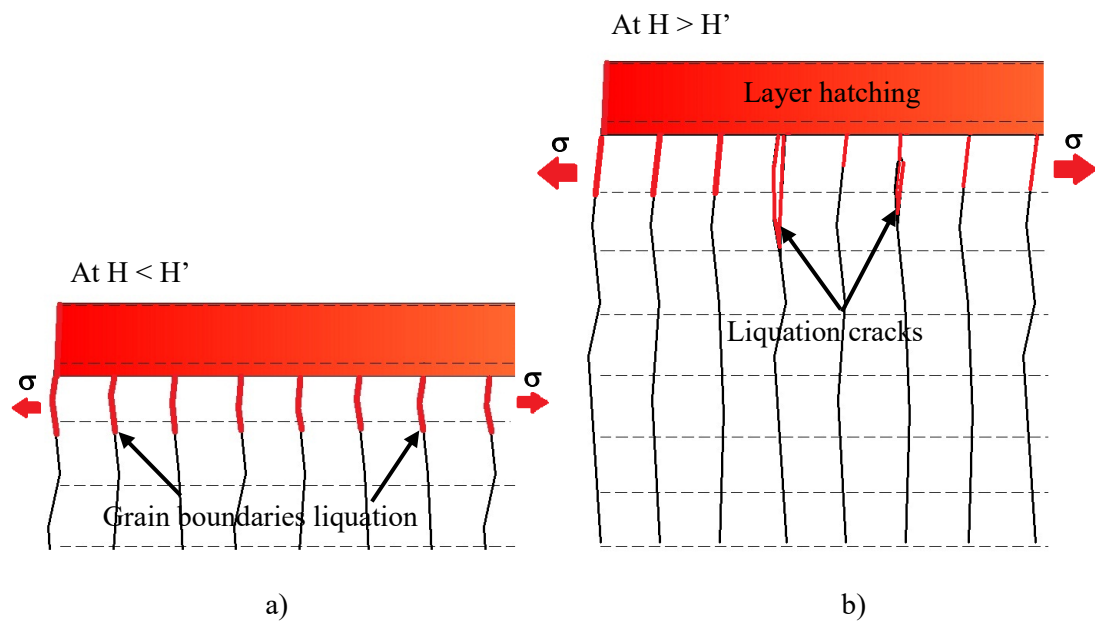


Figure 135. Schematic illustration suggesting the liquation cracking initiation. (a). Grain boundary liquation always occurs but no liquation cracking at  $H < H'$ ; (b). As  $H > H'$ , thermal stresses are sufficient to trigger liquation cracking to occur. The value of  $h'$  depends on the sample's geometry and the used EB-PBF parameters

#### 6.1.2. Cracks propagation

The crack network characterized in chapter 5 has revealed how cracks appear during grinding downward layer-by-layer. The un-cracked grain boundaries orientated more aligned with the last layer's scan direction  $SD_{Final}$  appear to have cracked in lower and lower layers. As compared to the FO25 sample, the FO50 sample does not have H-dendrites, therefore cracks are able to grow to the top surface. In addition, there are more layers obtained after grinding process for FO50 than the FO25 sample, thus the examination of the crack growth using the FO50 sample is more advantage. The sequence of crack development observed in chapter 5 is now further analyzed in depth with respect to the suggestion of crack propagation mechanism.

The sequence of crack development as observed and explained in chapter 5 is shown again in Figure 136. This suggests that if there was another layer (i.e. Layer 0 on top of Layer 1<sup>st</sup>), the crack would have actually grown to the sample surface, after hypothetical Layer 0. This is because, during Layer 0 building, the crack would be normal to the  $SD_{Final}$ . In other words, if there was a Layer 0, the crack should be seen in all the layers from Layer 0 to Layer 5<sup>th</sup>. For the same reasoning, before Layer 1<sup>st</sup> (last layer), there was a crack in Layer 2<sup>nd</sup>. It can be reasoned that, during the melting of Layer 1<sup>st</sup>, liquid has backfilled the crack found in Layer 2<sup>nd</sup>. However, re-cracking has not occurred as the stress state level during Layer 1<sup>st</sup> building is adverse to the formation of solidification cracking in the layer 1<sup>st</sup> and of liquation cracking (re-

cracking) in Layer 2<sup>nd</sup>. The fact that the crack in Layer 3<sup>rd</sup> and 4<sup>th</sup> may not be fully continuous have suggested that the liquid backfilling may actually have reached to Layer 3<sup>rd</sup> or even down to Layer 4<sup>th</sup> at least locally, as illustrated in Figure 136.

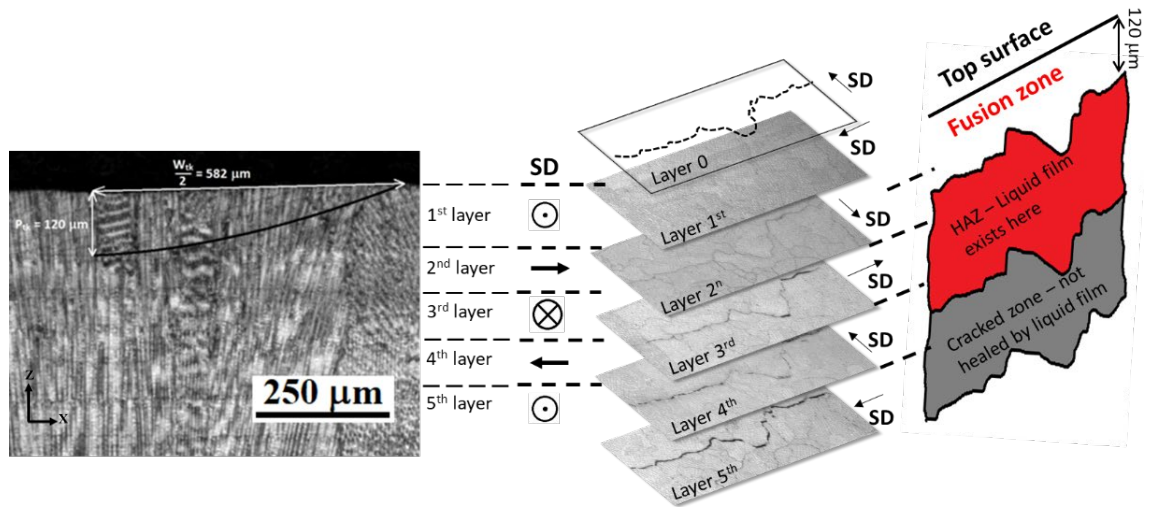


Figure 136. Schematic illustration the sequence of crack growth from Layer 5<sup>th</sup> to a hypothetical Layer 0 of area 1 outlined in Figure 131 for the FO50 sample. The suggestion of a liquid film backfills the crack and how the crack is healed and re-cracked with respect to the scan direction. Further investigation on the liquid backfilling is conducted near the top surface from XZ viewing direction. Figure 137 shows SEM images of the examined location. The last layer together with track boundaries can be seen. A crack from below is observed growing toward the last layer. However, it could not reach the top surface as the liquid from the scanning track had backfilled. Higher magnifications (Figure 137b, Figure 137c, Figure 137d) show re-solidified microstructure observed not only at the grain boundary but also at sub-cell boundaries. The re-solidified microstructure appears to be thicker as compared with that observed in the single-track sample. This can be the result of heat accumulation from the overlapping of tracks. As can be seen in Figure 137a, the examined grain boundary microstructure may have been remelted and/or backfilled four times, from track  $n$  to track  $(n+3)$ .

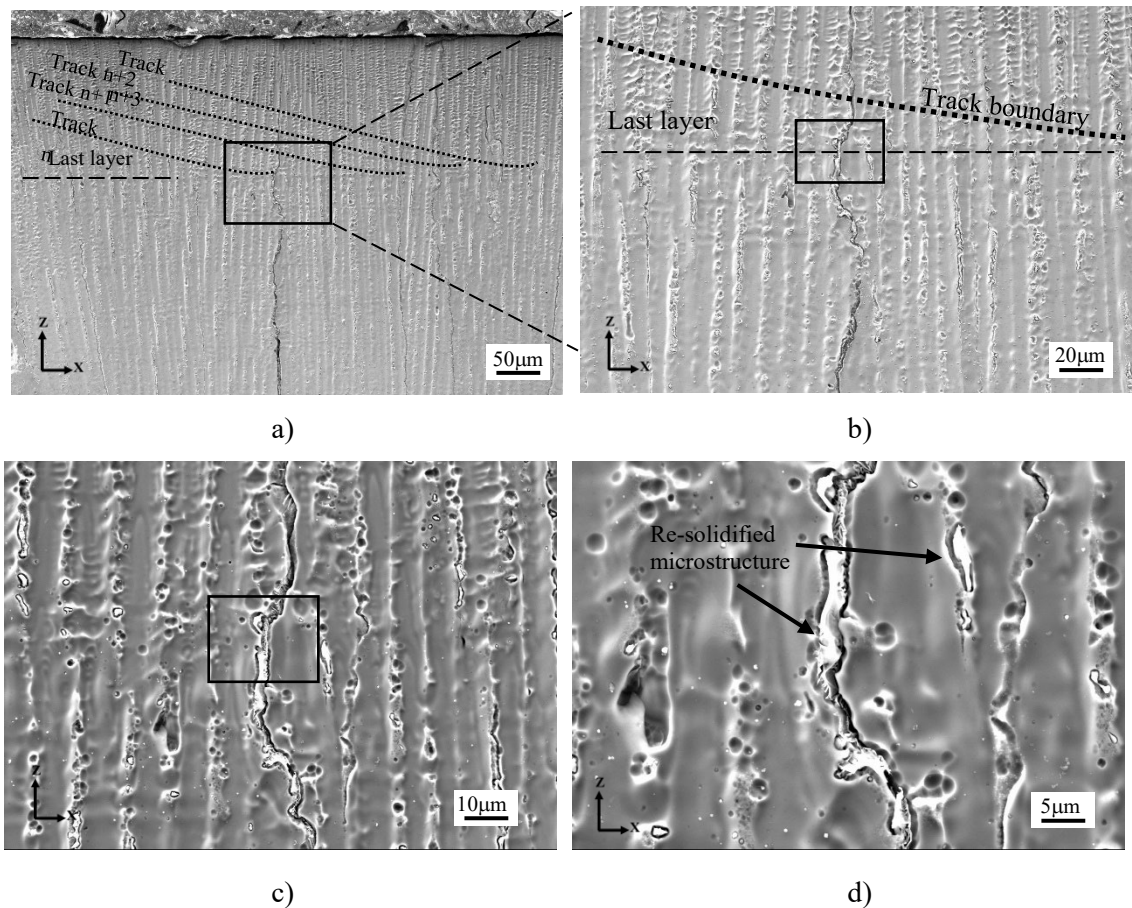


Figure 137. SEM images showing (a). Observation of the re-solidified microstructure indicating backfilled healing that prevents crack to propagate to the top surface. (b). Higher magnification of the selected area in (a); (c). Higher magnifications of the selected area in (b) and (d). Higher magnifications of the selected area in (c). The re-solidified microstructure is shown by the black arrow

The above discussion suggests a mechanism explaining how a crack may grow on and off alternately following the alternating scan directions. This is illustrated schematically in Figure 138a. Starting with layer 4<sup>th</sup>, during solidification, the hot crack along the dendritic grain boundaries had grown to start from the liquated boundary of columnar grains. During layer 3<sup>rd</sup> scanning, liquid has backfilled the crack below the melt track for a distance, and thus no liquation and no solidification cracking occur as the direction of thermal stress is not favorable for cracking. During layer 2<sup>nd</sup> solidification, however, thermal stress is favorable and thus promotes cracking again (liquation cracking first and then solidification cracking). The scanning process in the top layer (layer 1<sup>st</sup>) is the same as that in layer 3<sup>rd</sup>, and thus no cracking occurs in both layer 1<sup>st</sup> and largely layer 2<sup>nd</sup>. Cycles of cracking and healing locally repeat alternately for the top two layers as the build continues, resulting in the actual growth of a long crack. Solidification cracking occurs in each alternating cycle but the final long cracks have actually resulted from liquation cracking.

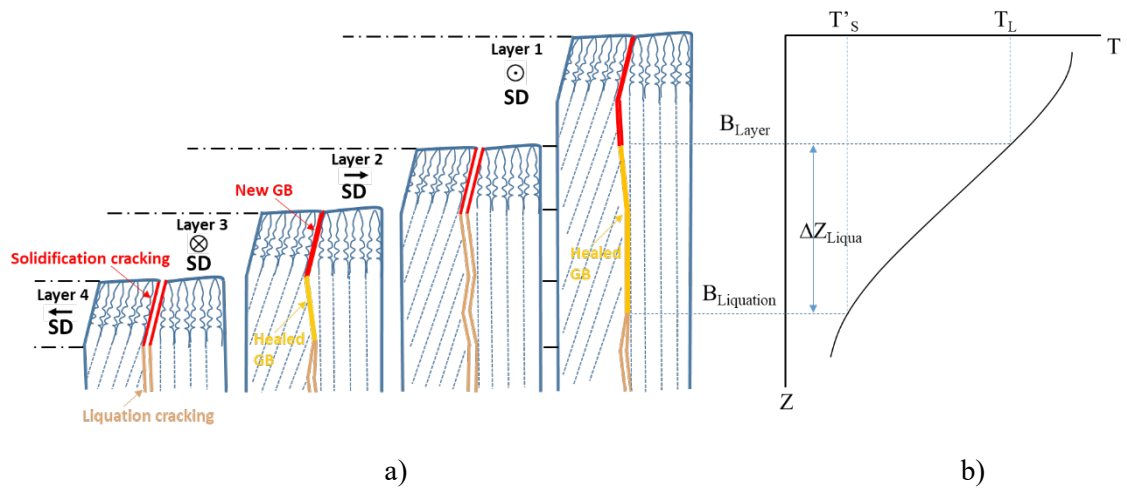


Figure 138. Illustration of (a). Hot cracking through cycles of liquation cracking and solidification cracking, healing of crack and then liquation cracking and solidification cracking again during building and (b). Temperature distribution near layer boundary.

The mechanism illustrated in Figure 138a and the depth of liquation refilling ( $\Delta Z_{Liqua}$ ) should correspond to the temperature distribution near the layer boundary ( $B_{Layer}$ ) as illustrated in Figure 138b. The liquid can reach to the depth location (liquation boundary,  $B_{Liquation}$  in Figure 138b) at which the temperature is the last solidification point of the alloy. In order to properly estimate the  $\Delta Z_{Liqua}$ , further observation of cracks without etching the sample should be done. As seen in SEM images in Figure 137, sample after electrolytic treatment may deepen the grain boundaries that can cause confusion when identifying crack's tip for measuring the  $\Delta Z_{Liqua}$ . Figure 139 shows two OM images of the mechanically polished the FO50 sample. The ZY-direction image shows a crack that has grown to the top surface (Figure 139a). In Figure 139b, two cracks have terminated in that ZX cross-section. The crack A stops at  $\approx 200 \mu\text{m}$  and the crack B stops at  $\approx 250 \mu\text{m}$  from the sample surface. In addition, grain boundaries without having experienced hot cracking in the top region are not revealed in the polished sample. This is consistent with the crack healing and re-cracking that have been demonstrated.

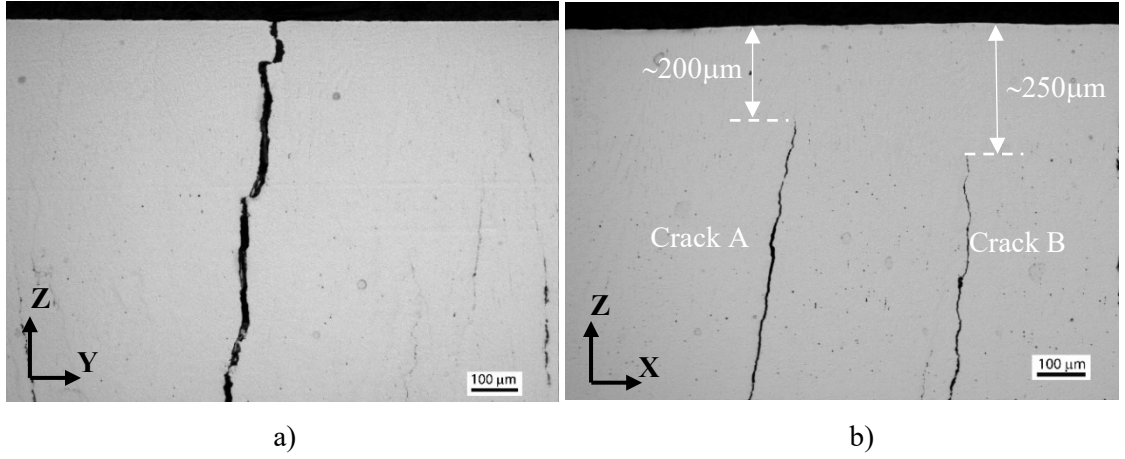


Figure 139. OM images showing the as-polished the FO50 sample: (a) ZY cross-section and (b) ZX cross-section.

The length of the liquid film, or  $\Delta Z_{Liqua}$ , is measured from the tips of the cracks ( $B_{Liquation}$ ) to the last layer's boundary (bottom of the melt/track) which is  $\approx 120\mu\text{m}$  from the top surface. Then,  $\Delta Z_{Liqua}$  is around  $80\mu\text{m}$  to  $130\mu\text{m}$ , as measured from crack A and crack B in Figure 139.  $\Delta Z_{Liqua}$  is approximately equal to the solidification range ( $\Delta T' = T_L - T_S'$  where  $T_L$  is the liquidus and  $T_S'$  is the actual solidus of the alloy) over the temperature gradient of the solid-liquid interface ( $G_{L-S}$ ) at the layer boundary. Ronan's extensive measurements [13] indicate  $\Delta T'$  is approximately 180 K. Then:

$$G_{L-S} \approx \frac{\Delta T'}{\Delta Z_{Liqua}} = \frac{180 \text{ K}}{(0.8 \sim 1.3) \times 10^{-4} \text{ m}} = (1.4 \sim 2.25) \times 10^6 \frac{\text{K}}{\text{m}} \approx 2 \times 10^6 \frac{\text{K}}{\text{m}}$$

The estimated result of  $G_{L-S}$  is compared to the calculated value of  $G = 6 \times 10^6 \text{ K/m}$  in chapter 4, chapter 4.3.1, which has been explained, is an overestimated value.

No detailed research has been found in the literature on studying  $G_{L-S}$  during EB-PBF of Co-superalloys. There has been, however, a series of studies on EB-PBF of Ni-superalloy IN718 where  $G_{L-S}$  is a major consideration. Raghavan et al. [30] conduct numerical modeling and predict maximum  $G_{L-S}$  which should be at TB during EB-PBF of IN718 to be  $5 \times 10^6$  to  $1 \times 10^7 \text{ K/m}$ . More recently, Raghavan et al. [150] estimate  $G_{L-S}$  at track bottom TB during EB-PBF to be  $\sim 1 \times 10^6 \text{ K/m}$  based on comparing the predicted value of primary dendrite arm spacing ( $\lambda_1$ ), which were also obtained based on a theoretical model of  $\lambda_1$  relating to  $G_{L-S}$  and  $R_{L-S}$  (solidification rate), to the measured  $\lambda_1$  value. The values of  $G_{L-S}$  and  $R_{L-S}$  were obtained based on simulation. Recently, Lee et al. [151] also based largely on simulation, predict maximum  $G_{L-S}$  to be between  $5 \times 10^5$  and  $1 \times 10^6 \text{ K/m}$ . The value of maximum  $G_{L-S}$  at  $(1.4 \sim 2.25) \times 10^6 \text{ K/m}$  estimated in this work is close to the values of the more recent work of Raghavan et al. [150] and of Lee et al. [151].

### Compare to EB-PBF of F75 alloy at same fabricating conditions (FO50 conditions)

From the analysis above, as is also commonly understood for welding, solidification freezing range of the alloy plays a crucial role in enhancing or diminishing the grain boundary liquation. As has been explained in chapter 2, the EB-PBF of Co-29Cr-6Mo alloy fabricated with the same conditions as the FO50 sample presented in no cracking. An example is shown in Figure 140a and Figure 140b. The thermal analysis results in chapter 4 have shown that Co-29Cr-6Mo alloy has a narrow solidification freezing range, which is 15-25 °C. If the Eq. 11 is applied with the estimated value of the thermal gradient of  $\approx 2 \times 10^6$  K/m (as same EB-PBF conditions used), then the estimated liquid film during EB-PBF Co-29Cr-6Mo alloy will be:

$$\Delta Z_{Liqua.} \approx \frac{\Delta T'}{G_{L-S}} = \frac{25 \text{ K}}{2 \times 10^6 \frac{\text{K}}{\text{m}}} = 12.5 \times 10^{-6} \text{ m} \approx 12.5 \mu\text{m}$$

The  $\Delta Z_{Liqua.}$  in EB-PBF of Co-29Cr-6Mo alloy is much shorter than that of Co-29Cr-10Ni-7W alloy. This suggests that the grain boundary liquation is very low compared to EB-PBF Co-29Cr-10Ni-7W alloy. Thus, there is not a good condition for liquation cracking or solidification cracking to occur. To clarify this, microstructure at the layer boundary of EB-PBF Co-29Cr-6Mo sample is then examined. Figure 140c and Figure 140d show high magnification SEM images taken at the selected location in Figure 140a.

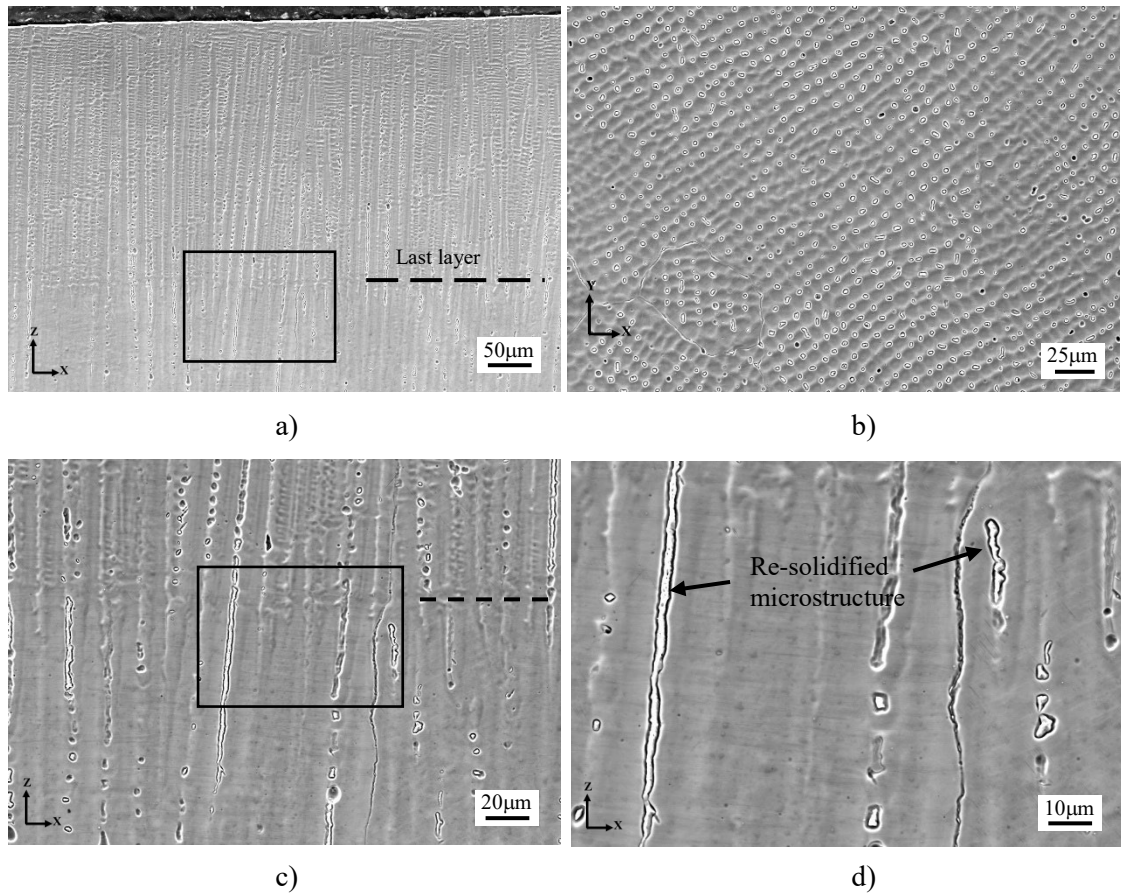


Figure 140. SEM images showing EB-PBF Co-29Cr-6Mo sample: (a). ZX cross-section of the last layer; (b). YX cross-section of the last layer; (c). High magnification of selected location in Figure 140a and (d). High magnification of selected location in Figure 140c. Grain boundary with no re-solidified microstructure shown in (b), (c-d) indicates very low grain boundary liquation

As can be seen in Figure 140c and Figure 140d, the re-solidified microstructure is not clear at the grain boundary, even observed at high magnification. However, a high amount of the re-solidified microstructure is observed at the sub-cells boundary. This is in good agreement with the observation in EB-PBF Co-29Cr-6Mo alloy at low carbon content (0.05 wt%) in the work of Chauhan [123] since only inter-dendritic precipitates are observed. Since hot cracking always occurs intergranular, the low content of the second phase observed at grain boundaries may not provide a good condition for the liquation to occur. Thus, this is unfavorable for liquation cracking.

Regarding the present Co-29Cr-10Ni-7W alloy, despite the fact that it is different in major alloying elements to Co-29Cr-6Mo alloy, the present alloy, however, contains higher carbon content (0.15 wt% C), which is the main element of eutectic carbides and/or precipitates former [152]. Thus the segregation of the carbon to grain boundaries will increase and result in considerable second phase observed, as shown in Figure 141. Higher carbon content (0.15 wt% C) is also observed to increase the amount of the second phase at grain boundaries in EB-PBF Co-29Cr-6Mo alloy [123] and consequently, cracks were also reported.

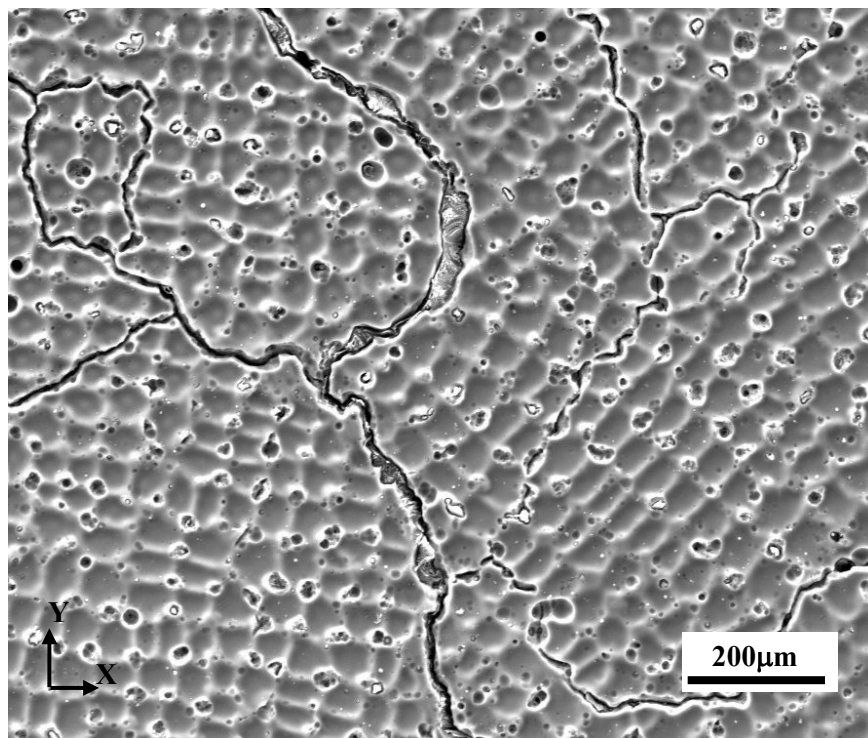


Figure 141. SEM image showing a considerable amount of the second phase observed at grain boundaries in EB-PBF Co-29Cr-10Ni-7W alloy

The effect of carbon to hot cracking sensitivity (HCS) in EB-PBF Co-29Cr-10Ni-7W and Co-29Cr-6Mo alloys can be explained by referring to literature on HCS in casting. The HCS index proposed by Rappaz et al. [83] and is expressed by Eq. 15 (in chapter 2.3.1) describes the maximum strain rate that the mushy zone can withstand prior to a void forms. The authors showed that the HCS index of Al-Cu alloy relates to the Cu content following a  $\Lambda$ -shape curve, as shown in Figure 142. The increasing of Cu content from 0-3wt pct shows a dramatic increase and decrease in HCS with a peak at around 1.4wt pct. Similar  $\Lambda$ -shape curve relationship between HCS index and Cu content can be found in the work of Dou and Phillion [79] and Liu and Kou [153]. The influence of alloying elements was also reported for casting IN792 Ni-based alloy [77] and cast steel [71], however in a non-linear relationship. In their work [77], Zhang and Singer observed that by increasing the Ti addition from 2 wt% to 4.5 wt%, the IN792 alloy's castability is lowered which results in higher HCS. Chojecki et al [71] showed that the brittle-ductile transition temperature increases as the carbon content is increased from 0.11 wt% to 0.6 wt% in their cast steel samples. Consequently, the alloy becomes more sensitive to hot tearing.

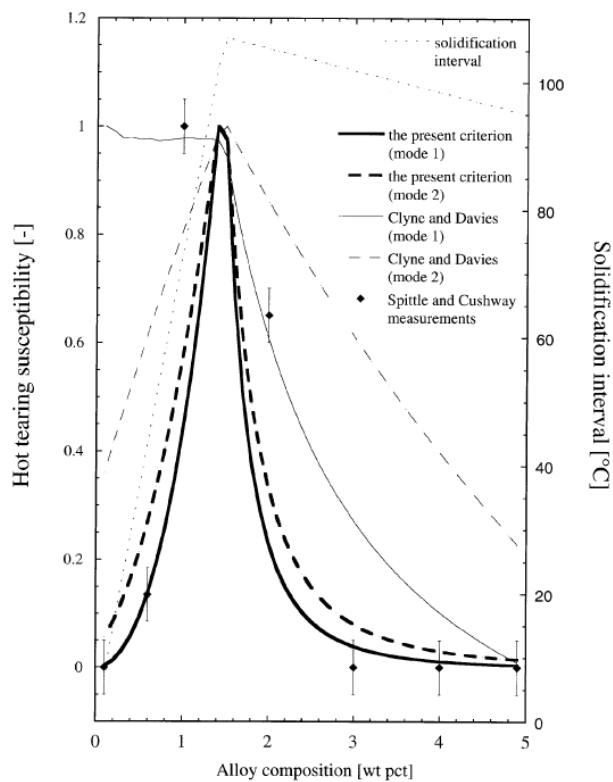


Figure 142.  $\Lambda$ -shape curve showing concentration dependence of the HCS criterion as compared from various studies by Rappaz et al. [83]

The above brief summary of HCS in literature for casting suggests that carbon may have a similar effect to HCS of Co-29Cr-10Ni-7W and Co-29Cr-6Mo alloys. In the work of Chauhan [123] cracking was observed for the Co-29Cr-6Mo alloy at 0.15 wt% C, but not for those with 0.05 wt% and 0.1 wt%. Moreover, the carbon content is approximately 0.24 wt% was used in other studies on EB-PBF Co-29Cr-6Mo [35, 39, 154] and no cracking was reported. Therefore, it can be suggested that the effect of carbon to HCS for Co-29Cr-6Mo alloy may follow the  $\Lambda$ -shape curve, as illustrated in Figure 143. The suggested  $\Lambda$ -shape relationship may also be applied to Co-29Cr-10Ni-7W alloy. Han [7] developed an estimation of hot tearing tendency ( $H$ ) based on the alloy's compositions. This is similar to the HCS index in evaluating hot cracking sensitivity.  $H$  is shown to be 2.647 and 2.118 for the present Co-29Cr-10Ni-7W alloy (0.15 wt% C) and the ASM nominal alloy specification (with 0.25 wt% C). This shows that increasing the carbon content can reduce the HCS. The narrow solidification freezing range  $\Delta T' = 25$  K in combination with low carbon content (0.01 wt%C), can be the reasons that no hot cracking has been observed during EB-PBF of the present Co-29Cr-6Mo alloy. On the other hand, the present Co-29Cr-10Ni-7W alloy has wide  $\Delta T' = 180$  K and 0.15 wt% C, therefore, it is very prone to hot cracking. However, to clarify the suggestion, further investigation on the role of carbon in Co-29Cr-10Ni-7W alloy needs to be thoroughly conducted.

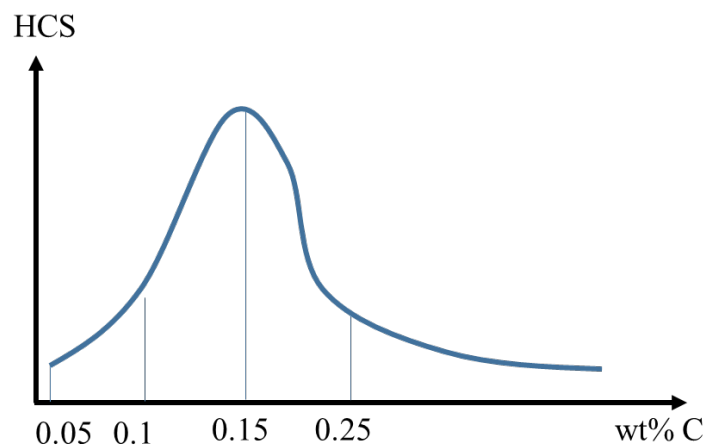


Figure 143. Hot cracking sensitivity versus carbon content suggested for Co-29Cr-6Mo alloy.

## 6.2. Other influential factors to hot cracking

How hot cracking may have initiated and developed during EB-PBF has been suggested and discussed. The discussion shows that grain boundary liquation plays a crucial role. The length of the liquid film, as shown in Eq. 11, depends on the alloy's  $\Delta T'$  and the process thermal gradient  $G$ . Moreover, it has been shown that the grain boundary misorientation also affects the hot

cracking susceptibility in PBF-AM processes [112, 113, 120, 126]. Studies on grain boundary misorientation [112, 113, 120, 126] are conducted on ZX or ZY cross-sections. The EBSD orientation map from these views normally shows crack between two or three adjacent misoriented columnar grains. However, crack growth is shown to occur through many grains when observed in XY cross-section. This has shown the limitation of ZX and ZY cross-sectional EBSD maps on an understanding of how the misorientation angle affects the overall crack network growth. Thus, the influence of grain boundary misorientation on crack growth should be examined by the XY cross-sectional EBSD map.

In addition to grain boundary misorientation, how stresses orientation affecting crack growth needs to be investigated. Based on previous observation of how cracks orientate on the top surface as well as how they may be healed/re-cracked from layer to layer, the 90° rotation of scan direction is shown to affect the stresses orientation. Thus, the relationship between the scan direction and stresses orientation needs to be clarified. This will be done by using numerical simulation. How stresses orientate and affect the cracking behavior during an EB-PBF single scan will be visualized and analyzed.

#### 6.2.1. Grain boundary misorientation

It is known, after Wang et al.'s [155] theoretical and experimental work, that solidification cracking is promoted above a certain grain boundary misorientation angles. Wang et al. [155] found that there is a critical angle of misorientation (of 13° in their work) between two neighboring dendrite grains in the solidification direction above which solidification cracking develops. The misorientation of neighboring grains corresponding to hot cracking is presented in Figure 144 for the crack network observed in the present work. For clarity, the crack network in Figure 144a is traced and is superimposed in the XY-EBSD orientation maps Figure 144b and Figure 144c. In the “normal” map (Figure 144b), the color is not much different and this means a preferred growth of [001] along the build direction. In the other two maps (Figure 144c), it is clear that the colors of both sides along a crack are highly different meaning high angles of misorientation for most of the crack network.

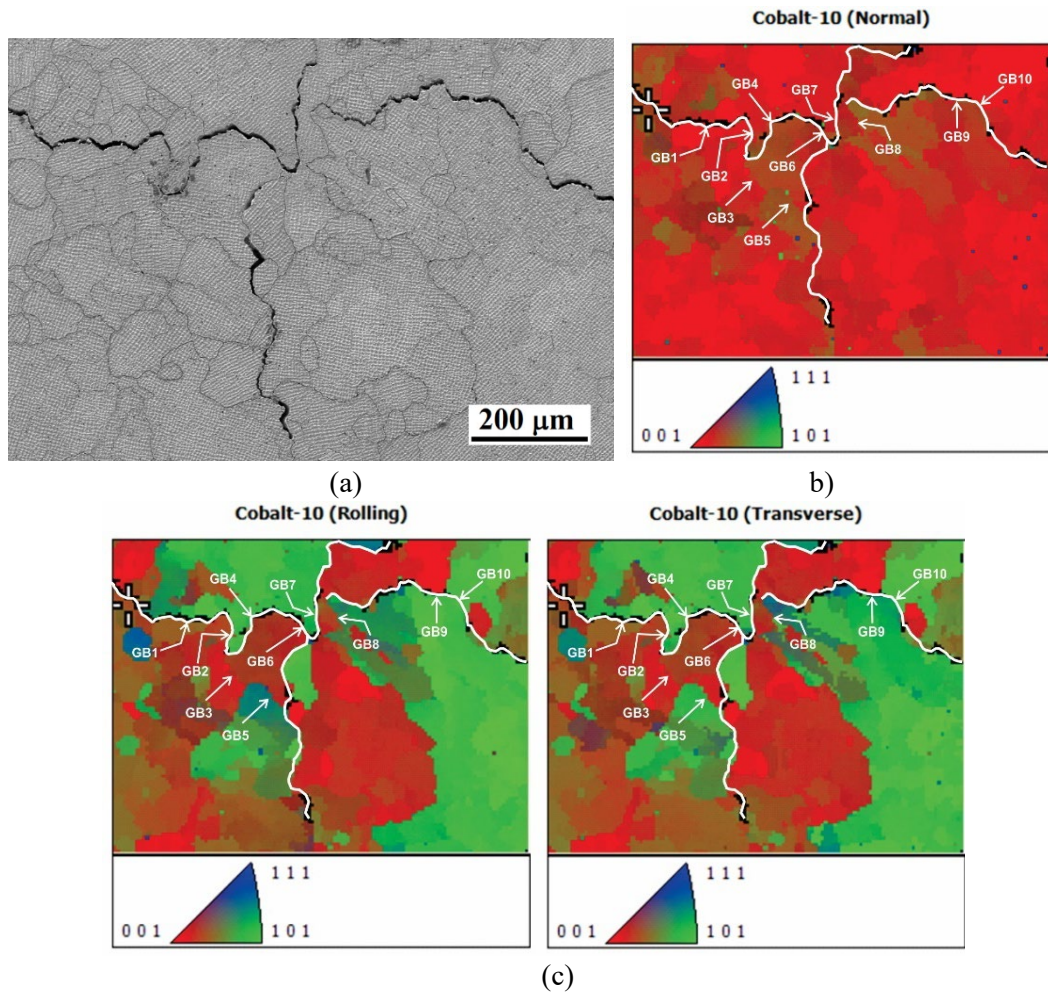


Figure 144. Evidence showing crack growth may be more relating to growth of high misorientation of secondary dendrites.

Table 5 lists the misorientation angles of neighboring grains indicated in Figure 144. The three values in red are for GBs next to but not part of the crack path. Misorientation angles of GBs in the crack network range from  $29.8^\circ$  to  $51.3^\circ$ , except GB10 for which the angle is low at  $13.7^\circ$ . This means that a small section of a low angle section GB can also be a small part of a crack path. GB3 is next to the crack path and as it is low angle misorientation, cracking did not select this GB to form a crack path. GB4 is a high angle boundary but, as GB3 is a low angle GB and thus had not cracked for a crack to propagate to GB4. Instead, cracking occurs on the other side of the grain bordering the next grain in a high misorientation angle. For the same reason, the relatively low angle of GB8 has not become part of the crack path. These features of grain misorientation affecting the development of crack network can be revealed better by using XY-EBSD maps, as in Figure 144, than those in maps normally based on EBSD scanning in ZX or ZY planes commonly presented in the literature.

Table 5. Grain boundary (GB) number and the corresponding misorientation angle of the two neighboring grains.

GB no.	GB1	GB2	GB3	GB4	GB5	GB6	GB7	GB8	GB9	GB10
Angle	30.4°	28.8°	14.5°	39.0°	37.3°	51.3°	46.0°	22.9°	45.4°	13.7°

### 6.2.2. Thermal stresses prediction

Hot cracking is constituted by two fundamental factors. These are the existence of liquid film at grain boundary as the intrinsic cause, and the triggered thermal stresses as the extrinsic cause. The crack network characterization shows that cracks tend to be perpendicular to the scan direction. This implies the possibility of dominant tensile stress with the stress tensors in the same direction as the scan direction. Therefore, in this section, numerical simulation of a single electron beam scan was conducted to predict as well as confirm the suggestion of the tensile loading direction emerging during the scan. Details of the simulation software and how the model was constructed has been demonstrated in chapter 3.

Transient thermal simulation using a Gaussian heat flux distribution profile was adapted from [156], expressed by the following equations:

$$Q = Q_0 \exp\left(-\frac{r^2}{r_0^2}\right) \quad \text{Eq. 19}$$

$$Q_0 = \frac{\eta VI}{\pi r_0^2} \quad \text{Eq. 20}$$

where  $Q$  is absorbed heat flux,  $r$  is the radial distance from the center of the heat source,  $r_0$  is the beam diameter,  $\eta$  is the beam efficiency coefficient,  $V$  is the voltage and  $I$  is the beam current. Details of parameters used for Eq. 19 and Eq. 20 are shown in Table 6. The movement of the heat source is defined by the beam scanning speed over the pre-defined path in the 3D block model, as shown in Figure 86. Initially, the beam speed of 400 mm/s was set. This aimed to match with the scanning speed recorded in experimental EB-PBF. However, as aforementioned, the 3D block model is smaller in size (10x10x5 mm), 400 mm/s beam speed resulted in a short life-time of the melt pool (0.025 s). This had caused longer processing time of the simulation when observing the temperature distribution at different time points. For example, if the result is displayed at five time points, then the time step is very small (0.005 s). Moreover, the aim of the simulation is to investigate the stresses orientation, the value of the beam speed is not very significant. Therefore, a beam speed of 200mm/s is selected. The life-time of the melt pool is 0.05 s. The temperature distribution is observed and analyzed at several time points  $t = 0.01$  s, 0.03 s, 0.06s, and 0.1 s. Thermal analysis results are then inputted for further thermal-stress analysis.

Table 6. Parameters used in simulation

Parameters	Unit of measurement	Values
Accelerated voltage $V$	V	60000
Beam current $I$	A	0.0057
Absorption efficiency	%	80 [156]
Assumed beam diameter $r_0$	m	0.001
Start plate temperature	°C	850

The element birth and death technique in ANSYS APDL is used to simulate the different material properties between solid and powder. Before melted by the heat source (e-beam), the powder has its own thermal properties. When heated, the powder is melted and solidifies, thus it has the solid thermal properties. During the simulation, ANSYS “killed” the elements, which are pre-assigned to powder materials. These elements are deactivated and all the elements’ load (e.g. thermal load) will be almost zeroed out. When the heat flux is applied, these “killed” elements are reactivated which will carry the solid properties. Therefore, the thermal load will be recorded and the thermal stresses can be calculated.

The heat flux boundary was set to be on the surface of the model. In addition, the solid substrate’s temperature was set to be 850 °C. The mechanical boundary used for the thermal-stresses simulation is shown in Figure 145. During the beam scan, the solidified part of the scanned track is constrained at two locations. The first location is at the solid-powder boundary, which causes restraining forces in the transverse direction with respect to the scan direction. The second location is at the tail-end of the moving molten pool. This tail-end will shrink after fully solidifying causing tensile load along the scan direction. Other locations that are in touch with powder material are free of restraint. Figure 146 plots out the thermo-mechanical properties of Co-29Cr-10Ni-7W alloy used in the model. The data was experimentally obtained and provided by CSIRO Clayton, Melbourne, Australia.

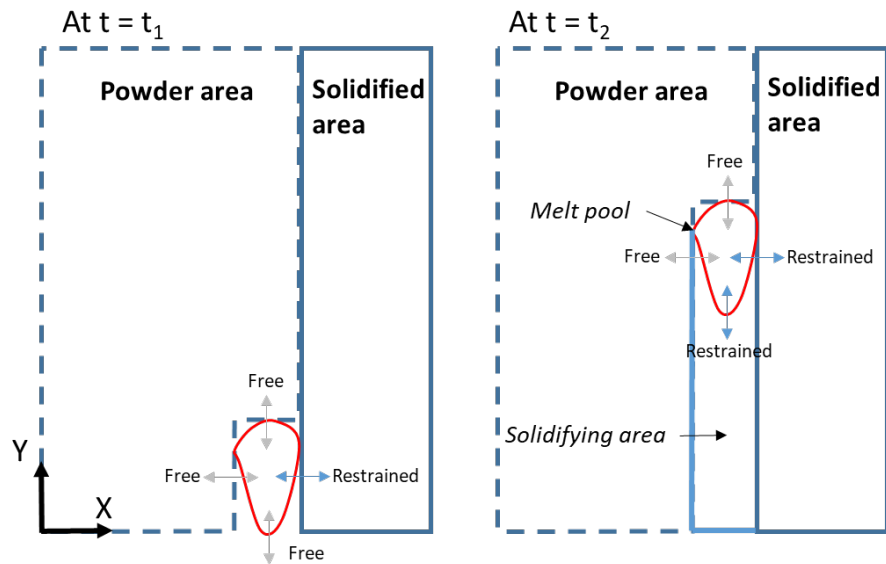


Figure 145. Mechanical boundary conditions used in the model

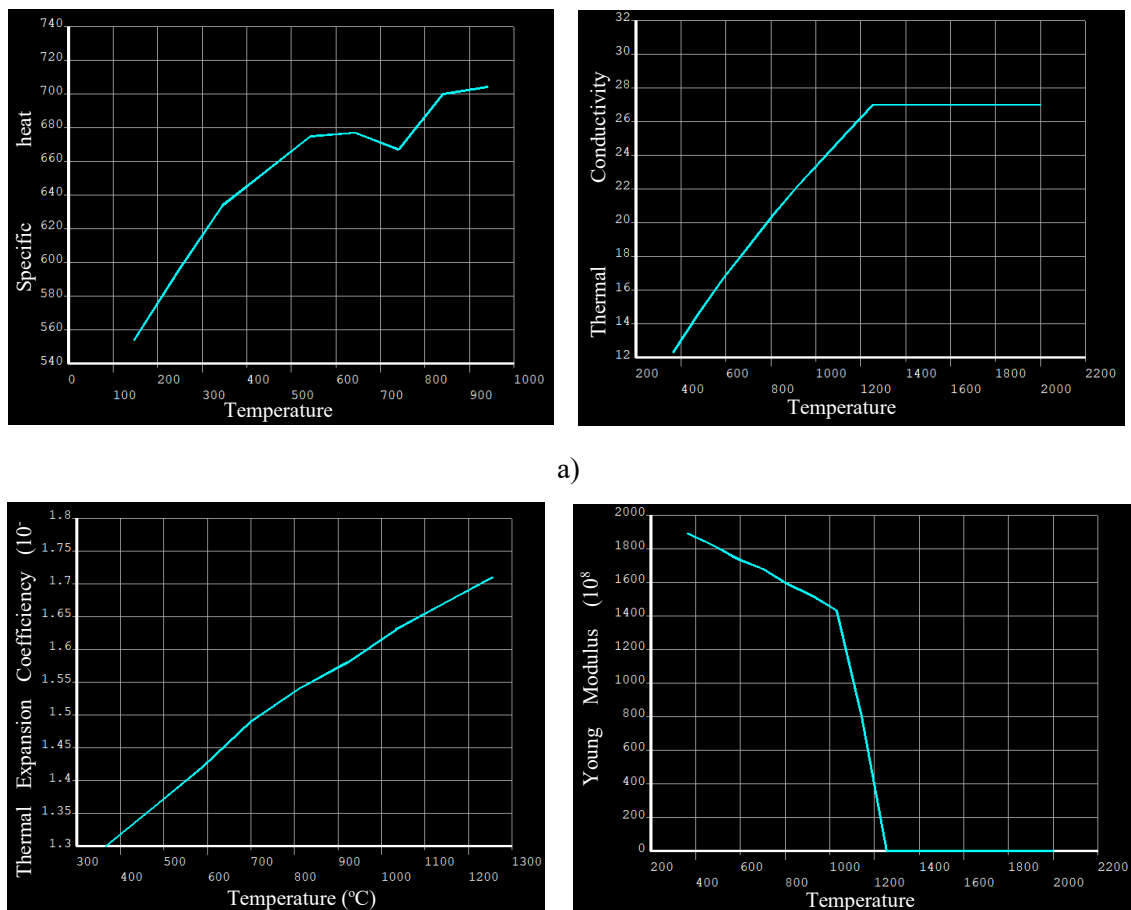


Figure 146. Temperature-dependent material properties of Co-29Cr-10Ni-7W alloy: (a). Specific heat; (b). Thermal conductivity; (c) Thermal expansion co-efficiency and (d). Young modulus

Figure 147 and Figure 148 illustrate the thermal and thermal-stresses simulation results at several time points from the initiation to the end of the scan. The scan direction is along Y-axis. The temperature distribution along the track is shown together with the corresponding stress component in the XY plane at each time point. At the beginning of the scan (Figure 147a), the melt pool has an elliptical shape. The peak temperature is approximately 2190 °C and the lowest value is the preheat temperature of the substrate 850 °C. The stress state of front and the surrounding area of the melt pool is in compression. This is due to the rapid increase in the temperature of the melt pool that results in expansion of the material. This material expansion then induces compression to surrounding materials. However, the degree of stress is not significant.

At  $t = 0.03$  s (Figure 147b), the melt pool is now elongated and has a tear-drop shape. The tail-end of the melt pool has a temperature around 1298 °C while the peak temperature remains nearly unchanged at 2190 °C. It is observed that beyond the tail-end of the melt pool, there is a cooling down area that has temperature from 999 °C to 1148 °C. In comparison to that of the stress component in the XY plane, this area has the highest tensile stress recorded as  $0.216 \times 10^9$  Pa. The degree of tensile stress gradually reduces when getting closer to the melt pool. At the track's starting point, the material has solidified and cooled down to 850 °C. As it is cooling down, thermal shrinkage occurs that pulls material backward along the scan direction. The shrinkage level is determined by the thermal expansion coefficient of the solid material and significantly depends on the local temperatures. As a result, tensile stress is imposed on this part of the scanned track (Figure 147b).

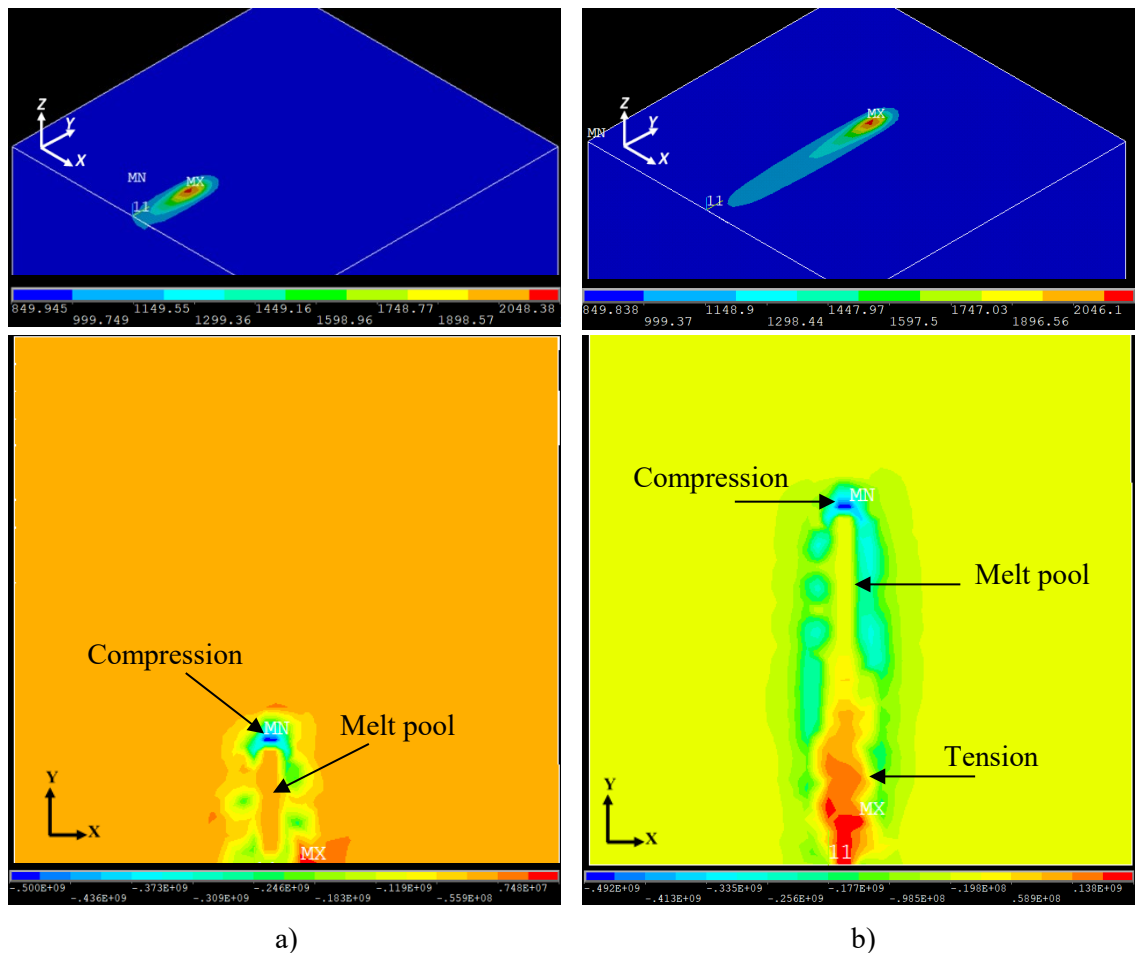
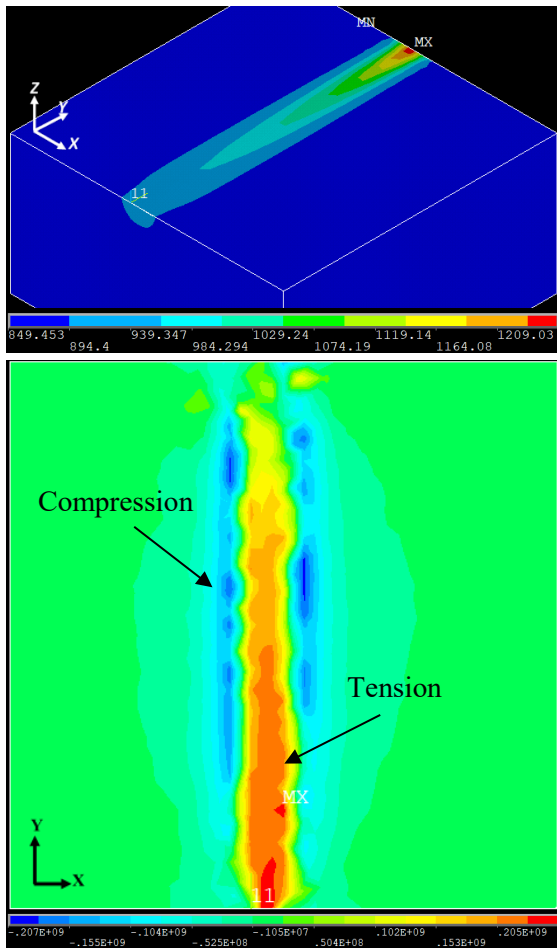
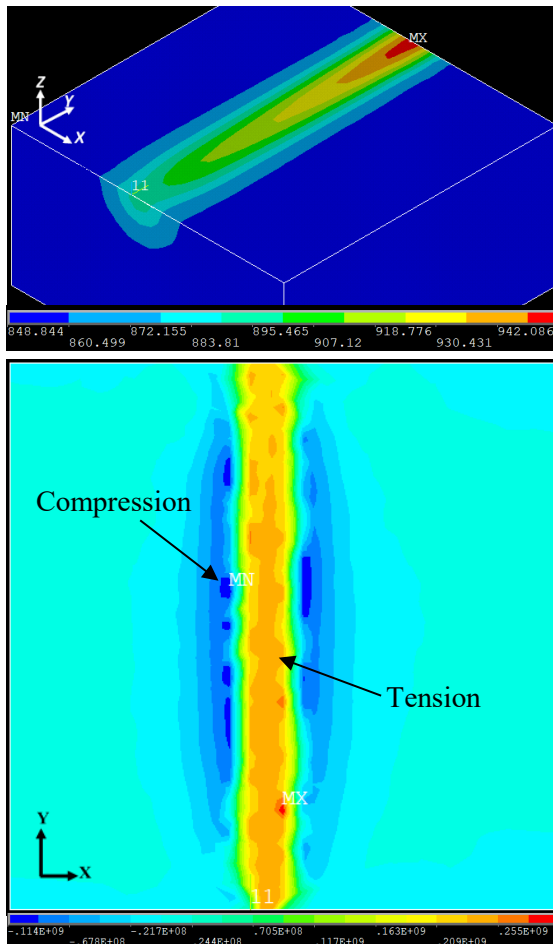


Figure 147. Simulation illustrating the melt pool and corresponding XY-stress component along the track at (a).  $t = 0.01$  s and (b).  $t = 0.03$  s

The tensile stress along the track is more obvious at  $t = 0.06$  s and  $t = 0.1$  s, as shown in Figure 148. It is noted that the scan ends at  $t = 0.05$  s for the simulation. Thus, Figure 148a and Figure 148b show the temperature distribution and the corresponding XY-stresses after the scan has finished 0.01 s and 0.05 s, respectively. The peak temperature has dropped down from 2190 °C to 1253 °C at the final location while the rest of the track has a lower temperature ranging from 890 °C to 1119 °C. Respectively, the XY-stress component at the end of the track shows the lowest tensile stress of  $0.5 \times 10^8$  Pa. In contrast, the highest stress is still at the beginning of the track where the temperature has cooled down to 850 °C. The low-temperature region results in more significant shrinkage that possibly imposes tensile stress. In Figure 148b, at  $t = 0.1$  s, the whole tracks' temperature cooled down below 1000 °C. The stress distribution is now more uniform along the track. The positive value of stress illustrates that tensile stress is the dominant state. In contrast, areas along the tracks' longitudinal edges are observed to have compressive stress imposed. This is the effect of the material expansion from the track and shrinkage from the surrounding.





a)

b)

Figure 148. Simulation showing temperature distribution and corresponding XY-stress component along the track at (a).  $t = 0.06$  s and (b).  $t = 0.1$  s, after the scan ends at  $t = 0.05$  s

In order to provide a better illustration, the principal stresses' vectors are plotted and shown in Figure 149. Considering a single element that has a cubic shape, at a specific orientation with respect to the sample coordinate (XYZ) that the shear stresses components are zero, the normal stresses to the element's faces are the principal stresses, denoted as  $\sigma_1$ ,  $\sigma_2$  and  $\sigma_3$  in which  $\sigma_1 > \sigma_2 > \sigma_3$ . In Figure 149, the arrows' directions of these stress vectors illustrate the tensile or compressive states at that location. If the arrows face into each other, it shows that the particular element is under compressive stress and vice versa. In addition, the scale of the arrows displays the intensity of the imposed stress. As can be seen in Figure 149a, at the terminal stage of the beam scan ( $t = 0.05$  s), there are no stresses recorded at the melt pool area (which is at the end of the track). However,  $\sigma_1$  stress vectors (white color) are observed throughout the rest of the track both in large amount and intensity. These vectors appear as a sign of tensile stress since the arrows are facing outward to each other. In addition, the  $\sigma_1$  vectors' directions are dominant along the scan direction with only a few of those having other directions. This suggests that the

track has undergone significant tensile stress along the scan direction as  $\sigma_1$  is the maximum principal stress.

The second principal stress  $\sigma_2$  (yellow color) can be seen spreading throughout the track, excepting the melt pool area. The intensity of  $\sigma_2$  can be seen as similar as the  $\sigma_1$ , however, the amount is less than the  $\sigma_1$ . The  $\sigma_2$  directions are perpendicular to the scan direction. The  $\sigma_2$  stress vectors indicate that they are tensile stresses. The last principal stress  $\sigma_3$  (blue color) distributes mainly along the tracks' longitudinal edges. The stress vectors indicate that they are compressive stress and are not significant in intensity.

In Figure 149b, at  $t = 0.1$  s, the principal stresses have fully developed as the scan has finished and the track has been cooling down. The  $\sigma_1$  and  $\sigma_2$  still dominate along the track, which imposes tensile stresses in both directions, parallel and perpendicular to the scan direction, respectively. In addition, the distribution density is higher than those observed in Figure 149a. This is because the track is now fully solid and the restraining forces between elements are much greater. Since  $\sigma_1$  has the highest intensity and amount, tensile stresses along the scan direction are the highest. It is of note that the  $\sigma_2$  intensity is lower than the  $\sigma_1$  can be due to the pre-defined mechanical boundary conditions, as shown in Figure 145. The track is only constrained at the solid side and free at the other side where it is in contact with the powder. Therefore, the most significant tensile stress imposed on the track is along the scan direction.

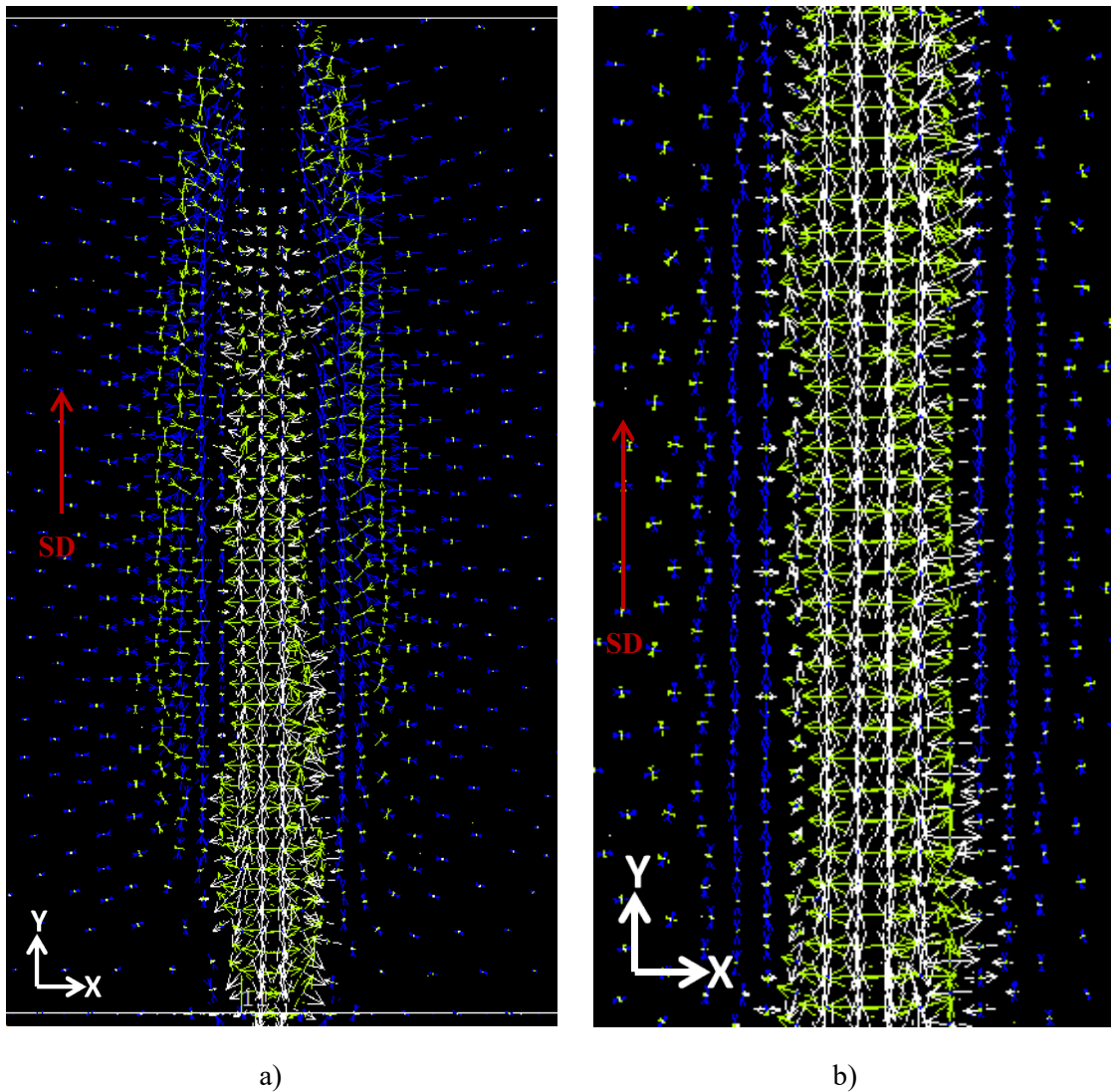


Figure 149. Simulation result showing the principal stresses' vectors distributed throughout the track at (a).  $t = 0.05$  s and (b).  $t = 0.1$  s (at higher magnification). White, yellow and blue arrows represent for the  $\sigma_1$ ,  $\sigma_2$  and  $\sigma_3$  principle stresses, respectively. The size of the arrows illustrates the stress intensity. Outward arrow demonstrates tensile stress and vice versa.

The simulation results obtained from both Figure 147, Figure 148 and Figure 149 have confirmed the suggestion of scan direction related to crack orientation. Moreover, this can be used to explain the observation of cracks perpendicular to the scan direction presented in chapter 5. The simulation is also in good agreement with the study of Tadano et al. [156]. The thermal-stress analysis model of EB-PBF René 80 Ni-based alloy shows that the in-plane stresses distribution is anisotropic, in which the tracks' longitudinal direction has the highest tensile stress. However, in their study [156], the authors establish the restraining boundary conditions at both ends of the scanning track, which therefore is expected to cause higher stress along the scan direction. This is not quite appropriate, as ahead of the melt pool is loose powder material. In addition, the moving melt pool is in liquid-state, therefore there should be no constraints at this end. Jamshidinia et al. [157] proposed the coupled CFD-FEM model of EB-

PBF of Ti-6Al-4V alloy. The structural model considers a single scan on a powder layer, which means there is no constraint set around the track and the material is free to expand/contract. The mechanical analysis result shows an expansion of solidified material at the two ends of the scanned track, which imposes a tension along the tracks' scan direction. Despite the model is simple and not close to the real situation, the non-uniform stress distribution analyzed by Jamshidinia et al. [157] also shows a similar result to Tadano et al. [156].

A more advanced thermo-mechanical stress analysis can be found in literature, however, it has been applied for the LB-PBF process. The basic thermal stress condition difference between LB-PBF and EB-PBF is the preheating stage of the build plate, which may cause thermal stress to be higher in LB-PBF than in EB-PBF. However, as the main point is how the stresses orientate during the scanning process, the thermal-mechanical analysis result for LB-PBF process can be applicable to EB-PBF. Parry et al. [158] considered a model simulating LB-PBF process of Ti-6Al-4V alloy. The thermal-mechanical boundary conditions are similar to the illustration in Figure 145. The analysis results show that higher tensile stress accumulates along the beam scan direction than in the transverse direction. The case is true for both a single scan as well as a full layer scan. It is shown that for a full layer scan, the longitudinal stresses highly distribute at the center of the hatching region and decrease in magnitude at the starting and ending locations. The lower stress values at the two ends of scanning tracks are not seen in this current work for EB-PBF process. The reason can be due to the additional single contour scanned after the hatching region done in the work of Parry et al. [158]. Clearly, the heat from the contour causes the temperature distribution more uniform, resulting in decreasing of material shrinkage and consequently reducing stresses on the two ends.

The thermal mechanical simulation results have been so far in good agreement with relevant studies found in the literature for LB-PBF and EB-PBF processes. The first principle stress has been found to be dominant along the scan direction. Therefore, perpendicular cracking to the scan direction closely relates to the longitudinal stresses. This has confirmed the hot cracking propagation mechanism suggested previously. Cracks belong to the network will keep growing to the top surface if they tend to be perpendicular to the  $SD_{Final}$ . In contrast, the insufficient stress will not result in re-cracking to those cracks that have been liquid backfilled if they orientate somewhat along the  $SD_{Final}$ .

## CHAPTER 7: CONCLUSION

The solidification and mechanisms of hot cracking during electron beam powder bed fusion (EB-PBF) of Co-29Cr-10Ni-7W alloy have been studied in this research. The significant findings of the study are:

1. Preliminary experiments with a wide range of EB-PBF parameters (speed function, line offset, focus offset) have shown cracking in every condition used, from the examination of sample surfaces. However, cracking has been observed to be different for different EB-PBF conditions. This is typified by samples made with a focus offset 25 mA (FO25) showing the low density of cracks and FO50 showing a high amount of cracks when other parameters are the same.
2. It has been confirmed that Co-29Cr-10Ni-7W alloy has wide solidification freezing range, which is 180 K determined in this work. This is consistent with cracking observed in samples from all the preliminary experiments. For comparison, the freezing range of the widely used Co-29Cr-6Mo alloy has been shown to be narrow (= 25 K).
3. The melt/track geometry has been shown to be focus offset dependent, with other parameters kept unchanged. It has been observed the melt pool during EB-PBF is as long as the sample width. The width and depth of the melt pool depend on the focus offset. For FO25, the width and depth are estimated to be approximately 700  $\mu\text{m}$  and 200  $\mu\text{m}$  and for FO50, they are approximately 1,160  $\mu\text{m}$  and 120  $\mu\text{m}$ , respectively. This is found to be consistent with the beam spot size ranged from 400  $\mu\text{m}$  in the most focused condition to over 1,000  $\mu\text{m}$ , as specified by the machine manufacturer.
4. The track spacing has been used to approximate the solidification growth rate (R). This together with the measurement of dendrite spacing has been used to estimate the temperature gradient (G) to be  $6 \times 10^6$  K/m and cooling rate ( $\dot{T}$ ) to be 2710 K/s. The G value is overestimated due to the possible underestimation of R. The G and R values estimated are consistent with the observed columnar dendritic growth, according to existing values in literature plotted in solidification map.
5. The use of the more focus offset will result in low melt/track aspect ratio (AR = width/depth). At low AR, the melt/track has been found to be more U-shape. Under this U-shape condition, dendrites growing horizontally in the top region, rather than just the very well known columnar growth in build direction, has been observed. The thickness of this horizontal dendrite layer can be up to 80  $\mu\text{m}$ . This growth feature has been used as a basis for a successful attempt to select EB-PBF parameters so that horizontal dendrites can be used as cracking prevention.

6. Examination of cracks surface in the as-built condition has ascertained that the cracks are (liquid) hot cracking. The single-track experiment has shown the initiation mechanism being liquation cracking. Crack networks have been demonstrated in a manner showing the scan direction dependent growth on-and-off alternatingly layer-by-layer. Of the crack networks, cracks that can be observed are predominantly normal to scan direction in the last three layers.
7. The networks of cracks that have been sequentially examined have revealed the major hot cracking mechanism to be cycles of crack growth, crack healing and crack growth again. In the first half of a cycle, liquation cracking starts normally from the existing crack below followed by solidification cracking (hot tear) during the solidification of the track in a layer building. In the second half of the cycle, crack channels in the partially melted zone are filled with liquid but this region and the liquid in the melt track do not crack subsequently during solidification in this layer building as stress state is not favorable. During the next layer building the half cycle, cracking condition is satisfied and thus cracks grow again.
8. The length of the backfilled liquid film in the partially melted zone has been approximately measured. Combining this length with the solidification freezing range of Co-29Cr-10Ni-7W alloy,  $G$  has been calculated to be  $2 \times 10^6$  K/m (not the overestimated value of  $6 \times 10^6$  K/m as stated previously). The experimentally determined values have generally agreed with  $G = 5 \times 10^5$  to  $1 \times 10^6$  K/m reported for EB-PBF of Ni-superalloys based on numerical simulation.
9. Grain boundary misorientation (GBM) has been shown to be an influential factor to hot cracking. The alternative use of EBSD orientation map in XY view (normal to build direction) in this study, has provided better observation on how grain boundary misorientation affects crack growth. Specifically, some low GBM boundaries also crack to act as bridges for the crack path.
10. Numerical simulation of PBF process has shown and confirmed that the first principle stress ( $\sigma_1$ ), which is positive, is dominantly along the scan direction during PBF. This explains why cracks observed on the surface are generally normal to the scan direction.

Based on the findings, there are recommendations for further work in the future:

1. The horizontal grains were shown to be an effective way in mitigating and even eliminating hot cracking. However, the experiment for the horizontal grains was only on a cuboidal block. Future experiments need to be done to assess and validate the application of the proposed scan strategy for acquiring the horizontal grains on different sample's geometries.

2. Further microstructure analysis needs to be conducted on the horizontal grain structure in terms of crystallographic orientation and how one grain may actually develop during the EB-PBF process. As the horizontal grains keep changing their growth directions, the question is that how the grains' shape look like? Are they in regular shape as the originally columnar grains or in an irregular shape?
3. Mechanical testing should also be conducted for both the original and horizontal grain structure for a comparison study. In addition, if the horizontal grains are in an irregular shape, an investigation needs to be done on how its effect on the mechanical properties.
4. The hot cracking of the alloys is due to the liquation of low melting elements at the grain boundaries. Despite that the hot cracking mechanism has been suggested, understanding of these low melting elements has not been studied. Therefore, elemental analysis at the grain boundary should be conducted to identify the exact compound of these elements. This can be achieved by using electron micro-probe analysis. The findings not only complement to the hot cracking understanding but also complete the solidification path of the Co-29Cr-10Ni-7W alloy.
5. Hot cracking sensitivity has been shown to be dependent on minor elements (i.e. carbon). Since the Co-29Cr-10Ni-7W alloy has been shown to have a significant amount of carbides formation at the grain boundaries (also the cracked zones), carbon element may play a crucial role. Therefore, further investigation can be done on evaluating the effect of carbon of the hot cracking sensitivity of EB-PBF of Co-29Cr-10Ni-7W alloy.

## References

- [1] I. Gibson, D. W. Rosen, and B. Stucker, *Additive Manufacturing Technologies: Rapid Prototyping to Direct Digital Manufacturing*: Springer-Verlag, 2010.
- [2] S. L. Ford, "Additive manufacturing technology: Potential implications for US manufacturing competitiveness," *Journal of International Commerce and Economics*, 2014.
- [3] C. Körner, "Additive manufacturing of metallic components by selective electron beam melting—a review," *International Materials Reviews*, pp. 1-17, 2016.
- [4] A. GE. Available: <http://www.arcam.com/technology/electron-beam-melting/hardware/>
- [5] J. Schwerdtfeger, R. F. Singer, and C. Körner, "In situ flaw detection by IR-imaging during electron beam melting," *Rapid Prototyping Journal*, vol. 18, pp. 259-263, 2012.
- [6] J. R. Davis, "ASM specialty handbook: nickel, cobalt, and their alloys," *ASM International, Member/Customer Service Center, Materials Park, OH 44073-0002, USA, 2000. 442*, 2000.
- [7] Q. Han, "Influence of Chemical Composition on Hot Tearing Susceptibility in FSX-414 Alloy," in *Transactions of the American Foundry Society and the One Hundred Eighth Annual Metalcasting Congress*, 2004, pp. 629-633.
- [8] M. Jahangiri and A. Fallah, "Effects of welding defects on reducing lifetimes of first stage nozzles of a 123 MW gas turbine made of FSX-414 alloy," *Materials & Design*, vol. 32, pp. 424-432, 2011.
- [9] K. Ronan, "A Statistical Analysis of Variations in Hot Tear Performance and Microporosity Formation Versus Composition in Investment Cast FSX-414," *Superalloys 2008*, pp. 357-366, 2008.
- [10] Available: [gasturbineworking.blogspot.com](http://gasturbineworking.blogspot.com)
- [11] C. T. Sims, "Contemporary view of cobalt-base alloys," General Electric Co., Schenectady, NY1969.
- [12] A. Beltran, "Superalloys II, CT Sims, NS Stoloff, and WC Hagel, Ed," ed: John Wiley & Sons, 1987, pp. 135-163.
- [13] K. P. Ronan, "The Effects of Small Changes in Alloy Chemistry on the Solidification Behaviour of the Cobalt-Base Superalloy FSX-414," Master Thesis, Auburn University, 2010.
- [14] J. Kasala, H. Mäsiar, and I. Pernis, "Investigation of selected thermo-physical Properties in the Co-based superalloy: Experiment and Application Study," *Arch. Foundry Eng.*, vol. 10, p. 203, 2010.
- [15] D. L. Oates, "Microstructural changes as a time temperature indicator in cobalt superalloys and a NiCoCrAlTaY coating," Doctoral Thesis, Loughborough University, 2007.
- [16] J. Campbell, *Castings*. Oxford: Butterworth Heinemann, 2003.
- [17] W. Kurz and D. J. Fisher, "Fundamentals of solidification," 1989.
- [18] P. C. Collins, D. A. Brice, P. Samimi, I. Ghamarian, and H. L. Fraser, "Microstructural Control of Additively Manufactured Metallic Materials," *Annual Review of Materials Research*, vol. 46, pp. 63-91, 2016.
- [19] M. Kirka, K. Unocic, N. Raghavan, F. Medina, R. Dehoff, and S. Babu, "Microstructure Development in Electron Beam-Melted Inconel 718 and Associated Tensile Properties," *JOM*, vol. 68, pp. 1012-1020, 2016.
- [20] A. Parsa, M. Ramsperger, A. Kostka, C. Somsen, C. Körner, and G. Eggeler, "Transmission electron microscopy of a CMSX-4 Ni-base superalloy produced by selective electron beam melting," *Metals*, vol. 6, p. 258, 2016.
- [21] H. E. Helmer, C. Körner, and R. F. Singer, "Additive manufacturing of nickel-based superalloy Inconel 718 by selective electron beam melting: Processing window and microstructure," *Journal of Materials Research*, vol. 29, pp. 1987-1996, 2014.
- [22] W. Kurz and R. Trivedi, "Rapid solidification processing and microstructure formation," *Materials Science and Engineering: A*, vol. 179, pp. 46-51, 1994.

- [23] P. Karimi, E. Sadeghi, P. Åkerfeldt, J. Ålgårdh, and J. Andersson, "Influence of successive thermal cycling on microstructure evolution of EBM-manufactured alloy 718 in track-by-track and layer-by-layer design," *Materials & design*, vol. 160, pp. 427-441, 2018.
- [24] C. Wang, X. Tan, E. Liu, and S. B. Tor, "Process parameter optimization and mechanical properties for additively manufactured stainless steel 316L parts by selective electron beam melting," *Materials & Design*, vol. 147, pp. 157-166, 2018.
- [25] Y. Zhong, L.-E. Rännar, L. Liu, A. Koptug, S. Wikman, J. Olsen, *et al.*, "Additive manufacturing of 316L stainless steel by electron beam melting for nuclear fusion applications," *Journal of Nuclear Materials*, vol. 486, pp. 234-245, 2017.
- [26] J. Valencia and P. Queded, "Thermophysical Properties," 2013.
- [27] C. Z. Hargather, S.-L. Shang, and Z.-K. Liu, "Data set for diffusion coefficients and relative creep rate ratios of 26 dilute Ni-X alloy systems from first-principles calculations," *Data in Brief*, vol. 20, pp. 1537-1551, 2018/10/01/ 2018.
- [28] J. Raplee, A. Plotkowski, M. M. Kirka, R. Dinwiddie, A. Okello, R. R. Dehoff, *et al.*, "Thermographic microstructure monitoring in electron beam additive manufacturing," *Scientific reports*, vol. 7, p. 43554, 2017.
- [29] A. Plotkowski, M. M. Kirka, and S. Babu, "Verification and validation of a rapid heat transfer calculation methodology for transient melt pool solidification conditions in powder bed metal additive manufacturing," *Additive Manufacturing*, vol. 18, pp. 256-268, 2017.
- [30] N. Raghavan, R. Dehoff, S. Pannala, S. Simunovic, M. Kirka, J. Turner, *et al.*, "Numerical modeling of heat-transfer and the influence of process parameters on tailoring the grain morphology of IN718 in electron beam additive manufacturing," *Acta Materialia*, vol. 112, pp. 303-314, 2016.
- [31] A. A. Antonysamy, J. Meyer, and P. Prangnell, "Effect of build geometry on the  $\beta$ -grain structure and texture in additive manufacture of Ti6Al4V by selective electron beam melting," *Materials characterization*, vol. 84, pp. 153-168, 2013.
- [32] S. S. Al-Bermani, M. L. Blackmore, W. Zhang, and I. Todd, "The Origin of Microstructural Diversity, Texture, and Mechanical Properties in Electron Beam Melted Ti-6Al-4V," *Metallurgical and Materials Transactions A*, vol. 41, pp. 3422-3434, 2010.
- [33] P. Wang, M. L. S. Nai, X. Tan, G. Vastola, R. Srinivasan, W. J. Sin, *et al.*, "Recent progress of additive manufactured Ti-6Al-4V by electron beam melting," in *26th Annual International Solid Freeform Fabrication Symposium—An Additive Manufacturing Conference, Austin, TX, Aug, 2016*, pp. 8-10.
- [34] H. Galarraga, R. J. Warren, D. A. Lados, R. R. Dehoff, M. M. Kirka, and P. Nandwana, "Effects of heat treatments on microstructure and properties of Ti-6Al-4V ELI alloy fabricated by electron beam melting (EBM)," *Materials Science and Engineering: A*, vol. 685, pp. 417-428, 2017/02/08/ 2017.
- [35] S.-H. Sun, Y. Koizumi, S. Kurosu, Y.-P. Li, H. Matsumoto, and A. Chiba, "Build direction dependence of microstructure and high-temperature tensile property of Co-Cr-Mo alloy fabricated by electron beam melting," *Acta Materialia*, vol. 64, pp. 154-168, 2014.
- [36] S. Gaytan, L. Murr, E. Martinez, J. Martinez, B. Machado, D. Ramirez, *et al.*, "Comparison of microstructures and mechanical properties for solid and mesh cobalt-base alloy prototypes fabricated by electron beam melting," *Metallurgical and Materials Transactions A*, vol. 41, pp. 3216-3227, 2010.
- [37] R. Kircher, A. Christensen, and K. Wurth, "Electron Beam Melted (EBM) Co-Cr-Mo Alloy for Orthopaedic Implant Applications," in *Solid Freeform Fabrication Proceedings*, 2009, pp. 428-36.
- [38] L. E. Murr, K. N. Amato, S. J. Li, Y. X. Tian, X. Y. Cheng, S. M. Gaytan, *et al.*, "Microstructure and mechanical properties of open-cellular biomaterials prototypes for total knee replacement implants fabricated by electron beam melting," *Journal of the Mechanical Behavior of Biomedical Materials*, vol. 4, pp. 1396-1411, 2011.

- [39] S.-H. Sun, Y. Koizumi, S. Kurosu, Y.-P. Li, and A. Chiba, "Phase and grain size inhomogeneity and their influences on creep behavior of Co–Cr–Mo alloy additive manufactured by electron beam melting," *Acta Materialia*, vol. 86, pp. 305-318, 2015.
- [40] T. Takashima, Y. Koizumi, Y. Li, K. Yamanaka, T. Saito, and A. Chiba, "Effect of building position on phase distribution in Co-Cr-Mo alloy additive manufactured by electron-beam melting," *Materials Transactions*, vol. 57, pp. 2041-2047, 2016.
- [41] A. Frenk and W. Kurz, "High speed laser cladding: solidification conditions and microstructure of a cobalt-based alloy," *Materials Science and Engineering: A*, vol. 173, pp. 339-342, 1993.
- [42] W. Shifeng, L. Shuai, W. Qingsong, C. Yan, Z. Sheng, and S. Yusheng, "Effect of molten pool boundaries on the mechanical properties of selective laser melting parts," *Journal of Materials Processing Technology*, vol. 214, pp. 2660-2667, 2014.
- [43] K. P. Monroy, J. Delgado, L. Sereno, J. Ciurana, and N. J. Hendrichs, "Effects of the Selective Laser Melting manufacturing process on the properties of CoCrMo single tracks," *Metals And Materials International*, vol. 20, pp. 873-884, 2014.
- [44] D. Wang, C. Song, Y. Yang, and Y. Bai, "Investigation of crystal growth mechanism during selective laser melting and mechanical property characterization of 316L stainless steel parts," *Materials & Design*, vol. 100, pp. 291-299, 2016.
- [45] D. Tomus, Y. Tian, P. A. Rometsch, M. Heilmaier, and X. Wu, "Influence of post heat treatments on anisotropy of mechanical behaviour and microstructure of Hastelloy-X parts produced by selective laser melting," *Materials Science and Engineering: A*, vol. 667, pp. 42-53, 2016.
- [46] S. A. Khairallah, A. T. Anderson, A. Rubenchik, and W. E. King, "Laser powder-bed fusion additive manufacturing: Physics of complex melt flow and formation mechanisms of pores, spatter, and denudation zones," *Acta Materialia*, vol. 108, pp. 36-45, 2016.
- [47] I. Yadroitsev, A. Gusarov, I. Yadroitsava, and I. Smurov, "Single track formation in selective laser melting of metal powders," *Journal of Materials Processing Technology*, vol. 210, pp. 1624-1631, 2010.
- [48] C. Teng, H. Gong, A. Szabo, J. Dilip, K. Ashby, S. Zhang, *et al.*, "Simulating Melt Pool Shape and Lack of Fusion Porosity for Selective Laser Melting of Cobalt Chromium Components," *Journal of Manufacturing Science and Engineering*, vol. 139, p. 011009, 2017.
- [49] Q. Shi, D. Gu, M. Xia, S. Cao, and T. Rong, "Effects of laser processing parameters on thermal behavior and melting/solidification mechanism during selective laser melting of TiC/Inconel 718 composites," *Optics & Laser Technology*, vol. 84, pp. 9-22, 2016.
- [50] K. Darvish, Z. Chen, and T. Pasang, "Reducing lack of fusion during selective laser melting of CoCrMo alloy: Effect of laser power on geometrical features of tracks," *Materials & Design*, vol. 112, pp. 357-366, 2016.
- [51] X. Zhou, K. Li, D. Zhang, X. Liu, J. Ma, W. Liu, *et al.*, "Textures formed in a CoCrMo alloy by selective laser melting," *Journal of Alloys and Compounds*, vol. 631, pp. 153-164, 2015.
- [52] J. Liu and A. C. To, "Quantitative texture prediction of epitaxial columnar grains in additive manufacturing using selective laser melting," *Additive Manufacturing*, vol. 16, pp. 58-64, 2017.
- [53] Z. Chen, M. Phan, and K. Darvish, "Grain growth during selective laser melting of a Co–Cr–Mo alloy," *Journal of materials science*, vol. 52, pp. 7415-7427, 2017.
- [54] K. Darvish, Z. Chen, M. Phan, and T. Pasang, "Selective laser melting of Co-29Cr-6Mo alloy with laser power 180–360 W: Cellular growth, intercellular spacing and the related thermal condition," *Materials Characterization*, vol. 135, pp. 183-191, 2018.
- [55] W. Yan, Y. Qian, W. Ge, S. Lin, W. K. Liu, F. Lin, *et al.*, "Meso-scale modeling of multiple-layer fabrication process in selective electron beam melting: inter-layer/track voids formation," *Materials & Design*, vol. 141, pp. 210-219, 2018.
- [56] M. F. Zäh and S. Lutzmann, "Modelling and simulation of electron beam melting," *Production Engineering*, vol. 4, pp. 15-23, 2010.

- [57] B. Cheng and K. Chou, "Melt pool geometry simulations for powder-based electron beam additive manufacturing," in *24th Annual International Solid Freeform Fabrication Symposium—An Additive Manufacturing Conference, Austin, TX, USA, 2013*, pp. 644-654.
- [58] M. Jamshidinia, F. Kong, and R. Kovacevic, "Numerical modeling of heat distribution in the electron beam melting® of Ti-6Al-4V," *Journal of Manufacturing Science and Engineering*, vol. 135, p. 061010, 2013.
- [59] T. Scharowsky, F. Osmanlic, R. Singer, and C. Körner, "Melt pool dynamics during selective electron beam melting," *Applied Physics A*, vol. 114, pp. 1303-1307, 2014.
- [60] D. Riedlbauer, T. Scharowsky, R. F. Singer, P. Steinmann, C. Körner, and J. Mergheim, "Macroscopic simulation and experimental measurement of melt pool characteristics in selective electron beam melting of Ti-6Al-4V," *The International Journal of Advanced Manufacturing Technology*, vol. 88, pp. 1309-1317, 2017.
- [61] S. Price, B. Cheng, J. Lydon, K. Cooper, and K. Chou, "On process temperature in powder-bed electron beam additive manufacturing: process parameter effects," *Journal of Manufacturing Science and Engineering*, vol. 136, p. 061019, 2014.
- [62] H. Gong, K. Rafi, T. Starr, and B. Stucker, "The Effects of Processing Parameters on Defect Regularity in Ti-6Al-4V Parts Fabricated By Selective Laser Melting and Electron Beam Melting," in *24th Annual International Solid Freeform Fabrication Symposium—An Additive Manufacturing Conference, Austin, TX, Aug, 2013*, pp. 12-14.
- [63] J. C. Lippold, *Welding metallurgy and weldability*: Wiley Online Library, 2015.
- [64] S. Kou and Y. Le, "Nucleation mechanism and grain refining of weld metal," *Welding Journal*, vol. 65, pp. 305-320, 1986.
- [65] A. Basak and S. Das, "Epitaxy and Microstructure Evolution in Metal Additive Manufacturing," *Annual Review of Materials Research*, 2016.
- [66] P. Rajamaeki, "Fusion weld metal solidification: Continuum from weld interface to centerline," 2008.
- [67] S. Kou, *Welding metallurgy*: John Wiley & Sons, 2003.
- [68] L. E. Murr, S. M. Gaytan, D. A. Ramirez, E. Martinez, J. Hernandez, K. N. Amato, *et al.*, "Metal fabrication by additive manufacturing using laser and electron beam melting technologies," *Journal of Materials Science & Technology*, vol. 28, pp. 1-14, 2012.
- [69] D. Coutsouradis, A. Davin, and M. Lamberigts, "Cobalt-based superalloys for applications in gas turbines," *Materials Science and Engineering*, vol. 88, pp. 11-19, 1987.
- [70] D. Eskin and L. Katgerman, "Mechanical properties in the semi-solid state and hot tearing of aluminium alloys," *Progress in Materials Science*, vol. 49, pp. 629-711, 2004.
- [71] A. Chojecki, I. Telejko, and T. Bogacz, "Influence of chemical composition on the hot tearing formation of cast steel," *Theoretical and applied fracture mechanics*, vol. 27, pp. 99-105, 1997.
- [72] C. Monroe and C. Beckermann, "Development of a hot tear indicator for steel castings," *Materials Science and Engineering: A*, vol. 413, pp. 30-36, 2005.
- [73] S. Kou, "Solidification and liquation cracking issues in welding," *JOM*, vol. 55, pp. 37-42, 2003.
- [74] S. Li, "Hot tearing in cast aluminum alloys: measures and effects of process variables," 2010.
- [75] E.-J. Chun, K. Nishimoto, and K. Saida, "Evaluation of solidification cracking susceptibility in laser welds for type 316FR stainless steel," *Welding in the World*, vol. 60, pp. 217-231, 2016.
- [76] C. Cross, "On the origin of weld solidification cracking," in *Hot cracking phenomena in welds*, ed: Springer, 2005, pp. 3-18.
- [77] J. Zhang and R. Singer, "Hot tearing of nickel-based superalloys during directional solidification," *Acta Materialia*, vol. 50, pp. 1869-1879, 2002.
- [78] D. Eskin and L. Katgerman, "A quest for a new hot tearing criterion," *Metallurgical and Materials Transactions A*, vol. 38, pp. 1511-1519, 2007.

- [79] R. Dou and A. Phillion, "Application of a Pore Fraction Hot Tearing Model to Directionally Solidified and Direct Chill Cast Aluminum Alloys," *Metallurgical and Materials Transactions A*, pp. 1-9.
- [80] M. O. El-Bealy, "On the formation of macrosegregation and interdendritic cracks during dendritic solidification of continuous casting of steel," *Metallurgical and Materials Transactions B*, vol. 45, pp. 988-1017, 2014.
- [81] Y. Li, Q. Bai, J. Liu, H. Li, Q. Du, J. Zhang, *et al.*, "The Influences of Grain Size and Morphology on the Hot Tearing Susceptibility, Contraction, and Load Behaviors of AA7050 Alloy Inoculated with Al-5Ti-1B Master Alloy," *Metallurgical and Materials Transactions A*, pp. 1-14, 2016.
- [82] I. I. Novikov, "Hot-Shortness of Nonferrous Metals and Alloys," DTIC Document 1968.
- [83] M. Rappaz, J.-M. Drezet, and M. Gremaud, "A new hot-tearing criterion," *Metallurgical and Materials Transactions A*, vol. 30, pp. 449-455, 1999.
- [84] S. Lin, C. Aliravci, and M. Pekguleryuz, "Hot-tear susceptibility of aluminum wrought alloys and the effect of grain refining," *Metallurgical and Materials Transactions A*, vol. 38, pp. 1056-1068, 2007.
- [85] C. Dickhaus, L. Ohm, and S. Engler, "Mechanical properties of solidifying shells of aluminum alloys," *Transactions-American Foundrymen Society*, pp. 677-677, 1993.
- [86] D. J. Lahaie and M. Bouchard, "Physical modeling of the deformation mechanisms of semisolid bodies and a mechanical criterion for hot tearing," *Metallurgical and Materials Transactions B*, vol. 32, pp. 697-705, August 01 2001.
- [87] J. A. Williams, and Singer, A. R. E., *Journal of Institute of Metals*, vol. 96, pp. 5-12, 1968.
- [88] N. Prokhorov, "Resistance to hot tearing of cast metals during solidification," *Russian castings production*, vol. 2, pp. 172-175, 1962.
- [89] R. W. Messler, *Joining of advanced materials*: Butterworths, 1993.
- [90] J. Lippold, W. Baeslack, and I. Varol, "Heat-affected zone liquation cracking in austenitic and duplex stainless steels," *Welding Journal(USA)*, vol. 71, p. 1, 1988.
- [91] C. Huang and S. Kou, "Liquation cracking in full-penetration Al-Cu welds," *Welding Journal-New York*, vol. 83, pp. 50-S, 2004.
- [92] J. C. Lippold, *Welding metallurgy and weldability*: John Wiley & Sons, 2014.
- [93] N. E. Nissley, M. G. Collins, G. Guaytima, and J. C. Lippold, "Development of the Strain-to-Fracture Test for Evaluating Ductility-Dip Cracking in Austenitic Stainless Steels and Ni-Base Alloys," *Welding in the World*, vol. 46, pp. 32-40, 2002.
- [94] A. J. Ramirez and J. C. Lippold, "High temperature behavior of Ni-base weld metal: Part II – Insight into the mechanism for ductility dip cracking," *Materials Science and Engineering: A*, vol. 380, pp. 245-258, 2004.
- [95] A. J. Ramirez, J. W. Sowards, and J. C. Lippold, "Improving the ductility-dip cracking resistance of Ni-base alloys," *Journal of materials processing technology*, vol. 179, pp. 212-218, 2006.
- [96] J. C. Lippold and N. E. Nissley, "Further Investigations of Ductility-Dip Cracking in High Chromium, Ni-Base Filler Metals," *Welding in the World*, vol. 51, pp. 24-30, 2007.
- [97] N. Nissley and J. Lippold, "Ductility-dip cracking susceptibility of nickel-based weld metals part 1: strain-to-fracture testing," *Welding Journal*, vol. 87, pp. 257s-264s, 2008.
- [98] N. Nissley and J. Lippold, "Ductility-dip cracking susceptibility of nickel-based weld metals: part 2—microstructural characterization," *Weld. J.*, vol. 88, pp. 131s-140s, 2009.
- [99] D. J. Lee, Y. S. Kim, Y. T. Shin, E. C. Jeon, S. H. Lee, H. J. Lee, *et al.*, "Contribution of Precipitate on Migrated Grain Boundaries to Ductility-Dip Cracking in Alloy 625 Weld Joints," *Metals And Materials International*, vol. 16, pp. 813-817, 2010.
- [100] R. Qin, H. Wang, and G. He, "Investigation on the Microstructure and Ductility-Dip Cracking Susceptibility of the Butt Weld Welded with ENiCrFe-7 Nickel-Base Alloy-Covered Electrodes," *Metallurgical and Materials Transactions A*, vol. 46, pp. 1227-1236, 2015.
- [101] V. C. Kreuter V and J. C. Lippold, "Ductility-Dip Cracking Susceptibility of Commercially Pure Ni and Ni-Base Alloys Utilizing the Strain-to-Fracture Test," in

- Cracking Phenomena in Welds IV*, T. Boellinghaus, J. C. Lippold, and C. E. Cross, Eds., ed Cham: Springer International Publishing, 2016, pp. 145-159.
- [102] C. Fink, M. Zinke, and S. Jüttner, "An investigation of ductility-dip cracking in the base metal heat-affected zone of wrought nickel base alloys—part II: correlation of PVR and STF results," *Welding in the World*, vol. 60, pp. 951-961, 2016.
- [103] N. Nissley and J. Lippold, "Development of the strain-to-fracture test," *Welding Journal*, vol. 82, pp. 355-364, 2003.
- [104] J. Q. Chen, H. Lu, C. Yu, J. M. Chen, and M. L. Zhang, "Ductility dip cracking mechanism of Ni–Cr–Fe alloy based on grain boundary energy," *Science and Technology of Welding and Joining*, vol. 18, pp. 346-353, 2013/05/01 2013.
- [105] J. Q. Chen, H. Lu, W. Cui, J. M. Chen, and Y. F. Huang, "Effect of grain boundary behaviour on ductility dip cracking mechanism," *Materials Science and Technology*, vol. 30, pp. 1189-1196, 2014/08/01 2014.
- [106] F. Noecker and J. DuPont, "Metallurgical investigation into ductility dip cracking in Ni-based alloys: Part II," *Welding Journal*, vol. 88, pp. 62s-77s, 2009.
- [107] F. Noecker and J. DuPont, "Metallurgical investigation into ductility dip cracking in Ni-based alloys: Part I," *Welding Journal*, vol. 88, pp. 7S-20S, 2009.
- [108] G. Gottstein and L. S. Shvindlerman, *Grain boundary migration in metals: thermodynamics, kinetics, applications*: CRC press, 2009.
- [109] J. Caron, S. Babu, and J. Lippold, "The Weld Heat-Affected Zone Liquation Cracking Susceptibility of Naval Steels," *Welding Journal*, 2013.
- [110] M. Qian and J. Lippold, "The effect of multiple postweld heat treatment cycles on the weldability of Waspaloy®," *Welding Journal-New York*, vol. 81, pp. 233-S, 2002.
- [111] J. C. Lippold, S. D. Kiser, and J. N. DuPont, *Welding metallurgy and weldability of nickel-base alloys*: John Wiley & Sons, 2011.
- [112] M. Cloots, P. J. Uggowitzer, and K. Wegener, "Investigations on the microstructure and crack formation of IN738LC samples processed by selective laser melting using Gaussian and doughnut profiles," *Materials & Design*, vol. 89, pp. 770-784, 2016.
- [113] E. Chauvet, P. Kontis, E. A. Jäggle, B. Gault, D. Raabe, C. Tassin, *et al.*, "Hot cracking mechanism affecting a non-weldable Ni-based superalloy produced by selective electron Beam Melting," *Acta Materialia*, vol. 142, pp. 82-94, 2018.
- [114] D. Tomus, T. Jarvis, X. Wu, J. Mei, P. Rometsch, E. HERNY, *et al.*, "Controlling the Microstructure of Hastelloy-X Components Manufactured by Selective Laser Melting," *Physics Procedia*, vol. 41, pp. 823-827, 2013.
- [115] N. J. Harrison, I. Todd, and K. Mumtaz, "Reduction of micro-cracking in nickel superalloys processed by Selective Laser Melting: A fundamental alloy design approach," *Acta Materialia*, vol. 94, pp. 59-68, 2015.
- [116] L. N. Carter, M. M. Attallah, and R. C. Reed, "Laser powder bed fabrication of nickel-base superalloys: influence of parameters; characterisation, quantification and mitigation of cracking," *Superalloys 2012*, pp. 577-586, 2012.
- [117] B. Rutttert, M. Ramsperger, L. M. Roncery, I. Lopez-Galilea, C. Körner, and W. Theisen, "Impact of hot isostatic pressing on microstructures of CMSX-4 Ni-base superalloy fabricated by selective electron beam melting," *Materials & Design*, vol. 110, pp. 720-727, 2016.
- [118] M. Ramsperger, R. F. Singer, and C. Körner, "Microstructure of the Nickel-Base Superalloy CMSX-4 Fabricated by Selective Electron Beam Melting," *Metallurgical and Materials Transactions A: Physical Metallurgy and Materials Science*, vol. 47, pp. 1469-1480, 2016.
- [119] M. Rappaz, A. Jacot, and W. J. Boettinger, "Last-stage solidification of alloys: Theoretical model of dendrite-arm and grain coalescence," *Metallurgical and Materials Transactions A*, vol. 34, pp. 467-479, 2003.
- [120] E. Chauvet, C. Tassin, J.-J. Blandin, R. Dendievel, and G. Martin, "Producing Ni-base superalloys single crystal by selective electron beam melting," *Scripta Materialia*, vol. 152, pp. 15-19, 2018.

- [121] H. Peng, Y. Shi, S. Gong, H. Guo, and B. Chen, "Microstructure, mechanical properties and cracking behaviour in a  $\gamma'$ -precipitation strengthened nickel-base superalloy fabricated by electron beam melting," *Materials & Design*, vol. 159, pp. 155-169, 2018.
- [122] D. Ramirez, L. Murr, E. Martinez, D. Hernandez, J. Martinez, B. Machado, *et al.*, "Novel precipitate–microstructural architecture developed in the fabrication of solid copper components by additive manufacturing using electron beam melting," *Acta Materialia*, vol. 59, pp. 4088-4099, 2011.
- [123] M. Chauhan, "Microstructural characterization of cobalt chromium (ASTM F75) cubes produced by EBM technique," 2017.
- [124] M. L. Montero Sistiaga, R. Mertens, B. Vrancken, X. Wang, B. Van Hooreweder, J.-P. Kruth, *et al.*, "Changing the alloy composition of Al7075 for better processability by selective laser melting," *Journal of Materials Processing Tech.*, vol. 238, pp. 437-445, 2016.
- [125] P. Mercelis and J.-P. Kruth, "Residual stresses in selective laser sintering and selective laser melting," *Rapid Prototyping Journal*, vol. 12, pp. 254-265, 2006.
- [126] Y. Chen, K. Zhang, J. Huang, S. R. E. Hosseini, and Z. Li, "Characterization of heat affected zone liquation cracking in laser additive manufacturing of Inconel 718," *Materials & Design*, vol. 90, pp. 586-594, 2016.
- [127] W. Sames, F. List, S. Pannala, R. Dehoff, and S. Babu, "The metallurgy and processing science of metal additive manufacturing," *International Materials Reviews*, pp. 1-46, 2016.
- [128] M. Kahnert, S. Lutzmann, and M. Zaeh, "Layer formations in electron beam sintering," in *Solid freeform fabrication symposium*, 2007, pp. 88-99.
- [129] W. J. Sames, K. A. Unocic, R. R. Dehoff, T. Lolla, and S. S. Babu, "Thermal effects on microstructural heterogeneity of Inconel 718 materials fabricated by electron beam melting," *Journal of Materials Research*, vol. 29, pp. 1920-1930, 2014.
- [130] P. Prabhakar, W. J. Sames, R. Dehoff, and S. S. Babu, "Computational modeling of residual stress formation during the electron beam melting process for Inconel 718," *Additive Manufacturing*, vol. 7, pp. 83-91, 2015/07/01/ 2015.
- [131] W. Kan, B. Chen, C. Jin, H. Peng, and J. Lin, "Microstructure and mechanical properties of a high Nb-TiAl alloy fabricated by electron beam melting," *Materials & Design*, vol. 160, pp. 611-623, 2018/12/15/ 2018.
- [132] C. Smith, S. Tammam-Williams, E. Hernandez-Nava, and I. Todd, "Tailoring the thermal conductivity of the powder bed in Electron Beam Melting (EBM) Additive Manufacturing," *Scientific reports*, vol. 7, p. 10514, 2017.
- [133] M. Galati and L. Iuliano, "A literature review of powder-based electron beam melting focusing on numerical simulations," *Additive Manufacturing*, vol. 19, pp. 1-20, 2018.
- [134] M. Fousová, D. Vojtěch, K. Doubrava, M. Daniel, and C.-F. Lin, "Influence of inherent surface and internal defects on mechanical properties of additively manufactured Ti6Al4V alloy: Comparison between selective laser melting and electron beam melting," *Materials*, vol. 11, p. 537, 2018.
- [135] T. R. Mahale, "Electron beam melting of advanced materials and structures," Doctoral Dissertation, 2009.
- [136] W. J. Boettinger, U. R. Kattner, K.-W. Moon, and J. H. Perepezko, "DTA and heat-flux DSC measurements of alloy melting and freezing," in *Methods for phase diagram Determination*, ed: Elsevier, 2007, pp. 151-221.
- [137] P. Gabbott, "A practical introduction to differential scanning calorimetry," *Principles and applications of thermal analysis*, pp. 1-50, 2008.
- [138] NETZSCH. Available: <https://www.netzsch-thermal-analysis.com/us/products-solutions/differential-scanning-calorimetry/>
- [139] Industrialheating. Available: [www.industrialheating.com](http://www.industrialheating.com)
- [140] MyScope. Available: <https://myscope.training/>
- [141] A. J. Schwartz, M. Kumar, B. L. Adams, and D. P. Field, *Electron backscatter diffraction in materials science*: Springer, 2000.
- [142] EBSD. Available: [www.ebsd.com](http://www.ebsd.com)

- [143] S. Kurosu, H. Matsumoto, and A. Chiba, "Isothermal phase transformation in biomedical Co-29Cr-6Mo alloy without addition of carbon or nitrogen," *Metallurgical and Materials Transactions A*, vol. 41, pp. 2613-2625, 2010.
- [144] A. Saldivar-Garcia and H. Lopez, "Temperature effects on the lattice constants and crystal structure of a Co-27Cr-5Mo low-carbon alloy," *Metallurgical and Materials Transactions A*, vol. 35, pp. 2517-2523, 2004.
- [145] M. V. Mergulhão and M. Neves, "Characteristics of Biometallic Alloy to Additive Manufacturing Using Selective Laser Melting Technology," *Journal of Biomaterials and Nanobiotechnology*, vol. 9, p. 89, 2017.
- [146] T. Kilner, R. Pilliar, G. Weatherly, and C. Allibert, "Phase identification and incipient melting in a cast Co - Cr surgical implant alloy," *Journal of biomedical materials research*, vol. 16, pp. 63-79, 1982.
- [147] L. Ramírez-Vidaurre, M. Castro-Roman, M. Herrera-Trejo, C. Garcia-Lopez, and E. Almanza-Casas, "Cooling rate and carbon content effect on the fraction of secondary phases precipitate in as-cast microstructure of ASTM F75 alloy," *Journal of Materials Processing Technology*, vol. 209, pp. 1681-1687, 2009.
- [148] Y. Zhao, Y. Koizumi, K. Aoyagi, D. Wei, K. Yamanaka, and A. Chiba, "Molten pool behavior and effect of fluid flow on solidification conditions in selective electron beam melting (SEBM) of a biomedical Co-Cr-Mo alloy," *Additive Manufacturing*, vol. 26, pp. 202-214, 2019.
- [149] Z. Chen, T. Guraya, K. Darvish, M. Phan, and T. Pasang, "Solidification During Selective Laser Melting of Co-29Cr-6Mo Alloy," *JOM*, vol. 71, pp. 691-696, 2019.
- [150] N. Raghavan, S. Simunovic, R. Dehoff, A. Plotkowski, J. Turner, M. Kirka, *et al.*, "Localized melt-scan strategy for site specific control of grain size and primary dendrite arm spacing in electron beam additive manufacturing," *Acta Materialia*, vol. 140, pp. 375-387, 2017.
- [151] Y. Lee, M. M. Kirka, S. Kim, N. Sridharan, A. Okello, R. R. Dehoff, *et al.*, "Asymmetric Cracking in Mar-M247 Alloy Builds During Electron Beam Powder Bed Fusion Additive Manufacturing," *Metallurgical and Materials Transactions A*, vol. 49, pp. 5065-5079, 2018.
- [152] X. Tan, P. Wang, Y. Kok, W. Toh, Z. Sun, S. Nai, *et al.*, "Carbide precipitation characteristics in additive manufacturing of Co-Cr-Mo alloy via selective electron beam melting," *Scripta Materialia*, vol. 143, pp. 117-121, 2018.
- [153] J. Liu and S. Kou, "Crack susceptibility of binary aluminum alloys during solidification," *Acta Materialia*, vol. 110, pp. 84-94, 2016.
- [154] S. M. Gaytan Guillen, "Fundamental studies of Cobalt-base superalloy biomedical prototypes fabricated by electron beam melting: microstructures and microstructural architecture," 2011.
- [155] N. Wang, S. Mokadem, M. Rappaz, and W. Kurz, "Solidification cracking of superalloy single- and bi-crystals," *Acta Materialia*, vol. 52, pp. 3173-3182, 2004.
- [156] S. Tadano, T. Hino, and Y. Nakatani, "A modeling study of stress and strain formation induced during melting process in powder-bed electron beam melting for Ni superalloy," *Journal of materials processing technology*, vol. 257, pp. 163-169, 2018.
- [157] M. Jamshidinia, F. Kong, and R. Kovacevic, "The coupled CFD-FEM model of electron beam melting®(EBM)," 2013.
- [158] L. Parry, I. Ashcroft, and R. D. Wildman, "Understanding the effect of laser scan strategy on residual stress in selective laser melting through thermo-mechanical simulation," *Additive Manufacturing*, vol. 12, pp. 1-15, 2016.